Gyrokinetic Simulation of Microtearing Turbulence

Dissertation

zur Erlangung des Doktorgrades
Dr. rer. nat.

der Fakultät für Naturwissenschaften
der Universität Ulm

vorgelegt von

Hauke Doerk

aus

Lüneburg

Ulm 2012

Amtierender Dekan
Prof. Dr. Axel Groß

Erstgutachter
Prof. Dr. Frank Jenko

Zweitgutachter
Prof. Dr. Peter Reineker

Datum der Promotion
9.01.2013

Zusammenfassung

In modernen Fusionsexperimenten wird die Güte des Plasmaeinschlusses in einem magnetischen Feld größtenteils durch turbulente Prozesse bestimmt. Tiefergehendes theoretisches Verständnis in diesem Bereich trägt somit zur Weiterentwicklung heutiger und zukünftiger Fusionsexperimente bei. Ziel der Fusionsforschung ist es, Kernfusion als sichere und langfristige Energiequelle nutzbar zu machen und so zur nachhaltigen Energieversorgung der Menschheit beizutragen. Besonders in großen Maschinen, wie dem zur Zeit im Aufbau befindlichen Experiment ITER oder einem zukünftigen Fusionskraftwerk, wirkt die Plasmaheizung vorwiegend auf die Elektronenspezies. Es ist daher wichtig, unser Verständnis des Elektronenwärmetransportes zu erweitern. Neben Mikroinstabilitäten auf der Skala von Elektronengyroradien kann auch ein stochastisches Magnetfeld zu erhöhtem Elektronenwärmetransport beitragen. Als mögliche Quelle solcher stochastischen Magnetfelder wird seit den 1970er Jahren die sogenannte 'Microtearing Mode' diskutiert. Diese Namensgebung resultiert aus deren Eigenschaft die Magnetfeldtopologie aufzubrechen, um kleinskalige magnetische Inseln zu formen. Die zugrundeliegende Plasmainstabilität und ihr nichtlineares, turbulentes Verhalten wird in dieser Arbeit untersucht. Zu diesem Zweck werden Simulationen mit dem Turbulenzcode GENE durchgeführt.

Die zugrundeliegenden gyrokinetischen Gleichungen sind nicht nur geeignet, um turbulente Prozesse zu beschreiben, sondern eignen sich auch zur Berechnung des neoklassischen Transports. Letzteres beinhaltet interessante Physik auf relativ langen Zeitskalen, stellt aber außerdem einen exzellenten Test für den Landau-Boltzmann Stoßoperator dar, der in GENE implementiert ist. Es zeigt sich, dass eine genauere Berücksichtigung einer gewissen Symmetrie (der Selbstadjungiertheit) zu einer besseren Übereinstimmung mit dem etablierten neoklassischen Code NEO führt. Der Vergleich mit NEO verwendet die lokale Näherung, doch auch der radial globale Stoßoperator wird erfolgreich gegen den PIC code ORB5 getestet. Die durchgeführten neoklassischen Studien sind auch für die Berechnung von Mikroturbulenz von Belang, da Stoßprozesse beispielsweise einen wichtigen Beitrag zum Instabilitätsmechanismus von Microtearing Moden leisten.

Unter Berücksichtigung von Plasmaparametern, die realistisch für das Fusionsexperiment ASDEX Upgrade sind, finden sich Microtearing Instabilitäten in GENE Simulationen. Diese Parameter lassen sich auch auf gewisse ITER Szenarien übertragen. Die relevanten Wellenlängen liegen leicht oberhalb des Ionengyroradius, es zeichnen sich jedoch wesentlich feinere radiale Strukturen ab. Obwohl nichtlineare Simulationen wegen dieser Anisotropie extrem anspruchsvoll sind, gelingt es erstmalig, Microtearing-Turbulenz in gyrokinetischen Simulationen zu berechnen. Übersteigen die Magnetfeldfluktuationen eine gewisse Amplitude, so lässt sich der re-

sultierende Elektronenwärmefluss gut mit einem einfachen Diffusivitätsmodell nach Rechester und Rosenbluth beschreiben, das stochastische Magnetfelder voraussetzt. Die Magnetfeld-Diffusivität wird in den Simulationen gemessen, zeigt sich aber auch rein graphisch in Poincaré-Schnitten.

Insgesamt etablieren unsere Berechnungen Microtearing-Turbulenz als weitere mögliche Ursache für den erhöhten Elektronenwärmetransport in Tokamak-Fusionsexperimenten.

Summary

In modern fusion experiments, plasma turbulence is responsible for the radial heat transport and thus determines the plasma confinement within the magnetic field of tokamak devices. Deeper theoretical understanding is needed to explain today's and future fusion experiments. The goal of fusion research is to establish nuclear fusion as a safe and sustainable energy source. In future fusion power plants, and also in large fusion experiments like the presently constructed ITER, plasma heating predominantly affects the electron species. The reason is of fundamental nature: the collisional cross section of fast ions that are produced by the heating systems is larger for thermal electrons than for thermal ions. It is thus essential to correctly predict electron thermal transport, but the overall picture still continues to evolve. Besides microinstabilities on the electron gyroradius scales, also a stochastized magnetic field can contribute to enhanced electron transport. Already since the 1970's, the so-called microtearing instability is discussed as a source of stochastic fields. This microinstability deserves its name for breaking up the magnetic field structure by forming small-scale magnetic islands. The linear microtearing instability and its nonlinear, turbulent behavior is investigated in this thesis by means of numerical simulations with the gyrokinetic turbulence code GENE.

The underlying gyrokinetic equations are not only appropriate to predict turbulent transport, but also describe neoclassical transport that is drift-kinetic in nature. Besides revealing interesting physics on long time scales, solving the neoclassical equation serves as an excellent test for the numerical implementation of the collision operator in GENE. Focusing on the local limit, it is found that a modification of this implementation that considers certain symmetries is necessary to obtain a satisfactory agreement with the well-established drift-kinetic neoclassical code NEO. Also the radially global implementation of collisions is successfully benchmarked against the PIC code ORB5. Validation of the collision operator is of relevance for microturbulence simulations as well, since collisional effects, for example, play an important role in the instability mechanism of microtearing modes.

Considering plasma parameters that are realistic for the fusion experiment ASDEX Upgrade, a standard tokamak device, microtearing modes are found in GENE simulations. These parameters are also relevant for certain ITER scenarios. The most unstable toroidal wavelength lies somewhat above the ion gyroradius, but much finer radial scales are developed. Although this inherent multiscale feature causes nonlinear simulations to be extremely challenging, such gyrokinetic simulations of microtearing turbulence succeed for the first time in the coarse of this work. An outstanding feature of these simulations is that the radial transport of (electron) heat is well described by a simple diffusivity model, as long as the magnetic field

fluctuations exceed a certain threshold. The employed Rechester-Rosenbluth type of model crucially relies on magnetic field stochasticity. To show that this condition is fulfilled, the value for the magnetic field diffusivity is computed from the simulation data.

Since the resulting transport level is found to be experimentally relevant, our simulations establish microtearing turbulence as an additional candidate to explain enhanced electron thermal transport in standard tokamaks.

Contents

1. Introduction

1.1. The physics of plasmas

Plasma constitutes the fourth state of matter and is generally defined as an ionized gas. Unlike in a neutral gas, electromagnetic forces play a central role in plasmas. This opens a field of research that offers great variety and diversity. A large amount of matter in the universe is in the plasma state. The interstellar medium consists of a dilute and cold plasma, developing extremely large scale magnetic fields. Stars themselves, including our Sun, are formed of more condensed, but very hot plasmas. In the core of the Sun, temperatures of 15 million Kelvin are reached. On Earth, plasmas are found in nature—lightnings are a popular example—as well as in laboratory experiments. Every-day applications like fluorescent lamps are ubiquitous, but also high-tech applications of plasma physics exist, one example is plasma etching of surfaces. Moreover, the methods of plasma physics prove useful to trap anti-protons, thereby helping to study the fundamental symmetry between matter and antimatter.[1]

Plasmas of all scales, in space and in the laboratory, often exhibit nonlinear redistribution of energy in a turbulent way. Supernova explosions, for example, drive turbulence in the interstellar medium. Such processes have become experimentally accessible with radio-wave measurements. Also the development of astrophysical phenomena like jets and accretion discs is largely determined by plasma turbulence.[2, 3] Due to a much larger number of degrees of freedom, plasma turbulence is more diverse than its fluid counterpart. Importantly, plasma turbulence plays a key role in one of the most complex technologies that are presently developed—fusion power plants. Extreme temperatures of more than 100 million Kelvin are reached in fusion experiments. The goal of fusion research is to establish nuclear fusion as a safe, sustainable, and environmentally friendly energy source for humanity.[1] It turns out that energy confinement—that is related to energy gain—is mainly limited by plasma turbulence.[5] Accurate predictions thus require theoretical understanding of the underlying physics and the overall picture continues to evolve. In the following, we motivate fusion research in magnetic confinement devices and develop the basic concepts of energy (and particle) transport in these devices.

[1] Interesting material on the scientific progress in fusion research can be found on the ITER website Ref. [4]

1.2. Fusion energy

Fusion is the energy source in the core of stars. Beginning with the lightest element, hydrogen, nuclear fusion is also responsible for the formation of heavier elements, up to iron. Energy is released, because these heavier elements are often more strongly bound by nuclear forces. We note in passing that even heavier elements are created in Supernova explosions of stars in which fusion reactions ceased after all fuel had been burned. Our Sun is a comparably small star, but nevertheless every second it turns 600 million tons of hydrogen into helium, thereby releasing an enormous amount of energy. The main nuclear reaction achieving this is called proton-proton chain. Involving a variety of sub-reactions, it can be summarized as

$$4\,{}^{1}_{1}\mathrm{H} \rightarrow {}^{4}_{2}\mathrm{He} + 2\mathrm{e}^{+} + 2\nu_{e^-} + 2\gamma + 25.7\,\mathrm{MeV}\,.$$

In the first half of the 20th century, the discovery of nuclear fusion to be responsible for energy production in the Sun—and therefore enabling life on Earth—was indeed astonishing. Ever since, scientists aim at harnessing fusion energy on Earth. Because the proton-proton chain involves the weak nuclear interaction to transform protons into neutrons, this reaction is too slow to be efficiently realized on earth. Instead, the most promising fusion reaction begins with the hydrogen isotopes deuterium and tritium,

$${}^{2}_{1}\mathrm{D} + {}^{3}_{1}\mathrm{T} \rightarrow {}^{4}_{1}\mathrm{He} + {}^{1}_{0}\,\mathrm{n} + 17.59\,\mathrm{MeV}\,,$$

creating a helium nucleus that carries 20% of the released energy and a neutron that gets 80% of the released energy, according to the mass ratio. The D-T fusion reaction is actually the most efficient fusion reaction which exists.

The potential of fusion energy

As a matter of fact, the world-wide energy consumption is predicted to increase by a factor of five until to end of the century. Today's energy production mostly relies on the combustion of fossil fuels, releasing enormous amounts of CO_2 into the Earth's atmosphere. It is commonly accepted that severe environmental problems are the result, including climate change. As a reaction to these circumstances, governments of many countries agree on saving energy and support programs to research technologies to overcome combustion of fossil fuels. One established alternative technology are nuclear fission power plants that are virtually free of CO_2-release. They are, however, controversially discussed because the danger of severe accidents exists[2] and long-lived radioactive waste is produced. Another alternative is given by regenerative energy forms like wind, water, and solar power. Despite great recent progress in that area, it is difficult to provide sufficient supply with these technologies alone.

[2] Chernobyl 1986: control over chain reaction was lost.
Fukushima 2011: after shut-down of chain reactions, the cooling system broke down that is required to remove the afterheat that emanates from further decay of the fission products.

The reason is mainly seen in the need for massive energy storage to be installed in order to balance daily and seasonal fluctuations in wind strength and sunshine duration. Further development of techniques to greatly exceed the installed (and easily accessible) storage capacity is needed.

In that framework, fusion power plants enter the discussion as another energy source. The main motivation for fusion research, despite all technological difficulties, is the superior efficiency of the D-T fusion reaction and its safety. The energy released in a single fusion event exceeds that of a single combustion reaction by a factor of a million. Moreover, fusion energy is virtually free of CO_2 release and the danger of an uncontrolled chain reaction does not exist. The fusion reaction itself does not produce radioactive materials. Radioactive isotopes are created in the reactor wall, which has to be stored (only) for a few decades after the reactor is shut down. This storage is thus much less problematic than that of radioactive waste of a fission power plant.

Fusion requirements

The main challenge of initiating nuclear fusion is to overcome the repulsive Coulomb forces between two positively charged nuclei. The strong nuclear forces that bind the helium nucleus only have a range of the order of 10^{-15} m. The corresponding potential barrier that the fusion partners have to overcome is as large as a few 100 keV.[3] Highly energetic collisions are required that are commonly realized by strongly heating a deuterium tritium mixture. Fortunately, the quantum mechanical tunneling effect yields an enhanced probability of fusion reactions even at an average kinetic energy of 10-20 keV, well below the height of the Coulomb barrier. Ultimately, it is this quantum mechanical effect that makes fusion reactors feasible. Still, the required kinetic energy corresponds to temperatures of 100-200 million Kelvin, which by far exceed the atomic (electron) binding energy. As a consequence, the plasma state of matter is reached under these conditions.

Technical realization: Magnetic confinement

The most promising method for creating and maintaining such a high-temperature plasma is the confinement in a magnetic field.[6] The Lorentz force $(q/m)\mathbf{v} \times \mathbf{B}$ prohibits free particle motion perpendicular to the magnetic field. End-losses are prevented by constructing toroidal devices. Plasmas confined in simple ring-shaped magnetic fields, however, are subject to drifts and thus unstable. Good confinement can be reached when the field lines are helically twisted, as shown in Fig. 1.2.1. Major advances have been made in the 1950's, when Soviet scientists developed a machine called *tokamak*. In 1968, the first quasistationary thermonuclear fusion reaction was documented in the T-4 tokamak. The translation of this Russian acronym is *toroidal chamber with magnetic coils*. These main field coils are axisymmetric and

[3] In plasma physics, temperature is often given in energy units of eV, implying the conversion with Boltzmann's constant: $1\,\mathrm{K} \hat{=} 8.6 \cdot 10^{-5}$ eV.

create a purely toroidal (not twisted) magnetic field. Additionally, a plasma current is induced by transformer coils, using the plasma itself as the secondary transformer winding, which adds a poloidal field component. Altogether, a helical field structure is generated that is suited for plasma confinement. An obvious problem intrinsic to the tokamak principle is that the plasma current can only be maintained for a certain time. This restriction is overcome in a second type of magnetic confinement devices, the stellarator, which operates without a plasma current. Instead, stellarators are built with specially shaped field-coils (see Fig. 1.2.1) that generate a helical guiding field. The complex shape of the field coils can only be determined with powerful computers, but also possibilities of optimization exist. At present, both machine types are subject to research.

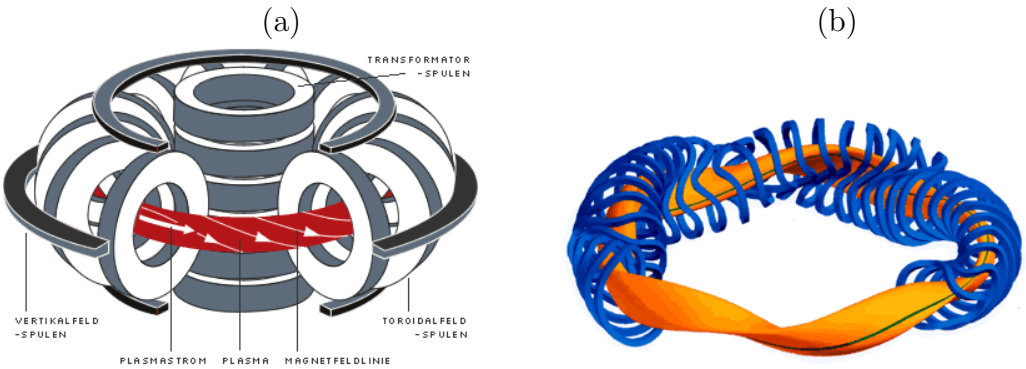

Figure 1.2.1.: Schematic drawings of the two main concepts of magnetic confinement fusion: The tokamak (a) and the stellarator (b), source: *www.ipp.mpg.de*

Plasma confinement can be characterized by the triple product of density n, temperature T, and energy confinement time τ_E. The latter is defined as the ratio of the plasma energy content and the heating power in steady state. The ASDEX Upgrade tokamak, with a plasma volume of $14\,\mathrm{m}^3$, reaches an energy confinement time of about $0.15\,\mathrm{s}$, for example.[6] The Lawson criterion of a D-T plasma at $T = 10\,\mathrm{keV}$

$$nT\tau_E > 3 \times 10^{21} \frac{\mathrm{keV\ s}}{\mathrm{m}^3}$$

gives a threshold for the triple product to reach a self-sustaining (burning) plasma, in which fusion power overcomes convection and radiation losses.[6] Since the beginning of fusion research, this quality factor was enhanced by a factor of about 10,000, constituting great progress. While the required density and temperatures are already realized in modern experiments, the energy confinement time is still to be increased to ensure net energy generation. A power plant must maintain a fusion power that overcomes the heating power significantly. Theoretical predictions as well as experimental findings suggest to increase the system size in order to improve on the energy confinement time. The currently running tokamak experiment

JET (Joint European Torus) with a plasma volume of $200\,\mathrm{m}^3$ is much larger than ASDEX Upgrade. JET has closely approached break-even by reaching a fusion power of 60% of the heating power. Following these lines, the ITER tokamak is presently constructed as an international cooperation.[4] With a plasma volume of $800\,\mathrm{m}^3$, ITER is about 4 times larger than JET and aims at an amplification factor of 10.

1.3. Cross-field transport in tokamaks

Achieving a large energy confinement time τ_E is crucial to creating a burning plasma. Besides inevitable radiation losses, collisional and convectional cross-field transport of energy and particles are limiting the confinement. It is the task of transport theory to better understand the underlying physics and predict the resulting heat and particle fluxes. Transport in tokamaks is often viewed as a type of diffusion of heat and particles (although the underlying processes are often convective). The energy confinement time is then given by the (heat) diffusivity χ as

$$\tau_E \simeq \frac{a^2}{\chi}\,,$$

where the minor tokamak radius a gives the distance across the field, along which matter and energy have to diffuse to leave the machine. A brief overview over transport mechanisms is provided in this section. We make use of the particle picture for plasma description, meaning that we focus on describing the trajectories of single particles that occur in magnetic confinement.

Classical transport

Some concepts are introduced by discussing classical diffusive transport, although it is shown to be negligible under fusion conditions. A simple random walk model for the particle diffusivity gives

$$D = \frac{\Delta x^2}{\Delta t}\,,$$

where Δx denotes a typical step size and Δt is the typical step time. For diffusive transport across the confining magnetic field $\Delta x \sim \rho_a$ is a thermal Larmor radius (the index a denotes the plasma species) and the time scale is given by the inverse Coulomb collision rate $\Delta t \sim 1/\nu_a$. In high-temperature plasmas, ν_a is a small quantity. Since also the Larmor radii ρ_e and ρ_i of electrons and ions are small compared to the plasma diameter, one finds the diffusion coefficients to be $D_e^{\mathrm{class}} = D_i^{\mathrm{class}} \sim \nu_e \rho_e^2 \sim 10^{-3}\,\mathrm{m}^2/\mathrm{s}$ (for typical fusion plasmas with $T \sim 10\,\mathrm{keV}$, $n \sim 10^{20}\,\mathrm{m}^{-3}$, $B \sim 3\mathrm{T}$). This diffusivity is negligible compared to actual measurements of $\sim 1\,\mathrm{m}^2/\mathrm{s}$. Note that the classical diffusion is equal for electrons and ions, since the (by a factor of $\sqrt{m_i/m_e}$) smaller step size for electrons is balanced by a

collision rate that is by a factor m_i/m_e larger.[7] The classical heat diffusivity has a similar form $\chi^{\text{class}} \sim \nu_a \rho_a^2$ and the expected confinement time exceeds the values determined in experiments by several orders of magnitude.

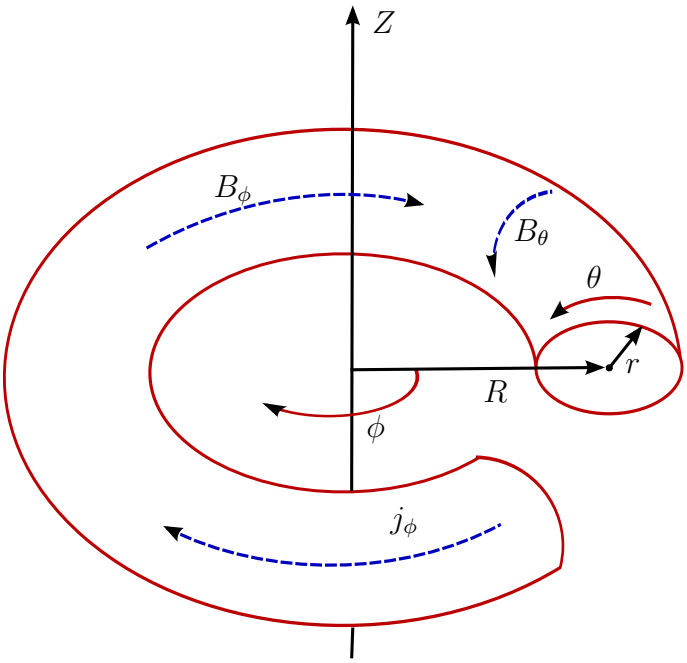

Figure 1.3.1.: Tokamak geometry relations.

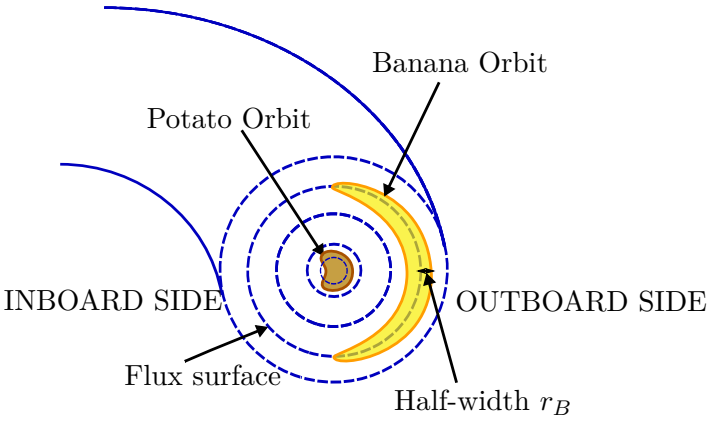

Figure 1.3.2.: Trapped particle orbits in tokamak geometry, projected on a poloidal plane. Most important effects are attributed to banana orbits. Potato-shaped orbits are found only close to the magnetic axis, and we refer to them in a later section.

Neoclassical transport

Toroidal geometry (illustrated in Fig. 1.3.1) yields modified particle trajectories, thereby introducing larger length scales in particle and heat diffusion. This so-called neoclassical transport collects various effects, and collisionality determines which of these mechanisms is most significant. Here, we discuss neoclassical effects in a phenomenological manner. A more precise treatment is found in the following Chapters 2 and 4. At low collisionalities typical of high-temperature fusion plasmas, a process called *banana* transport dominates. The naming becomes clear when considering the particle orbits of Fig. 1.3.2. These orbits are influenced by the fact that in toroidally shaped plasmas, the magnetic field is inhomogeneous. It is stronger on the inboard side than on the outboard side of the torus. Particles follow spiral paths along the field, where their magnetic moment $\mu = mv_\perp^2/2B$ is an adiabatic invariant. Additionally, the kinetic energy $\varepsilon = mv^2/2 = mv_\parallel^2 + \mu B$ is a conserved quantity. In consequence, only highly energetic particles can travel freely along the field line. Low energy particles are trapped on the low field side, and the fraction of trapped particles is given by

$$f_t = \left(\frac{2r}{R_0 + r}\right)^{1/2} \sim \sqrt{2}\epsilon^{1/2}\,.$$

where R_0 and r are the major and minor radii of the particles flux surface (see Fig.1.3.1), and $\epsilon = r/R_0$ is the local inverse aspect ratio. These trapped particles perform a periodic motion between their bounce points, with a bounce-frequency of $\omega_B = (r/2R_0)^{1/2} v_\perp/(qR_0)$, thereby changing the sign of the parallel velocity $v_\parallel$. The magnetic drifts change direction with $v_\parallel$ and the resulting trapped particle orbit reminds of a banana in projection on the poloidal plane, as shown in Fig. 1.3.2. The banana width is given by

$$r_B \approx \frac{q\rho_a}{\epsilon^{1/2}}\,,$$

where we have introduced the safety factor $q \approx (r/R_0)\, B_\phi/B_\theta$. Generally, $q/\sqrt{\epsilon}$ is larger than one, so that $r_B > \rho_a$. Consequently, collisional de-trapping and re-trapping has a much larger step-size than classical processes. Additionally, the effective collision rate is enhanced as

$$\nu_{\text{eff}} = \nu_a/\epsilon\,,$$

since ν_a gives the average rate for a 90 degree deflection, but the scattering angle for a dislocation of r_B turns out to be smaller than 90 degrees. Together, the banana diffusion is

$$D_B = f_t \nu_{\text{eff}} r_B^2 \approx \frac{q^2}{\epsilon^{3/2}} \nu_a \rho_a^2\,,$$

which is up to two orders of magnitude larger than the classical value.

As collisionality increases, the collision rate eventually becomes larger than the bounce frequency, $\nu_{\text{eff}} \gtrsim \omega_B$.[4] Then, collisional decorrelation occurs before banana orbits are completed, which reduces the radial step length. In the limit of large aspect ratio it is possible to show that in this moderate collisionality regime, transport does not depend on collisionality. Thus, one speaks of the plateau regime.[8]

The third effect of toroidal geometry on collisional transport is known as Pfirsch-Schlüter diffusion. It has a diffusion coefficient of

$$D_{PS} = q^2 \rho_e^2 \nu_e \,.$$

Since this coefficient is smaller than the banana coefficient, Pfirsch-Schlüter transport becomes relevant only at large collisionality.

Overall, neoclassical effects yield cross-field transport roughly two orders of magnitude larger than the classical value, constituting a minimum level of transport present in every toroidal magnetic confinement device. Although ion transport is sometimes down to neoclassical limits, one generally finds an even shorter confinement time in plasma experiments, giving rise to the statement that tokamak transport is *anomalous*.

Turbulent transport

At this point we have to overcome the single particle picture and introduce collective phenomena like plasma waves. It is well established that plasma turbulence, driven by unstable small-scale plasma waves, leads to enhanced (convective) transport of heat and particles. The intuitive picture is as follows. To reach the extreme conditions required for fusion in the plasma core, a large pressure gradient is built up across the magnetic field. This gradient, however, provides a source of free energy that destabilizes small-scale plasma waves. Complex nonlinear processes lead to a statistically stationary state far from thermodynamic equilibrium. In this turbulent state, convection due to electromagnetic perturbations result in enhanced transport.

Turbulent fluctuations are indeed measured in present-day fusion experiments. These fluctuations are of rather small magnitude. For the plasma density, for example, one finds $\tilde{n}/n \sim 10^{-2}$ to 10^{-3} in the plasma core (larger fluctuations are possible towards the edge). Also the plasma electric field exhibits fluctuations $\tilde{E}$, leading to a perpendicular $\tilde{E} \times B$ drift velocity

$$\tilde{v}^r_{E\times B} = \frac{\tilde{E}_\perp \times B_0}{B_0^2} \sim \frac{\tilde{E}_\perp}{B_0}$$

of which we denote the radial component. When density fluctuations are in phase with such radial drifts, the associated advection efficiently enhances the particle flux

$$\Gamma^{\text{turb}} = \langle \tilde{n} \tilde{v}^r_{E\times B} \rangle \,.$$

[4] Often, the ratio $\nu^* = (\nu_a/\epsilon)/\omega_b \lesssim 1$ is utilized to define the banana regime

In the same fashion, a finite radial heat flux arises from advection of the pressure perturbations

$$Q^{\text{turb}} = \frac{3}{2}\langle \tilde{p}\tilde{v}^r_{E\times B}\rangle \,.$$

If density/temperature gradients exist, convection relaxes these gradients. We can define the heat diffusivity χ by writing

$$Q = -n\chi\nabla T \,, \tag{1.3.1}$$

which can be a function of the gradients and other plasma parameters, keeping in mind that the underlying physics is not inherently diffusive. Furthermore, Eq. (1.3.1) implies the relation to be local, although it is in principle possible that radial variations of ∇T, for example, influence the heat fluxes.

Importantly, even for small fluctuations, the associated fluxes can be large enough to explain the experimental measurements.

Electron thermal transport in stochastic fields

Yet another transport channel is associated to magnetic field perturbations that destroy the structure of nested flux surfaces (see Fig. 1.3.2) in such a way that the magnetic field becomes stochastic. In stochastic fields, field-line following particles randomly obtain a radial component in their motion (see Fig. 1.3.3).

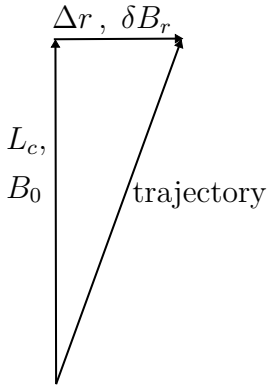

Figure 1.3.3.: The relation of a radial magnetic perturbation to the step-size of a random walk process is shown.

Describing this process as a random walk, the step length and time are estimated as

$$\Delta x = \frac{\tilde{B}_r}{B_0}L_c \,, \qquad \Delta t = \frac{L_c}{v_{te}} \,, \qquad D_{st.} = \frac{\Delta x^2}{\Delta t} = v_{te}L_c\left(\frac{\tilde{B}_r}{B_0}\right)^2 \,,$$

to find that diffusivity crucially depends on the strength of the magnetic field perturbation. We find that D_{st} can be as large as a few m^2/s, assuming the correlation length $L_c = \pi qR \sim 30\,\mathrm{m}$, a fluctuation amplitude of $\tilde{B}/B_0 \sim 5 \times 10^{-4}$, which is consistent with experimental measurements, and a (electron) thermal velocity of $390\,\mathrm{km/s}$ at a temperature of $T_e = 10\,\mathrm{keV}$. Note that the resulting heat transport is particularly relevant for the electrons, since their thermal velocity v_{te} is much larger than the ion thermal velocity.

Gaining a better understanding of electron thermal transport is of major importance for future large-scale fusion experiments like ITER, because in such devices, the common heating systems are more efficient for electrons than for ions. While electron cyclotron frequency heating naturally affects electrons directly, both neutral beam injection and cyclotron heating create fast ions that have a large collisional cross-section with (approximately) equally fast thermal electrons. Thermalization between highly energetic ions and the bulk of thermal ions is slower. Also fusion-created α particles give their energy mostly to electrons.

Since the 1970's a particular type of microinstability, the microtearing mode, has been considered as a source for such minute magnetic perturbations and stochastic transport. However, their analytical theory proves extremely complicated. Numerical methods and computational resources have only very recently evolved far enough to address this topic. Some contribution to this numerical work is reported in the course of this thesis (see also [9, 10]) and indicates a role of such modes in standard tokamaks, including ITER.

1.4. Plasma modeling

A rigorous description of plasma physics in fusion devices is necessary to reliably predict the effects of neoclassical effects and plasma turbulence on cross-field transport. The probably most intuitive framework considers the trajectories of single particles. This particle picture has been used in the previous section to discuss neoclassical and classical transport, as well as electron transport in stochastic fields. It is clear, however, that a plasma is a complex system made up by a large number of interacting particles.

1.4.1. Collisional kinetic theory

A complete description on the particle level is given by the exact 'microscopic' distribution function $\mathcal{F}_a(\mathbf{x}, \mathbf{v}, t)$ for each plasma species (denoted by the index a). Phase space conservation requires

$$\frac{\partial \mathcal{F}_a}{\partial t} + \mathbf{v} \cdot \nabla \mathcal{F}_a + \mathbf{a}_a \cdot \frac{\partial \mathcal{F}_a}{\partial \mathbf{v}} = 0 \tag{1.4.1}$$

where particle acceleration $\mathbf{a}_a = \frac{q_a}{m_a}(\mathbf{E} + \mathbf{v} \times \mathbf{B})$ is given by the Lorentz force. Hence, knowledge of the electromagnetic fields determines the evolution of $\mathcal{F}_a$. However,

the plasma itself consists of charged particles and thus contributes to the fields. A self-consistent description is given by Maxwell's equations

$$\begin{aligned}
\nabla \times \mathbf{E} &= -\frac{1}{\mathrm{c}}\frac{\partial \mathbf{B}}{\partial t} \\
\nabla \times \mathbf{B} &= \frac{4\pi}{\mathrm{c}} \sum_a \int q_a \mathbf{v} \mathcal{F}_a(\mathbf{x}, \mathbf{v}, t) \mathrm{d}^3 v - \frac{1}{\mathrm{c}}\frac{\partial \mathbf{E}}{\partial t} \\
\nabla \cdot \mathbf{E} &= \sum_a \int q_a \mathcal{F}_a(\mathbf{x}, \mathbf{v}, t) \mathrm{d}^3 v \\
\nabla \cdot \mathbf{B} &= 0
\end{aligned} \tag{1.4.2}$$

where we have normalized $\mathcal{F}_a(\mathbf{x}, \mathbf{v}, t)$ such that the configuration space density $n_a = \int \mathcal{F}_a(\mathbf{x}, \mathbf{v}, t) \mathrm{d}^3 v$ is obtained by the velocity space integral of $\mathcal{F}_a$. Solving the set of equations (1.4.1) and (1.4.2) is in principle possible. However, this would be equivalent to determining each single particle trajectory of the electromagnetic many-body problem, involving scales from the quantum level up to macroscopic system size, which is obviously highly impractical. Reducing complexity not only facilitates *ab-initio* calculations, but is also motivated from plasma experiments. Measurements can only access macroscopic quantities (like the plasma density), and thus the description on the single particle level is not necessary. Instead, a statistical formulation is appropriate. We take the ensemble average

$$f_a = \bar{\mathcal{F}}_a = \langle \mathcal{F}_a \rangle_{\text{ensemble}}$$

to obtain a substantially smoother (and more relevant) distribution f_a. The problem in averaging Eq. (1.4.1) lies in the last, nonlinear term, because $\mathbf{a}_a$ and $\mathcal{F}_a$ are not statistically independent. Formally we can write

$$\langle \mathbf{a}_a \cdot \frac{\partial \mathcal{F}_a}{\partial \mathbf{v}} \rangle_{\text{ensemble}} = \bar{\mathbf{a}} \frac{\partial f_a}{\partial \mathbf{v}} - C_a[f]$$

to collect all statistical correlations in the quantity $C_a[f]$. Most of these correlations originate from particle collisions that are interactions at small distances of the order of a Debye length, where $\mathbf{E}$ and $\mathbf{B}$ are large. This is why $C_a[f]$ is generally called the collision operator, which depends on all plasma species and includes self-collisions. In this way we find the statistically averaged kinetic equation

$$\frac{\partial f_a}{\partial t} + \mathbf{v} \cdot \nabla f_a + \bar{\mathbf{a}}_a \cdot \frac{\partial f_a}{\partial \mathbf{v}} = C_a[f] \,, \tag{1.4.3}$$

where $\bar{\mathbf{a}}_a = \frac{q_a}{m_a}(\bar{\mathbf{E}} + \mathbf{v} \times \bar{\mathbf{B}})$ is now determined from f_a with Maxwell's equations self-consistently. Henceforth we understand $\mathbf{E} = \bar{\mathbf{E}}$ and $\mathbf{B} = \bar{\mathbf{B}}$ to be macroscopic quantities (averaged over particle discreteness) and thus these fields do not vary much over a few Debye lengths. The resulting macroscopic kinetic equation forms the basis of our studies. It is named Fokker-Planck-equation, since we make use of the Fokker-Planck collision operator that is introduced in Sec. 2.1.2.

1.4.2. Limits: Fluid models and the Vlasov equation

Instead of solving the kinetic equation, one is often interested in velocity space integrated quantities $\int v^{\mathrm{m}} f_a \mathrm{d}^3 v$, such as the density ($m = 0$), the temperature ($m = 2$) and the heat flux ($m = 3$).[5] For their evolution, so-called fluid equations are obtained by taking corresponding velocity space moments of the kinetic equation. From the fact that Eq. (1.4.3) contains f_a as well as terms of the type '$v \cdot f_a$', it is obvious that the kinetic equation is equivalent to an infinite hierarchy of fluid moment equations. Closed fluid models are derived by truncating this hierarchy and making a physically motivated assumption on the higher order moments. Importantly, simple closures are possible for high collision rate, because in this case f_a is known to be close to a Maxwellian distribution.[11]

By additionally neglecting electron inertia and finite Larmor radius effects, the well-known magneto-hydrodynamic (MHD) model is derived. It describes the plasma as a single, magnetized fluid and is well suited to predict macroscopic plasma stability. Requiring the time derivatives to vanish, the equilibrium condition

$$\nabla p_0 = \frac{1}{\mathrm{c}} \mathbf{j}_0 \times \mathbf{B}_0 \,, \tag{1.4.4}$$

is obtained, which links the radial profiles of plasma pressure p_0, current density $\mathbf{j}_0$ and magnetic field $\mathbf{B}_0$.

Such fluid models have the advantage to be solvable with moderate effort. Unfortunately, they are often not applicable for the description of plasma waves in hot and dilute fusion plasmas, which are weakly collisional. In this case, velocity space dynamics plays a central role and kinetic theory is to be applied. Particle trapping, Landau damping and the influence of finite Larmor radius are exemplary effects that require a kinetic treatment. In the limit of extremely weak collisions, one can set $C_a = 0$ in Eq. (1.4.3), to obtain the so-called Vlasov equation.

However, in actual fusion plasmas (and also in astrophysical plasmas) collisionality is often not negligible, even if it is small. Including collisional dynamics in the kinetic framework does not only alter the collision-free physics, but can also lead to new phenomena. Mathematically, the collision-free kinetic equation is very different from the case of weak, but finite collisionality.

1.5. Thesis outline

In this thesis the gyrokinetic turbulence code GENE is used to simulate microtearing turbulence as a possible source of stochastic fields in tokamaks, thereby enhancing electron heat transport. Collisional dynamics is an important ingredient to the physics of microtearing modes. To define a test scenario for collision operators, neoclassical theory proves valuable. The theoretical framework for turbulence computations is given by gyrokinetic theory, whereas neoclassics appears as a certain

[5] Here, we have suppressed prefactors.

subset of this theory. The layout of this thesis is organized as follows. In Chapter 2 we introduce the gyrokinetic ordering to begin with an outline of the derivation of the gyrokinetic equations. Binary collisions are included. The collision operator is linearized and split into test-particle and field-particle collisions. An improved model for the latter is presented. We observe that the drift-kinetic equation–used to describe neoclassical transport phenomena–is obtained when imposing neoclassical ordering to the collisional gyrokinetic equation. Furthermore, the definitions for computing turbulent and neoclassical transport from the gyrokinetic distribution function are given. Chapter 3 summarizes the equations implemented in GENE and introduces appropriate normalization. Moreover, we give some details on the numerical solvers used in GENE. In the following, we turn to simulation results, beginning with neoclassical GENE simulations in Chapter 4. Based on the fact that collisions play a major and delicate role for neoclassical transport, appropriate numerical implementations of the collision operator are identified. The problem is much simpler than turbulent transport, so that even analytical expressions for the cross-field transport can be obtained and compared to numerical results. For a particular (self-adjoint) form of the field-particle collision operator, a successful benchmark against the neoclassical NEO code is presented. The global code version is employed to study system-size effects and the neoclassical heat continuity equation. Global neoclassical computations are finally benchmarked against the ORB5 code. Having tested our numerical model of collisions, we turn to the microtearing problem in Chapter 5. After giving an overview of existing literature, we turn to the simulation of global microtearing modes in realistic geometry of the ASDEX Upgrade tokamak. This motivates several studies on the linear physics, including system-size effects, the variation of important physical parameters, and the comparison to analytical models. Finally, we present recent nonlinear simulation results that suggest that microtearing turbulence can play some role in standard tokamaks, including ITER.

2. Aspects of gyrokinetic theory

2.1. Collisional gyrokinetic theory

Although the kinetic equation Eq. (1.4.3) is already simplified compared to the single-particle description, it is still very expensive to solve it in practice. It proves extremely useful to adapt the equations to the properties of the system we want to describe, which is a high-temperature plasma that is strongly magnetized by a guiding magnetic field. We begin by identifying certain small parameters, motivated by experimental findings and theoretical considerations. The kinetic equation is then transformed and expanded in these small parameters to yield a reduced–gyrokinetic–equation that is significantly more tractable. We develop gyrokinetic theory in three steps, involving different phase space coordinates. In a first step, we linearize the collision operator and write it in Fokker-Planck form. The phase space coordinates for this step are particle coordinates $\mathbf{z}^{(pc)} = (\mathbf{x}, \mathbf{v})$. The following two steps describe phase space transformations to obtain coordinates in which the particle trajectories that are greatly influenced by the magnetic field become more simple. The first of those is the guiding center (gc) transformation that yields $\mathbf{Z}^{(gc)}$ coordinates. We particularly focus on transforming the collision operator to (gc) coordinates. The last step accounts for small-scale electromagnetic field fluctuations. To that aim a near-identity gyrocenter (gy) transformation is applied to obtain $\mathbf{Z}^{(gy)}$ coordinates. The resulting kinetic equation is further modified by splitting the distribution function and introducing a field-aligned coordinate system, which brings us to a form suitable for numerical implementation. The gyrokinetic Maxwell equations are formulated to enable self-consistent computation of the electromagnetic fields, closing the equations.

2.1.1. The gyrokinetic ordering

Kinetic theory is generally applied to hot and dilute plasmas that are weakly collisional. Particle correlations are given by binary Coulomb collisions and each collision changes the velocity vector of a particle only by a small angle. Nevertheless, the plasma parameter $\Lambda = \lambda_D / r_{min} \gg 1$, defined as the ratio of the Debye length and the distance of closest approach, is large. Together, this motivates the use of a Fokker-Planck model for collisions. Before giving more details on the collision model, we turn to ordering properties of plasma turbulence and plasma microinstabilities that form the basis of gyrokinetic theory. In magnetic confinement experiments, a strong guiding field $\mathbf{B}_0$ introduces a striking scale separation between parallel and perpen-

dicular dynamics.[1] This can most intuitively be understood when observing the trajectory of a single charged particle. While the particle is free in its parallel motion, the Lorentz force $q_a/m_a(\mathbf{v}\times\mathbf{B}_0)$ lets the particle perform a spiral path around a field line. The angular frequency of this gyromotion is the Larmor frequency $\Omega_a = q_aB_0/m_ac$ and the radius of the perpendicular orbit is the Larmor radius $\rho_a = v_\perp/\Omega_a$, where $v_\perp = \sqrt{v^2 - v_\parallel^2}$ is the perpendicular velocity and $v_\parallel = \mathbf{b}_0\cdot\mathbf{v}$ is the parallel velocity and $\mathbf{b}_0 = \mathbf{B}_0/B_0$. In typical tokamak experiments a magnetic field $B_0 \sim 1-5T$ and temperatures of $5-20$ keV are reached. The thermal velocity $v_{Ta} = \sqrt{2T_{0a}/m_a}$ is introduced to find that the thermal ion gyroradius is of the order of $\rho_i \sim 0.1$ cm and the electron thermal gyroradius $\rho_e \sim \sqrt{m_e/m_i}\rho_i$ is smaller still, given that the temperatures are similar. Together with experimental findings one obtains a set $\{\epsilon_\alpha\}$ of small parameters

1. Primarily, the Larmor radius is much smaller than the scale length of the magnetic field L_B, justifying the assumption of purely circular gyro-orbits. We find the small parameter $\epsilon_B = \rho_i/L_B \ll 1$. Also the spatial variation in the temperature and density profile, characterized by the gradient lengths $L_T = -\nabla\ln T$ and $L_n = -\nabla\ln n$ are large compared to the gyroradius. The quantities $\rho_i/L_T \sim \rho_i/L_n \sim \epsilon_B \ll 1$ are ordered as the magnetic field inhomogeneity.

2. Further, one concludes from measurements that fusion plasmas are highly turbulent systems that develop very small fluctuations around some slowly varying background. Thus, quantities like $\delta T/T \sim \delta n/n \sim \epsilon_\delta \ll 1$ are typically very small, at least in the core of a fusion plasma.

3. The above mentioned gyro-trajectories enforce a strong anisotropy of the turbulent fluctuations that are to be described. While perpendicular correlation lengths are 10-100ρ_i, along the magnetic field, correlation lengths of up to several 10 meters are typical. In terms of characteristic wave numbers, one can write $k_\parallel/k_\perp \sim \epsilon_\parallel \ll 1$.

4. Measurement of the frequency spectrum of density and temperature fluctuations yield $\omega \sim 10-500$ kHz. Indeed, the Larmor frequency is much larger and we order $\omega/\Omega \sim \epsilon_t \ll 1$.

5. In high temperature plasmas the collision frequency $\nu \sim n/T^{3/2}$, the rate of collisional dissipation, is much smaller than the Larmor frequency, because particles of high velocity spend only short times within a zone of interaction with another particle. The corresponding small parameter is $\nu_a/\Omega_a \sim \epsilon_\nu \ll 1$. For thermal particles, one finds $\nu_a/\Omega_a = \rho_a/\lambda_{\mathrm{mfp}}$ with λ_{mfp} denoting the collisional mean free path. Relating ϵ_ν to the magnetic field inhomogeneity, one

[1] Here and in the following, parallel and perpendicular directions refer to the guiding magnetic field, unless specified otherwise.

has the parameter $\Delta = \epsilon_\nu/\epsilon_B = L_B/\lambda_{\mathrm{mfp}}$ that defines the degree of collisionality of the system. $\Delta \gg 1$ denotes a collisional regime in which particles do not complete a full gyro-orbit before collisional decorrelations occur. The neoclassical regime and weakly collisional regimes are defined as $\Delta \lesssim 1$ and $\Delta \ll 1$, respectively. The latter is most relevant for high temperature fusion plasmas, where the collisional mean free path is of the order of the major radius R of the device, and often larger. Then, from $\epsilon_\nu \ll \epsilon_B$ one can see that these two smallness parameters are quite distinct.

A plasma that fulfills the constraints (1)-(5) can be described by reduced (gyrokinetic) equations. In particular constraint (4) allows the fast gyration time scale to be removed. This is equivalent to removing the gyroangle θ from the equations, or, more precisely, decouple the dynamics related to θ from the comparably slow dynamics we are interested in. Extensive analytical work has been done along these lines since the 1970's and various approaches are pursued since then. Here, the method of two consecutive coordinate transformations is briefly outlined. The first is called guiding center (gc) transformation. It removes the fast orbital time scales introduced by a time-independent background magnetic field, implying that particle gyration is much faster than changes in the plasma equilibrium along the trajectory of a particle. In a second step, time-dependent electromagnetic fields are introduced in the form of the electrostatic potential $\phi_1(t)$, and the vector potential $\mathbf{A}_1(t)$. These fluctuating fields spatially vary on gyroradius scales and thus re-introduce the gyroangle. Therefore, a second phase space transformation, the gyrocenter (gy) transformation is performed. As a result one obtains a set of coordinates $\mathbf{Z}^{(gy)} = \{\mathbf{X}, v_\parallel, \mu, \theta\}$ and a kinetic equation in which both the θ dependence is removed and the dynamics is reduced in the sense that μ is an adiabatic invariant.

2.1.2. Fokker-Planck collision operator in particle space

In very hot and dilute plasmas, collisions between two particles can be considered rare, which essentially constitutes the necessity of a kinetic description. Three-particle collisions are rarer still, we thus restrict ourselves to binary collisions that can be decomposed into the contributions

$$C[f_a] = \sum_b C_{ab}[f_a, f_b]$$

from all plasma species b (including self-collisions defined by $a = b$). To determine the properties of the collision operator it is useful to first examine one single collisional event between two particles with the charges q_a, and q_b, the relative mass m_* and the relative velocity $u = v - v'$. From the Coulomb force one derives (in cgs units) a deflection angle

$$\alpha = \frac{2 q_a q_b}{r m_* u^2} \tag{2.1.1}$$

where r is the impact parameter of the collision. In many laboratory plasmas, such as fusion devices, the number of particles inside a sphere of radius of the Debye length $\lambda_D = \sqrt{T/4\pi ne^2}$ is large. One can write $n\lambda_D^3 \gg 1$ and thus λ_D is a typical impact parameter. For $r \sim \lambda_D$ one finds $\alpha \ll 1$ at thermal velocity $u = v_{Ta}$, which justifies the claim that most deflections only lead to a small change $\Delta\mathbf{v}$ of the velocity vector. Defining $r_{\min} = 2q_a q_b/m_* v_{ta}^2$, this circumstance is expressed by the largeness of the plasma parameter $\Lambda = \lambda_D/r_{\min} \gg 1$. In this limit, the collision operator effectively describes drag and diffusion in velocity space and one can derive the Fokker-Planck operator

$$C_{ab}[f_a, f_b] = \left(\frac{\partial f_a(v,t)}{\partial t}\right)_{c,ab} = -\frac{\partial}{\partial v_k}\left(\frac{\langle \Delta v_k\rangle_{ab}}{\Delta t} f_a\right) + \frac{\partial^2}{\partial v_k \partial v_l}\left(\frac{\langle \Delta v_k \Delta v_l\rangle_{ab}}{2\Delta t} f_a\right)$$

in the limit $\Delta t \to 0$. Here, Δv_k are the (small) Cartesian components of $\Delta\mathbf{v}$. Higher-order derivatives can be shown to be smaller by one order in $(1/\ln\Lambda)$. It is thus essential that the Coulomb logarithm $\ln\Lambda$ is indeed large. The Fokker-Planck operator is much simpler than the Boltzmann operator of kinetic gas theory and therefore appropriate for numerical computation and analytical work. The actual expectation values $\langle \Delta v_k\rangle/\Delta t$ and $\langle \Delta v_k \Delta v_l\rangle/2\Delta t$ are to be computed from the field-particle distribution f_b. This essentially involves integration the Coulomb potential over impact parameters leading to a logarithmically divergent integral

$$\gamma_{ab} = 2\pi q_a^2 q_b^2 \int_{r_{\min}}^{\lambda_D} \frac{1}{r}\mathrm{d}r = 2\pi q_a^2 q_b^2 \ln\Lambda$$

that has to be cut off at both ends. For the lower boundary one takes $r_{\min}$ defined above, which is the distance of closest approach at thermal velocity. For distances much larger than the Debye length, the electric potential of the charge q_b is effectively shielded by the surrounding plasma. Thus, no deflection can be expected and the integral is cut off at $r_{\max} = \lambda_D$.[2] The Coulomb logarithm $\ln\Lambda = \ln(\lambda_D/r_{\min})$ is difficult to calculate, but numerical values for various plasma regimes are found, for example, in Ref. [12]. In this way one obtains the Landau-Boltzmann operator

$$C_{ab}[f] = -\frac{\gamma_{ab}}{m_a}\frac{\partial}{\partial v_k}\int U_{kl}\left(\frac{f_a(v)}{m_b}\frac{\partial f_b(v')}{\partial v_l'} - \frac{f_b(v')}{m_a}\frac{\partial f_a(v)}{\partial v_l}\right)\mathrm{d}^3 v' \tag{2.1.2}$$

that has originally been derived by Landau in 1936 [13]. Derivations are found also in [7, 14]. Here, summation over repeated indices is understood and the velocity space tensor

$$U_{kl} = \frac{u^2\delta_{kl} - u_k u_l}{u^3} \tag{2.1.3}$$

[2] This rough estimate is possible because the integral (only) diverges logarithmically.

has been introduced with $\mathbf{u} = \mathbf{v} - \mathbf{v}'$. Due to the symmetric form of U_{kl}, Eq. (2.1.2) is well suited to demonstrate the conservation

$$\begin{aligned} \int C_{ab}\,\mathrm{d}^3v &= 0 \\ \int C_{ab} m\mathbf{v}\,\mathrm{d}^3v &= -\int C_{ba} m_b\mathbf{v}\,\mathrm{d}^3v \\ \int C_{ab} m_a v^2\,\mathrm{d}^3v &= -\int C_{ba} m_b v^2\,\mathrm{d}^3v \end{aligned} \tag{2.1.4}$$

of particles, momentum, and energy, respectively. These conservation laws are fulfilled at each point in space, expressing the fact that the Fokker-Planck operator describes local interactions. Non-local processes, like interaction with waves, are treated explicitly in the kinetic equation and are not included in the collision operator.

Another important property that can be inferred from Eq. (2.1.2) is that of Boltzmann's H-theorem. Defining entropy as

$$S_a = -\int \mathrm{d}^3v\, f_a \ln f_a\,,$$

it can be seen from the Fokker-Planck equation Eq. (1.4.3) that entropy production is exclusively due to collisions, because the other terms vanish in the integral [7]. We obtain the entropy production

$$\begin{aligned} \frac{\partial}{\partial t} S_a = -\frac{\partial}{\partial t}\int \mathrm{d}^3v\, f_a \left(\ln f_a\right) &= -\int \mathrm{d}^3v\, \left(C_a[f] + \left(\ln f_a\right) C_a[f]\right) \\ &= -\int \mathrm{d}^3v\, \left(\ln f_a\right) C_a[f_a] \\ &\approx \int \frac{f_{1a}}{f_{Ma}} C_a[f_a]\mathrm{d}^3v \geq 0\,, \end{aligned} \tag{2.1.5}$$

where in the first step we have used particle conservation $\int \mathrm{d}^3v\, C_a[f] = 0$ and in the last step the distribution function is split to $f = f_M + f_1$ with $f_1/f_M \sim \epsilon_\delta \ll 1$ and terms of order $\mathcal{O}(\epsilon_\delta^2)$ are neglected. The splitting of f is made more explicit in the next section. Positivity of entropy change can be traced back to positivity of the tensor U in the Landau operator Eq. (2.1.2). Let us finally mention that collisional equilibrium ($\frac{\partial}{\partial t} S_a = 0$) is reached for Maxwellian distributions $f = f_M$ with equal temperature and velocity (see Eq. (2.1.7)).

2.1.2.1. Linearization of collision operators

Gyrokinetic ordering allows for a linearization of the collision operator, which is of great advantage in numerical and analytical work. In particular the smallness of ϵ_δ is used to split the distribution function $f = f_0 + f_1$ into a background f_0 and a perturbed part f_1. The treatment of collision operators is significantly simplified

when the background is taken to be a Maxwellian distribution. We use the unshifted Maxwellian

$$f_{0a} = f_{Ma} = \frac{n_a}{\pi^{3/2} v_{Ta}^3} e^{-v^2/v_{Ta}^2}$$

for the following analysis. The bilinear collision operator

$$\left(\frac{\mathrm{d}}{\mathrm{d}t}\right)_c f_a = \sum_b C_{ab}$$
$$C_{ab} = \underbrace{C[f_{Ma}, f_{Mb}]}_{=0 \text{ for } T_{0a}=T_{0b}} + \underbrace{C[f_{1a}, f_{Mb}] + C[f_{Ma}, f_{1b}]}_{C_{ab}^L} + \underbrace{C[f_{1a}, f_{1b}]}_{\text{higher order}} \tag{2.1.6}$$

yields four terms. The first term describes collisional interaction between the background distribution functions. It is evaluated as

$$C[f_{Ma}, f_{Mb}] = -\frac{2\gamma_{ab} n_b}{m_a m_b v_{Tb} v_{Ta}^2} \left(1 - \frac{T_b}{T_a}\right) \left[\frac{\mathrm{erf}(x_b)}{x_b} - \left(1 - \frac{m_b T_a}{m_a T_b}\right) erf'(x_b)\right] f_{Ma}, \tag{2.1.7}$$

where $x_b = v/v_{Tb}$ is a velocity normalized to the thermal velocity $v_{Tb} = \sqrt{2T_{0b}/m_b}$ of species b and $\mathrm{erf}(x_b) = (2/\sqrt{\pi}) \int_0^{x_b} e^{-t^2} \mathrm{d}t$ is the error function.[14] This term describes collisional thermalization between two species and it obviously vanishes for like-species collisions or equal temperatures. For unequal temperatures, it describes collisional thermalization between two species. The associated thermalization time can be considered large and of the order of the characteristic equilibrium time scales, such that the term $C[f_{Ma}, f_{Mb}]$ is neglected. Since in our δf modeling the background distributions do not evolve in time, we are not able to take this term into account anyway. The fourth term is usually neglected because it is of second order in ϵ_δ of the gyrokinetic ordering. The remaining terms constitute the linearized Landau-Boltzmann collision operator

$$C_{ab}^L[f_a, f_b] = C[f_{1a}, f_{Mb}] + C[f_{Ma}, f_{1b}] \tag{2.1.8}$$

for which conservation of particle number, momentum and energy can be proven. The first term in Eq.(2.1.8) is often referred to as the test-particle operator $C_{ab}^T[f_{1a}] = C[f_{1a}, f_{Mb}]$. The second term is called field-particle operator $C^F[f_{1b}] = C_{ab}[f_{Ma}, f_{1b}]$; it accounts for the correct transfer of energy and parallel momentum. In the following, we derive a self-adjoint model for C_{ab}^F from the test-particle operator.

2.1.2.2. Collisions with Maxwellian background: The test-particle operator

It is often useful to express the Landau-Boltzmann operator in terms of certain integrals of the distribution function

$$G_b(\mathbf{v}) = \int \mathrm{d}^3 v' f_b u \quad , \qquad H_b(\mathbf{v}) = \int \mathrm{d}^3 v' f_b \frac{1}{u} ,$$

the so-called Rosenbluth potentials with $u = |\mathbf{v} - \mathbf{v}'|$. Equation (2.1.2) is then cast in the form of an advection-diffusion operator

$$C[f_a, f_b] = \frac{\partial}{\partial \mathbf{v}} \cdot \left(\overleftrightarrow{\mathcal{D}}_{ab} \cdot \frac{\partial}{\partial \mathbf{v}} - \mathbf{R}_{ab} \right) f_a, \tag{2.1.9}$$

where $\overleftrightarrow{D}_{ab}$ is the diffusion tensor and the vector $\mathbf{R}_{ab}$ is called the dynamical friction coefficient given by

$$\overleftrightarrow{\mathcal{D}}_{ab} = \frac{\gamma_{ab}}{m_a m_b} \frac{m_b}{m_a} \frac{\partial G_b}{\partial \mathbf{v} \partial \mathbf{v}} \qquad \mathbf{R}_{ab} = \frac{\gamma_{ab}}{m_a m_b} 2 \frac{\partial H_b}{\partial \mathbf{v}}$$

In the case of a Maxwellian distribution $f_b = f_{Mb}$, the Rosenbluth potentials can be evaluated analytically as

$$H_{Mb}(x_b) = \frac{n_b}{v_{Tb} x_b} \mathrm{erf}(x_b) \qquad G_{Mb}(x_b) = \frac{n_b v_{Tb}}{2 x_b} \left[\mathrm{erf}'(x_b) + (1 + 2x_b^2) \mathrm{erf}(x_b) \right], \tag{2.1.10}$$

which has been done for example in Ref. [7, 14]. Then, the coefficients $\overleftrightarrow{\mathcal{D}}$ and $\mathbf{R}$ take the form[3]

$$\begin{aligned} \overleftrightarrow{\mathcal{D}}_{ab} &= \frac{\gamma_{ab} n_b T_b}{m_a^2 m_b} \frac{1}{v^3} \left[\mathbf{1}_{\mathbf{v}} \Phi_1(x_b) + 3 \frac{\mathbf{vv}}{v^2} \Phi_2(x_b) \right] \\ \mathbf{R}_{ab} &= -\frac{\gamma_{ab} n_b}{m_a m_b} \frac{\mathbf{v}}{v^3} \Phi_3(x_b) \end{aligned} \tag{2.1.11}$$

where the abbreviations

$$\begin{aligned} \Phi_1(x_b) &= x_b \mathrm{erf}'(x_b) + (2x_b^2 - 1) \mathrm{erf}(x_b) \\ \Phi_2(x_b) &= (1 - \frac{2}{3} x_b^2) \mathrm{erf}(x_b) - x_b \mathrm{erf}'(x_b) \\ \Phi_3(x_b) &= 2\mathrm{erf}(x_b) - 2x_b \mathrm{erf}'(x_b) \\ &= \Phi_1(x_b) + 3\Phi_2(x_b) \end{aligned} \tag{2.1.12}$$

have been introduced,[4] and $x_b = v/v_{Tb}$. While Eq. (2.1.9) gives our final analytical form of the test-particle operator, it is also possible to cast the collision operator into

$$C^T(f_{1a}) = C[f_{1a}, f_{Mb}] = \frac{\partial}{\partial \mathbf{v}} \cdot \left[f_{Ma} \overleftrightarrow{\mathcal{D}}_{ab} \cdot \frac{\partial}{\partial \mathbf{v}} - \left(1 - \frac{T_b}{T_a} \right) f_{Ma} \mathbf{R}_{ab} \right] \frac{f_{1a}}{f_{Ma}} \tag{2.1.13}$$

[3] For comparison to the literature it may be useful to note that the final result of $\mathbf{R}_{ab}$ in Ref. [14] (their Eq. (7.71)) and also in Ref. [15] is given with the wrong sign. Further, Eq. (2.1.10) has been corrected compared to Ref. [14].

[4] A useful property of $\mathrm{erf}(x)$ is the relation $\mathrm{d}\,\mathrm{erf}(x)/\mathrm{d}x = \mathrm{erf}'(x) = 2\exp(-x^2)/\sqrt{\pi}$.

such that its argument is the normalized distribution function f_{1a}/f_{Ma}. Inserting the inverse product rule

$$\frac{\partial}{\partial \mathbf{v}} f_{1a} = f_{Ma} \frac{\partial}{\partial \mathbf{v}} \frac{f_{1a}}{f_{Ma}} - \frac{2}{v_{Ta}^2} \mathbf{v} f_{1a}, \qquad \overleftrightarrow{\mathcal{D}}_{ab} \cdot \frac{2}{v_{Ta}^2} \mathbf{v} = -\frac{T_b}{T_a} \mathbf{R}_{ab}$$

into Eq. (2.1.9), one indeed finds equivalence to Eq. (2.1.13). This last version Eq. (2.1.13) is suited to prove conservation properties and possibly offers advantages for numerical implementation.

2.1.2.3. Scalar product and self-adjointness

A fundamental property of the Landau-Boltzmann operator, the self-adjointness, can be observed in Eq. (2.1.13), when temperatures are equal. To make this clear, a scalar product

$$\langle f | g \rangle = \int \mathrm{d}^3 v \, f(v) g(v) \tag{2.1.14}$$

and the operator notation

$$C_{ab}[f_b, \cdot] | g_a \rangle = C[g_a, f_b] \tag{2.1.15}$$

are defined, so that the self-adjointness relation is written as the symmetry of the functional

$$S[g_a, f_a] = \langle g_a | \frac{1}{f_{Ma}} C[f_{Mb}, \cdot] | f_a \rangle = S[f_a, g_a]. \tag{2.1.16}$$

When the temperatures $T_a = T_b$ are equal, Eq. (2.1.16) is easily proven by inserting Eq. (2.1.13) and integrating by parts to obtain the symmetric expression

$$\begin{aligned} \langle g_a | \frac{1}{f_{Ma}} C[f_{Mb}, \cdot] | f_a \rangle &= -\int \mathrm{d}^3 v \left(\frac{\partial}{\partial \mathbf{v}} \frac{g_a}{f_{Ma}} \right) \cdot f_{Ma} \overleftrightarrow{D}_{ab} \cdot \left(\frac{\partial}{\partial \mathbf{v}} \frac{f_a}{f_{Ma}} \right) \\ &= \langle f_a | \frac{1}{f_{Ma}} C[f_{Mb}, \cdot] | g_a \rangle \, . \end{aligned}$$

One clearly does not obtain a symmetric expression for non-equal temperatures, since then, the prefactor of the dynamical friction term $\mathbf{R}_{ab}$ does not vanish. This symmetry breaking is connected with the fact that we have linearized with respect to a non-equilibrium state when $T_a \neq T_b$. Collisional thermalization processes between the background of different species are dropped when neglecting the zeroth order term $C[f_{0a}, f_{0b}]$, and this breaks the symmetry of the test-particle operator. Since self-adjointness is required in neoclassical computations and also related to energy conservation (see Sec. 4.2) there lies a potential problem that can be treated various ways. One may demand self-adjointness even for $T_a \neq T_b$ and find a modified operator for that purpose. The modification presented by Sugama [16] takes into

account that in the limit $\sqrt{m_b/m_a}(1 - T_b/T_a) \ll 1$ the symmetry breaking terms may be neglected. Otherwise their operator is still symmetric, but different from the linearized Landau-Boltzmann form. Alternatively one can simply work with equal temperatures.[17, 18, 19] The approach pursued here is to neglect the symmetry breaking in case of $T_a \neq T_b$ to only keep exact conservation of particles, momentum, and energy as physical constraints on the operator. A corresponding field-particle operator is described in the next section.

2.1.2.4. The field-particle operator

Calculating the full field particle operator is possible, in principle, but computationally expensive, for it involves the evaluation of the Rosenbluth potentials of the perturbed distribution functions.[5] It is often sufficient to replace the exact field-particle operator by an ad-hoc model capturing the most relevant physics, which is the conservation of particles, momentum, and energy. A certain self-adjointness symmetry, is often required of the collision operator, since it is used to derive Onsager symmetry in neoclassical transport theory (see Sec. 4.2). It turns out that Boltzmann's H-Theorem of entropy increase is related to self-adjointness as well.[7, 20, 21, 22]

Following Ref. [22], an operator $C^F_{ab}(f_{1b})$ is derived by using the notation of Eqs. (2.1.14) and (2.1.15) and defining an orthogonal projection operator

$$P_{ba} = \frac{|f_{Mb}\mathbf{v}\rangle \cdot \langle f_{Mb}\mathbf{v}|\frac{1}{f_{Mb}}C_{ba}[f_{Ma},\cdot]}{\frac{1}{3}\langle f_{Mb}\mathbf{v}|\cdot\frac{1}{f_{Mb}}C_{ba}[f_{Ma},\cdot]|f_{Mb}\mathbf{v}\rangle} + \frac{|f_{Mb}v^2\rangle\langle f_{Mb}v^2|\frac{1}{f_{Mb}}C_{ba}[f_{Ma},\cdot]}{\langle f_{Mb}v^2|\frac{1}{f_{Mb}}C_{ba}[f_{Ma},\cdot]|f_{Mb}v^2\rangle}$$

that can be viewed as the first two terms of an expansion in spherical harmonics. A model for the field particle operator is then obtained from the test-particle operator by projection

$$\frac{1}{f_{Ma}}C^F_{ab} = \frac{1}{f_{Ma}}C_{ab}[\cdot, f_{Ma}] \circ P_{ab}$$

Making use of symmetry and conservation properties of C_{ab} (that hold for equal temperatures) leads to

$$\begin{aligned}\frac{1}{f_{Ma}}C^F_{ab}|f_{1a}\rangle = &-\frac{m_b}{m_a}\frac{\langle f_{Mb}\mathbf{v}|\frac{1}{f_{Mb}}C_{ba}[f_{Ma},\cdot]|f_{1b}\rangle}{\frac{1}{3}\langle f_{Ma}\mathbf{v}|\cdot\frac{1}{f_{Ma}}C_{ab}[f_{Mb},\cdot]|f_{Mb}\mathbf{v}\rangle}\cdot\frac{1}{f_{Ma}}C_{ab}[f_{Mb},\cdot]|f_{Ma}\mathbf{v}\rangle \\ &-\frac{m_b}{m_a}\frac{\langle f_{Mb}v^2|\frac{1}{f_{Mb}}C_{ba}[f_{Ma},\cdot]|f_{1b}\rangle}{\langle f_{Ma}v^2|\frac{1}{f_{Ma}}C_{ab}[f_{Mb},\cdot]|f_{Ma}v^2\rangle}\frac{1}{f_{Ma}}C_{ab}[f_{Mb},\cdot]|f_{Ma}v^2\rangle\,.\end{aligned}$$

Resolving the bracket structure of the scalar product gives

[5] One numerical difficulty arises from the fact that $v_{Te}/v_{Ti} \sim \sqrt{m_i/m_e} \gg 1$. In consequence, the electron distribution function is usually significantly broader in ion velocity space and in turn the ion distribution is very narrow when seen by the electrons. For an accurate integral, both scales should be resolved, which is possible, but expensive.

$$C^F_{ab}(f_{1b}) = \frac{\delta\dot{\mathcal{P}}_{\parallel ba}}{\int \mathrm{d}^3v'\, v_\parallel C_{ab}(v_\parallel f_{Ma}, f_{Mb})} C^T_{ab}(v_\parallel f_{Ma}) \tag{2.1.17}$$

$$\frac{\delta\dot{\boldsymbol{\mathcal{P}}}_{\perp ba}}{\frac{1}{2}\int \mathrm{d}^3v'\, \mathbf{v}_\perp \cdot C_{ab}(\mathbf{v}_\perp f_{Ma}, f_{Mb})} C^T_{ab}(\mathbf{v}_\perp f_{Ma}) \tag{2.1.18}$$

$$+ \frac{\delta\dot{\mathcal{E}}_{ba}}{\int \mathrm{d}^3v'\, m_a v^2 C_{ab}(v^2 f_{Ma}, f_{Mb})} C^T_{ab}(v^2 f_{Ma}) \tag{2.1.19}$$

where the rates of collisional transfer of parallel momentum and energy from species b to species a are computed as velocity space moments

$$\begin{aligned}
\delta\dot{\mathcal{P}}_{\parallel ba} &= -\int m_b v_\parallel C^T_{ba}(f_{1b})\mathrm{d}^3v \\
\delta\dot{\boldsymbol{\mathcal{P}}}_{\perp ba} &= -\int m_b \mathbf{v}_\perp C^T_{ba}(f_{1b})\mathrm{d}^3v \\
\delta\dot{\mathcal{E}}_{ba} &= -\int m_b v^2 C^T_{ba}(f_{1b})\mathrm{d}^3v
\end{aligned} \tag{2.1.20}$$

of the test-particle operator $C^T_{ba}(f_{1b})$. In view of our further treatment described in Appendix A, we only consider parallel momentum transfer, which is correct in the drift-kinetic limit (i.e. $k_\perp\rho \to 0$). The perpendicular momentum transfer is strongly suppressed in that limit. Note that the model operator Eq. (2.1.17) is written as it appears in the Fokker-Planck equation for species a. It preserves self-adjointness and conservation laws. When explicitly evaluating the expressions $C^T_{ab}(v^2 f_{Ma})$ and $C^T_{ab}(v_\parallel f_{Ma})$ one obtains

$$\begin{aligned}
C^F_{ab}(f_{1a}) =& \frac{f_{Ma}}{n_{0a}(x)} B^P_{ab}(x_b) \frac{v_\parallel}{v_{Tb}(x)} \frac{\delta\dot{\mathcal{P}}_{\parallel ba}}{m_b v_{Tb}(x)} + \frac{f_{Ma}}{n_{0a}(x)} B^E_{ab}(x_b) \frac{\delta\dot{\mathcal{E}}_{ba}}{m_b v^2_{Tb}(x)} \\
B^P_{ab}(x_b) =& \frac{\sqrt{2\pi}}{2}(1+\frac{m_b}{m_a})^{3/2} 6H(x_b) \\
B^E_{ab}(x_b) =& \frac{\sqrt{2\pi}}{2}(1+\frac{m_b}{m_a})^{3/2} \left\{ \left[\left(1+\frac{m_a}{m_b}\right) 2x_b^2 - 1 \right] H(x_b) - K(x_b) \right\}
\end{aligned} \tag{2.1.21}$$

which for self-collisions $a = b$ reduces to the form proposed by Lin *et al.* [22, 23, 24] The functions H and K are defined as

$$\begin{aligned}
H(x_b) &= \frac{1}{2^{3/2}x_b^3}\left[\mathrm{erf}(x_b) - \sqrt{\frac{1}{\pi}} 2x_b e^{-x_b^2}\right] \\
K(x_b) &= \frac{1}{2^{3/2}x_b^3}(x_b^2 - 1)\mathrm{erf}(x_b) + \sqrt{\frac{1}{\pi}} 2x_b e^{-x_b^2}
\end{aligned}$$

where $x_b = v/v_{Tb}$ is the common normalized velocity. A field-particle model operator of this form, together with the test particle operator $C^T_{ab}(f_{1a})$, analytically conserves particles, energy and momentum for the case of equal temperatures $T_{0a} = T_{0b}$ and is furthermore self-adjoint.

Correction of numerical errors

Unfortunately, numerical errors are usually introduced by discretization of the velocity space and by the use of a finite simulation domain. Nevertheless, conservation properties are desired, and thus a correction term is added to Eq. (2.1.21),

$$\begin{aligned} C^F_{ab}(f_{1a}) =& c_{1,ab}\frac{f_{Ma}}{n_{0a}(x)}B^P_{ab}(x_b)\frac{v_\parallel}{v_{Tb}(x)}\frac{\delta\dot{\mathcal{P}}_{\parallel ba}}{m_b v_{Tb}(x)} \\ &+ c_{2,ab}\frac{f_{Ma}}{n_{0a}(x)}B^E_{ab}(x_b)\frac{\delta\dot{\mathcal{E}}_{ba}}{m_b v^2_{Tb}(x)} + c_{3,ab} f_{Ma}\delta\dot{\mathcal{E}}_{ba}\,, \end{aligned} \tag{2.1.22}$$

where the coefficients $c_{1,ab}$, $c_{2,ab}$, and $c_{3,ab}$ are introduced. Technically, these modifications have the drawback of breaking the self-adjointness symmetry. However, we have previously shown that in the case of unequal temperatures, self-adjointness is not given anyway. Only in this case of unequal temperatures, the $c_{i,ab}$ become significant; otherwise they only provide a small correction to ensure conservation to machine precision. For the coefficients $c_{1,ab}, c_{2,ab}, c_{3,ab}$, a system of equations is obtained by inserting Eq. (2.1.22) into the constraints

$$\begin{aligned} \int C^F_{ab}(f_{1b})\,\mathrm{d}^3v &= 0\,, \\ \int C^F_{ab}(f_{1b}) m_a v_\parallel\,\mathrm{d}^3v = -\int C^T_{ba}(f_{1a}) m_b v_\parallel\,\mathrm{d}^3v &= \delta\dot{\mathcal{P}}_{\parallel ba}\,, \\ \int C^F_{ab}(f_{1b}) m_a v^2\,\mathrm{d}^3v = -\int C^T_{ba}(f_{1a}) m_b v^2\,\mathrm{d}^3v &= \delta\dot{\mathcal{E}}_{ba}\,, \end{aligned} \tag{2.1.23}$$

in which the equation for $c_{1,ab}$ decouples, because of the odd $v_\parallel$ symmetry of the B^P term as opposed to the even $v_\parallel$ symmetry of the remaining terms. Defining the integrals

$$I_{1,ab} = \int f_{Ma}\,\mathrm{d}^3v \qquad I_{2,ab} = \int f_{Ma}B^E_{ab}\,\mathrm{d}^3v \qquad I_{3,ab} = \int v^2 f_{Ma}B^E_{ab}\,\mathrm{d}^3v$$

$$I_{4,ab} = \int v^2 f_{Ma}\,\mathrm{d}^3v \qquad I_{5,ab} = \int v_\parallel^2 f_{Ma}B^P_{ab}\,\mathrm{d}^3v$$

and solving the system of equations gives the coefficients

$$c_{1,ab} = \frac{n_{0a}v^2_{Tb}m_b}{m_a}\frac{1}{I_{5,ab}} \qquad c_{2,ab} = \frac{m_b n_{0a}v^2_{Tb}}{m_a}\frac{I_{1,ab}}{I_{3,ab}I_{1,ab} - I_{2,ab}I_{4,ab}}$$

$$c_{3,ab} = -\frac{1}{m_a}\frac{I_{2,ab}}{I_{3,ab}I_{1,ab} - I_{2,ab}I_{4,ab}}$$

which turns Eq. (2.1.22) into

$$C^F_{ab}(f_{1a}) = \frac{B^P_{ab}(x_b)}{I_{5,ab}}\frac{v_\parallel f_{Ma}}{m_a}\delta\dot{\mathcal{P}}_{\parallel ba} + \frac{I_{1,ab}B^E_{ab}(x_b) - I_{2,ab}}{I_{3,ab}I_{1,ab} - I_{2,ab}I_{4,ab}}\frac{f_{Ma}}{m_a}\delta\dot{\mathcal{E}}_{ba}\,. \tag{2.1.24}$$

Conservation to machine precision is reached by computing the integrals $I_{i,ab}$ numerically instead of evaluating them analytically.

The Xu-Rosenbluth model

At this point we note that the Xu-Rosenbluth operator [25] is obtained by choosing the coefficients

$$B^{P,\mathbf{XR}}_{ab}(x_b) = 1, \qquad B^{E,\mathbf{XR}}_{ab}(x_b) = x_b^2$$

of simpler velocity space structure (which gives an intrinsically non-self-adjoint operator). The Xu-Rosenbluth model described in Ref. [15] follows the same procedure of solving a system of equations to preserve particles, momentum, and energy.

2.1.3. Guiding center transformation including collisions

So far, the Fokker-Planck collision operator has been discussed in detail using particle coordinates. The corresponding kinetic equation Eq. (1.4.3) formally reads

$$\frac{\mathrm{d}}{\mathrm{d}t}f_a = \sum_b C_{ab}[f_a, f_b]\,, \tag{2.1.25}$$

with the collision-free Vlasov operator on the left hand side and the collision operator on the right hand side. We now employ a phase space transformation that removes the fast gyration timescale introduced by the guiding magnetic field. In traditional gyrokinetic theory, only the collision-free (Vlasov) operator is transformed (see e.g. [26, 27]). Following a paper by Brizard [28], we outline a guiding center transformation that additionally includes collisional dynamics. Therefor, it is important that the Fokker-Planck operator C is bi-linear in its two arguments. The basic idea is to first introduce guiding center coordinates $\mathbf{Z}^{(gc)} = \{\mathbf{X}^{(gc)}, v_\parallel, \mu, \theta\}$ with parallel velocity $v_\parallel$, magnetic moment $\mu = \frac{1}{2}mv_\perp^2/B_0$, and gyroangle θ as velocity space coordinates, where $v_\perp^2 = v_x^2 + v_y^2$. The particle coordinates $\mathbf{x} = \{x, y, z\}$ are expressed as

$$\mathbf{x} \;=\; \mathbf{X}^{(gc)} + \boldsymbol{\rho}^{(gc)} \tag{2.1.26}$$

in terms of the guiding center position $\mathbf{X}^{(gc)}$ and the gyro-vector $\boldsymbol{\rho}^{(gc)}$. We take the gyration vector and velocity as

$$\begin{array}{rclrcl} \boldsymbol{\rho}^{(gc)} & = & \frac{v_\perp}{\Omega}\hat{\mathbf{a}} & \hat{\mathbf{a}} & = & [\hat{\mathbf{e}}_1\cos\theta - \hat{\mathbf{e}}_2\sin\theta] \\ \mathbf{v} & = & v_\parallel \mathbf{b}_0 + v_\perp \hat{\mathbf{c}} & \hat{\mathbf{c}} & = & -[\hat{\mathbf{e}}_1\sin\theta + \hat{\mathbf{e}}_2\cos\theta] \end{array}$$

in a local rectangular coordinate system with the perpendicular unit vectors $\hat{\mathbf{e}}_1$ and $\hat{\mathbf{e}}_2$.[6] The velocity space Jacobian of this transformation is $J_v = B_0/m$.

2.1.3.1. Transformation of the collision-free part

For the formal guiding center transformation of the collision-free part, we implicitly define the transformed zeroth order guiding center one-form Γ_0 from the Lagrangian L_0 by writing

$$\int \Gamma_0 \mathrm{d}t = L_0 \,.$$

It can be shown with the appropriate choice of the Lie transform that

$$\Gamma_0 = \frac{q}{c}A_0^* \cdot d\mathbf{X} + \frac{\mu B_0(X)}{\Omega(X)}\mathrm{d}\theta - H_0(X, v_\parallel, \mu)\mathrm{d}t \,, \tag{2.1.27}$$

which indeed has decoupled gyroangle-dependency.[7] Here $H_0(\mathbf{X}, v_\parallel, \mu) = \frac{1}{2}mv_\parallel^2 + \mu B_0(\mathbf{X})$ denotes the zeroth-order guiding center Hamiltonian. The effective vector potential $\mathbf{A}_0^* = \mathbf{A}_0 + \frac{mc}{q}v_\parallel \mathbf{b}_0$ has been used to write Eq. (2.1.27) in a compact from, adding a term proportional to the unit vector $\mathbf{b}_0 = \mathbf{B}_0/B_0$ to the equilibrium vector potential $\mathbf{A}_0$. From the zeroth order guiding center one form one can derive the drift-kinetic equation, which is often used in plasma modeling. Neoclassical theory, for example, makes use of the drift kinetic framework. We derive the corresponding equations by taking the appropriate limit of the gyrokinetic equations in Sec. 2.2, however.

2.1.3.2. Formal transformation of the collision operator

Some authors define the guiding center transformation in a more rigorous way, obtaining $J_v = B_{\parallel 0}^*/m$ for the Jacobian [27]. These authors formulate the guiding center coordinate transformation as a Lie transform $\mathbf{Z}^{(gc)} = \mathcal{T}_{(gc)}\,\mathbf{z}$ with generating functions G_1 and G_2, such that the gyration vector

$$\boldsymbol{\rho}_\epsilon(\mathbf{Z}^{(gc)}) = \rho_0 - \epsilon(G_2^{\mathbf{X}} + \frac{1}{2}G_1 \cdot d\boldsymbol{\rho}_0)$$

[6] Note that the choice of the sign of θ makes $\{\hat{\mathbf{e}}_\parallel, \hat{\mathbf{e}}_\mu, \hat{\mathbf{e}}_\theta\}$ a left-handed coordinate system, which has to be consistently accounted for also in the field equation for $B_{1\parallel}$ in Sec. 2.1.8.

[7] See, also Ref. [29], for example.

includes corrections of the order $\epsilon \sim \epsilon_B$ due to magnetic field inhomogeneity. This more involved approach offers the possibility of expansion in ϵ_B within a rigorous formalism. The guiding center phase space coordinates are denoted as $\mathbf{Z}^{(gc)}$. The coordinate transformation is associated with a push-forward operator

$$T^{-1}_{(gc)} : f \to F^{(gc)} \equiv T^{-1}_{(gc)} f$$

transforming a scalar field f on particle phase space to a scalar field F on the guiding center phase space. Conversely, the pull-back operator

$$T_{(gc)} : F \to f \equiv T_{(gc)} F^{(gc)}$$

transforms a scalar field F on guiding center phase space to a scalar field f on the particle space. The transformation rule for operators $\mathcal{A} : f \to \mathcal{A}f$ is then given by

$$\mathcal{A}F^{(gc)} \equiv T^{-1}_{(gc)} \mathcal{A}(T_{(gc)} F^{(gc)}) \,, \tag{2.1.28}$$

when $\mathcal{A}f$ is a scalar, just as f.

Using this induced transformation on the collision operator yields

$$C_{ab,\epsilon}[F^{(gc)}_a](\mathbf{Z}^{(gc)}, t) = T^{-1}_{(gc)} C_{ab}[T_{(gc)} F^{(gc)}_a](\mathbf{Z}^{(gc)}, t) \,,$$

where the transformations of the field-particle species $F^{(gc)}_b$ is not explicitly needed here. In this way the Fokker-Planck equation Eq. (2.1.25) is turned into a set of two kinetic equations

$$\left(\frac{\mathrm{d}}{\mathrm{d}t}\right)^{(gc)} \langle F^{(gc)} \rangle = \langle C_\epsilon[F^{(gc)}] \rangle \equiv \langle C_\epsilon[\langle F^{(gc)} \rangle] \rangle + \langle C_\epsilon[\tilde{F}^{(gc)}] \rangle$$

$$\left(\Omega \frac{\partial}{\partial \theta} + \left(\frac{\mathrm{d}}{\mathrm{d}t}\right)^{(gc)}\right) \tilde{F}^{(gc)} = C_\epsilon[F^{(gc)}] - \langle C_\epsilon[F^{(gc)}] \rangle$$

that are coupled by collisions.[8] One equation determines the θ averaged distribution $\langle F^{(gc)} \rangle$, the other is for the θ dependent part $\tilde{F}^{(gc)}$. The reduced Vlasov operator $(\mathrm{d}/\mathrm{d}t)^{(gc)}$ is not θ dependent by definition of the guiding center coordinate transformation. However, such transformations are not designed to remove gyroangle-dependencies from the collision operator. Expanding $\tilde{F}$ in a Fourier series in θ, one can write

$$\left(\frac{\mathrm{d}}{\mathrm{d}t}\right)^{(gc)} \langle F^{(gc)} \rangle = C^{(gc)}[\langle F^{(gc)} \rangle]$$

with

$$C^{(gc)}[\langle F^{(gc)} \rangle] = \langle T^{-1}_{(gc)} C[T_{(gc)} \langle F^{(gc)} \rangle] \rangle + \mathcal{O}(\epsilon_\nu) \,. \tag{2.1.29}$$

[8] Note that we have used the bilinearity of C.

Generally it is assumed that the zeroth order expression is sufficient in practice, giving the desired result of a collision operator that requires knowledge of the gyroaveraged part $\left\langle F^{(gc)} \right\rangle$ only. Thus, it becomes clear that within the gyrokinetic formalism ϵ_ν plays the special role to remove gyroangle-dependencies after θ is eliminated from the collision-free part. Already, first order terms in ϵ_ν are neglected to yield a closed form of the kinetic equation for the gyroaveraged part of F. This last point is of great importance for numerical computation, allowing one to evaluate the collision operator from the guiding center distribution without inconvenient back-and-forth transformation. As stated above, one typically has $\epsilon_\nu \ll \epsilon_B$ in fusion plasmas, further supporting the above treatment. We have outlined the formal transformation of the collisional term so far. An explicit transformation is performed in an Appendix A and the result actually used in the GENE code are summarized in the next section.

2.1.4. Transformation to gyrocenter coordinates

Plasma microturbulence requires to include small-scale fluctuating electromagnetic fields. In the framework of the previously discussed guding center transformation, it is not possible to remove fast gyroangle dynamics in a straightforward manner. The basic ideas behind a more sophisticated treatment, the gyrocenter transformation, are presented this section. It is developed to account for the effects of small-scale electromagnetic field fluctuations ϕ_1 and $\mathbf{A}_1$, without depending directly on the gyroangle θ. These fluctuations introduce order-ϵ_δ perturbations of the guiding-center one-form and Hamiltonian function as

$$\begin{aligned} \Gamma &= \Gamma_0 + \Gamma_1 \\ H &= H_0 + H_1 \,. \end{aligned}$$

The perturbations read

$$\begin{aligned} H_1 &= q\phi_1(x,t) \\ \Gamma_1 &= \frac{q}{c}\mathbf{A}_1 \cdot \mathrm{d}\mathbf{X} + \frac{q}{c}\mathbf{A}_1 \cdot \frac{\partial \boldsymbol{\rho}}{\partial \mu}\mathrm{d}\mu + \frac{q}{c}\mathbf{A}_1 \cdot \frac{\partial \boldsymbol{\rho}}{\partial \theta}\mathrm{d}\theta - H_1 \mathrm{d}t \,. \end{aligned}$$

A near-identity Lie-transform, the gyrocenter transformation, is applied to obtain

$$\begin{aligned} H_1^{(gy)} &= q\left\langle \phi_1 + \frac{\mu}{q} B_{1\parallel} \right\rangle \equiv q\langle \psi_1 \rangle \\ \Gamma_1^{(gy)} &= \left[\frac{q}{c}\mathbf{A}_0^* + \frac{q}{c}\langle A_{1\parallel} \rangle \mathbf{b}_0 \right] \cdot \mathrm{d}\mathbf{X} + \frac{\mu B_0}{\Omega}\mathrm{d}\theta - [H_0 + q\langle \psi_1 \rangle]\mathrm{d}t \end{aligned}$$

where the gyroaverage $\langle\rangle = \frac{1}{2\pi}\int_0^{2\pi} \mathrm{d}\theta$ has been introduced. Appropriate choices for the generating functions and gauge functions that define this gyrocenter Lie

transform are found in Ref. [29], for example. The resulting gyrocenter Fokker-Planck equation reads

$$\frac{\partial}{\partial t}F^{(gy)} + \dot{\mathbf{X}} \cdot \nabla F^{(gy)} + \dot{v}_\parallel \frac{\partial F^{(gy)}}{\partial v_\parallel} = \langle C_a[F^{(gy)}] \rangle \,, \tag{2.1.30}$$

where the Vlasov operator on the left hand side does not contain a μ derivative, since by construction of gyrocenter coordinates $\dot{\mu} = 0$. The term $\partial_\theta F$ disappears as well and F is taken to be independent on θ. The model for the gyrokinetic collision operator is discussed in the next subsection. The perturbed equations of motion are consistently derived in Ref. [29] from the associated Poisson brackets $\dot{\mathbf{X}} = \{\mathbf{X}, H\}$ and $\dot{v}_\parallel = \{v_\parallel, H\}$. One gets

$$\begin{aligned}
\dot{\mathbf{X}} &= v_\parallel \hat{\mathbf{b}}_0 + \frac{B}{B^*_\parallel}\mathbf{v}_D \\
\dot{v}_\parallel &= -\frac{1}{m v_\parallel}\dot{\mathbf{X}} \cdot \left(q\nabla\bar{\phi}_1 + \mu\nabla(B_0 + \bar{B}_{1\parallel}) \right) - \frac{q}{mc}\dot{\bar{A}}_{1\parallel}
\end{aligned}$$

where the overbars label gyroaveraged quantities. With the gyroaveraged modified potential

$$\bar{\chi}_1 = \bar{\phi}_1 - \frac{v_\parallel}{c}\bar{A}_{1\parallel} + \frac{\mu}{q}\bar{B}_{1\parallel} \,,$$

the gyrocenter drift velocity is written as

$$\mathbf{v}_D = \mathbf{v}_{\bar{\chi}} + \mathbf{v}_{\nabla B_0} + \mathbf{v}_c \,, \tag{2.1.31}$$

which is the sum of the generalized $E \times B$ velocity

$$\mathbf{v}_{\bar{\chi}} = \frac{c}{B_0^2}\mathbf{B}_0 \times \nabla\bar{\chi}_1 \,, \tag{2.1.32}$$

the gradient-B velocity

$$\mathbf{v}_{\nabla B_0} = \frac{\mu c}{q B_0^2}\mathbf{B}_0 \times \nabla B_0 \tag{2.1.33}$$

and the magnetic curvature drift velocity

$$\mathbf{v}_c = \frac{v_\parallel^2}{\Omega}\left(\nabla \times \mathbf{B}_0\right)_\perp \,. \tag{2.1.34}$$

as also derived in [30]. Using Ampères law and the MHD equilibrium condition Eq. (1.4.4), the curvature drift is rewritten as

$$\mathbf{v}_c = \frac{v_\parallel^2 mc}{q B_0^2}\left(\mathbf{B}_0 \times \left[\frac{\nabla B_0}{B_0} + \frac{\beta_p}{2}\frac{\nabla p_0}{p_0}\right]\right) \,, \tag{2.1.35}$$

where $\beta_p = 8\pi p_0 / B_0^2$ denotes the kinetic to magnetic pressure ratio[12].

The gyrokinetic full-F equation

Altogether, the gyrokinetic full-F equation reads

$$\frac{\partial F_a}{\partial t} - \frac{q_a}{m_a c}\dot{\bar{A}}_{1\parallel}\frac{\partial F_a}{\partial v_\parallel} + \left[\frac{B_0}{B^*_{0\parallel}}\left(v_\parallel \hat{\mathbf{b}}_0 + \mathbf{v}_D\right)\right]\cdot \left\{\nabla F_a - \left(q_a \nabla \bar{\phi}_1 + \mu \nabla (B_0 + \bar{B}_{1\parallel})\right)\frac{1}{m_a v_\parallel}\frac{\partial F_a}{\partial v_\parallel}\right\} = \langle C_a[F]\rangle\,, \tag{2.1.36}$$

where we abbreviate the gyrocenter distribution $F_a = F_a^{(gy)}$ and its gyrocenter phase space as $\mathbf{Z}^{(gy)} = \{\mathbf{X}, v_\parallel, \mu\}$. The collision operator on the right hand side is described in the next section.

2.1.5. The model for collisions

To treat collisional dynamics, it is of great advantage to expand the distribution function $F_a = F_{0a} + F_{1a} + \ldots$ into a background part that is constant in time, and a small fluctuating part $F_{1a} \sim \epsilon_\delta F_{0a}$. This allows to linearize the Fokker-Planck equation conveniently. A constant background is justified, when only processes faster than the equilibrium time scale are considered. Here, we choose a local Maxwellian distribution

$$F_{0a} = F_{Ma}(\mathbf{x}, v_\parallel, \mu) = \frac{n_{0a}(x)}{\pi^{3/2} v_{Ta}^3(x)} \exp\left[-\frac{m_a v_\parallel^2/2 + \mu B_0(\mathbf{x})}{T_{0a}(x)}\right] \tag{2.1.37}$$

with vanishing flow velocity.[9] The guiding center collision operator, Eq. (2.1.29) $C^{(gc)}[\langle F^{(gc)}\rangle]$ has been explicitly evaluated in Ref. [28] for an isotropic background F_0 and expanded in terms of ϵ_B.[10] The lowest order operator is equivalent to the test-particle operator implemented in GENE, as also described in Ref. [15]. However, for the actual evaluation of collisions in the gyrocenter equation, we ignore the difference of $F^{(gc)}$ and $F^{(gy)}$ and further take $F^{(gy)}$ to be independent of the gyroangle to compute

$$\langle C_a[F]\rangle = \langle C^{(gc)}[F^{(gy)}]\rangle\,. \tag{2.1.38}$$

The difference of the guiding center (gc) and gyrocenter (gy) distribution is given the gyrocenter pull-back operation

$$F_a^{(gc)} = T^{(gy)*} F_{1a}^{(gy)} = F_{1a}^{(gy)} - \left\{q_a(\phi_1 - \bar{\phi}_1^{(gy)}) - \mu \bar{B}_{1\parallel}^{(gy)}\right\}\frac{F_{0a}}{T_{0a}}\,. \tag{2.1.39}$$

[9] The property *local* refers to the fact that F_0 is a function of position $\mathbf{x}$ and defines local temperature and density at that position.

[10] (F_{Ma} is isotropic)

of the near-identity transform that we take from Ref. [29] for a local Maxwellian F_{0a}, keeping only first order terms in ϵ_B . Equation (2.1.39) yields the identity $F_a^{(gc)} = F_a^{(gy)}$ in the drift-kinetic limit $k_\perp \rho_a \to 0$, when additionally $B_{1\parallel}$ fluctuations are not considered. This limit is well applicable, for example, in neoclassical computations. Also, electron collisions are correctly described by Eq. 2.1.38, since $k_\perp \rho_e \ll 1$, provided that $k_\perp \rho_i \lesssim 1$. The problems considered in this thesis all fulfill these conditions. We will thus, in the following take $F_a = F_a^{(gy)}$ to evaluate collisions. The linearized Fokker-Planck collision operator introduced in Sec. 2.1.2 is transformed to guiding center coordinates in Appendix A to have the gyroaveraged form

$$\left\langle C_a^L \right\rangle = \left[\sum_b \langle C_{ab}^T \rangle + \langle C_{ab}^F \rangle \right]$$

The final form of the test-particle operator turns Eq. (2.1.13) into

$$\begin{aligned} \langle C_{ab}^T \rangle =& \frac{\gamma_{ab} n_{0b}}{m_a m_b} \frac{\partial}{\partial \mathbf{V}} \cdot F_{Ma} \left(\frac{T_{0b}}{m_a v^5} \begin{bmatrix} \frac{2\mu B_0}{m_a} \Phi_1 + v_\parallel^2 \Phi_2 & 6\mu v_\parallel \Phi_2 \\ 6\mu v_\parallel \Phi_2 & \frac{2m_a}{B_0} v_\parallel^2 \mu \Phi_1 + 4\mu^2 \Phi_3 \end{bmatrix} \cdot \frac{\partial}{\partial \mathbf{V}} \right. \\ & \left. + \left(1 - \frac{T_{0b}}{T_{0a}} \right) \frac{\Phi_3}{v^3} \begin{bmatrix} v_\parallel \\ 2\mu \end{bmatrix} \right) \frac{F_a}{F_{Ma}} \end{aligned} \tag{2.1.40}$$

where $\partial/\partial \mathbf{V}$ summarizes $\left(\partial/\partial v_\parallel, \partial/\partial \mu\right)$. For field-particle collisions, Eq. (2.1.24) turns into the model operator

$$\left\langle C_{ab}^F (F_{1a}) \right\rangle = \frac{B_{ab}^P(x_b)}{I_{5,ab}} \frac{v_\parallel F_{Ma}}{m_a} \delta \dot{\mathcal{P}}_{\parallel ba} + \frac{I_{1,ab} B_{ab}^E(x_b) - I_{2,ab}}{I_{3,ab} I_{1,ab} - I_{2,ab} I_{4,ab}} \frac{F_{Ma}}{m_a} \delta \dot{\mathcal{E}}_{ba} \tag{2.1.41}$$

with the integrals for collisional momentum and energy transfer rates

$$\begin{aligned} \delta \dot{\mathcal{P}}_{\parallel ba} &= - \int m_b v_\parallel \left\langle C_{ba}^T [F_b] \right\rangle_b \mathrm{d}^3 v \\ \delta \dot{\mathcal{E}}_{ba} &= - \int m_b v^2 \left\langle C_{ba}^T [F_b] \right\rangle_b \mathrm{d}^3 v \end{aligned} \tag{2.1.42}$$

evaluated from the guiding-center test-particle operator. For the prefactors B_α (and thereby I_α), different choices are possible. In Sec. 2.1.2 we have discussed the Xu-Rosenbluth model, as well as a self-adjoint form. The corresponding integrals are performed in guiding center space, inserting the gyrocenter distribution, according to our convention.

2.1.6. Further transformation of the gyrocenter equation

In the framework of δf splitting it is consistent to neglect the (slow) thermalization term of the collision operator. Because equilibrium quantities like F_0 can be evaluated at particle position $\mathbf{x}$ or gyrocenter position $\mathbf{X}$, the zeroth order collisional

term is identical to Eq. (2.1.7) and is taken to vanish. The resulting zeroth order kinetic equation

$$\langle C_a[F_0]\rangle = 0 = v_\parallel \mathbf{b}_0 \cdot \left[\nabla F_{0a} - \frac{1}{m_a v_\parallel}\mu \nabla B_0 \frac{\partial F_{0a}}{\partial v_\parallel}\right],$$

is fulfilled by our choice of F_{0a}, which can easily be verified by inserting Eq. (2.1.37). The remaining terms of Eq. (2.1.36), to first order in ϵ_i are

$$\begin{aligned}\langle C_a^L[F]\rangle =& \frac{\partial F_{1a}}{\partial t} - \dot{\bar{A}}_{1\parallel}\frac{q_a}{m_a c}\frac{\partial F_{0a}}{\partial v_\parallel} \\ &+ \frac{B_0}{B_{0\parallel}^*} v_\parallel \hat{\mathbf{b}}_0 \cdot \Bigg\{ \left[\nabla F_{1a} - \mu \nabla B_0 \frac{1}{m_a v_\parallel}\frac{\partial F_{1a}}{\partial v_\parallel}\right] \\ &- \left(q_a \nabla \bar{\phi}_1 + \mu \nabla \bar{B}_{1\parallel}\right)\frac{1}{m_a v_\parallel}\frac{\partial F_{0a}}{\partial v_\parallel}\Bigg\} \\ &+ \frac{B_0}{B_{0\parallel}^*}\mathbf{v}_D \cdot \left\{\nabla\left(F_{0a}+F_{1a}\right) - \left(q_a\nabla\bar{\phi}_1 + \mu\nabla(B_0+\bar{B}_{1\parallel})\right)\frac{1}{m_a v_\parallel}\frac{\partial F_{0a}}{\partial v_\parallel}\right\}\end{aligned} \tag{2.1.43}$$

where on the left hand side, the linearized collision operator appears. Higher order terms will not be considered in this work. They involve the nonlinearity of the collision operator $\langle C_{ab}^N[F_{1a}, F_{1b}]\rangle$ as well as the so-called $v_\parallel$ *nonlinearity* or *parallel nonlinearity* given to all orders by

$$\begin{aligned}N_{\parallel a} =& -\dot{\bar{A}}_{1\parallel}\frac{q_a}{m_a c}\frac{\partial F_{1a}}{\partial v_\parallel} - \frac{B_0}{B_{0\parallel}^*} v_\parallel \hat{\mathbf{b}}_0 \cdot \left\{\left(q_a\nabla\bar{\phi}_1 + \mu\nabla(\bar{B}_{1\parallel})\right)\frac{1}{m_a v_\parallel}\frac{\partial F_{1a}}{\partial v_\parallel}\right\} \\ &- \frac{B_0}{B_{0\parallel}^*}\mathbf{v}_D \cdot \left\{\left(q_a\nabla\bar{\phi}_1 + \mu\nabla(B_0+\bar{B}_{1\parallel})\right)\frac{1}{m_a v_\parallel}\frac{\partial F_{1a}}{\partial v_\parallel}\right\}\end{aligned}$$

as appearing on the right hand side of the equation. The collisional nonlinearity is commonly neglected in computational models. Its influence is discussed in [17] in the context of neoclassical transport. The parallel nonlinearity is discussed in the literature in the context of maintaining an energy conservation law for the gyrokinetic equation. Nevertheless, it has been shown in [31, 32, 33] that no significant contribution is expected for medium-size and large tokamaks.

We further simplify Eq. (2.1.43) by explicitly evaluating the derivatives of the Maxwellian background distribution

$$\frac{\partial F_{0a}}{\partial v_\parallel} = -\frac{m_a v_\parallel}{T_{0a}}F_{0a}, \qquad \frac{\partial F_{0a}}{\partial \mu} = -\frac{B_0}{T_{0a}}F_{0a}\,, \tag{2.1.44}$$

and

$$\nabla F_{0a} = \left[\frac{\nabla n_{0a}}{n_{0a}} + \frac{\nabla T_{0a}}{T_{0a}}\left(\frac{m_a v_\parallel^2/2 + \mu B_0}{T_{0a}} - \frac{3}{2}\right) - \frac{\mu \nabla B_0}{T_{0a}}\right]F_{0a}\,. \tag{2.1.45}$$

Note that the first two terms are purely radial, because they involve gradients of density n_{0a} and temperature T_{0a}, which are flux surface quantities. The last term in ∇F_{0a} cancels with a $\mu\nabla B_0$ term in Eq. (2.1.43). The appearance of this term essentially is a consequence of our choice of velocity space coordinates $\{v_\parallel,\mu\}$. This becomes more clear in Sec. 2.2.4, where the neoclassical equation is compared to other formulations. In Eq. (2.1.43), two terms involving time derivatives exist. It is of computational advantage to combine these two terms on the left hand side by defining a modified distribution function

$$g_{1a} = F_{1a} - \bar{A}_{1\parallel}\frac{q_a}{m_a c}\frac{\partial F_{0a}}{\partial v_\parallel} = F_{1a} + v_\parallel \bar{A}_{1\parallel}\frac{q_a}{c}F_{0a}$$

that is evolved in time. In summary, the gyrokinetic equation turns into

$$\begin{aligned}\frac{\partial g_{1a}}{\partial t} =& -\frac{B_0}{B^*_{0\parallel}}v_\parallel \hat{\mathbf{b}}_0 \cdot \Bigg\{ \left[\nabla F_{1a} - \mu\nabla B_0 \frac{1}{m_a v_\parallel}\frac{\partial F_{1a}}{\partial v_\parallel}\right] \\ &\qquad + \left(q_a\nabla\bar{\phi}_1 + \mu\nabla\bar{B}_{1\parallel}\right)\frac{1}{T_{0a}}F_{0a}\Bigg\} \\ &- \frac{B_0}{B^*_{0\parallel}}\mathbf{v}_D \cdot \left\{\nabla F_{1a} + \left(q_a\nabla\bar{\phi}_1 + \mu\nabla\bar{B}_{1\parallel}\right)\frac{1}{T_{0a}}F_{0a}\right\} \\ &- \frac{B_0}{B^*_{0\parallel}}\mathbf{v}_D \cdot \left\{\left[\frac{\nabla n_{0a}}{n_{0a}} + \frac{\nabla T_{0a}}{T_{0a}}\left(\frac{m_a v_\parallel^2/2 + \mu B_0}{T_{0a}} - \frac{3}{2}\right)\right]F_{0a}\right\} \\ &+ \langle C_a^L[F]\rangle \end{aligned} \tag{2.1.46}$$

2.1.6.1. The field-aligned coordinate system

We exploit the strong anisotropy between parallel and perpendicular length scales that is introduced by the guiding magnetic field, by employing a field-aligned coordinate system. A useful introduction to field-aligned coordinates in plasma physics is given in Ref. [34]. The transformation to a general curvilinear coordinate system $u^{(1,2,3)} = (x, y, z)$ is described by the (contravariant) metric tensor

$$(g^{ij}) = (\nabla u^i \cdot \nabla u^j) = \begin{pmatrix} g^{xx} & g^{yx} & g^{zx} \\ g^{xy} & g^{yy} & g^{zy} \\ g^{xz} & g^{yz} & g^{zz} \end{pmatrix}.$$

We utilize a Clebsch coordinate system by writing the magnetic field as

$$\mathbf{B}_0 = \mathcal{C}\,[\nabla x \times \nabla y]$$

and thereby find the Jacobian of the transformation

$$J^{-1} = [\nabla x \times \nabla y] \cdot \nabla z = \frac{\mathbf{B}_0 \cdot \nabla z}{\mathcal{C}}.$$

Here, z denotes the 'parallel' coordinate along the field line, x is the flux-surface label (the radial coordinate) and y is the field-line label (binormal coordinate). The vector relations occurring in Eq. (2.1.36) are now expanded in terms of the introduced metric tensor. The salient feature of these field-aligned coordinates is that the parallel derivative

$$\begin{aligned}\mathbf{B}_0 \cdot \nabla &= \mathcal{C}\left[\nabla x \times \nabla y\right] \cdot \nabla u^i \partial_i \\ &= \frac{\mathcal{C}}{J}\partial_z\end{aligned}$$

only has one component. The drift velocities involve outer vector products of the type

$$\begin{aligned}\frac{1}{B_0^2}\left(B_0 \times \nabla A\right) \cdot \nabla &= \frac{\mathcal{C}}{B_0^2}\left(\left[\nabla x \times \nabla y\right] \times \partial_i A \nabla u^i\right) \cdot \nabla u^j \partial_j \\ &= \frac{1}{\mathcal{C}}\frac{g^{1i}g^{2j} - g^{2i}g^{1j}}{\gamma_1}\partial_i A \partial_j\end{aligned}$$

where for the function A we insert $p_0, B_0, \bar{\chi}_1$ in Eq. (2.1.36). We introduce the abbreviations

$$\begin{aligned}\gamma_1 &= g^{11}g^{22} - g^{21}g^{12} \\ \gamma_2 &= g^{11}g^{23} - g^{21}g^{13} \\ \gamma_3 &= g^{12}g^{23} - g^{22}g^{13}\end{aligned}$$

as well as the curvature terms

$$K_x = -\frac{1}{\mathcal{C}}\left(\partial_y B_0 + \frac{\gamma_2}{\gamma_1}\partial_z B_0\right) \qquad \text{and} \qquad K_y = \frac{1}{\mathcal{C}}\left(\partial_x B_0 + \frac{\gamma_3}{\gamma_1}\partial_z B_0\right) \tag{2.1.47}$$

to facilitate notation. The transformation of the (radial component of the) drift velocities is given in Sec. 2.3 as an example. In particular, the field-aligned coordinates allow to identify small terms in the parallel-wavenumber ordering, which becomes apparent in the $E \times B$ drift velocity. We can write, for example, the radial component as

$$v_{\bar{\chi}}^x = -\frac{c}{\mathcal{C}}\left(\partial_y \bar{\chi} + \frac{\gamma_2}{\gamma_1}\partial_z \bar{\chi}\right) = -\frac{c}{\mathcal{C}}\partial_y \bar{\chi} + \mathcal{O}(\epsilon_\delta \epsilon_\parallel)$$

and neglect the parallel derivative, since it appears in direct combination with a perpendicular derivative. Thereby, the metric quantities γ_i, as well as their ratios are taken to be of order unity. We additionally introduce the abbreviations

$$\Gamma_{a,i} = \partial_i F_{1a} + \left(q_a \partial_i \bar{\phi}_1 + \mu \partial_i \bar{B}_{1\parallel}\right)\frac{F_{0a}}{T_{0a}}$$

with $i \in \{x, y, z\}$ so that altogether, the gyrokinetic equation turns into

$$
\begin{aligned}
\frac{\partial g_{1a}}{\partial t} = &+ \frac{c}{\mathcal{C}} \frac{B_0}{B_{0\parallel}^*} \left[\frac{\partial_x n_{0a}}{n_{0a}} + \frac{\partial_x T_{0a}}{T_{0a}} \left(\frac{m_a v_\parallel^2/2 + \mu B_0}{T_{0a}} - \frac{3}{2} \right) \right] F_{0a} \partial_y \bar{\chi}_1 \\
&- \frac{cB_0}{B_{0\parallel}^*} \frac{\mu B_0 + m_a v_\parallel^2}{q_a B_0} K_x \Gamma_{a,x} \\
&- \frac{cB_0}{B_{0\parallel}^*} \left[\frac{\mu B_0 + m_a v_\parallel^2}{q_a B_0} K_y + \frac{c}{\mathcal{C}} \frac{m_a}{q_a} v_\parallel^2 \frac{\beta_p}{2} \frac{\partial_x p_0}{p_0} \right] \Gamma_{a,y} \\
&- \frac{c}{\mathcal{C}} \frac{B_0}{B_{0\parallel}^*} \left((\partial_x \bar{\chi}_1) \, \Gamma_{a,y} - (\partial_y \bar{\chi}_1) \, \Gamma_{a,x} \right) \\
&- \frac{\mathcal{C}}{J B_0} v_\parallel \left[\Gamma_{a,z} - \mu \partial_z B_0 \frac{1}{m_a v_\parallel} \frac{\partial F_{1a}}{\partial v_\parallel} \right] \\
&+ \frac{cB_0}{B_{0\parallel}^*} \frac{\mu B_0 + m_a v_\parallel^2}{q_a B_0} K_x \left[\frac{\partial_x n_{0a}}{n_{0a}} + \frac{\partial_x T_{0a}}{T_{0a}} \left(\frac{m_a v_\parallel^2/2 + \mu B_0}{T_{0a}} - \frac{3}{2} \right) \right] F_{0a} \\
&+ \langle C_a^L[F] \rangle \, . \qquad (2.1.48)
\end{aligned}
$$

On the left-hand side we isolate the explicit time derivative, while on the right hand side we identify the terms (in order) as the drive term due to background density and temperature gradients, the x and y curvature terms[11], the generalized $E \times B$ nonlinearity including also magnetic flutter, the parallel advection, the neoclassical drive term that does not contain F_{1a} in any way, and finally the collision operator.

2.1.7. Moments of the distribution function

The gyrokinetic equations involve particle drifts that require a self-consistent description of the electromagnetic fields. These can be computed from the particle distribution with Maxwell's equations

$$
\begin{aligned}
-\nabla^2 \phi &= 4\pi \rho(x) = 4\pi \sum_a q_a n_a(\mathbf{x}) \qquad (2.1.49) \\
-\nabla^2 \mathbf{A} &= \frac{4\pi}{c} \mathbf{j}(\mathbf{x}) = \frac{4\pi}{c} \sum_a q_a n_a(\mathbf{x}) \mathbf{u}_a(\mathbf{x}) \, .
\end{aligned}
$$

Note that the requirement of low frequency waves described within the gyrokinetic framework allows us to neglect the displacement current in Ampères law. Here, we only compute the fluctuating parts of $\mathbf{A}$ and ϕ from the particle distribution. The the zeroth order plasma current density $\mathbf{j}_0$ that provides the poloidal component of the guiding magnetic field, as well as the vector potential generated by external coils are not considered. The zeroth order electric field $-\nabla \phi_0$ is moreover assumed to

[11] Note that the contribution of the pressure gradient to the y curvature term is $\mathcal{O}(\beta_p \epsilon_\delta)$ and thus often neglected.

vanish. The fluid moments, like density, flow velocity and temperature are computed as velocity space moments of the kinetic distribution function f_a in particle space

$$\begin{aligned} n_a(\mathbf{x}) &= \int f_a(\mathbf{x},\mathbf{v})\,\mathrm{d}^3v \\ \mathbf{u}_a(\mathbf{x}) &= \frac{1}{n_a(\mathbf{x})}\int \mathbf{v} f_a(\mathbf{x},\mathbf{v})\,\mathrm{d}^3v \\ T_a(\mathbf{x}) &= \frac{1}{n_a(\mathbf{x})}\int \frac{m_a}{2}(\mathbf{v}-\mathbf{u}_a)^2 f_a(\mathbf{x},\mathbf{v})\,\mathrm{d}^3v \end{aligned}$$

and these quantities enter Maxwell's equations Eq. (2.1.49). From the fact that the gyrokinetic equation evolves the gyrocenter distribution function, it is clear that a transformation to particle coordinates is required. It is therefore helpful to derive a general expression for these moments

$$\begin{aligned} M_a^{\mathrm{mn}}(x) &= \int v_\parallel^{\mathrm{m}} v_\perp^{\mathrm{n}} f_a^{(pc)}(\mathbf{x},\mathbf{v})\mathrm{d}^3v \\ &= \int \delta(\mathbf{X}-\mathbf{x}+\boldsymbol{\rho}) F_a^{(gc)}(\mathbf{X},\mathbf{V}) v_\parallel^{\mathrm{m}} v_\perp^{\mathrm{n}} \frac{B_{0\parallel}^*(\mathbf{x},\mathbf{v})}{m_a}\mathrm{d}\mathbf{X}\mathrm{d}v_\parallel\mathrm{d}\mu \\ &= \int \delta(\mathbf{X}-\mathbf{x}+\boldsymbol{\rho}) T^{(gy)*} F_a^{(gy)}(\mathbf{X},\mathbf{V}) \frac{B_{0\parallel}^*(\mathbf{x},\mathbf{v})}{m_a} v_\parallel^{\mathrm{m}} v_\perp^{\mathrm{n}}\mathrm{d}\mathbf{X}\mathrm{d}v_\parallel\mathrm{d}\mu\,, \end{aligned} \tag{2.1.50}$$

where, in two steps, the particle distribution function $f_a^{(pc)}$ is obtained from the gyrocenter distribution function. We refer to Refs. [27, 30] for the guiding center transformation (the first step) that yields the velocity space Jacobian $B_{0\parallel}^*(\mathbf{x},\mathbf{v})/m_a$. The second step involves the gyrocenter pull-back operation

$$F_a^{(gc)} = T^{(gy)*} F_{1a}^{(gy)} = F_{1a}^{(gy)} - \left\{ q_a(\phi_1^{(pc)} - \bar{\phi}_1^{(gy)}) - \mu \bar{B}_{1\parallel}^{(gy)} \right\} \frac{F_{0a}}{T_{0a}}\,. \tag{2.1.51}$$

(see Eq. 2.1.51) that we take from Ref. [29] for a local Maxwellian F_{0a} and keep only first order terms in ϵ_B . In the following we use the gyrocenter distribution $F_{1a} = F_{1a}^{(gy)}$ without explicitly marking it. By expressing

$$B_{0\parallel}^*(\mathbf{x},\mathbf{v}) = B_0 + \frac{m_a c}{q_a} v_\parallel \mathbf{b}_0 \cdot \nabla \times \mathbf{b}_0$$

we find the second term to be one order in ϵ_B smaller than the first term. We will thus neglect this second term in the following, which turns out to simplify and partially decouple Maxwell's equations. At this point we note that two forms of gyroaverages exist. The first form

$$\bar{\phi}_1(\mathbf{X}) = \frac{1}{2\pi}\int \phi_1(\mathbf{X}+\boldsymbol{\rho}_a)\mathrm{d}\theta$$

is denoted by $\cdot\bar{\cdot}\cdot$ and it appears in the transformation to gyrocenter coordinates, and thus also in the Vlasov equation. The second gyroaverage is introduced by taking velocity space moments as

$$\left\langle \bar{\phi} \right\rangle (\mathbf{x}) = \frac{1}{2\pi} \int \delta(\mathbf{X} - \mathbf{x} + \boldsymbol{\rho}_a) \bar{\phi}_1(\mathbf{X}) \mathrm{d}\mathbf{X} \mathrm{d}\theta \,.$$

By explicitly writing $\tilde{\phi}_1 = \phi_1^{(pc)}(\mathbf{x}) - \bar{\phi}_1^{(gy)}(\mathbf{X})$ it is clear that the first term is not affected by the $\langle \cdots \rangle$ type of gyroaverage, since it does not depend on $\mathbf{X}$. On the other hand, evaluating the $\cdot\bar{\cdot}\cdot$ type gyroaveraged function of the second term at the position $\mathbf{X} = \mathbf{x} - \boldsymbol{\rho}_a(\theta)$ actually re-introduces the gyroangle-dependence. Indeed, inserting the pull-back operation Eq. (2.1.51) into the moment Eq. (2.1.50) gives

$$\begin{aligned} M_a^{\mathrm{mn}}(\mathbf{x}) =& \frac{2\pi}{m_a} \int \left\langle \left\{ \left(\frac{2B_0}{m_a} \right)^{\mathrm{n}/2} B_0 \left[F_{1a} + q_a \bar{\phi}_1 + \mu \bar{B}_{1\parallel} \frac{F_{0a}}{T_{0a}} \right] \right\} \Big|_{\mathbf{x}-\boldsymbol{\rho}} \right\rangle v_\parallel^{\mathrm{m}} \mu^{\mathrm{n}/2} \mathrm{d}v_\parallel \mathrm{d}\mu \\ & - \frac{2\pi}{m_a} q_a \phi_1(\mathbf{x}) \int \left(\frac{2B_0}{m_a} \right)^{\mathrm{n}/2} B_0 \frac{F_{0a}}{T_{0a}} v_\parallel^{\mathrm{m}} \mu^{\mathrm{n}/2} \mathrm{d}v_\parallel \mathrm{d}\mu \end{aligned} \tag{2.1.52}$$

including consecutive gyroaverages of the form $\left\langle \bar{\phi}_1 \right\rangle$. Here, the factor $(2B_0/m_a)^{\mathrm{n}/2}$ appears due to the replacement of $v_\perp$ by the magnetic moment μ. The notation $\{\cdots\}|_{\mathbf{x}-\boldsymbol{\rho}}$ indicates that the bracketed expression is to be evaluated at the position $\mathbf{x} - \boldsymbol{\rho}_a$. Note that in Eq. (2.1.52), the equilibrium quantities are kept within the gyroaverage in order to preserve the symmetry of the Maxwell equations also in the (radially) global case. In some of the above terms in Eq. (2.1.52) it is possible to evaluate the velocity integrals analytically. In particular,

$$\frac{2\pi B_0}{m_a} \int F_{0a} \mathrm{d}v_\parallel \mathrm{d}\mu = \frac{n_{0a} B_0}{T_{0a}} \int \mathrm{e}^{-\mu B_0 / T_{0a}} \mathrm{d}\mu = n_0.$$

2.1.8. Gyrokinetic form of Maxwell's equations

We now turn to the gyrokinetic field equations by inserting the appropriate moments into Maxwell's equations.

2.1.8.1. Gyrokinetic Poisson equation

The Poisson equation reads

$$\begin{aligned} \nabla_\perp^2 \phi_1(\mathbf{x}) =& -4\pi \sum_a q_a M_a^{00}(\mathbf{x}) \\ =& -8\pi^2 \sum_a \frac{q_a}{m_a} \int \left[\left\langle \{B_0 F_1\} \Big|_{\mathbf{x}-\boldsymbol{\rho}} \right\rangle + \left\langle \left\{ \left(q_a \bar{\phi}_1 + \mu \bar{B}_{1\parallel} \right) B_0 \frac{F_{0a}}{T_{0a}} \right\} \Big|_{\mathbf{x}-\boldsymbol{\rho}} \right\rangle \right. \\ & \left. - q_a \phi_1 B_0 \frac{F_{0a}}{T_{0a}} \right] \mathrm{d}v_\parallel \mathrm{d}\mu \end{aligned}$$

where the quasineutrality condition $\sum_a n_{0a} q_a = 0$ has been explicitly evaluated and the parallel wavenumber ordering has been used on the Laplacian. We rearrange the equation to have all terms containing the electrostatic potential on the left hand side

$$\begin{aligned}\nabla_\perp^2 \phi_1(\mathbf{x}) - 8\pi^2 \sum_a \frac{q_a^2}{m_a} \int \left[\left\langle \phi_1 B_0 \frac{F_{0a}}{T_{0a}} - \left\{ \bar{\phi}_1 B_0 \frac{F_{0a}}{T_{0a}} \right\} \Big|_{\mathbf{x}-\boldsymbol{\rho}} \right\rangle \right] \mathrm{d}v_\parallel \mathrm{d}\mu \\ = -8\pi^2 \sum_a \frac{q_a}{m_a} \int \left[\left\langle \{B_0 g_1\} \Big|_{\mathbf{x}-\boldsymbol{\rho}} \right\rangle + \left\langle \left\{ \mu \bar{B}_{1\parallel} B_0 \frac{F_{0a}}{T_{0a}} \right\} \Big|_{\mathbf{x}-\boldsymbol{\rho}} \right\rangle \right] \mathrm{d}v_\parallel \mathrm{d}\mu \,.\end{aligned}$$

Furthermore, we replace the distribution F_{1a} with the modified distribution g_1, which does not change the Poisson equation because the added term is anti-symmetric in $v_\parallel$ and its velocity integral vanishes. The operator on the left hand side can be formally inverted and applied on the right hand side to solve the equation. Note that $B_{1\parallel}$ fluctuations are coupled to ϕ_1 fluctuations.

2.1.8.2. Gyrokinetic Ampère's law

The gyrokinetic version of the perpendicular component of Ampère's law reads

$$\begin{aligned}\nabla_\perp A_{1\parallel}(x) &= -\frac{4\pi}{c} \sum_a q_a M_a^{10}(x) \\ &= -\frac{8\pi^2}{c} \sum_a \frac{q_a}{m_a} \int v_\parallel \left\langle \{B_0 F_1\} \Big|_{\mathbf{x}-\boldsymbol{\rho}} \right\rangle \mathrm{d}v_\parallel \mathrm{d}\mu \\ &= -\frac{8\pi^2}{c} \sum_a \frac{q_a}{m_a} \int \left[v_\parallel \left\langle \{B_0 g_{1a}\} \Big|_{\mathbf{x}-\boldsymbol{\rho}} \right\rangle - v_\parallel^2 \left\langle \left\{ B_0 \frac{F_{0a}}{T_{0a}} \bar{A}_{1\parallel} \right\} \Big|_{\mathbf{x}-\boldsymbol{\rho}} \right\rangle \right] \mathrm{d}v_\parallel \mathrm{d}\mu \,,\end{aligned}$$

where no equilibrium currents are taken into account, since they are stationary and accounted for in the equilibrium magnetic field. We have again introduced the g_1 distribution, which gives an extra term. Collecting all expressions including $A_{1\parallel}$ on the left hand side gives

$$\begin{aligned}\nabla_\perp A_{1\parallel}(x) - \frac{8\pi^2}{c} \sum_a \frac{q_a}{m_a} \int \left\langle \left\{ B_0 \frac{F_{0a}}{T_{0a}} \bar{A}_{1\parallel} \right\} \Big|_{\mathbf{x}-\boldsymbol{\rho}} \right\rangle v_\parallel^2 \mathrm{d}v_\parallel \mathrm{d}\mu \\ = -\frac{8\pi^2}{c} \sum_a \frac{q_a}{m_a} \int \left\langle \{B_0 g_{1a}\} \Big|_{\mathbf{x}-\boldsymbol{\rho}} \right\rangle v_\parallel \mathrm{d}v_\parallel \mathrm{d}\mu \,.\end{aligned}$$

We complete the field equations with the perpendicular component of Ampère's law

$$(\nabla \times \mathbf{B}_1)_\perp = \frac{4\pi}{c} \mathbf{j}_\perp \,.$$

An equation for compressional magnetic field fluctuations $B_{1\parallel}$ is obtained by evaluating the curl expression

$$\partial_y B_{1\parallel} \hat{\mathbf{e}}_1 - \partial_x B_{1\parallel} \hat{\mathbf{e}}_2$$

in terms of the two unit vectors perpendicular to the magnetic field. We also introduce the unit vector of perpendicular velocity

$$\hat{\mathbf{c}}(\theta) = -\sin\theta\hat{\mathbf{e}}_1 - \cos\theta\hat{\mathbf{e}}_2\,,$$

which is included in the moment M_a^{01} for obtaining a (vector-valued) expression for current $\mathbf{j}_\perp$, to get

$$\begin{pmatrix} \partial_y B_{1\parallel} \\ -\partial_x B_{1\parallel} \end{pmatrix} = \frac{4\pi^2}{c}\sum_a q_a \left(\frac{2}{m_a}\right)^{3/2} \int \left\langle \left\{ \hat{\mathbf{c}} B_0^{3/2} \left[F_{1a} + q_a \bar{\phi}_{1a} \frac{F_{0a}}{T_{0a}} + \mu \bar{B}_{1\parallel} \frac{F_{0a}}{T_{0a}} \right] \right\} \Big|_{\mathbf{x}-\boldsymbol{\rho}} \right\rangle \sqrt{\mu} \mathrm{d}v_\parallel \mathrm{d}\mu\,.$$

Here, we use the fact that the term $\langle \phi_1 \hat{\mathbf{c}} \rangle = 0$ vanishes on gyroaverage. A more detailed derivation is given in Ref. [29, 30]. We note that the equation for $A_{1\parallel}$ is decoupled from the other field equations (because we have not considered equilibrium currents). The remaining equations for ϕ and $B_{1\parallel}$ form a coupled system of equations. Its solution is described in Ref. [15] for the local limit.

2.1.8.3. The local limit

In the local (flux-tube) limit, the equilibrium quantities can be taken out of the gyroaverages. The equations thus reduce to

$$\nabla_\perp^2 \phi_1 - 8\pi^2 \sum_a \frac{q_a^2}{m_a} \frac{B_0}{T_{0a}} \int F_{0a} \left[\phi_1 - \left\langle \bar{\phi}_1 \right\rangle \right] \mathrm{d}v_\parallel \mathrm{d}\mu = - 8\pi^2 \sum_a \frac{q_a}{m_a} B_0 \int \left[\langle g_1 \rangle + \frac{F_{0a}}{T_{0a}} \mu \left\langle \bar{B}_{1\parallel} \right\rangle \right] \mathrm{d}v_\parallel \mathrm{d}\mu$$

$$\nabla_\perp A_{1\parallel}(x) - \frac{8\pi^2}{c} \sum_a \frac{q_a}{m_a} \frac{B_0 F_{0a}}{T_{0a}} \int \left\langle \bar{A}_{1\parallel} \right\rangle v_\parallel^2 \mathrm{d}v_\parallel \mathrm{d}\mu = - \frac{8\pi^2}{c} \sum_a \frac{q_a B_0}{m_a} \int \langle g_{1a} \rangle \, v_\parallel \mathrm{d}v_\parallel \mathrm{d}\mu\,.$$

$$\begin{pmatrix} \partial_y B_{1\parallel} \\ -\partial_x B_{1\parallel} \end{pmatrix} = \frac{4\pi^2}{c} \sum_a q_a \left(\frac{2B_0}{m_a}\right)^{3/2} \int \left[\langle \hat{\mathbf{c}} F_{1a} \rangle + q_a \left\langle \hat{\mathbf{c}} \bar{\phi}_1 \right\rangle \frac{F_{0a}}{T_{0a}} + \mu \left\langle \hat{\mathbf{c}} \bar{B}_{1\parallel} \right\rangle \frac{F_{0a}}{T_{0a}} \right] \sqrt{\mu} \mathrm{d}v_\parallel \mathrm{d}\mu.$$

Furthermore, the gyroaverages $\cdot\bar{}\cdot$ and $\langle \cdots \rangle$ both can be replaced by multiplying with the same Bessel function $J_0(k_\perp \rho_a)$, as outlined in Refs. [15, 30]. A special role is thereby played by the $B_{1\parallel}$ gyroaverage, that requires the Bessel function $J_1(k_\perp\rho)/(k_\perp\rho)$, due to the additional $\sin\theta$ and $\cos\theta$ terms of the vector $\hat{\mathbf{c}}$.

2.2. Neoclassical theory as a subset of gyrokinetics

We have derived the gyrokinetic equations suited to describe (electromagnetic) plasma microturbulence. In this section, we show that this equation contains the neoclassical transport problem as a subset, which thus can be solved with gyrokinetic codes such as GENE. The standard theory for neoclassical transport is summarized in the review paper of Hinton and Hazeltine [8]. The underlying equation is the drift-kinetic equation, which we obtain by imposing further assumptions (the neoclassical ordering) on our gyrokinetic equation.

2.2.1. The neoclassical ordering

Just as the gyrokinetic ordering, neoclassical transport ordering relies on the smallness of the parameter $\epsilon_\delta = \rho_i/L_0 \ll 1$ with ρ_i denoting the ion gyroradius and L_0 the macroscopic scale length of background density, temperature, and magnetic field. One expands the distribution function in powers of ϵ_δ as $F = F_0 + F_1 + F_2 + \ldots$ where the lowest order distribution function is Maxwellian $F_0 = F_M$. The neoclassical transport coefficients can be obtained by solving the first-order kinetic equation for F_1. Throughout this work, electric fields and magnetic field perturbations are neglected, since they do not contribute to the neoclassical fluxes to lowest order (see, for example, [35]). We thus have $\bar{\phi}_1 = 0$, $\bar{A}_{1\parallel} = 0$, and $\bar{B}_{1\parallel} = 0$. In this case, $\mathbf{v}_D$ reduces to $\mathbf{v}_d = \mathbf{v}_{\nabla B} + \mathbf{v}_c$. If one instead wishes to consider the self-consistent electric field, ϕ_0 should be included, with its correct ordering, in the single particle Hamiltonian before Lie perturbation methods are applied, but this is left for future work. Neoclassical ordering is summarized as

1. The perturbed distribution is ordered as $F_1/F_0 \sim \epsilon_\delta$
2. The drift velocity is ordered as $v_D/v_\parallel \sim \epsilon_\delta$
3. The advection terms are ordered as $\mathbf{v}_D \cdot \nabla F_1 \sim \epsilon_\delta \mathbf{v}_D \cdot \nabla F_0 = \mathcal{O}(\epsilon_\delta^2)$.

Note that there is a subtle difference to gyrokinetic turbulence ordering, where the advection term $\mathbf{v}_D \cdot \nabla F_1 = \mathcal{O}(\epsilon_\delta)$ is one order larger (and gives the $E \times B$ nonlinearity). This is because the perpendicular derivatives of the perturbed distribution are ordered as $\nabla_\perp F_1 \sim F_1/\rho_i \sim F_0/L_0$ in gyrokinetics. The standard neoclassical ordering can be understood in connection with the locality of neoclassical transport. As long as particle orbits do not strongly deviate from the original flux surface, the coupling between neighboring flux surfaces is weak. This lets F_1 vary on the scale length of background density and temperature only.

2.2.2. The neoclassical equation

Applying the above discussed ordering on Eq. (2.1.46), we have the zeroth order equation fulfilled by a Maxwellian distribution function. The first order gyrokinetic equation (without electromagnetic field perturbations) reduces to

$$\begin{aligned}\frac{\partial F_{1a}}{\partial t} =& -\left\langle C_a^L[F]\right\rangle + \frac{B_0}{B_{0\|}^*} v_\| \hat{\mathbf{b}}_0 \cdot \left[\nabla F_{1a} - \mu \nabla B_0 \frac{1}{m_a v_\|} \frac{\partial F_{1a}}{\partial v_\|}\right] \\ &+ \frac{B_0}{B_{0\|}^*} \mathbf{v}_d \cdot \left\{ \left[\frac{\nabla n_{0a}}{n_{0a}} + \frac{\nabla T_{0a}}{T_{0a}} \left(\frac{m_a v_\|^2/2 + \mu B_0}{T_{0a}} - \frac{3}{2}\right)\right] F_{0a} \right\} \\ &+ \frac{B_0}{B_{0\|}^*} \mathbf{v}_d \cdot \nabla F_{1a}\end{aligned} \tag{2.2.1}$$

and includes the additional term $\mathbf{v}_D \cdot \nabla F_1$ that is formally of second neoclassical order. The standard neoclassical theory truncates the equation at first neoclassical order. The last term can thus be understood as the nonlocal correction to the standard neoclassical equation. It is argued in Ref. [17] that including this term can actually disturb the physics and that a consistent description would remove it from the first order equation and, instead, add the second order equation

$$\left\langle C_a^{\mathrm{NL}}[F_1]\right\rangle = \frac{\partial F_{2a}}{\partial t} + \frac{B_0}{B_{0\|}^*} \mathbf{v}_d \cdot \nabla F_{1a} + \frac{B_0}{B_{0\|}^*} \mathbf{v}_d \cdot \left\{ \frac{1}{m_a v_\|} \mu \nabla B_0 \frac{\partial F_{1a}}{\partial v_\|} \right\} \tag{2.2.2}$$

that includes the nonlinearity of the collision operator $\left\langle C_a^{NL}[f_1]\right\rangle = \sum_b \left\langle C[F_{1a}, F_{1b}]\right\rangle$, as well as a term that is part of the *parallel nonlinearity*. It is, however, not clear how large the effect of the additional second-order terms is, which we do not consider here. Let us note that the collisional nonlinearity is $\mathcal{O}(\epsilon_\delta^2)$ and, depending on the collision rate, probably smaller. The drift term on the other hand, can involve nonlocal effects by extreme peaking of the temperature gradient (like in transport barriers), even in cases in which ϵ_δ is small. Neglecting the collisional nonlinearity is thus formally correct in some cases. One example that requires an extension to standard neoclassical theory is found near the magnetic axis where particles follow potato shaped orbits rather than banana shaped orbits. These orbits are illustrated in Fig. 1.3.2. As a consequence, the standard neoclassical approximation breaks down in such a way that $\mathbf{v}_D \nabla F_1$ is comparable to $\mathbf{v}_D \nabla F_0$ and thus formally becomes first-order.[24, 36] Helander states explicitly that due to variations of F_1 on the potato-orbit scale the gradient ∇F_1 becomes large without breaking $F_1 \sim \epsilon_\delta F_0$.[36] In this case the neglect of the collisional and parallel nonlinearity is justified. Vernay has shown by means of global PIC simulations that including $\mathbf{v}_D \nabla F_1$ in the first-order equation yields unmodified local transport even where the standard neoclassical ordering is valid.[24] Interestingly, near the magnetic axis, where the ordering breaks down, including the nonlocal drift term actually removes the the strong increase of neoclassical heat flux that is artificially obtained with local models.

2.2.3. The local limit and the decoupling of neoclassical and turbulent transport

The neoclassical equation is axisymmetric; it is independent of the binormal (y) coordinate. In a Fourier decomposition of F_{1a}, only the $k_y = 0$ part contributes, which is linearly stable, but nonlinearly interacts with turbulent fluctuations. Without the drift term $\mathbf{v}_D \cdot \nabla F_{1a}$, Eq. (2.2.1) reduces to the standard neoclassical problem that is intrinsically local in the radial direction. In this local limit, the neoclassical equilibrium on a given flux surface is thus determined by the plasma parameters (such as temperature and magnetic field) on that flux surface. In consequence, one can solve for the neoclassical equilibrium on each individual flux surface separately, which fully decouples the neoclassical problem from turbulent fluctuations. This decoupling is seen by an additional Fourier decomposition in x: The neoclassical drive only affects the $k_x = k_y = 0$ part of F_{1a}, which in turn does not contribute to the $E \times B$ velocity that is responsible for nonlinear interactions and turbulent transport (defined in Eqs. (2.3.8) and (2.3.5)). Furthermore, we will see in Sec. 2.2.4 that the (second order) neoclassical fluxes do not require to compute the electric field in the local limit. It is thus valid to set $\phi(k_\perp = 0) = 0$ for neoclassical computations. In this context it is worth mentioning that the gyrokinetic Poisson equation is not defined for $k_\perp = 0$, which is a consequence of the ordering $k_\parallel^2 \ll k_\perp^2$. Even in the radially global case, the neoclassical equilibrium can be computed separately by focussing on the $k_y = 0$ Fourier mode. Nevertheless, the turbulent and neoclassical transport problems are coupled by nonlinear dynamics in that case.

2.2.4. Equivalence to other formalisms and independence of first order electric fields

Having derived the drift-kinetic equation in neoclassical ordering from the full-f gyrokinetic equation, one is interested to compare the result to the equations of other authors. The focus lies on the local limit here. Helander's equation[12] for the equilibrium solution $\partial_t F_1 = 0$ reads

$$v_\parallel \mathbf{b}_0 \cdot \nabla F_{1a} + \mathbf{v}_D \cdot \nabla F_{0a} + q_a v_\parallel E_\parallel^{(A)} \frac{\partial F_{0a}}{\partial \varepsilon} = C_a^L[F_{1a}] \tag{2.2.3}$$

where $E_\parallel^{(A)} = -\partial_t A_{0\parallel}/c$ is the inductive electric field used for Ohmic heating. Importantly, the derivative $\mathbf{b}_0 \cdot \nabla$ is taken at constant particle energy ε and magnetic moment μ. Since these two velocity space coordinates are constants of motion to lowest order, we have $\dot{\varepsilon} = 0$ and $\dot{\mu} = 0$, such that no velocity derivative appears in the drift kinetic equation.

[12] Ref. [7] Eq. (8.13)

For implementation in the NEO code, the first-order equation

$$v_\parallel \mathbf{b}_0 \cdot \nabla F_{1a} - \frac{q_a}{m_a} v_\parallel \mathbf{b}_0 \cdot \nabla \phi_1 \frac{\partial F_{0a}}{\partial \varepsilon} + \mathbf{v}_D \cdot \nabla F_{0a} - q_a v_\parallel \Phi_0' \frac{\partial F_{0a}}{\partial \varepsilon} = C_a^L[F_{1a}] \tag{2.2.4}$$

is derived with Φ_0 denoting some background electric potential that is constant on Flux surfaces and ϕ_1 the first-order potential.[35] We begin the analysis by transforming Eq.(2.2.4) to the nonadiabatic part

$$h_{1a} = F_{1a} + \frac{q_a}{T_{0a}} \phi_1 F_{0a}$$

of the distribution. With $\partial_\varepsilon F_{0a} = -(m_a/T_{0a}) F_{0a}$ we obtain

$$v_\parallel \mathbf{b}_0 \cdot \nabla h_{1a} + \mathbf{v}_D \cdot \nabla F_{0a} - q_a v_\parallel \Phi_0' \frac{\partial F_{0a}}{\partial \varepsilon} = C_a^L[h_{1a}]\,, \tag{2.2.5}$$

where we use that the linearized collision operator annihilates Maxwellian distributions (for equal temperatures). For comparison one thus can interpret F_1 in our Eq. (2.2.1), as h_{1a}. According to Ref. [35], the second-order particle flux is computed as

$$\Gamma_a^{\text{neo}} = \langle \int h_{1a} v_d^r d^3 v \rangle$$

so that determining ϕ_1 is not necessary to that order. The definition of the heat flux follows the same rules, and together the neoclassical fluxes agree with our definitions given in Sec. 2.3 when $F_1 = h_1$ is implied. Apparently, when comparing to Eqs. (2.2.3) and (2.2.5), our Eq. (2.2.1) does not consider the background fields $E_\parallel^{(A)}$ and Φ_0'.

Moreover, the magnetic mirror term $-\mu \mathbf{b}_0 \cdot \nabla B_0 \partial_{v_\parallel} F_{1a}/(m_a v_\parallel)$ is missing in Eqs. (2.2.5) and (2.2.3), which can be attributed to the fact that $\mathbf{b}_0 \cdot \nabla$ is taken at constant energy ε opposed to performing the partial derivative at constant parallel velocity $v_\parallel$. In field-aligned coordinates, one has $\mathbf{b}_0 \cdot \nabla = \mathcal{C}/J \partial_z$ and the relation $v_\parallel = \sigma(v_\parallel)\sqrt{(2\varepsilon - 2\mu B_0(z))/m_a}$, with $\sigma(v_\parallel) = v_\parallel/|v_\parallel|$, gives

$$\frac{\partial v_\parallel}{\partial z} = -\frac{1}{2} \frac{\sigma(v_\parallel)}{\sqrt{(2\varepsilon - 2\mu B_0(z))/m_a}} 2\mu \frac{\partial B_0}{\partial z} = -\frac{\mu}{m_a v_\parallel} \frac{\partial B_0}{\partial z}\,,$$

such that the parallel derivative is written as

$$\begin{aligned} v_\parallel \mathbf{b}_0 \cdot \nabla f \Big|_\varepsilon &= \frac{\mathcal{C}}{J} v_\parallel \frac{\partial f}{\partial z}\Big|_{v_\parallel} + \frac{\mathcal{C}}{J} v_\parallel \frac{\partial f}{\partial v_\parallel} \frac{\partial v_\parallel}{\partial z} \\ &= v_\parallel \mathbf{b}_0 \cdot \nabla f \Big|_{v_\parallel} - \frac{\mu}{m_a} \mathbf{b}_0 \cdot \nabla B_0 \frac{\partial f}{\partial v_\parallel} \end{aligned}$$

where the notation $|_{(\varepsilon, v_\parallel)}$ denotes the derivative at constant $(\varepsilon, v_\parallel)$ and the last term is the magnetic mirror term. Thus, when background electric fields are not considered (which is done throughout this work), all three equations are equivalent.

2.3. Cross-field transport in the kinetic framework

2.3.1. Turbulent and neoclassical transport

We have developed the electromagnetic gyrokinetic equations to describe the evolution of the distribution function f_a. Their solution is suited to compute both neoclassical and turbulent transport. Energy and matter are advected by the drift velocity $\mathbf{v}_D$. Cross-field transport of heat, particles and momentum is thus obtained by taking appropriate velocity space moments of f_a with the radial drift velocity

$$v_D^r = \mathbf{v}_D \cdot \hat{\mathbf{e}}_r$$

that is obtained by projection on the radial unit vector $\hat{\mathbf{e}}_r = \nabla x/|\nabla x| = \nabla x/\sqrt{g^{11}}$ of our curvilinear Clebsch coordinates. We decompose the drift velocity $\mathbf{v}_D = \mathbf{v}_\chi + \mathbf{v}_d$ into the magnetic drift $\mathbf{v}_d = \mathbf{v}_{\nabla B_0} + \mathbf{v}_c$ and the generalized $E \times B$ drift $\mathbf{v}_\chi$. Furthermore, we denote the distribution function as $f_a = f_{Ma} + \langle f_{1a}\rangle_y + \tilde{f}_{1a}$, thereby separating the y-averaged (neoclassical) part from the rest of the perturbed distribution.[13] These decompositions ultimately allow us to define neoclassical and turbulent transport.[14] Importantly, $\chi_1 = \phi_1 - \frac{v_\parallel}{c} A_\parallel - \frac{1}{c}\mathbf{v}_\perp \cdot \mathbf{A}_{1\perp}$ is the scalar potential in the gyrocenter moving frame that in general depends on the gyroangle.

Radial drift velocities

Before turning to the fluxes, we denote the drift velocity in radial projection. For $\mathbf{v}_\chi$ we have

$$\begin{aligned} v_\chi^r = \mathbf{v}_\chi \cdot \frac{\nabla x}{|\nabla x|} &= \frac{1}{\sqrt{g^{11}}} \frac{c}{\mathcal{C}} \frac{g^{1i} g^{21} - g^{2i} g^{11}}{\gamma_1} \partial_i \chi \\ &= -\frac{c}{\tilde{\mathcal{C}}} \left(\partial_y \chi + \frac{\gamma_2}{\gamma_1} \partial_z \chi \right) = v_{\chi,y}^r + v_{\chi,z}^r \end{aligned} \tag{2.3.1}$$

implicitly defining the drifts due to the y and z derivative, respectively.[15] Here, $\tilde{\mathcal{C}} = \sqrt{g^{11}}\mathcal{C}$ is a geometric factor. The curvature drift is

$$\begin{aligned} v_c^r &= -\frac{v_\parallel^2 m_a c}{q_a} \frac{1}{\tilde{\mathcal{C}}} \left(\frac{1}{B_0} \left(\partial_y B_0 + \frac{\gamma_2}{\gamma_1} \partial_z B_0 \right) + \frac{\beta_p}{2 p_0} \left(\partial_y p_0 + \frac{\gamma_2}{\gamma_1} \partial_z p_0 \right) \right) \\ &= -\frac{v_\parallel^2 m_a c}{q_a} \frac{1}{B_0} \frac{1}{\tilde{\mathcal{C}}} \left(\partial_y B_0 + \frac{\gamma_2}{\gamma_1} \partial_z B_0 \right) . \end{aligned}$$

[13] In a Fourier decomposition, the axisymmetric part of f_1, $\langle f_1 \rangle_y$, is the $k_y = 0$ mode of the perturbed distribution.

[14] We have argued in the introduction that classical transport due to collisional diffusion is negligible.

[15] At a later stage we make use of $v_{\chi,z}^r / v_{\chi,y}^r \sim \mathcal{O}(\epsilon_\parallel)$ in gyrokinetic ordering (but not in neoclassical ordering)

In the last step we make use of the fact that the MHD equilibrium pressure p_0 is a function of x alone. Similarly we have

$$v^r_{\nabla B_0} = -\frac{\mu c}{q_a}\frac{1}{\tilde{\mathcal{C}}}\left(\partial_y B_0 + \frac{\gamma_2}{\gamma_1}\partial_z B_0\right)$$

for the ∇B drift. Thus, the magnetic drift velocity can be combined as

$$v^r_d = v^r_{\nabla B_0} + v^r_c = \frac{\tilde{K}_x}{\Omega_a}\left(\frac{\mu B_0}{m_a} + v_\parallel^2\right) = \frac{\tilde{K}_x}{\Omega_a}\left(\frac{v_\perp^2}{2} + v_\parallel^2\right) \tag{2.3.2}$$

where $\tilde{K}_x = -\frac{1}{\tilde{\mathcal{C}}}\left(\partial_y B_0 + \frac{\gamma_2}{\gamma_1}\partial_z B_0\right)$ (compare Eq. (2.1.47)).

Flux surface average in field-aligned coordinates

One is often interested in the transport through a given flux surface. Thus, a flux-surface average is appropriate. In the field-aligned coordinate system, this flux surface average for any quantity $\mathcal{A}$ is defined as

$$\langle \mathcal{A} \rangle(x) = \frac{\iiint J\mathcal{A}(\mathbf{x}')\delta(x-x')\,\mathrm{d}x'\mathrm{d}y'\mathrm{d}z'}{\iiint J\delta(x-x')\,\mathrm{d}x'\mathrm{d}y'\mathrm{d}z'} \tag{2.3.3}$$

where J denotes the Jacobian of the transformation to field-aligned coordinates. In axisymmetric systems like tokamaks, the periodic boundary conditions allow for a Fourier decomposition in the binormal coordinate y. Then, the Jacobian does not depend on y and the y integral performs trivially: Only the $k_y = 0$ Fourier mode of $\mathcal{A}$ contributes to the flux surface average.

Particle fluxes

Let us now turn to the resulting flux surface averaged radial fluxes. The particle flux for species a is calculated as

$$\begin{aligned}\Gamma_a(x) =& \left\langle \int v^r_D f_a(\mathbf{x},\mathbf{v})\,\mathrm{d}^3 v \right\rangle \\ =& \Gamma_a^{\mathrm{turb}}(x) + \Gamma_a^{\mathrm{neo}}(x)\end{aligned} \tag{2.3.4}$$

and decomposed into the turbulent and neoclassical part as follows. The turbulent contribution

$$\Gamma_a^{\mathrm{turb}}(x) = \left\langle \int \tilde{f}_{1a}(\mathbf{x}) v^r_{\chi,y}\,\mathrm{d}^3 v \right\rangle \tag{2.3.5}$$

is associated to $v^r_{\chi,y}$ advection of small-scale fluctuations $\tilde{f}_{1a}$, to which $\langle f_{1a}\rangle_y$ does not contribute. We also applied the parallel wavenumber ordering of strongly magnetized plasmas to neglect the $v^r_{\chi,z}$ term with respect to $v^r_{\chi,y}$ (see also Sec. 2.1.6.1).

The advection of f_0 and $\langle f_1 \rangle_y$ due to $v^r_{\chi,y}$ indeed vanishes on flux surface average. Neoclassical particle transport collects the remaining contributions of $\langle f_1 \rangle_y$ and f_0 as

$$\Gamma^{\mathrm{neo}}_a(x) = \left\langle \int \left(\langle f_{1a} \rangle_y + f_{0a} \right)(x,z) \left(v^r_d + v^r_{\chi,z} \right) \, \mathrm{d}^3 v \right\rangle \tag{2.3.6}$$

where we keep $v^x_{\chi,z}$, because $v^x_{\chi,y}$ averages out (in axisymmetric systems) and thus the parallel wavenumber ordering does not directly apply.

Energy fluxes

Similar to the particle flux, the energy flux for species a

$$Q_a(x) = Q^{\mathrm{turb}}_a(x) + Q^{\mathrm{neo}}_a(x) + Q^{\mathrm{pot}}_a(x) \tag{2.3.7}$$

is written as the sum of the turbulent kinetic energy flux

$$Q^{\mathrm{turb}}_a(x) = \left\langle \int \frac{1}{2} m_a v^2 v^r_{\chi,y} \tilde{f}_{1a}(\mathbf{x}) \, \mathrm{d}^3 v \right\rangle \tag{2.3.8}$$

and the neoclassical kinetic energy flux

$$Q^{\mathrm{neo}}_a(x) = \left\langle \int \frac{1}{2} m_a v^2 \left(v^r_{\chi,z} + v^r_d \right) \left(f_{0a}(x,z) + \langle f_{1a} \rangle_y (x,z) \right) \, \mathrm{d}^3 v \right\rangle . \tag{2.3.9}$$

Contributions of f_0 are mainly due to the v^r_χ term [24], the v_d term vanishes exactly in up-down symmetric tokamaks, as shown in Eq. (2.3.12). In addition to the kinetic energy fluxes, one has the potential energy flux

$$Q^{\mathrm{pot}}_a(x) = \left\langle \int q_a \phi_1 v^r_D f_{0a}(x,z) \, \mathrm{d}^3 v \right\rangle \tag{2.3.10}$$

where f_{1a} is neglected, since including it would yield a third order flux. The role of the potential energy flux is discussed for the electron species, while no major effect is expected for ions since the ion kinetic energy flux is by itself larger. It has been argued that the potential energy flux balances the $v^r_{\chi,z}$ contribution in Eq. (2.3.9) and this must be kept in mind in the analysis. [24, 37]

Momentum fluxes

Analogously, one has the fluxes of parallel momentum

$$\begin{aligned} \Pi_{\parallel a} &= m \left\langle \int v^r_D v_\parallel f_a(\mathbf{x}, \mathbf{v}) \, \mathrm{d}^3 v \right\rangle \\ &= \Pi^{\mathrm{turb}}_{\parallel a}(x) + \Pi^{\mathrm{neo}}_{\parallel a}(x) \, , \end{aligned}$$

which can be split into the turbulent and neoclassical parts as well. In the limit of large toroidal field $B_{0\theta} \gg B_{0\phi}$ (and using the axisymmetry of tokamaks), one can approximate the toroidal momentum flux as the toroidal projection $qR\mathcal{C}/(JB_0)\times\Pi_{\parallel a}$ of the parallel momentum flux. For the turbulent component we again neglect $v_{\chi,z}$ due to parallel wavenumber ordering, which yields

$$\Pi^{\mathrm{turb}}_{\parallel a}(x) = \left\langle \int m_a v_\parallel v^r_{\chi,y} \tilde{f}_{1a}(\mathbf{x})\, \mathrm{d}^3 v \right\rangle$$
$$\Pi^{\mathrm{neo}}_{\parallel a}(x) = \left\langle \int m_a v_\parallel \left(v^r_d + v^r_{\chi,z}\right) \left(f_{0a}(x,z) + \langle f_{1a}\rangle_y(x,z)\right)\, \mathrm{d}^3 v \right\rangle .$$

Neoclassical fluxes without electric field

Generally, it is stated that one needs not consider any electric field for second order neoclassical fluxes (see Sec. 2.2.4). Also, due to low β, magnetic fluctuations are not considered. Throughout this work, χ_1 is thus neglected for the computation of neoclassical transport. Setting $\chi_1 = 0$, the potential energy flux clearly vanishes. The neoclassical fluxes become

$$\Gamma^{\mathrm{neo}}_a(x) = \left\langle \int f_{0a} v^r_d\, \mathrm{d}^3 v \right\rangle + \left\langle \int \langle f_{1a}\rangle_y(x,z) v^r_d\, \mathrm{d}^3 v \right\rangle ,$$
$$Q^{\mathrm{neo}}_a(x) = \left\langle \int \frac{1}{2} m_a v^2 v^r_d f_{0a}(x,z)\, \mathrm{d}^3 v \right\rangle + \left\langle \int \frac{1}{2} m_a v^2 v^r_d \langle f_{1a}\rangle_y(x,z)\, \mathrm{d}^3 v \right\rangle ,$$
$$\Pi^{\mathrm{neo}}_{\parallel a}(x) = \left\langle \int m_a v_\parallel v^r_d \langle f_{1a}\rangle_y(x,z)\, \mathrm{d}^3 v \right\rangle , \tag{2.3.11}$$

and we have have split them into the (in ϵ_δ) first-order fluxes that contain f_0 and the usual second order fluxes containing $\langle f_{1a}\rangle_y$.[16] By inserting the Maxwellian, as well as Eq. (2.3.2) we explicitly evaluate these f_0 contributions as

$$\Gamma^{\mathrm{neo}}_{0a}(x) = \left\langle \int v^r_d f_0\, \mathrm{d}^3 v \right\rangle = v^2_{Ta}(x) \frac{n_{0a}(x) m_a c}{q_a} \left\langle \frac{\tilde{K}_x(x,z)}{B_0(x,z)} \right\rangle ,$$
$$Q^{\mathrm{neo}}_{0a}(x) = \left\langle \int m_a v^2/2 v^r_d f_0 \mathrm{d}^3 v \right\rangle = \frac{5}{4} \frac{n_{0a}(x) v^4_{Ta}(x) m^2_a c}{q_a} \left\langle \frac{\tilde{K}_x(x,z)}{B_0(x,z)} \right\rangle ,$$
$$\Pi^{\mathrm{neo}}_{0a}(x) = \left\langle \int m_a v_\parallel v^r_d f_0 \mathrm{d}^3 v \right\rangle = 0 , \tag{2.3.12}$$

where we have made use of the identities

$$\int_{-\infty}^{\infty} x^n e^{-x^2} = \begin{cases} \sqrt{\pi} \frac{n!}{2^n (n/2)!} & n \geq 0, \text{ even}, \\ 0 & n > 0, \text{ odd}, \end{cases}$$
$$\int_0^{\infty} x^n e^{-x} = n! .$$

[16] The formal ordering is also visible in the normalized fluxes of Sec. 3.2.5

It is clear, that under the further assumption of up-down symmetric geometry the first order fluxes vanish on flux-surface average.[17] The f_{0a} contribution to the momentum flux vanishes also in up-down asymmetric geometry, as long as f_0 is even in $v_\parallel$, like the Maxwellian is. Although these f_0 fluxes are formally of first order in ϵ_δ, the asymmetry in the curvature terms might be small, however. If that is the case, the f_0 fluxes are negligible.

2.3.2. Fluxes in terms of moments of the distribution function

It is useful for the implementation in GENE to write the transport quantities in terms of general moments of the perturbed, modified gyrocenter distribution function g_1. The necessary pullback operation has already been introduced in Sec. 2.1.7 to obtain the gyrokinetic Maxwell equations. These moments are

$$M_a^{\mathrm{mn}}(\mathbf{x}) = \int \delta(\mathbf{X} - \mathbf{x} + \boldsymbol{\rho}) \left[F_{1a} - \left\{ q_a \tilde{\phi}_1 - \mu \bar{B}_{1\parallel} \right\} \frac{F_{0a}}{T_{0a}} \right] \frac{B_0}{m_a} v_\parallel^{\mathrm{m}} v_\perp^{\mathrm{n}} \mathrm{d}\mathbf{X} \mathrm{d}v_\parallel \mathrm{d}\mu \mathrm{d}\theta$$

In the local approximation, the fluxes caused by compressional magnetic fluctuations are evaluated by defining another type of moment

$$N_a^{\mathrm{mn}}(\mathbf{x}) = \pi \left(\frac{2B_0}{m_a} \right)^{\mathrm{n}/2+1} \int \left[F_{1a} - \left\{ q_a J_0 \phi_1 - \mu I_1 B_{1\parallel} \right\} \frac{F_{0a}}{T_{0a}} \right] \mu I_1 v_\parallel^{\mathrm{m}} \mu^{\mathrm{n}/2} \mathrm{d}\mathbf{X} \mathrm{d}v_\parallel \mathrm{d}\mu$$

where gyroaverages have been written in terms of Bessel functions $J_0(k_\perp \rho_a)$ and $J_1(k_\perp \rho_a)$ with the abbreviation $I_1(k_\perp \rho_a) = 2J_1(k_\perp \rho_a)/(k_\perp \rho_a)$.

The turbulent fluxes are further decomposed into the contributions of electrostatic and magnetic field fluctuations by writing

$$v_{\chi,y}^r = -\frac{c}{\tilde{\mathcal{C}}} \frac{\partial \phi_1}{\partial y} + \frac{v_\parallel}{\tilde{\mathcal{C}}} \frac{\partial A_{1\parallel}}{\partial y} + \frac{1}{\tilde{\mathcal{C}}} \mathbf{v}_\perp \cdot \frac{\partial \mathbf{A}_{1\perp}}{\partial y} \,.$$

This is convenient, because the dependencies on $v_\parallel$ and $v_\perp$ lead to higher order moments for the magnetic contributions. Together, we obtain for the particle fluxes

$$\begin{aligned} \Gamma_a^{\mathrm{turb}}(x) &= \left\langle -\frac{c}{\tilde{\mathcal{C}}} \frac{\partial \phi_1}{\partial y} M_a^{00}(\mathbf{x}) + \frac{1}{\tilde{\mathcal{C}}} \frac{\partial A_{1\parallel}}{\partial y} M_a^{10}(\mathbf{x}) - \frac{c}{q_a \tilde{\mathcal{C}}} \frac{\partial B_{1\parallel}}{\partial y} N_a^{00}(\mathbf{x}) \right\rangle \\ \Gamma_{1a}^{\mathrm{neo}}(x) &= \Gamma_{0a}^{\mathrm{neo}}(x) + \left\langle \frac{\tilde{K}_x}{\Omega_a} \left(\frac{1}{2} M_a^{02}(\mathbf{x}) + M_a^{20}(\mathbf{x}) \right) \right\rangle \,, \end{aligned} \tag{2.3.13}$$

the energy fluxes are

[17] Up-down symmetry implies that $K_x(z) = K_x(-z)$ in field-aligned coordinates. The same symmetry holds for B_0.

$$
\begin{aligned}
Q_a^{\mathrm{turb}}(x) = \frac{m_a}{2}\Bigg\langle & -\frac{c}{\tilde{\mathcal{C}}}\frac{\partial \phi_1}{\partial y}\left(M_a^{20}(\mathbf{x}) + M_a^{02}(\mathbf{x})\right) \\
& + \frac{1}{\tilde{\mathcal{C}}}\frac{\partial A_{1\parallel}}{\partial y}\left(M_a^{30}(\mathbf{x}) + M_a^{12}(\mathbf{x})\right) - \frac{c}{q_a\tilde{\mathcal{C}}}\frac{\partial B_{1\parallel}}{\partial y}\left(N_a^{20}(\mathbf{x}) + N_a^{02}(\mathbf{x})\right)\Bigg\rangle \\
Q_a^{\mathrm{neo}}(x) = Q_{0a}^{\mathrm{neo}}(x) + \frac{m_a}{2}&\left\langle \frac{\tilde{K}_x}{\Omega_a}\left(\frac{1}{2}M_a^{04}(\mathbf{x}) + \frac{3}{2}M_a^{22}(\mathbf{x}) + M_a^{40}(\mathbf{x})\right)\right\rangle , \quad (2.3.14)
\end{aligned}
$$

and finally, the momentum fluxes read

$$
\begin{aligned}
\Pi_a^{\mathrm{turb}}(x) &= m_a\Bigg\langle -\frac{c}{\tilde{\mathcal{C}}}\frac{\partial \phi_1}{\partial y}M_a^{10}(\mathbf{x}) + \frac{1}{\tilde{\mathcal{C}}}\frac{\partial A_{1\parallel}}{\partial y}M_a^{20}(\mathbf{x}) - \frac{c}{q_a\tilde{\mathcal{C}}}\frac{\partial B_{1\parallel}}{\partial y}N_a^{10}(\mathbf{x})\Bigg\rangle \\
\Pi_a^{\mathrm{neo}}(x) &= \frac{m_a}{2}\left\langle \frac{\tilde{K}_x}{\Omega_a}\left(\frac{1}{2}M_a^{12}(\mathbf{x}) + M_a^{30}(\mathbf{x})\right)\right\rangle . \quad (2.3.15)
\end{aligned}
$$

Note that all moments of the f_1 distribution entering the second-order neoclassical fluxes indeed depend on the axisymmetric part $\langle f_{1a}\rangle$ only. This is because the magnetic drifts are axisymmetric in a tokamak. In all neoclassical fluxes we do not consider electromagnetic fields. Including a background electric field would add terms to the neoclassical fluxes and also requires to compute the potential energy flux.

2.3.3. Further observables and the bootstrap current

Besides the fluxes of particles, momentum, and energy, other moments of the distribution function can be monitored. The turbulence code GENE outputs the density n_{1a}, the parallel flow velocity $u_{1\parallel a}$, parallel and perpendicular temperature $T_{1\parallel a}$ and $T_{1\perp a}$. Furthermore, the parallel and perpendicular heat current densities $q_\parallel$ and $q_\perp$, are computed. An important quantity determined by the the neoclassical equilibrium is the bootstrap current. It is defined according to Ref. [24] as the flux surface average

$$
\begin{aligned}
j_{Ba} =& q_a\langle u_{\parallel a}B_0\rangle = q_a\left\langle B_0\int \mathrm{d}^3v\; v_\parallel \left\langle f_a\right\rangle_y\right\rangle \\
=& q_a\left\langle B_0 M_a^{10}(\mathbf{x})\right\rangle \quad (2.3.16)
\end{aligned}
$$

of the mean parallel velocity $u_\parallel$, weighted with the magnetic field. The total bootstrap current is, of course, the sum of the contributions of all species $j_B = \sum_a j_{Ba}$.

2.4. Chapter summary

In this chapter the gyrokinetic eqations have been presented that form the basis of the numerical work done in this thesis. A transformation to gyrocenter coordinates is outlined that effectively removes the fast gyration time scale from the dynamics without losing finite Larmor radius effects. The equations have been further evaluated by splitting the distribution function into a constant background and a small fluctuating part and by introducing a field-aligned coordinate system. All of these steps allow the application of the gyrokinetic ordering and we have kept only terms up to first order in the small parameters $\{\epsilon_\alpha\}$. We also discussed methods of including the linearized Landau-Boltzmann collision operator. Test-particle and field-particle collision operators have been derived in guiding-center coordinates with the intent to preserve the self-adjointness property. For application in a gyrokinetic code, it has been argued that neglecting the difference between the guiding-center and gyrocenter distribution function in the collision operator is consistent in the drift-kinetic limit ($k_\perp \rho_a \to 0$). Fluctuations of the electric potential ϕ_1 and magnetic vector potential $\mathbf{A}_1$ have been calculated self-consistently with the gyrokinetic Maxwell equations. The resulting set of equations is suited to study plasma microturbulence including collisions and electromagnetic fluctuations.

Moreover, we have seen that the gyrokinetic equations contain the neoclassical transport problem as a subset, with the limitation of neglecting background electric fields, as well as the fluctuating quantities ϕ_1 and $\mathbf{A}_1$.

Cross-field transport has been divided into the turbulent and neoclassical contributions by splitting the drift velocity into the $\bar{\chi} \times B$ and the magnetic drifts. It has been shown that in the local limit, turbulent transport is fully attributed to the fluctuating part of F_1, while neoclassical transport is attributed to the background F_0 and the y averaged part of F_1 and these transport problems are actually decoupled. For both types, the expressions to compute the fluxes of particles, momentum and energy from the distribution function are derived by taking the appropriate moments.

3. A numerical implementation of the gyrokinetic equations

3.1. Introduction

The implementation of the gyrokinetic equations in the GENE code requires some further preparation that is provided in this chapter. First of all, the expressions are conveniently normalized in Sec. 3.2. Furthermore, Sec. 3.3 discusses GENE's discretization schemes and numerical solvers for the partial differential equation at hand. Finally, we add Krook-type sources and sinks to the equation in order to reach a stationary state also in radially global simulations. Alternatives are briefly discussed.

3.2. Summary of the equations and normalization

3.2.1. Normalization

Naturally, computer codes work with dimensionless quantities. Here, a convenient normalization is introduced in such a way that the dimensional reference quantities reflect the gyrokinetic ordering. Every expression is substituted according to the rule $B_0 = B_{\mathrm{ref}}\hat{B}_0$, exemplified by the background magnetic field $\hat{B}_0$, normalized to the reference field strength B_{ref}. Following this scheme, the reference temperature is T_{ref}, the reference density is n_{ref}, the reference mass is m_{ref}, the reference charge is $e = |e|$ and the macroscopic length scale is L_{ref}. Derived reference quantities like the reference sound velocity c_{ref}, gyroradius ρ_{ref}, Larmor frequency Ω_{ref} and plasma beta β_{ref} are defined as

$$\begin{aligned} c_{\mathrm{ref}} &= \sqrt{T_{\mathrm{ref}}/m_{\mathrm{ref}}} & \Omega_{\mathrm{ref}} &= eB_{\mathrm{ref}}/(m_{\mathrm{ref}}c) \\ \rho_{\mathrm{ref}} &= c_{\mathrm{ref}}/\Omega_{\mathrm{ref}} & \beta_{\mathrm{ref}} &= 8\pi n_{\mathrm{ref}}T_{\mathrm{ref}}/B_{\mathrm{ref}}^2\,. \end{aligned}$$

In global geometry, radially dependent quantities, like the temperature are normalized to a reference (central) flux surface x_0. This gives $T_{0a}(x) = T_{\mathrm{ref}}\hat{T}_{0a}(x_0)\hat{T}_{pa}(x)$ where $\hat{T}_{pa}(x) = T_{0a}(x)/T_{0a}(x_0)$ contains the radial profile information. Equivalently one has $n_{0a}(x) = n_{\mathrm{ref}}\hat{n}_{0a}(x_0)n_{pa}(x)$ for the density and

$$v_{Ta}(x) = \sqrt{2T_{0a}(x)/m_a} = c_{\mathrm{ref}}\hat{v}_{Ta}(x) = c_{\mathrm{ref}}\sqrt{\hat{T}_{pa}(x)}\hat{v}_{Ta}(x_0)$$

for the thermal velocity. The perpendicular scales are normalized to ρ_{ref}, the parallel coordinate z is angle like and thus already dimensionless. In summary, spatial

coordinates and geometric quantities are normalized as

$$\begin{array}{rclcrclcrcl} x & = & \rho_{\mathrm{ref}}\hat{x} & & k_x & = & \frac{1}{\rho_{\mathrm{ref}}}\hat{k}_x & & \gamma_1 & = & \hat{\gamma}_1 \\ y & = & \rho_{\mathrm{ref}}\hat{y} & & k_y & = & \frac{1}{\rho_{\mathrm{ref}}}\hat{k}_y & & \gamma_2 & = & \frac{1}{L_{\mathrm{ref}}}\hat{\gamma}_2 \\ z & = & \hat{z} & & q_a & = & e\hat{q}_a & & \gamma_3 & = & \frac{1}{L_{\mathrm{ref}}}\hat{\gamma}_3 \\ t & = & \frac{L_{\mathrm{ref}}}{c_{\mathrm{ref}}}\hat{t} & & B_0 & = & B_{\mathrm{ref}}\hat{B}_0 & & \mathcal{C} & = & B_{\mathrm{ref}}\hat{\mathcal{C}} \\ \Omega_a & = & \Omega_{\mathrm{ref}}\hat{\Omega}_a & & B^*_{0\|} & = & B_{\mathrm{ref}}\hat{B}_0 & & J & = & L_{\mathrm{ref}}\hat{J} \\ & & & & K_x & = & \frac{1}{L_{\mathrm{ref}}}\hat{K}_x & & K_y & = & \frac{1}{L_{\mathrm{ref}}}\hat{K}_y\,, \end{array}$$

where it is apparent that equilibrium quantities vary on the macroscopic scale L_{ref}. The velocity space coordinates are normalized species dependently as

$$\begin{array}{rclcrcl} v_{Ta}(x_0) & = & c_{\mathrm{ref}}\hat{v}_{Ta}(x_0) & & v_\perp & = & \hat{v}_{Ta}(x_0)c_{\mathrm{ref}}\hat{v}_\perp \\ v_\| & = & \hat{v}_{Ta}(x_0)c_{\mathrm{ref}}\hat{v}_\| & & \mu & = & \hat{T}_{0a}(x_0)\frac{T_{\mathrm{ref}}}{B_{\mathrm{ref}}}\hat{\mu}\,. \end{array}$$

The potentials and fields are expressed as

$$\begin{array}{rclcrcl} \phi_1 & = & \frac{T_{\mathrm{ref}}}{e}\frac{\rho_{\mathrm{ref}}}{L_{\mathrm{ref}}}\hat{\phi}_1 & & F_{0a} & = & \frac{n_{\mathrm{ref}}}{c^3_{\mathrm{ref}}}\frac{\hat{n}_{0a}(x_0)}{\hat{v}^3_{Ta}(x_0)}\hat{F}_{0a} \\ A_{1\|} & = & \rho_{\mathrm{ref}}B_{\mathrm{ref}}\frac{\rho_{\mathrm{ref}}}{L_{\mathrm{ref}}}\hat{A}_{1\|} & & F_{1a} & = & \frac{n_{\mathrm{ref}}}{c^3_{\mathrm{ref}}}\frac{\rho_{\mathrm{ref}}}{L_{\mathrm{ref}}}\frac{\hat{n}_{0a}(x_0)}{\hat{v}^3_{Ta}(x_0)}\hat{F}_{1a} \\ B_{1\|} & = & B_{\mathrm{ref}}\frac{\rho_{\mathrm{ref}}}{L_{\mathrm{ref}}}\hat{B}_{1\|} & & (\Gamma_{a,x},\Gamma_{a,y},\Gamma_{a,z}) & = & \frac{n_{\mathrm{ref}}}{c^3_{\mathrm{ref}}L_{\mathrm{ref}}}\frac{\hat{n}_{0a}(x_0)}{\hat{v}^3_{Ta}(x_0)}(\hat{\Gamma}_{a,x},\hat{\Gamma}_{a,y},\rho_{\mathrm{ref}}\hat{\Gamma}_{a,z})\,. \end{array}$$

We now turn to the velocity space volume element $\mathrm{d}^3v = J_v\mathrm{d}v_\|\mathrm{d}\mu\mathrm{d}\theta$. The velocity space Jacobian $J_v = B^*_{0\|}(\mathbf{X}, v_\|)/m_a$ (derived in Ref. [27]) is often approximated by $J_v = B_0/m_a$. Due to the relation

$$\hat{B}^*_{0\|} = \hat{B}_0 + \beta_{\mathrm{ref}}\sqrt{\frac{\hat{m}_a\hat{T}_{0a}(x_0)}{2}}\frac{\hat{j}_{0\|}}{\hat{q}_a\hat{B}_0}\hat{v}_\|\,,$$

this is correct in the limit of low β_{ref}, in which one neglects the contribution of the equilibrium current density j_0. Since the gyroangle-dependence has been removed from the integrands by Lie-transform, θ integrations can be performed immediately to write

$$\begin{aligned} \int(\cdots)\,\mathrm{d}^3v &= \int\left[c^3_{\mathrm{ref}}\hat{v}^3_{Ta}(x_0)\,(\cdots)\right]\,\mathrm{d}^3\hat{v} \\ &= \int_0^\infty \mathrm{d}\hat{\mu}\int_{-\infty}^\infty \mathrm{d}\hat{v}_\|\left[c^3_{\mathrm{ref}}\hat{v}^3_{Ta}(x_0)\pi\hat{B}_0\,(\cdots)\right] \end{aligned} \tag{3.2.1}$$

The collision operator is normalized as

$$C^{T/F}_{ab} = \frac{c_{\mathrm{ref}}}{L_{\mathrm{ref}}}\frac{n_{\mathrm{ref}}\hat{n}_{0a}(x_0)}{c^3_{\mathrm{ref}}\hat{v}^3_{Ta}(x_0)}\frac{\rho_{\mathrm{ref}}}{L_{\mathrm{ref}}}\hat{C}^{T/F}_{ab} \tag{3.2.2}$$

3.2.2. Normalized gyrokinetic equation

We now apply the above rules to the gyrokinetic equation (2.1.48). We keep the time derivative of g on the left hand side and conveniently group the right hand side terms into the linear operator $L[g_1]$, the nonlinear operator $N[g_1, g_1]$ and the constant term Z_0 to have

$$\begin{aligned}
\frac{\partial \hat{g}_{1a}}{\partial \hat{t}} &= L[\hat{g}_{1a}] + N[\hat{g}_{1a}, \hat{g}_{1a}] + Z_0 \\
L[\hat{g}_1] &= \langle \hat{C}_a^L[\hat{F}] \rangle \\
&\quad - \frac{1}{\hat{\mathcal{C}}} \frac{\hat{B}_0}{\hat{B}_{0\|}^*} \left[\frac{1}{\hat{L}_{na}} + \frac{1}{\hat{L}_{Ta}} \left(\frac{\hat{v}_\|^2 + \hat{\mu}\hat{B}_0}{\hat{T}_{pa}} - \frac{3}{2} \right) \right] \hat{F}_{0a} \partial_{\hat{y}} \hat{\bar{\chi}} \\
&\quad - \frac{\hat{B}_0}{\hat{B}_{0\|}^*} \frac{\hat{T}_{0a}(x_0)}{\hat{q}_a} \frac{\hat{\mu}\hat{B}_0 + 2\hat{v}_\|^2}{\hat{B}_0} \hat{K}_x \hat{\Gamma}_{a,x} \\
&\quad - \frac{\hat{B}_0}{\hat{B}_{0\|}^*} \left[\frac{\hat{T}_{0a}(x_0)}{\hat{q}_a} \frac{\hat{\mu}\hat{B}_0 + 2\hat{v}_\|^2}{\hat{B}_0} \hat{K}_y - \frac{\hat{T}_{pa}(x_0)\hat{v}_\|^2}{\hat{q}_a \hat{B}_0 \hat{\mathcal{C}}} \beta_{\mathrm{ref}} \frac{\hat{p}_{0a}}{\hat{B}_0} \frac{1}{\hat{L}_{pa}} \right] \hat{\Gamma}_{a,y} \\
&\quad - \hat{v}_{Ta}(x_0) \frac{\hat{\mathcal{C}}}{\hat{J}\hat{B}_0} \hat{v}_\| \left[\hat{\Gamma}_{a,z} - \frac{1}{2} \hat{\mu} \left(\partial_{\hat{z}} \hat{B}_0 \right) \frac{1}{\hat{v}_\|} \frac{\partial \hat{F}_{1a}}{\partial \hat{v}_\|} \right] \\
N[\hat{g}_1, \hat{g}_1] &= - \frac{1}{\hat{\mathcal{C}}} \frac{\hat{B}_0}{\hat{B}_{0\|}^*} \left(\partial_{\hat{y}} \hat{\bar{\chi}}_1 \hat{\Gamma}_{a,x} - \partial_{\hat{x}} \hat{\bar{\chi}}_1 \hat{\Gamma}_{a,y} \right) \\
Z_0 &= + \frac{\hat{B}_0}{\hat{B}_{0\|}^*} \frac{\hat{T}_{0a}(x_0)}{\hat{q}_a} \frac{\hat{\mu}\hat{B}_0 + 2\hat{v}_\|^2}{\hat{B}_0} \hat{K}_x \left[\frac{1}{\hat{L}_{na}} + \frac{1}{\hat{L}_{Ta}} \left(\frac{\hat{v}_\|^2 + \hat{\mu}\hat{B}_0}{\hat{T}_{pa}} - \frac{3}{2} \right) \right] \hat{F}_{0a} \,,
\end{aligned} \tag{3.2.3}$$

where the normalized gradient lengths

$$\frac{1}{\hat{L}_{Ta}} = -\frac{L_{\mathrm{ref}}}{T_{0a}} \partial_x T_{0a}(x), \qquad \frac{1}{\hat{L}_{na}} = -\frac{L_{\mathrm{ref}}}{n_{0a}} \partial_x n_{0a}(x) \quad \text{, and} \qquad \frac{1}{\hat{L}_{pa}} = -\frac{L_{\mathrm{ref}}}{p_{0a}} \partial_x p_{0a}(x)$$

of temperature T_{0a}, density n_{0a} and pressure $p_{0a} = n_{0a} T_{0a}$ have been introduced.

3.2.3. Normalized collision operator

3.2.3.1. Test particle operators

We define a species-independent dimensionless collisionality

$$\nu_c = \frac{\pi e^4 n_{\mathrm{ref}} L_{\mathrm{ref}} \ln \Lambda}{\sqrt{2}^3 T_{\mathrm{ref}}^2} \,,$$

which is related to the usual notation of the electron-ion collision rate

$$\nu_{ei} = \frac{4\pi n_i Z_i^2 e^4 \ln\Lambda}{(2T_e)^{3/2} m_e^{1/2}} \qquad \text{as} \qquad \nu_{ei} = 4\frac{n_i}{n_{\text{ref}}}\left(\frac{T_{\text{ref}}}{T_e}\right)^2 Z_i^2 \frac{v_{te}}{L_{\text{ref}}}\nu_c\,.$$

Using ν_c, we find the normalized test particle operators in $\hat{\mathbf{V}} = (\hat{v}_\parallel, \hat{\mu})$ velocity space

$$\begin{aligned}\langle \hat{C}_{ab}^{T,V} \rangle =& \nu_c \frac{\hat{q}_a^2 \hat{q}_b^2 \hat{n}_{0b}(x)}{\hat{m}_b \hat{T}_{0a}(x_0)^{3/2} m_a^{-1/2}} \times \\ & \frac{\partial}{\partial \hat{\mathbf{V}}} \cdot \hat{F}_{Ma} \Bigg(\frac{\hat{T}_{0b}(x)}{\hat{T}_{0a}(x_0)} \frac{1}{\hat{v}^5} \begin{bmatrix} B_0\hat{\mu}\Phi_1 + \hat{v}_\parallel^2\Phi_3 & 6\hat{\mu}\hat{v}_\parallel\Phi_2 \\ 6\hat{\mu}\hat{v}_\parallel\Phi_2 & \frac{4}{B_0}v_\parallel^2\mu\Phi_1 + 4\hat{\mu}^2\Phi_3 \end{bmatrix} \cdot \frac{\partial}{\partial \hat{\mathbf{V}}} \\ & + \left(1 - \frac{\hat{T}_{0b}(x)}{\hat{T}_{0a}(x)}\right) \frac{2\Phi_3}{\hat{v}^3} \begin{bmatrix} \hat{v}_\parallel \\ 2\hat{\mu} \end{bmatrix} \Bigg) \frac{\hat{F}_{1a}}{\hat{F}_{Ma}}\end{aligned} \tag{3.2.4}$$

that analytically equals the form acting

$$\begin{aligned}\langle \hat{C}_{ab}^{T,V} \rangle =& \nu_c \frac{\hat{q}_a^2 \hat{q}_b^2 \hat{n}_{0b}(x)}{\hat{m}_b \hat{T}_{0a}(x_0)^{3/2} m_a^{-1/2}} \times \\ & \frac{\partial}{\partial \hat{\mathbf{V}}} \cdot \Bigg(\frac{\hat{T}_{0b}(x)}{\hat{T}_{0a}(x_0)} \frac{1}{\hat{v}^5} \begin{bmatrix} B_0\hat{\mu}\Phi_1 + \hat{v}_\parallel^2\Phi_3 & 6\hat{\mu}\hat{v}_\parallel\Phi_2 \\ 6\hat{\mu}\hat{v}_\parallel\Phi_2 & \frac{4}{B_0}v_\parallel^2\mu\Phi_1 + 4\hat{\mu}^2\Phi_3 \end{bmatrix} \cdot \frac{\partial}{\partial \hat{\mathbf{V}}} + \frac{2\Phi_3}{\hat{v}^3} \begin{bmatrix} \hat{v}_\parallel \\ 2\hat{\mu} \end{bmatrix} \Bigg) \hat{F}_{1a}\,.\end{aligned} \tag{3.2.5}$$

The (dimensionless) arguments of the coefficients $\Phi_i(\hat{x}_b)$ are $\hat{x}_b = \frac{v_{Ta}(x_0)}{v_{Tb}(x)}\hat{v}$ and thus contain the radial temperature profile. In Appendix A, Eq. (A.1.4) we derive the gyrocenter diffusion part of the collision operator. Its normalized form is

$$\langle \hat{C}_{ab}^{T,\perp} \rangle = \nu_c \frac{\hat{q}_b^2 \hat{n}_{0b}(x) \hat{T}_{0b}(x) m_a^{3/2}}{\hat{m}_b \hat{B}_0^2 T_{0a}^{3/2}(x_0)} \frac{1}{\hat{v}^5} \left(2\hat{v}^2\Phi_1 + 3\hat{B}_0\hat{\mu}\Phi_2\right) \hat{\nabla}_\perp \cdot \hat{F}_{Ma} \hat{\nabla}_\perp \frac{\hat{F}_a}{\hat{F}_{Ma}} \tag{3.2.6}$$

3.2.3.2. Field particle operator

The field-particle operator involves the energy and momentum transfer rates Eq. (2.1.20). Their normalization is given by

$$\begin{aligned}\delta\mathcal{P}_{\parallel ba} =& -\int m_b v_\parallel C_{ba}^T(\delta f_b) \mathrm{d}^3 v \\ =& \frac{c_{\text{ref}}}{L_{\text{ref}}} \frac{\rho_{\text{ref}}}{L_{\text{ref}}} n_{\text{ref}} m_{\text{ref}} c_{\text{ref}} \left(\hat{n}_{0b}(x_0)\hat{m}_b\hat{v}_{Tb}(x_0)\right) \left(\delta\hat{\mathcal{P}}_{\parallel ba}\right), \\ \delta\hat{\mathcal{P}}_{\parallel ba} =& -\int \hat{m}_b \hat{v}_\parallel \hat{C}_{ba}^T(\delta\hat{f}_b) \pi \hat{B}_0 \mathrm{d}^3\hat{v}_\parallel \mathrm{d}\hat{\mu}\end{aligned}$$

$$\begin{aligned}\delta\mathcal{E}_{ba} =& -\int m_b v^2 C_{ba}^T(\delta f_b)\mathrm{d}^3 v\\ =&\frac{c_{\mathrm{ref}}}{L_{\mathrm{ref}}}\frac{\rho_{\mathrm{ref}}}{L_{\mathrm{ref}}} n_{\mathrm{ref}} m_{\mathrm{ref}} c_{\mathrm{ref}}^2 \left(\hat{n}_{0b}(x_0)\hat{m}_b\hat{v}_{Tb}^2(x_0)\right)\left(\hat{\delta\mathcal{E}}_{ba}\right),\\ \hat{\delta\mathcal{E}}_{ba} =& -\int \hat{m}_b(\hat{v}_\parallel + \hat{\mu}\hat{B}_0)\hat{C}_{ba}^T(\delta\hat{f}_b)\pi\hat{B}_0\mathrm{d}\hat{v}_\parallel\mathrm{d}\hat{\mu}\end{aligned}$$

Note that the species dependent normalization of the transfer rates from species b to species a are performed with respect to species b, reflecting that momentum and energy are transferred in physically correct units. We normalize the field particle operator to obtain

$$\begin{aligned}\hat{C}_{ab}^F(f_{1a}) =&\frac{\hat{F}_{Ma}\hat{B}_{ab}^P(\hat{x}_b)\hat{v}_\parallel}{\left(\hat{I}_{5,ab}\right)}\frac{\hat{n}_{0b}(x_0)\hat{v}_{Tb}(x_0)\hat{m}_b}{\hat{n}_{0a}(x_0)\hat{v}_{Ta}(x_0)\hat{m}_a}\delta\hat{\mathcal{P}}_{\parallel ba}\\ &+\frac{\left(\hat{I}_{1,ab}\right)\hat{F}_{Ma}\hat{B}_{ab}^E(\hat{x}_b) - \left(\hat{I}_{ab}^2\right)\hat{F}_{Ma}}{\left(\hat{I}_{1,ab}\right)\left(\hat{I}_{3,ab}\right) - \left(\hat{I}_{2,ab}\right)\left(\hat{I}_{4,ab}\right)}\frac{\hat{n}_{0b}(x_0)\hat{v}_{Tb}^2(x_0)\hat{m}_b}{\hat{n}_{0a}(x_0)\hat{v}_{Ta}^2(x_0)\hat{m}_a}\delta\hat{\hat{\mathcal{E}}}_{ba},\end{aligned} \tag{3.2.7}$$

where the the Xu-Rosenbluth coefficients

$$\hat{B}_{ab}^{P,\mathrm{XR}}(\hat{x}_b) = 1, \qquad \hat{B}_{ab}^{E,\mathrm{XR}}(\hat{x}_b) = \hat{x}_b^2, \tag{3.2.8}$$

or the self-adjoint coefficients

$$\begin{aligned}\hat{B}_{ab}^{P,\mathrm{SA}}(\hat{x}_b) =&\frac{\sqrt{2\pi}}{2}(1+\frac{m_b}{m_a})^{3/2}6H(\hat{x}_b)\\ \hat{B}_{ab}^{E,\mathrm{SA}}(\hat{x}_b) =&\frac{\sqrt{2\pi}}{2}(1+\frac{m_b}{m_a})^{3/2}\left\{\left[\left(1+\frac{m_a}{m_b}\right)2\hat{x}_b^2-1\right]H(\hat{x}_b) - K(\hat{x}_b)\right\},\end{aligned} \tag{3.2.9}$$

are inserted, respectively. These coefficients are dimensionless by definition, but contain radial profile information due to $\hat{x}_b = \hat{x}_b(x) = \frac{\hat{v}_{Ta}(x_0)}{\hat{v}_{Tb}(x_0)}\hat{v}/\sqrt{\hat{T}_{pb}(x)}$. The integral expressions

$$\hat{I}_{1,ab} = \int \hat{F}_{Ma}\,\mathrm{d}^3 v \qquad \hat{I}_{2,ab} = \int \hat{F}_{Ma}\hat{B}_{ab}^E\,\mathrm{d}^3\hat{v} \qquad \hat{I}_{3,ab} = \int v^2\hat{f}_{Ma}\hat{B}_{ab}^E\,\mathrm{d}^3\hat{v}$$

$$\hat{I}_{4,ab} = \int \hat{v}^2\hat{F}_{Ma}\,\mathrm{d}^3\hat{v} \qquad \hat{I}_{5,ab} = \int \hat{v}_\parallel^2\hat{F}_{Ma}\hat{B}_{ab}^P\,\mathrm{d}^3\hat{v}$$

are normalized for species a.

3.2.4. Normalized field equations

The gyrokinetic Poisson equation becomes

$$\hat{\lambda}_D^2 \hat{\nabla}_\perp^2 \hat{\phi}_1(\mathbf{x}) - \sum_a \pi \hat{q}_a^2 \frac{\hat{n}_{0a}(x_0)}{T_{0a}(x_0)} \int \left[\hat{\phi}_1 \hat{B}_0 \frac{\hat{F}_{0a}}{\hat{T}_{pa}} - \left\langle \left\{ \hat{\bar{\phi}}_1 \hat{B}_0 \frac{\hat{F}_{0a}}{\hat{T}_{pa}} \right\} \Big|_{\mathbf{x}-\boldsymbol{\rho}} \right\rangle \right] \mathrm{d}\hat{v}_\parallel \mathrm{d}\hat{\mu}$$
$$= -\sum_a \pi \hat{q}_a \hat{n}_{0a}(x_0) \int \left[\left\langle \left\{ \hat{B}_0 \hat{g}_1 \right\} \Big|_{\mathbf{x}-\boldsymbol{\rho}} \right\rangle + \hat{\mu} \left\langle \left\{ \hat{\bar{B}}_{1\parallel} \hat{B}_0 \frac{\hat{F}_{0a}}{\hat{T}_{pa}} \right\} \Big|_{\mathbf{x}-\boldsymbol{\rho}} \right\rangle \right] \mathrm{d}\hat{v}_\parallel \mathrm{d}\hat{\mu} \,,$$

where the combined normalization prefactors can be identified as the normalized Debye length

$$\hat{\lambda}_D = \frac{\lambda_D}{\rho_{\mathrm{ref}}} = \sqrt{\frac{T_{\mathrm{ref}}}{4\pi {\rho_{\mathrm{ref}}}^2 n_{\mathrm{ref}} e^2}} = \sqrt{\frac{B_{\mathrm{ref}}^2}{4\pi n_{\mathrm{ref}} m_{\mathrm{ref}} c^2}} \,.$$

The parallel component of the Ampère equation becomes

$$\hat{\nabla}_\perp \hat{A}_{1\parallel}(x) - \pi \beta_{\mathrm{ref}} \sum_a \frac{\hat{q}_a^2}{\hat{m}_a} \hat{n}_{0a}(x_0) \int \left\langle \left\{ \hat{B}_0 \frac{\hat{F}_{0a}}{\hat{T}_{pa}} \hat{\bar{A}}_{1\parallel} \right\} \Big|_{\mathbf{x}-\boldsymbol{\rho}} \right\rangle \hat{v}_\parallel^2 \mathrm{d}\hat{v}_\parallel \mathrm{d}\hat{\mu} =$$
$$- \pi \frac{\beta_{\mathrm{ref}}}{2} \sum_a \hat{q}_a \hat{v}_{Ta}(x_0) \hat{n}_{0a}(x_0) \int \left\langle \left\{ \hat{B}_0 \hat{g}_{1a} \right\} \Big|_{\mathbf{x}-\boldsymbol{\rho}} \right\rangle \hat{v}_\parallel \mathrm{d}\hat{v}_\parallel \mathrm{d}\hat{\mu}$$

and for the perpendicular Ampère equation, we get

$$\begin{pmatrix} \partial_{\hat{y}} \hat{B}_{1\parallel} \\ -\partial_{\hat{x}} \hat{B}_{1\parallel} \end{pmatrix} = \pi \frac{\beta_{\mathrm{ref}}}{2} \sum_a \hat{q}_a \hat{v}_{Ta}(x_0) \hat{n}_{0a}(x_0) \cdot$$
$$\int \left\langle \left\{ \hat{\mathbf{c}} \hat{B}_0^{3/2} \left[\hat{F}_{1a} + \hat{q}_a \hat{\bar{\phi}}_1 \frac{\hat{F}_{0a}}{T_{0a}(x_0) \hat{T}_{pa}} + \hat{\mu} \hat{\bar{B}}_{1\parallel} \frac{\hat{F}_{0a}}{\hat{T}_{pa}} \right] \right\} \Big|_{\mathbf{x}-\boldsymbol{\rho}} \right\rangle \sqrt{\hat{\mu}} \mathrm{d}\hat{v}_\parallel \mathrm{d}\hat{\mu}.$$

3.2.5. Normalized cross-field fluxes

In order to derive the dimensionless expressions of the fluxes, we begin with the drift velocities

$$v_\chi^r = -c_{\mathrm{ref}} \frac{\rho_{\mathrm{ref}}}{L_{\mathrm{ref}}} \left(\frac{1}{\hat{\bar{\mathcal{C}}}} \left(\partial_{\hat{y}} \hat{\chi}_1 \right) \right) \tag{3.2.10}$$

$$v_d^r = c_{\mathrm{ref}} \frac{\rho_{\mathrm{ref}}}{L_{\mathrm{ref}}} \left(\frac{\hat{T}_{0a}(x_0)}{\hat{q}_a} \frac{\hat{\mu} \hat{B}_0 + 2\hat{v}_\parallel^2}{\hat{B}_0} \hat{\bar{K}}_x \right) \,. \tag{3.2.11}$$

Note the formal first order in $\rho_{\mathrm{ref}}/L_{\mathrm{ref}}$. The general moments Eq. (2.1.50) become

$$M_a^{\mathrm{mn}}(\mathbf{x}) = n_{\mathrm{ref}} n_{0a}(x_0) c_{\mathrm{ref}}^{\mathrm{m+n}} v_{Ta}^{\mathrm{m+n}}(x_0) \frac{\rho_{\mathrm{ref}}}{L_{\mathrm{ref}}} \hat{M}_a^{\mathrm{mn}}(\mathbf{x})$$
$$N_a^{\mathrm{mn}}(\mathbf{x}) = p_{\mathrm{ref}} p_{0a}(x_0) c_{\mathrm{ref}}^{\mathrm{m+n}} v_{Ta}^{\mathrm{m+n}}(x_0) \frac{\rho_{\mathrm{ref}}}{L_{\mathrm{ref}}} \hat{N}_a^{\mathrm{mn}}(\mathbf{x})$$

in accordance with Ref. [38]. Note that the N-type moments are associated to $B_{1\parallel}$ fluctuations, which are implemented in the local GENE version. In the global version, N-type moments do not appear, since $B_{1\parallel}$ fluctuations are not featured. Using these moments, we find the fluxes Eqs. (2.3.13),(2.3.14) and (2.3.15), to be normalized to gyro-Bohm fluxes $\Gamma_{GB} = n_{\mathrm{ref}} c_{\mathrm{ref}} \frac{{\rho_{\mathrm{ref}}}^2}{L_{\mathrm{ref}}^2}$, $Q_{GB} = p_{\mathrm{ref}} c_{\mathrm{ref}} \frac{{\rho_{\mathrm{ref}}}^2}{L_{\mathrm{ref}}^2}$, and $\Pi_{GB} = n_{\mathrm{ref}} m_{\mathrm{ref}} c_{\mathrm{ref}}^2 \frac{{\rho_{\mathrm{ref}}}^2}{L_{\mathrm{ref}}^2}$. The particle flux is

$$
\begin{aligned}
\frac{\Gamma_a^{\mathrm{turb}}(x)}{\Gamma_{GB}} &= \hat{n}_{0a}(x_0) \left\langle -\frac{1}{\hat{\bar{\mathcal{C}}}} \frac{\partial \hat{\phi}_1}{\partial \hat{y}} \hat{M}_a^{00}(\hat{\mathbf{x}}) + \frac{\hat{v}_{Ta}(x_0)}{\hat{\bar{\mathcal{C}}}} \frac{\partial \hat{A}_{1\parallel}}{\partial \hat{y}} \hat{M}_a^{10}(\hat{\mathbf{x}}) - \frac{1}{\hat{\bar{\mathcal{C}}}} \frac{\hat{T}_{0a}(x_0)}{\hat{q}_a} \frac{\partial \hat{B}_{1\parallel}}{\partial \hat{y}} \hat{N}_a^{00}(\hat{\mathbf{x}}) \right\rangle \\
\frac{\Gamma_a^{\mathrm{neo}}(x)}{\Gamma_{GB}} &= \frac{L_{\mathrm{ref}}}{\rho_{\mathrm{ref}}} \hat{\Gamma}_{0a}^{\mathrm{neo}} + \left\langle 2\hat{\bar{K}}_x \frac{\hat{n}_{0a}(x_0) \hat{T}_{0a}(x_0)}{\hat{q}_a \hat{B}_0} \left(\frac{1}{2} \hat{M}_{02,a} + \hat{M}_{20,a} \right) \right\rangle \\
\hat{\Gamma}_{0a}^{\mathrm{neo}} &= \frac{\hat{n}_{0a}(x) 2 \hat{T}_{0a}(x_0) \hat{T}_{pa}(x)}{\hat{q}_a} \left\langle \frac{\hat{\bar{K}}_x(\hat{x}, \hat{z})}{\hat{B}_0(\hat{x}, \hat{z})} \right\rangle ,
\end{aligned}
\tag{3.2.12}
$$

the energy flux is found to be

$$
\begin{aligned}
\frac{Q_a^{\mathrm{turb}}(x)}{Q_{GB}} =& - \hat{n}_{0a}(x_0) \hat{T}_{0a}(x_0) \Big\langle - \frac{1}{\bar{\mathcal{C}}} \frac{\partial \hat{\phi}_1}{\partial \hat{y}} \left(\hat{M}_a^{20}(\hat{\mathbf{x}}) + \hat{M}_a^{02}(\hat{\mathbf{x}}) \right) \\
& - \frac{\hat{v}_{Ta}(x_0)}{\hat{\bar{\mathcal{C}}}} \frac{\partial \hat{A}_{1\parallel}}{\partial \hat{y}} \left(\hat{M}_a^{30}(\hat{\mathbf{x}}) + \hat{M}_a^{12}(\hat{\mathbf{x}}) \right) - \frac{\hat{T}_{0a}(x_0)}{\hat{q}_a \hat{\bar{\mathcal{C}}}} \frac{\partial \hat{B}_{1\parallel}}{\partial \hat{y}} \left(\hat{N}_a^{20}(\hat{\mathbf{x}}) + \hat{N}_a^{02}(\hat{\mathbf{x}}) \right) \Big\rangle \\
\frac{Q_a^{\mathrm{neo}}(x)}{Q_{GB}} =& \frac{L_{\mathrm{ref}}}{\rho_{\mathrm{ref}}} \hat{Q}_{0a} + \frac{2 n_{0a}(x_0) \hat{T}_{0a}^2(x_0)}{\hat{q}_a} \left\langle \frac{\hat{\bar{K}}_x}{\hat{B}_0} \left(\frac{1}{2} \hat{M}_a^{04}(\mathbf{x}) + \frac{3}{2} \hat{M}_a^{22}(\mathbf{x}) + \hat{M}_a^{40}(\mathbf{x}) \right) \right\rangle \\
\hat{Q}_{0a}^{\mathrm{neo}} =& \frac{5 \hat{T}_{0a}^2(x_0) \hat{T}_{pa}^2(x) \hat{n}_{0a}(x)}{\hat{q}_a} \left\langle \frac{\hat{\bar{K}}_x(x, z)}{\hat{B}_0(x, z)} \right\rangle ,
\end{aligned}
\tag{3.2.13}
$$

and the parallel momentum flux is

$$
\begin{aligned}
\frac{\Pi_a^{\mathrm{turb}}(x)}{\Pi_{GB}} =& - \hat{n}_{0a}(x_0) \hat{m}_a \hat{v}_{Ta}(x_0) \Big\langle \frac{1}{\bar{\mathcal{C}}} \frac{\partial \hat{\phi}_1}{\partial \hat{y}} \hat{M}_a^{10}(\hat{\mathbf{x}}) \\
& - \frac{\hat{v}_{Ta}(x_0)}{\hat{\bar{\mathcal{C}}}} \frac{\partial \hat{A}_{1\parallel}}{\partial \hat{y}} \hat{M}_a^{20}(\hat{\mathbf{x}}) + \frac{\hat{T}_{0a}(x_0)}{\hat{q}_a \hat{\bar{\mathcal{C}}}} \frac{\partial \hat{B}_{1\parallel}}{\partial \hat{y}} \hat{N}_a^{10}(\hat{\mathbf{x}}) \Big\rangle
\end{aligned}
\tag{3.2.14}
$$

$$
\frac{\Pi_a^{\mathrm{neo}}(x)}{\Pi_{GB}} = \frac{\hat{n}_{0a}(x_0) \hat{m}_a^2 \hat{v}_{Ta}^3(x_0)}{2 \hat{q}_a} \left\langle \frac{\hat{\bar{K}}_x}{\hat{B}_0} \left(\frac{1}{2} \hat{M}_a^{12}(\hat{\mathbf{x}}) + \hat{M}_a^{30}(\hat{\mathbf{x}}) \right) \right\rangle .
\tag{3.2.15}
$$

For neoclassical computations we additionally monitor the bootstrap current. Equation (2.3.16) becomes

$$j_{Ba} = \langle u_{\parallel a} B_0 \rangle(x) = B_{\mathrm{ref}} n_{\mathrm{ref}} c_{\mathrm{ref}} \frac{\rho_{\mathrm{ref}}}{L_{\mathrm{ref}}} \left\{ \frac{\int \mathrm{d}\hat{z}\ \hat{B}_0^2(\hat{x},\hat{z}) \hat{J}(\hat{x},\hat{z}) \hat{n}_{0a} \hat{v}_{Ta} \pi \int\int \langle \hat{f}_{1a} \rangle_y (\hat{x},\hat{z}) \hat{v}_\parallel \mathrm{d}\hat{v}_\parallel \mathrm{d}\hat{\mu}}{\int \mathrm{d}\hat{z} \hat{J}(\hat{x},\hat{z})} \right\}, \tag{3.2.16}$$

explicitly denoting the flux surface average that involves the Jacobian of the field-aligned coordinate system.

3.3. Discretization and numerical solution

GENE discretizes the distribution function on a fixed five-dimensional phase space grid, such that g_1 can be seen as a vector, whose number of elements corresponds to the number of grid points. Phase space derivatives are written in terms of finite differences or more sophisticated schemes that preserve certain conservation properties. The most recent methods of discretization of the Vlasov operator and the time stepping scheme implemented in GENE are found in Refs. [15, 29, 39]. In the following, numerical solvers are described, hyperdiffusion terms are added to remove sub-grid structures and the finite volume discretization of the test-particle collision operator is introduced.

Initial value solver

The gyrokinetic equation is a partial integro-differential equation in phase space and time. It is formally written as

$$\partial_t g_1 = L g_1 + N[g_1] + Z_0 \tag{3.3.1}$$

with the linear operator L (including linearized collisions), the nonlinearity operator N and the neoclassical drive term Z_0 that is independent of g_1. Time evolution of the distribution g_1 is determined in GENE according to the *method of lines*: In a first step, the right hand side of Eq. (3.3.1) is discretized on a fixed grid in phase space, leaving only the time dimension continuous. In this way, the original partial differential equation is turned into a system of ordinary differential equations in time that can be solved as an initial value problem. The distribution at time t_n is denoted g_1^n and its time evolution to g_1^{n+1} is achieved with a (fully explicit) Runge-Kutta time stepping scheme, starting with an initial condition g_1^0. This initial value solver can be used for nonlinear (turbulence), linear (microinstabilities) and neoclassical computations. The time step limit is determined by the stability of the time stepping scheme (see Ref. [15] for details). In linear computations the maximum stable time step can be computed from the spectral radius of the linear

operator L, in nonlinear computations an additional Courant-Friedrichs limit is set by estimating the advection velocity of the nonlinearity [40]. Also a statistical analysis of the nonlinear time trace is performed for time step control.

Linear computations and the eigenvalue solver

An eigenmode equation for linear microinstabilities is obtained by switching off the nonlinearity N and the neoclassical term Z to have

$$\partial_t g_1 = L g_1 \,. \tag{3.3.2}$$

By means of an initial value computation, the fastest exponentially growing mode can be determined, because it eventually dominates. Growth rate γ and frequency ω can be extracted by fitting an exponential function. With the ansatz $g_1 = \tilde{g}_1 \exp[\gamma + i\omega]$, the eigenvalues $(\gamma + i\omega)$ and corresponding mode structures $\tilde{g}_1$ can also be computed as an eigenvalue problem. This offers an alternative to initial value computations and furthermore allows to solve for a certain subset of eigenmodes, instead of the fastest growing mode only. GENE features an interface to various iterative solvers of the SLEPc package. Recent developments are reported in Ref. [41, 42]. Furthermore, a direct solver with an interface to scaLAPAC[1] is implemented to compute all eigenmodes, which is possible for relatively small problems.

The algebraic solver for neoclassical equilibrium

The structure of the neoclassical equation does not include any linear instability, because the linear drive term of L is proportional to $\partial_y \bar{\chi}_1$, while the neoclassical problem is axisymmetric with $\partial_y = 0$. Therefore, in Fourier representation ($\partial_y \to ik_y$) only the $k_y = 0$ mode is involved in the neoclassical problem. The equilibrium solution $\partial_t g_1 = 0$, can be found by an initial value computation. However, the typical time scale for convergence is given by the inverse collision rate, resulting in long simulation times at low collisionality. On the other hand, the equilibrium solution satisfies the equation

$$L g_1 = -Z_0 \,, \tag{3.3.3}$$

which is a set of algebraic equations of the type $A\vec{x} = \vec{b}$ that can be solved for g_1 directly. For that purpose, an interface to the PETSc library is implemented. A computation with this algebraic solver is much faster than the initial value problem, provided the number of grid points is not too large. Local (two species) neoclassical computations with $1 \times 1 \times 24 \times 48 \times 16$ grid points in $x \times y \times z \times v_\parallel \times \mu$ phase space, for example, take less than 10 second on 16 cores, where initial value computations

[1] A software package provided by Univ. of Tennessee; Univ. of California, Berkeley Univ. of Colorado Denver; and NAG Ltd. (*http://www.netlib.org/scalapack/*) .

would take about two hours to converge.[2] However, the algorithms runtime scales with the number of grid points squared. In consequence, global problems with large x resolution, $(300\times1\times24\times64\times16)$ for example, are not accessible with the algebraic solver at present.

3.3.1. Differencing schemes and hyperdiffusion terms

GENE features a variety of differencing schemes to be chosen by the user. Periodic boundary conditions allow for a Fourier representation in the binormal and/or radial coordinate. Derivatives are then expressed as

$$f'_k = -ikf_k$$

which is numerically exact and stable. However, the remaining phase space $\{z, v_\parallel, \mu\}$ as well as global setups with Dirichlet or von Neumann boundary conditions in $\{x, y\}$ do not allow Fourier methods. In these cases, derivatives of a discretized function f_i can be approximated by a finite difference

$$f'_i = \sum_{j=i-\sigma}^{i+\sigma} c_\sigma f_j \,,$$

where c_σ are numerical stencil coefficients and σ is the stencil index. The number of nonzero elements of c_σ defines the stencil width that is generally related to the numerical accuracy. The default choice in the GENE code is a the fourth order centered finite difference scheme

$$f'_i = \frac{1}{12\Delta}\left[f_{i-2} - 8f_{i-1} + 8f_{i+1} - 1f_{i+2}\right]$$

with a constant grid spacing of Δ. This scheme can, for example, be used for derivatives with respect to the parallel coordinate z and parallel velocity coordinate $v_\parallel$. However, the above scheme tends to decouple next-neighbor grid points which might lead to spurious effects.To remove such artifacts introduced by the discretization, so called hyperdiffusion terms are introduced. They are typically fourth order derivatives with stencils of second order of the form

$$\mathcal{H}_i(f) = \eta\frac{1}{16\Delta}\left[-f_{i-2} + 4f_{i-1} - 6f_i + 4f_{i+1} - f_{i+2}\right]$$

with a numerical control parameter η that allows user defined adjustments. Hyperdiffusion operators can be employed in $x, z, v_\parallel$ space (the numerical coefficients being $\eta \in \{$hyp_x, hyp_v, hyp_z$\}$), and also $k_y, k_\perp$hyperdiffusion terms in the perpendicular plane are implemented.

[2](IV) simulation times strongly depend on collisionality and aspect ratio, reference values are $\nu_c = 0.001$ $\epsilon = 0.166$, (NC) computations do not converge for $\nu_c > 0.2$ (much larger than typical tokamak values).

Arakawa scheme for the parallel Poisson bracket

As an alternative to centered finite differences, GENE features the discretization of the terms containing z and $v_\parallel$ derivatives (that exhibit a Poisson-bracket structure) with an Arakawa scheme, which is advantageous with respect to conservation properties. Further details are found in Ref. [29].

Dealiasing methods

Furthermore, an important property of the centered differences to be emphasized is their non-dissipative character. However, some degree of numerical damping is necessary, when during the simulation small structures are created that are smaller than the grid spacing.[3] In this case, finite differences introduce errors and can even become unstable. In many transport simulations, only larger scales are of interest, the necessary damping of sub-grid fluctuations (dealiasing) can be provided by hyperdiffusion terms. More details on the implications of hyperdiffusion terms are found in Ref. [43].

If Fourier discretization is applied, the nonlinearity is computed after a back-transformation to real space, which is less costly than computing the nonlinearity in Fourier space. The required dealiasing is provided by the '3/2 rule', which means that 50% more modes are used to perform the computation (for each Fourier discretized dimension). These extra modes are removed afterwards.

3.3.2. Finite volume discretization of the collision operator

In this section we derive the finite volume method implemented in the collision operator of GENE. As a first step we introduce a flux $\mathcal{F}$ in velocity space by schematically writing the collision operator as

$$\begin{aligned}
\langle C^{T,V}[f]\rangle = \left(\frac{\partial}{\partial t}\right)_c f =& \frac{1}{J_v}\frac{\mathrm{d}}{\mathrm{d}\mathbf{v}} \cdot J_v \begin{bmatrix} D_{11}\partial f/\partial v_\parallel + D_{12}\partial f/\partial v_\perp + R_1 f \\ D_{21}\partial f/\partial v_\parallel + D_{22}\partial f/\partial v_\perp + R_2 f \end{bmatrix} \\
\equiv& \frac{1}{J_v}\frac{\mathrm{d}}{\mathrm{d}\mathbf{v}} \cdot J_v \begin{bmatrix} \mathcal{F}_1 \\ \mathcal{F}_2 \end{bmatrix} \\
\left(\frac{\partial}{\partial t}\right)_c f\, J_v =& \frac{\partial}{\partial v_\parallel} J_v \mathcal{F}_1 + \frac{\partial}{\partial v_\perp} J_v \mathcal{F}_2
\end{aligned} \tag{3.3.4}$$

Here the two velocity space coordinates $\{v_\parallel, v_\perp\}$ are used, but this easily generalizes to other choices like $\{v_\parallel, \mu\}$. We consider one grid value f_{lm} where the indices l and m label a point on the velocity grid. We further define a control volume $\Delta v_\perp \times \Delta v_\parallel$ centered around the considered (l, m) grid point. Its boundaries are placed half distance to the next neighboring grid point, so that $\Delta v_\parallel = (v_{\parallel l+1} - v_{\parallel l-1})/2$ and $\Delta v_\perp = (v_{\perp m+1} - v_{\perp m})/2 + (v_{\perp m} - v_{\perp m-1})/2$. Eq. (3.3.4) is integrated over this

[3] Phase mixing (associated to Landau damping) is an example of a physical process that generates such small-scale structures.

domain. In the lowest order finite-volume approach we may write the left-hand side as $\int f_{lm}\, J_v\, \mathrm{d}^2\mathbf{v} = \bar{f}_{lm}\, \bar{J}_v\, \Delta v_\perp \Delta v_\parallel$ and set the volume averaged functions $\bar{f}_{lm}$ and $\bar{J}_{v,lm}$ equal to their grid values f_{lm} and $J_{v,lm}$. On the right-hand-side, we can use the theorem of Gauß to eliminate the divergence as follows

$$\left(\frac{\partial}{\partial t}\right)_c f_{lm} = \frac{1}{\Delta v_{\parallel,lm} \Delta v_{\perp,lm} J_{v,lm}} \left(\int \frac{\partial}{\partial v_\parallel} J_v \mathcal{F}_1 \mathrm{d}v_\parallel \mathrm{d}v_\perp + \int \frac{\partial}{\partial v_\perp} J_v \mathcal{F}_2 \mathrm{d}v_\parallel \mathrm{d}v_\perp \right) \tag{3.3.5}$$

$$\left(\frac{\partial}{\partial t}\right)_c f_{lm} = \frac{1}{J_{v,lm}} \left(\frac{1}{\Delta v_{\parallel,lm}} \left(J_v \mathcal{F}_1\right) |_{l-1/2}^{l+1/2} + \frac{1}{\Delta v_{\perp,lm}} \left(J_v \mathcal{F}_2\right) |_{m-1/2}^{m+1/2} \right) \tag{3.3.6}$$

where we have, again identified the integral with the average value times the cell length as $\int F_2 \mathrm{d}v_\parallel = F_2 \Delta v_\parallel$ and $\int F_1 \mathrm{d}v_\perp = F_1 \Delta v_\perp$ for parallel and perpendicular flux. We compute the flux F at the cell boundaries using second order centered finite differences (see [15]) as

$$\left.\frac{\partial f}{\partial v_\parallel}\right|_{l-1/2} = \frac{f_l - f_{l-1}}{\Delta v_{\parallel,l}}$$

For $v_\perp$ derivatives at the $v_\parallel$ boundary of the grid cell (l, m), the average

$$\left.\frac{\partial f}{\partial v_\perp}\right|_{l-1/2} = \frac{1}{2} \left[\frac{f_{l,m-1} - f_{l,m+1}}{2\Delta v_{\perp,m}} + \frac{f_{l-1,m+1} - f_{l-1,m-1}}{2\Delta v_{\perp,m}} \right]$$

is taken. Generally, in GENE the perpendicular velocity grid is non-equidistant (Gauß-Laguerre knots are used for the μ grid by default), so one has to consider the appropriate grid spacing by adding four terms in total. In that case, the grid spacing $\Delta v_\perp$ used in differencing does not generally coincide with the integration weight, but the scheme derived here is still stable. At each boundary the velocity grid is extended by one point for the finite differencing scheme. In total, we have a nine point stencil for the computation of $\left(\frac{\partial}{\partial t}\right)_c f_{l,m}$. An appropriate boundary conditions is given by enforcing zero flux $\mathcal{F}$ at the upper and lower domain boundaries. This is done by choosing the coefficients D, R ,$\Delta v_\parallel$ and $\Delta v_\perp$ accordingly and does not require boundary cells outside the simulation domain.

The finite-volume discretized form of the operator has the very convenient property of automatically conserving the density. However, as the evaluation of the matrix elements at the cell boundaries introduces asymmetries, the self-adjointness relation Eq. (2.1.16) is not strictly fulfilled.

3.3.3. Gyroaverage operations

The essence of gyrokinetic theory is to separate the dynamics of a gyroaveraged field $\bar{A}$ from the quickly fluctuating angle-dependent part $\tilde{A}$. In consequence, the gyroaverage operation appears in the gyrokinetic equation that governs the time evolution of the gyrocenter distribution F_{1a}. Also the field equations that compute

the electromagnetic fields in particle coordinates from F_{1a} involve gyroaverages. Formally, the gyroaverage operator $\mathcal{G}$ acts on a distribution function F_{1a} or a three dimensional field ϕ as

$$\bar{\phi}(\mathbf{X}) = \frac{1}{2\pi}\int \phi(\mathbf{X}+\boldsymbol{\rho}_a)\mathrm{d}\theta = \mathcal{G}\cdot\phi(\mathbf{x})\,.$$

In the discretized version, $\mathcal{G}$ is represented by a matrix and ϕ is the vector of grid values of the function ϕ. The θ integration includes neighboring x grid values by employing a finite element interpolation, as described in Refs. [30, 39]. As it turns out, the second type of gyroaverage that has been introduced in Sec. 2.1.7, must be discretized as

$$\langle\phi\rangle(\mathbf{x}) = \frac{1}{2\pi}\int \delta(\mathbf{X}-\mathbf{x}+\boldsymbol{\rho}_a)\phi(\mathbf{X})\mathrm{d}\mathbf{X}\mathrm{d}\theta = \mathcal{G}^\dagger\cdot\phi(\mathbf{X})$$

with $\mathcal{G}^\dagger$ being the hermitian conjugate of the gyroaverage matrix $\mathcal{G}$. Evaluating the double gyroaverage appearing in the field equations as

$$\left\langle\bar{\phi}P\right\rangle(\mathbf{x}) = \mathcal{G}^\dagger\cdot\{P\mathcal{G}\cdot\phi(\mathbf{x})\}\ ,$$

preserves the symmetry of the field equations (see Ref. [29]). In the local limit, the profile factor P can be taken out of the gyroaverage. Moreover, the gyroaverage matrix $\mathcal{G}$ itself is then diagonal in x and can be represented by a Bessel function J_0 or J_1. Both types of gyroaverages ($\bar{\cdot\cdot}$ and $\langle\cdots\rangle$) are identical in this limit. The necessary algebra is found in Ref. [15], for example, and yields

$$\bar{\phi} = J_0(k_\perp\rho)\phi \qquad \bar{A}_\parallel = J_0(k_\perp\rho)A_\parallel \qquad \bar{F}_{1a} = J_0(k_\perp\rho)F_{1a}\,.$$

A special role is taken by the compressional magnetic field fluctuation. Because those involve the perpendicular velocity through the perpendicular current perturbation, the appropriate gyroaverage is

$$\bar{B}_{1\parallel} = I_1(k_\perp\rho)B_{1\parallel} = \frac{J_1(k_\perp\rho)}{k_\perp\rho}B_{1\parallel}\,.$$

It should be noted that the abbreviation I_1 does not equal the modified Bessel function.

3.4. Heat and particle sources in GENE

Global simulations allow heat and particle fluxes to relax the temperature and density profile of the plasma. To reach a steady state in the simulation, it is therefore necessary to introduce sources (and sinks) of energy and particles. Two different approaches are pursued to that aim. The so-called *flux-driven* simulations provide the radial profile of heat and particle sources. Density and temperature profiles result

from an balance between these sources and sinks and the cross-field transport in the coarse of the simulation. The use of the δf splitting method can, however, be problematic when the distribution function strongly deviates from the initially imposed background F_0. An automatic adaption of F_0 to the developed temperature and density is therefore implemented in GENE. In the following, we will, however, employ a second approach called *gradient driven* simulations.[4] Initially imposed temperature and density profiles are maintained throughout the simulation. For that purpose, Krook-type heat and particle sources are employed. Such heat sources have been motivated in Ref. [44] for the PIC code ORB5, using energy ϵ and magnetic moment μ as gyrokinetic velocity space variables. Due to the different choice of velocity space coordinates $\{v_\parallel, \mu\}$ in GENE, a symmetrized distribution function

$$f_{1a}(\mathbf{X}, |v_\parallel|, \mu) = \frac{f_{1a}(\mathbf{X}, v_\parallel, \mu) - f_{1a}(\mathbf{X}, -v_\parallel, \mu)}{2}$$

is used to ensure that no additional parallel momentum is introduced.[29] The particle source

$$\begin{aligned} S_{KP,a} = &- \gamma_P \cdot \Bigg(\Big\langle f_{1a}(\mathbf{X}, |v_\parallel|, \mu) \Big\rangle \\ &- \Big\langle F_{0a}(\mathbf{X}, |v_\parallel|, \mu) \Big\rangle \frac{\sum_b q_b \Big\langle \int \Big\langle f_{1a}(\mathbf{X}, |v_\parallel|, \mu) \Big\rangle \mathrm{d}^3 v \Big\rangle}{q_j n_{\mathrm{spec}} \Big\langle \int F_{0a}(\mathbf{X}, |v_\parallel|, \mu) \, \mathrm{d}^3 v \Big\rangle} \Bigg) \end{aligned} \tag{3.4.1}$$

is implemented for species a, where the second term in Eq. (3.4.1) ensures that the charge density

$$\sum_a q_a \Big\langle \int S_{KP,a} \, \mathrm{d}^3 v \Big\rangle = 0 \,,$$

introduced by the particle source vanishes, to preserve quasineutrality and n_{spec} is the number of considered plasma species. The corresponding Krook-type heat source term is given by

$$\begin{aligned} S_{KH,a} = &- \gamma_{\mathrm{eff}} \cdot \Bigg(\Big\langle f_{1a}(\mathbf{X}, |v_\parallel|, \mu) \Big\rangle \\ &- \Big\langle F_{0a}(\mathbf{X}, |v_\parallel|, \mu) \Big\rangle \frac{\Big\langle \int \Big\langle f_{1a}(\mathbf{X}, |v_\parallel|, \mu) \Big\rangle \mathrm{d}^3 v \Big\rangle}{\Big\langle \int F_{0a}(\mathbf{X}, |v_\parallel|, \mu) \, \mathrm{d}^3 v \Big\rangle} \Bigg) \,, \end{aligned} \tag{3.4.2}$$

where the second term ensures that no density perturbation is added by $S_{H,a}$ and thus

$$\Big\langle \int S_{KH,a} \, \mathrm{d}^3 v \Big\rangle = 0 \,.$$

[4] Local flux tube simulations are intrinsically *gradient driven*. No source terms are required due to periodic boundary conditions.

The total rate of heat input due to the S_H term (on a specific flux surface) is given by its second velocity moment

$$Q_{KH} = \left\langle \int \frac{1}{2} m_a v^2 S_{H,a} \, \mathrm{d}^3 v \right\rangle .$$

The effective coefficient γ_{eff} is constructed such that the heat input

$$Q_{KP} = \left\langle \int \frac{1}{2} m_a v^2 S_{P,a} \, \mathrm{d}^3 v \right\rangle \neq 0$$

due to the particle source is annihilated without destroying the above described conservation properties of the two terms, as described in Ref. [29]. In this way, the user-provided numerical coefficients γ_P and γ_H can be interpreted as some typical rates of particle and heat input into the plasma.

3.5. Chapter summary

In this chapter we have completed the system of equations that is suitable to compute neoclassical and turbulent cross-field transport, as it is implemented in the GENE code. After a summary of the normalized kinetic equation (including the collision operator), normalized versions of the Maxwell equations, as well as the fluxes are given. Three different ways of running the GENE code have been presented, the initial value, the eigenvalue and the neoclassical solver. Furthermore, the discretization methods of GENE were discussed with a focus on the finite volume discretization of the collision operator, as this plays a major role in this thesis. Finally, hyperdiffusion terms and heat sources and sinks have been introduced, since they have been employed to gain the results being presented in the following chapters.

4. Simulation of neoclassical transport with GENE

4.1. Overview

Neoclassical transport is defined as collisional heat, particle, and momentum transport that originates from the (toroidal) magnetic field topology [8, 45, 46]. In tokamak devices confining high temperature plasmas, neoclassical transport usually plays a minor role, as long as plasma turbulence is present. However, turbulence can be strongly suppressed, for example in internal transport barriers or edge transport barriers. This is where neoclassical transport may not be negligible and an accurate computation becomes important. Further, when magnetic drifts become larger in strongly shaped plasmas, neoclassical fluxes are expected to scale accordingly. Stellarators are optimized with respect to neoclassical transport and thus require accurate computation, as well. For a turbulence code like GENE, another motivation for computing neoclassical transport is given by the excellent opportunity of testing the implementation of the collision operator. Even benchmarks against analytical results can be undertaken.

The neoclassical equilibrium solution is discussed by monitoring the bootstrap current and the (second order) energy and particle fluxes, which are velocity space moments of the distribution function. The structure of the standard neoclassical equation allows to connect these fluxes to thermodynamic forces by means of a transport matrix. The associated transport coefficients can be shown to obey an Onsager symmetry, a direct consequence of the self-adjointness, momentum, and energy conservation of the collision operator. One can thus expect meaningful results for neoclassical transport when these properties are sufficiently well represented in the numerical implementation of the neoclassical set of equations.

The standard neoclassical equation is local in nature, i.e. the observables on a flux surface only depend on the plasma parameters on that particular flux surface. Terms that involve finite-size (ρ^*) effects (and thus interaction across flux surfaces) are formally of second order and therefore not considered in the standard equation. Some of these nonlocal effects are, however, accessible with the radially nonlocal version of the GENE code, taking into account radial variations of the plasma kinetic profiles and the geometry. The local limit is reached by letting $\rho^* \to 0$, thus the same results are expected from global and local computations at sufficiently small ρ^*. Even if the additional nonlocal terms are small in the equation, an important difference is that global computations allow for the relaxation of background profiles and furthermore include heat sources and sinks and thus are far more involved.

Interest in performing such global computations of the neoclassical equilibrium arises from the fact that turbulent and neoclassical transport are actually coupled when leaving the local flux tube limit.[47] This work provides a first step towards coupled neoclassics/turbulence simulations with GENE by studying the global neoclassical equilibrium alone. This intermediate step is important, because the requirements can, in principle, be different from those met in a turbulence computation.
In Sec. 4.2 some theoretical background on the structure of the neoclassical transport problem is given by introducing Onsager symmetry, that actually relates Boltzmann's H-theorem and the self-adjointness of the collision operator. We begin to present simulation results in Sec. 4.3, where benchmarks between the local version of GENE and the well-established drift-kinetic code Neo [35] are performed. Different implementations of the collision operator in GENE are tested and correlations between the self-adjointness properties of the operator and the agreement with the Neo code are observed. Initial results on global neoclassical computations are presented in Sec. 4.4 with a particular focus on comparisons to local results and reaching the the local limit within the global framework. It turns out that, in particular for large ρ^*, heat sources play an important role, and thus their influence for different values of ρ^* is studied in detail. Another important parameter for neoclassical computations is the collisionality. Thus, in Sec. 4.5 we explore numerical settings, like resolution, hyperdiffusion and heat source coefficients and discuss their implications on high and low collisionality cases. Finally, GENE is compared with the global particle-in-cell code ORB5.[24] The overall satisfying comparison with this numerically very different code, together with the additionally performed tests and the correctly captured local limit, establishes neoclassical transport simulations with the global GENE code and demonstrates the reliability of the collision operator in the studied cases.

4.2. Remarks on entropy production and Onsager symmetry

We begin with some theoretical considerations regarding neoclassical transport. The basic neoclassical theory has been studied for more than half a century now and two review papers already published in 1976 and 1981 give a rather complete picture .[8, 45] Nevertheless, relatively recent publications like the work of Sugama *et al.* 1996 [48] still address the structure of the equations (for non-axisymmetric geometry). It should be noted that numerical tools for specific applications still continue to evolve. In particular, effort is undertaken to preserve the self-adjointness (Eq. (2.1.16)) of the collision operator.[35, 48] The following considerations show, why the latter is expected to be an important ingredient when addressing the neoclassical transport problem. A first reason is given by the fact that an inherent property of neoclassical transport theory, the Onsager symmetry [49, 50], relies on the self-adjointness relation[46, 51]. Onsager symmetry becomes obvious when writ-

ing the solution of the neoclassical transport problem as a linear relation between *fluxes* and thermodynamic *forces*. The fluxes are the radial component of the particle flux, of the electron and ion heat fluxes, as well as the parallel electric current. They are conveniently grouped in a four-vector $\mathbf{J} = (J_1, J_2, J_3, J_4)$. The conjugate four-vector of forces $\mathbf{X} = (X_1, X_2, X_3, X_4)$ contains the radial components of the total pressure gradient and of the two temperature gradients, as well as the flux surface averaged externally induced parallel electric field. The first three quantities of $\mathbf{X}$ are flux surface functions to leading order. Using the enclosed volume V as a flux surface label and the notation $p' = \partial p/\partial V$, the fluxes and conjugate forces are defined in Ref. [51] as

$$\begin{array}{rclcrcl} J_1 & \equiv & \langle \mathbf{\Gamma}_e \cdot \boldsymbol{\nabla} V \rangle & & X_1 & \equiv & p_{0e}^{-1} p_{0e}' \\ J_2 & \equiv & T_{0e}^{-1} \langle \mathbf{q}_e \cdot \boldsymbol{\nabla} V \rangle & & X_2 & \equiv & T_{0e}^{-1} T_{0e}' \\ J_3 & \equiv & T_{0i}^{-1} \langle \mathbf{q}_i \cdot \boldsymbol{\nabla} V \rangle & & X_3 & \equiv & T_{0i}^{-1} T_{0i}' \\ J_4 & \equiv & B_0^{-1} \langle \mathbf{B}_0 \cdot \mathbf{j} \rangle & & X_4 & \equiv & B_0^{-1} \langle B_0 E_\parallel^{(A)} \rangle \end{array} \tag{4.2.1}$$

with $\langle \mathbf{B}_0 \cdot \mathbf{j} \rangle = \langle Ze B_0 u_{i\parallel} - e B_0 u_{e\parallel} \rangle$.[1] Considering the linear transport relation

$$J_r = \sum_{s=1}^{4} L_{rs} X_s$$

(extended) Onsager symmetry is found in the symmetry of

$$L_{rs}(\mathbf{b}_0) = -L_{sr}(-\mathbf{b}_0)$$

with respect to the magnetic field $\mathbf{b}_0$. The proof of this relation is shown to require self-adjointness of the collision operator in Ref. [51]. Simplified cases are discussed in Ref. [7].

The importance of self-adjointness of the collision operator is also apparent in another context, namely the positivity of entropy production. By definition (neglecting terms of the order ϵ_δ), the linearized entropy production rate

$$\dot{S}_a = -\frac{\partial}{\partial t} \int \mathrm{d}^3 v \, f_a \left(\ln f_a \right) = \sum_b \left\langle \int \frac{f_{1a}}{f_{0a}} C_a^L [f_{1a}, f_{1b}] \mathrm{d}^3 v \right\rangle \tag{4.2.2}$$

is entirely attributed to collisions, since the other terms in the Fokker-Planck equation are conservative, as stated already in Eq. (2.1.5). We require that entropy must increase ($\dot{S}_a \geq 0$), which is proven in Refs. [21, 48, 22, 7], making use of the self-adjointness of the Fokker-Planck operator (see Sec. 2.1.2.3) and the Schwartz inequality.

Interestingly, a link between Onsager symmetry and entropy production becomes apparent when calculating the transport matrix (L_{rs}) from Eq. 4.2.2. To that aim,

[1] In this work, derivatives with respect to the flux surface label r are employed, while Ref. [51] uses the enclosed volume V.

the collision-free part of the drift kinetic equation (the operator $\mathrm{d}f_a/\mathrm{d}t$) is is substituted for C_a^L in Eq. (4.2.2), since we have $\mathrm{d}f_a/\mathrm{d}t = C_a^L$. It turns out that one can write $\dot{S}$ in thermodynamic form

$$\dot{S} = -\sum_s J_s X_s$$

as a sum of fluxes and conjugate forces, which can be seen as a definition of the conjugate pairs. One term of the resulting sum is given by $-J_2 X_2 = -(\partial T_{0e}/\partial V)(\langle \mathbf{q}_e \cdot \boldsymbol{\nabla} V \rangle)/T_{0e}^2$. This term generates entropy by a heat flux in the direction of decreasing temperature, in accordance to the thermodynamic relation $dq = T\,\mathrm{d}S$.

The strict proof of Onsager symmetry for the transport matrix relating these conjugate pairs is rather comprehensive and has been performed in Ref. [48] for general (non-axisymmetric) toroidal geometry. Here we just highlight the fact that self-adjointness of the collision operator $C_a^L[f_{1a}, f_{1b}]$ is required.

The relevance of Onsager symmetry is not only discussed for neoclassical fluxes, but also for anomalous fluxes caused by plasma turbulence. It has, however, been shown that anomalous fluxes[2] $J_r^A = \sum_s L_{rs}^A X_s^A$ do generally not obey Onsager symmetry (although the collision operator might still be self-adjoint).[51] Instead, the dissipative nature of collisions is relevant for the energy balance in (long-time) turbulence simulations. When a δf scheme is used (e.g. in GENE), collisions provide the only physically motivated sink for free energy. Interestingly, the self-adjointness relation of the collision operator is desired in this context, since it guarantees dissipation of free energy.[16, 21]

In summary, the self-adjointness property of the collision operator is an essential ingredient for the calculation of neoclassical transport and could thus be a desirable feature to be preserved in numerical implementation. The GENE results presented in the next sections indeed support this conjecture.

4.3. Local benchmark between GENE and NEO

4.3.1. Simulation setup

We have motivated neoclassical transport computations with gyrokinetic codes as a method to test collision operators and to compare with anomalous transport. In this section we apply the local version of the GENE code and benchmark the results against the neoclassical code Neo, as the latter solves the drift-kinetic equation in the radially local approximation as well. The NEO code is well described in Refs. [18, 35]. Because NEO is properly benchmarked and implements (various) sophisticated collision operators, NEO results serve as a reference for GENE results, here. In particular, we take the results for the full linearized Fokker-Planck operator from Ref. [18] and indicate them with (FP).[3] Although, in principle, arbitrary flux

[2] Anomalous fluxes and forces are defined in analogy to their neoclassical counterparts.

[3] The full, linearized Fokker-Planck operator evaluates the Rosenbluth potentials of the perturbed distribution function δf_b, instead of applying a model for the back-reaction term $C_{ab}^F[f_{0a}, \delta f_b]$.

surface shaping can be treated, we focus on the $\hat{s} - \alpha$ equilibrium for simplicity. Plasma parameters are chosen according to the GA (General Atomics) standard case summarized in Tab. 4.3.2. Collisionality is numerically varied in the simulations. The collision operators for GENE are classified in Tab. 4.3.1.

type	test-particle operator C^T	field-particle operator C^F
(XR)	acting on F_{1a},Eq. (3.2.5)	Xu-Rosenbluth, Eq. (3.2.8)
(SA)	acting on F_{1a},Eq. (3.2.5)	Self-Adjoint, Eq. (3.2.9)
(noC^F)	acting on F_{1a},Eq. (3.2.5)	none

Table 4.3.1.: Classification of collision operators used in this section.

In GENE, the grid resolution is chosen to be $32 \times 48 \times 16$ points in the $\{z, v_\parallel, \mu\}$ directions and the velocity space domain is $l_{v_\parallel} = l_{v_\perp} = 3v_{Ta}$. It is important to neglect hyper-diffusion terms, in particular for low collisionality, because they can modify the neoclassical equilibrium when the numerical resolution is not very large. As described in Sec. 3.3, GENE can either be run as an initial value solver (IV) that converges to the equilibrium state in the long-time limit, or employ an algebraic solver (NC) of the PETSc library that directly solves for the equilibrium state.[52] The latter is usually much faster.[4]

$r/a = 0.5$	$a/L_{Te} = 3$
$R/a = 3$	$a/L_{Ti} = 3$
$\hat{s} = 1.0$	$a/L_n = 1$
$\alpha = 0$	$T_i/T_e = 1$
$q = 2.0$	$m_e/m_i = 2.732 \times 10^{-4}$

Table 4.3.2.: GA standard case for local neoclassical benchmarks in $\hat{s}-\alpha$ geometry.

This is computationally expensive and thus not considered for the turbulence code GENE. However, recently the full linearized operator has been implemented in NEO [18] and is compared to model operators like the (full) Hirshman-Sigmar operator and the *ad-hoc* self-adjoint field-particle model that we also use in GENE. As it turns out, their model operators only yield a deviation around 10-20% compared to the full linearized Fokker-Planck operator for the GA standard case parameters.

[4] However, the algebraic solver is slow for very large resolutions (it scales with the number of points to the third power) or large collision frequency (collision-dominated problems are harder to solve, for they are strongly non-block-diagonal due to the velocity space derivatives).

4.3.2. Comparison with analytical theory for adiabatic electrons

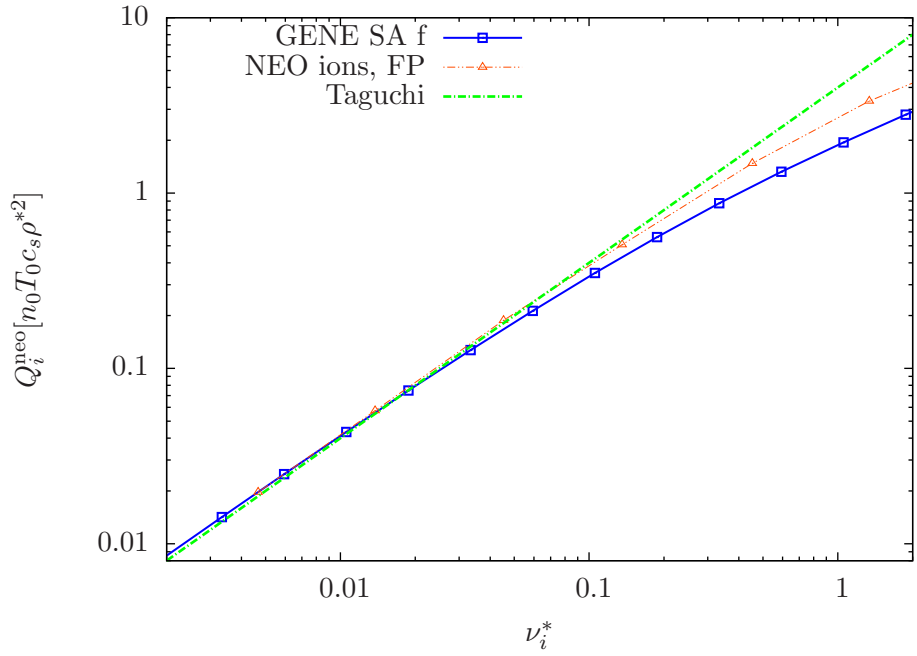

Figure 4.3.1.: Comparison of neoclassical ion energy flux from GENE with the Taguchi formula and the NEO code (taken from [18]) for adiabatic electrons.

We begin the code comparison in the limit of adiabatic electrons, in which analytical expressions for the neoclassical ion heat flux are available. The formula derived by Taguchi [7, 53] is known to work well in the (weakly collisional) banana regime, defined by $\nu_i^* = qR_0/(\tau_{ii} v_{ti} \epsilon^{3/2}) \lesssim 1$. In Fig. 4.3.1 we compare the analytical results to GENE and NEO for the GA standard case. The collision operator type (SA) is used in GENE. At small collisionality ($\nu_i^* \lesssim 0.05$) both codes coincide with the analytic prediction. The Taguchi formula is known to overestimate neoclassical fluxes when leaving the banana regime. Indeed, both GENE and NEO results deviate from the Taguchi formula when ν_i^* approaches unity. Deviations within 25% are found between GENE and NEO around $\nu_i^* \sim 1$, but the overall agreement is satisfactory.

4.3.3. Comparison of GENE and NEO for kinetic electrons

In the following, neoclassical studies with kinetic electrons are undertaken. Typical velocity space structures of the distribution function are shown in Fig. 4.3.2. At lower collision rate ν_c, structures at the trapped-passing boundary are clearly observed. These vanish for larger collisionality because strong collisions inhibit trapped particles from completing their orbits. They are thus strongly coupled to passing particles. Because F_{1i} is uneven in $v_\parallel$, the $\langle u_{\parallel i} \rangle$ moment (that is related to the bootstrap current) rises in this case.

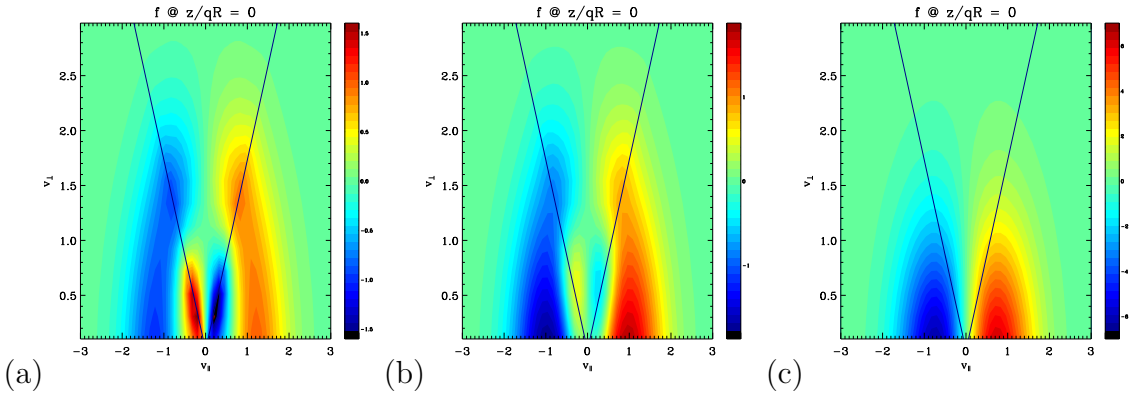

Figure 4.3.2.: Velocity space structure of the neoclassical equilibrium F_{1i} at the outboard midplane for different collision rates (a) $\nu_c = 10^{-5}$, (b) $\nu_c = 10^{-3}$ and (c) $\nu_c = 5.6 \times 10^{-2}$.

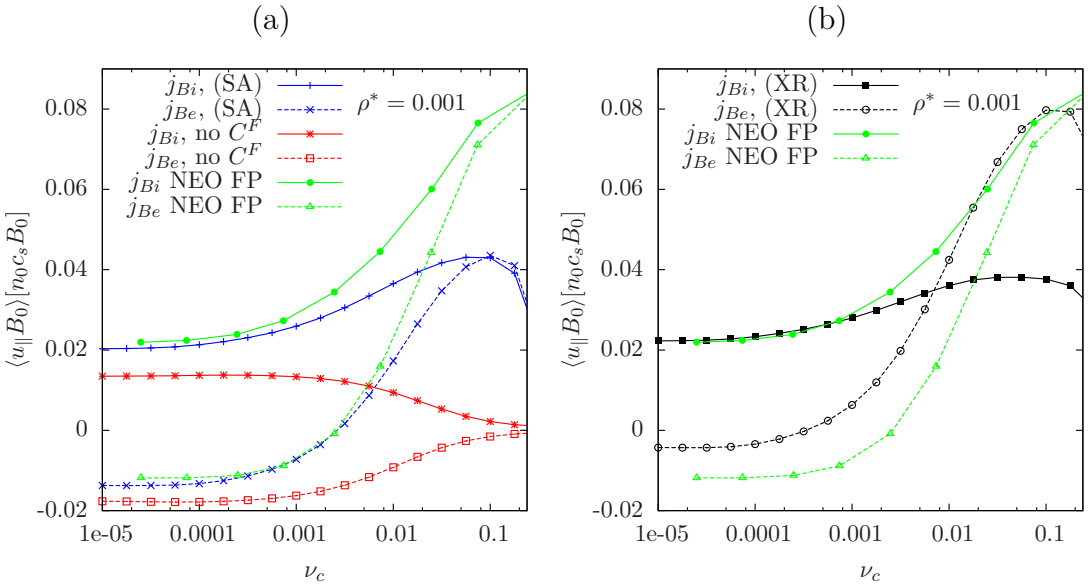

Figure 4.3.3.: The flow velocity $\langle u_{\parallel a} B_0 \rangle$ of electrons and ions is shown as a function of the (dimensionless) collisionality $\nu_c = \nu_{ei}/(4R/v_{te})$. (a) GENE data using the self-adjoint (SA) form of C^F is compared to the case without C^F, as well as NEO (FP) results. (b) GENE results for the Xu-Rosenbluth (XR) operator are compared with NEO. It has been confirmed by the author of Refs. [18, 35], that $\rho^* = 1/1000$, which is used for the normalization, is correct.

The importance of the field-particle part of the collision operator becomes clear when the flux surface averaged parallel flow velocity $\langle u_\parallel B_0 \rangle$ of the two species is considered in Fig. 4.3.3. We completely switch off the field-particle operator in GENE

(only keeping test-particle collisions) to observe that electron and ion flows are similar in magnitude (with opposing signs) and decrease to zero at larger collisionality. This break-down of $\langle u_{\parallel a} B_0 \rangle$ can be explained by noting that the energy scattering part of the collision operator acts as a sink of energy and thereby damps parallel flows.[54] The energy conserving C^F term is thus needed. In the following, we investigate the influence of the implementation of different functional forms for C^F in GENE. In particular, we use the Xu-Rosenbluth model operator,[25, 15] labeled by (XR), and the self-adjoint form, labeled by (SA). Fig. 4.3.3 also shows GENE results for $\langle u_{\parallel a} B_0 \rangle$ using the self-adjoint (SA) form of C^F. An about 40% larger value for $\langle u_{\parallel i} B_0 \rangle$ is obtained, when comparing to the previous case without C^F at low collisionality. Furthermore, a different functional dependency with increasing ν_{ei} is observed. Interestingly, the (SA) operator yields good agreement with NEO results up to $\nu_c \sim 0.005$, which corresponds to $\nu_i^* \sim 0.1$. At larger collisionality, the GENE result for $\langle u_{\parallel} B_0 \rangle$ is smaller. When using (XR) instead of (SA) type operators in GENE, larger deviations between GENE and NEO data are observed, particularly for the electron contribution $\langle u_{\parallel e} B_0 \rangle$.

We further compare heat and particle fluxes obtained with GENE and NEO in Fig. 4.3.4. Similarly, both codes do not observe a pronounced plateau regime that is often found in the literature, which confirms the relevance of finite aspect ratio (here: $\epsilon = 0.166$) effects. Within small deviations, the ion heat flux is reproduced in agreement with NEO by both operators. While the Xu-Rosenbluth model operator overestimates the particle flux and the electron heat flux (Fig. 4.3.4(a)), the self-adjoint form exhibits good agreement with NEO (Fig. 4.3.4(b)), which underlines the importance of preserving certain symmetries, as indicated in Sec. 4.2.

In summary, the benchmark with NEO shows that the GENE code—with the presently implemented collision operator—works reasonably well for neoclassical heat and particle transport in the local limit, also under consideration of kinetic electrons. The energy and momentum conserving terms C^F are essential for the correct computation of the neoclassical observables $\langle u_{\parallel a} B_0 \rangle$, Q_a^{neo} and Γ_a^{neo}. Thereby, the self-adjoint form of C^F improves the agreement with the NEO results, which use the full linearized Fokker-Planck operator.

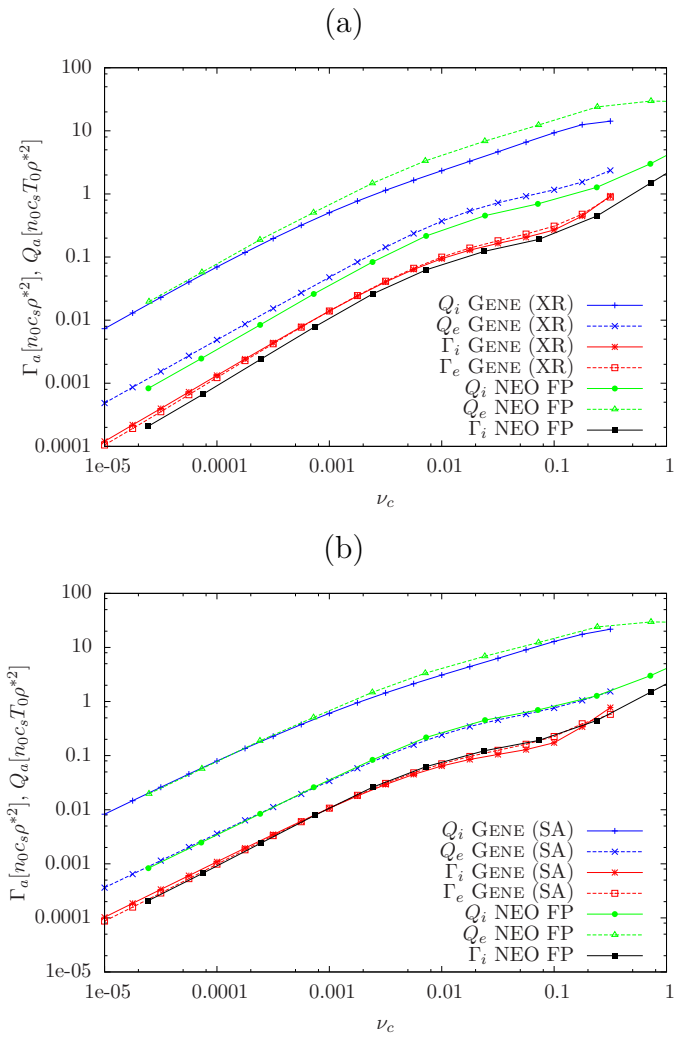

Figure 4.3.4.: Benchmark between GENE and NEO. Ion and electron heat and particle fluxes are shown in gyro-Bohm units as a function of the (dimensionless) collisionality $\nu_c = \nu_{ei}/(4R/v_{te})$. Significantly better agreement is found when replacing the (standard) Xu-Rosenbluth operator (XR) with the self-adjoint (SA) form of the field-part operator.

4.4. Finite-size investigations with GENE

Having demonstrated the ability to correctly predict neoclassical transport with GENE in the local framework, this section provides an introduction to addressing the radially global neoclassical transport problem. For that purpose, the global version of the GENE code is employed. From the computational point of view, the main differences to the local setup are given by non-periodic (Dirichlet) boundary conditions, the possibility of including sources and sinks, as well as actual finite size physics. Here, finite-size effects are taken into account by keeping the drift term

$\mathbf{v}_D \cdot \nabla F_1$ in the kinetic equation, which is neglected in the local limit. Because it contributes to the neoclassical drive ($\mathbf{v}_D \cdot \nabla F_0$), this term is expected to be important whenever relevant plasma scales—like the (temperature) gradient length or the width of a steep gradient zone—are comparable to the extent of the particle trajectories. In Sec. 4.4.1, we estimate typical trajectory widths in order to assess the relevance of such nonlocal effects and their scaling with the finite-size parameter $\rho^* = \rho_i/a$. Notably, internal or edge transport barriers might provide such a physical scenario, in which neoclassical transport gains additional importance due to the suppression of turbulence. Further interest in radially global computation arises from the fact that in this case, the neoclassical solution is actually coupled to turbulent fluctuations.[5]

As stated in Sec. **??**, another possible finite-size effect is given by the nonlinearity of the collision operator (and the parallel nonlinearity), which is formally of the same order as the $\mathbf{v}_D \cdot \nabla F_1$ term. The actual impact on the magnitude of neoclassical transport is not known at present. However, these terms are not considered here.

Within our framework, finite-size effects on the transport prediction are highlighted by comparing global to local results, considering that for sufficiently small values of ρ^*, the two versions must agree. Another important aspect of global computations is the fact that temperature and density profiles are allowed to relax due to heat and particle fluxes. Thus, in steady state, the balance between sources and transport is investigated in the following sections.

4.4.1. Estimates for finite-size effects in neoclassics

In general, the influence of finite-size effects (which are characterized by the parameter $\rho^* = \rho_i/a$) can be expected for two reasons. The typical particle orbits of plasma particles in tokamaks exhibit the shape of a banana when projected onto a poloidal cross section, as discussed in Sec. 1.3 and visualized in Fig. 1.3.2. As it turns out, the banana width r_B scales linearly with the gyroradius ρ_a (and ρ^*). A first finite-size effect is thus expected when r_B becomes comparable to macroscopic quantities like the temperature gradient length, or the width of a steep gradient zone. Close to the magnetic axis, particles follow potato-shaped orbits instead of banana-shaped orbits (see Fig. 1.3.2). The neoclassical ordering breaks down at distances within the potato width r_P from the magnetic axis, as stated in Refs. [36, 24]. Since $r_P \propto \rho^*$, this constitutes a second finite size effect.

To estimate when these nonlocal effects become relevant, a circular equilibrium with $B_0/B_p \sim q/\epsilon$ is assumed. Then, the poloidal gyroradius is given by $\rho_p = \rho_i q/\epsilon$ and the banana width is [7]

$$r_B = \sqrt{\epsilon}\rho_p = \frac{q}{\sqrt{\epsilon}}\rho_i \,. \tag{4.4.1}$$

This banana width r_B is to be compared with the gradient scale length L_T (or the width Δ_T of a steep temperature gradient zone) that typically is some factor

[5] In contrast, turbulence and neoclassics are decoupled in the local limit (see Sec. 2.2.3).

$1-10$ smaller than the minor radius a. When taking the typical values $a/L_T = 2.5$, $\Delta_T = 0.2\,a$, $\epsilon = 0.18$ and $q = 1.4$, the ratios

$$\frac{r_B}{L_T} \sim 8.2\rho^* \qquad \frac{r_B}{\Delta_T} \sim 16.4\rho^* \tag{4.4.2}$$

are still quite small, up to a relatively small machine with $\rho^* = 1/100$. One thus expects finite banana width effects when these ratios approach unity, for $\rho^* \gtrsim 1/100$ considering the chosen parameters. As mentioned above, the second nonlocal effect comes into play in the potato regime close to the magnetic axis, where r is smaller than the potato width $r_P = (q^2\rho_i^2 R)^{1/3}$.[7, 36] For the parameters considered above, $r_P = 0.06\,a$ for $\rho^* = 1/100$ ($r_P = 0.17\,a$ for $\rho^* = 1/50$). The potato effect thus is expected to be visible for $\rho^* \gtrsim 1/75$. Otherwise the radial extent of this regime is rather insignificant.

4.4.2. A setup for global neoclassical computations

The basic simulation setup for our global neoclassics computations is described in the following. We summarize the default parameters in Tab. 4.4.1 as "case I". The employed magnetic geometry has concentric circular flux surfaces (see Refs. [24, 55]) and uses r/a as the radial coordinate, where r is the distance of a flux surface from the magnetic axis. Actually, all macroscopic lengths are normalized to the reference length $L_{\mathrm{ref}} = a$, whereas the microscopic reference length is $\rho_{\mathrm{ref}} = \rho_i$, so that $\rho^* = \rho_{\mathrm{ref}}/L_{\mathrm{ref}}$ can be identified. The safety-factor profile is given by

$$q(r) = (\bar{q}_1 + \bar{q}_2(r/a)^2)/\sqrt{1-(r/R)^2}\,,$$

with the coefficients $\bar{q}_1 = 0.845$ and $\bar{q}_2 = 2.184$, such that $q(0.5) = 1.42$ and $\hat{s}(0.5) = 0.81$.[6] The radial profile of the logarithmic temperature and density gradients are expressed as

$$\frac{\mathrm{d}\ln T}{\mathrm{d}(r/a)} = -\kappa_T \left(\cosh\left(\frac{(r-r_c)/a}{\Delta_T}\right)\right)^{-2}$$

$$\frac{\mathrm{d}\ln n}{\mathrm{d}(r/a)} = -\kappa_n \left(\cosh\left(\frac{(r-r_c)/a}{\Delta_n}\right)\right)^{-2}$$

and peak at the center value $r_c/a = 0.5$ with the maximum logarithmic gradients $\kappa_T = 2.49$ and $\kappa_n = 0.79$ and the widths $\Delta_T = 0.2$ and $\Delta_n = 0.2$. Note that a/L_n, a/L_T, $\hat{s}$, and q correspond to the local cyclone base case (CBC) parameters at the center position $r_c = 0.5\,a$. The described setup is therefore referred to as global CBC. The computations are restricted to the ion species, which is

[6] GENE uses a 4th order polynomial in $q = \sum_{i=0}^{4} q_i (r/a)^i$. The coefficients q_i have been obtained by Taylor expansion with a resulting maximum deviation of ~2% at $(r/a) = 1$.

not influenced by electron dynamics, because no electric fields are considered and ion-electron collisions are negligible ($\nu_{ie} \ll \nu_{ii}$). The nominal collision frequency is chosen to be $\nu_i^* = 0.5$ (with $\nu_i^* = Rq/(\tau_{ii} v_{ti} \epsilon^{3/2})$ and $\tau_{ii} = 6\sqrt{\pi}/\bar{\nu}_{ii}$, where $\bar{\nu}_{ii} = 8\pi n_i q_i^4 ln\Lambda/(m_i v_{ti}^3) = 16\sqrt{2}\nu_c(v_{ti}/a)$). The relevant timescale is given by the ion-ion collision time $\tau_{ii} \approx 100\, a/c_s$. Thus, the choice of a rather large value for the collision rate facilitates computation due to comparably short saturation times. We get reasonably converged fluxes employing a phase-space resolution of $24 \times 64 \times 24$ grid cells in $\{z, v_\parallel, \mu\}$ phase space and between 100 and 300 grid points in radial direction. Typically, these simulations require about 100-1000 CPU hours.[7] Note that the electron species is not evolved in time in the described setup. If kinetic electrons are to be considered, the time step for numerical integration reduces by roughly the factor $\sqrt{m_i/m_e} \sim 60$ (assuming deuterium ions) and the simulation cost increases by at least twice that factor.

Table 4.4.1.: Parameter sets for global test cases. Variations are indicated in the text.

	ν_i^*	$q(x_0)$	$\hat{s}(x_0)$	κ_T	Δ_T	κ_n	Δ_n	ρ^*
case I	0.5	1.41	0.79	2.49	0.2	0.79	0.2	1/100, 1/300
case II	0.5	1.41	0.79	2.49	0.05	0.0	0.05	1/100
case III	0.5, 0.05	1.41	0.79	2.49	0.2	0.79	0.2	1/180

We do, by default, deactivate hyper-diffusion terms, because they can easily disturb the neoclassical equilibrium state as shown in Sec. 4.5. Instead, the numerical resolution has to be high enough to exclude errors in the discretized derivatives. The choice for the field-particle collision operator is the self-adjoint form, with the test-particle Operator acting on f (operator type (SA)). In the local version of GENE these collision operator settings have lead to good agreement with the NEO code in the collisionality regime considered here.

4.4.3. Global computations in the local limit

We now turn to simulation results of the global neoclassical problem and compare to local results. As a first step, we use the parameter case I of Tab. 4.4.1 with $\rho^* = 1/300$. Evaluating Eq. (4.4.2), the local neoclassical approximation is clearly expected to be valid. For the comparison to local results, it is important to keep in mind that global simulations allow temperature and density profiles to relax. Therefore, in a steady-state global simulation, the saturated value of the heat flux corresponds to the saturated value of the gradient profiles rather than the initial profile. Employing a Krook type heat source, as described in Sec. 3.4, can often

[7] For comparison, a turbulence computation of similar parameter cases requires at least 25000 CPU hours, due to nonlinear dynamics and the necessity to include about 32 toroidal (k_y) modes.

minimize this relaxation such that the saturated temperature and density are quite close to the initial profiles. Nevertheless, we routinely set up local simulations based on the (slightly relaxed) temperature and density profiles. For this purpose the logarithmic temperature and density gradients as well as the collisionality are evaluated on the relevant flux surface. For direct comparison, the Coulomb logarithm $\ln\Lambda$ that appears in the collisionality, is kept constant over the radius, although it actually would have a (weak) temperature and density dependence as well. Moreover, it is important to establish a consistent norm for global and local results. Here, gyro-Bohm units $Q_{GB}(x_0)$ on the reference flux surface of the global computation are used. In consequence, local fluxes (that are naturally normalized to local gyro-Bohm units $Q_{GB}(x) = n_0(x)c_s(x)T_0(x)\rho^{*2}(x)$) are re-normalized. Thereby, $\rho^*(x)/\rho^*(x_0) = \sqrt{T(x)/T(x_0)}$ is assumed, neglecting the (weak) influence of the $B_0(x)$ profile.

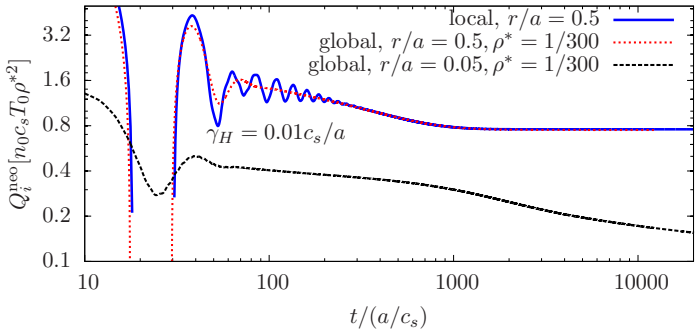

Figure 4.4.1.: Time traces of neoclassical heat flux computations of the local and global versions of the GENE code for $\rho^* = 1/300$ and Krook-type heating with $\gamma_H = 0.01$. The different time scales for the radial positions $r/a = 0.5$ and $r/a = 0.05$ is illustrated. For the time axis, a logarithmic scale is employed. The local initial value simulations (for $r/a = 0.5$) are based on the weakly relaxed, saturated temperature gradient profile (shown in Fig. 4.4.2).

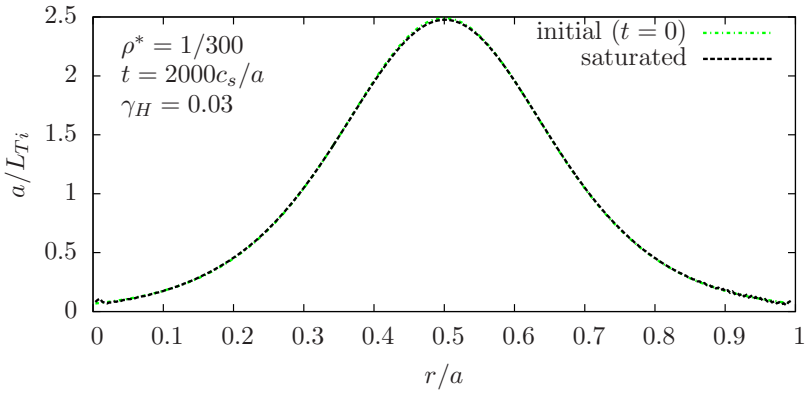

Figure 4.4.2.: Weakly relaxed temperature gradient profile for $\rho^* = 1/300$ and Krook-type heating with $\gamma_H = 0.01$, taken at the simulation time $t = 2000\, a/c_s$, where it is stationary.

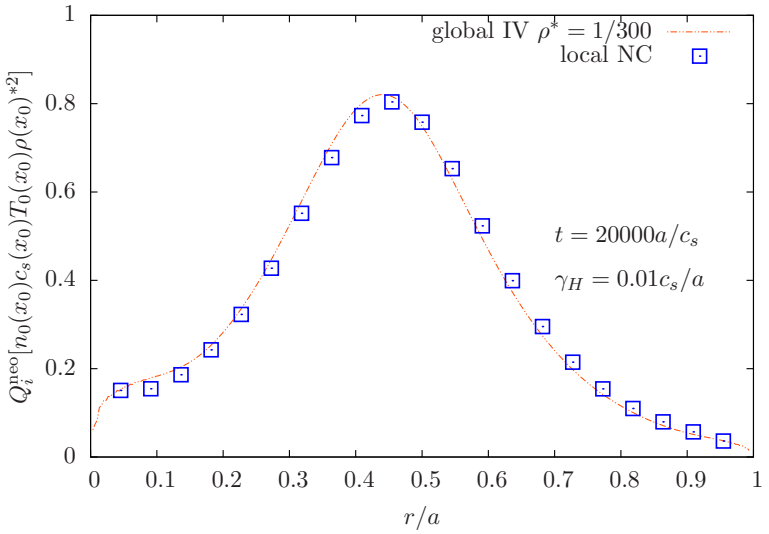

Figure 4.4.3.: Radial profiles of neoclassical heat flux are shown. Global results are taken at $t = 20000\, a/c_s$ where $Q_i^{\rm neo}$ is reasonably well converged (see Fig. 4.4.1); Here, we use $\rho^* = 1/300$ and $\gamma_H = 0.03$. Local (NC) simulations are based on the weakly relaxed final temperature profile of Fig. 4.4.2. For normalization, $Q_{GB} = n_0 T_0 c_s \rho^{*2}$ has been evaluated at $r/a = 0.5$.

In the time traces of Fig. 4.4.1 we show that global and local neoclassical fluxes agree quite well at $r/a = 0.5$. Obviously, multiple time scales for temporal convergence are involved. While the kinetic profiles of Fig. 4.4.2 are stationary for $t = 2000\, a/c_s$, the heat flux $Q_i^{\rm neo}$ is saturated for $t \gtrsim 2000\, a/c_s$ at mid-radius

$r/a = 0.5$, whereas at the inner radial boundary even at $t \gtrsim 20000 a/c_s$, the flux continues to gradually decrease. One can understand this from the fact that the saturation time-scale is given by the collision time $\tau_{ii} \sim v_{ti}/\nu_{ii}$, which is largest in the high temperature region close to the magnetic axis. Furthermore, the smallness of $\epsilon = r/R$ increases the neoclassical saturation time (see Ref. [7]), which is also observed in local simulations. The saturated radial profiles are very close to the initial profile ($a/L_{Ti}(r/a)$ is shown in Fig. 4.4.3). For the local results, it has been verified that the initial value solver (IV) and the algebraic solver (NC) agree. Here, we use the (NC) solver because it is faster. Overall, global and local results agree quite well—in the present case, the local limit is applicable.

4.4.4. Effects of large ρ^* and heat source

Next, we address the question at which value of ρ^* the global code starts to significantly deviate from the local version. The aforementioned modification related to potato orbits is not discussed further, because it only occurs at very small radii. Two aspects remain relevant when ρ^* becomes larger than our previous choice $\rho^* = 1/300$, for which the local approximation holds well. One of those effects is the increased influence of the particular form of the heat source, the other being actual finite-banana-width effects. The latter are expected for $\rho^* \gtrsim 1/100$ in Sec. 4.4.1. As a first step we modify the strength of the heat source in the $\rho^* = 1/300$ case. It is apparent from Fig. 4.4.4(a) that the magnitude of the heat source coefficient does not significantly influence the global flux profile, and also the relaxed gradient profiles are very similar. It is illustrated in in the zoom-in Fig. 4.4.4(b) that a very large simulation time of $t \gtrsim 20000\, a/c_s$ is needed for temporal convergence at the inner boundary for $\rho^* = 1/300$. We show that the influence of the heat source becomes significant when increasing ρ^* to 1/100 in Fig. 4.4.4(c). With a heating rate of $\gamma_H = 0.03$, the initial temperature profile can be maintained, but on the other hand, the global energy flux is more peaked than the local results marked by blue squares. Additionally, at $r/a = 0.7$ one has a minimum that does not correspond to a locally smaller gradient. Reducing the heating coefficient lets the profiles relax substantially, as depicted in Fig. 4.4.5. However, we find better agreement with the local results based on the relaxed profiles. The demonstrated increased influence of the heat source for larger values of ρ^* is actually consistent with the gyro-Bohm scaling $Q_i^{\mathrm{neo}} \sim \rho^{*2}$. The larger ρ^*, the larger is the heat flux and thus the relaxation of the background gradient. As a consequence, the particular choice of the heat source term is more relevant.

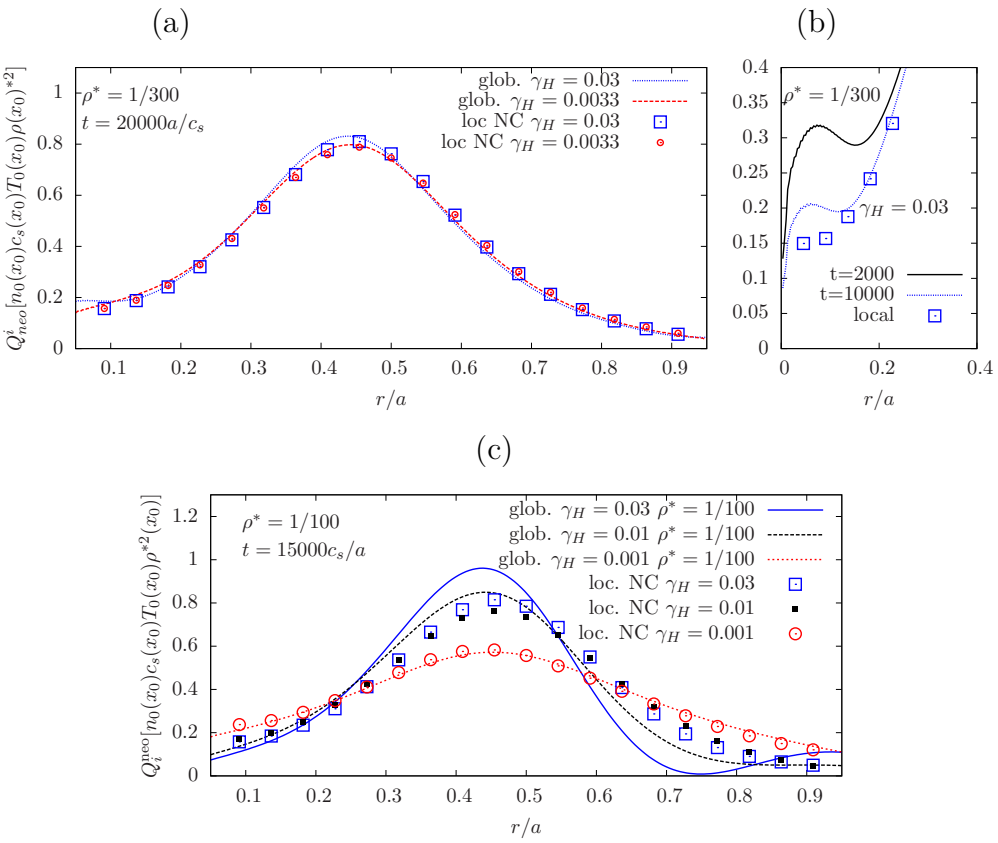

Figure 4.4.4.: Neoclassical heat flux profiles for different values of ρ^* and heating rate γ_H , compared to local results. The latter are obtained for the corresponding saturated gradient profiles that are shown in Fig. 4.4.5.

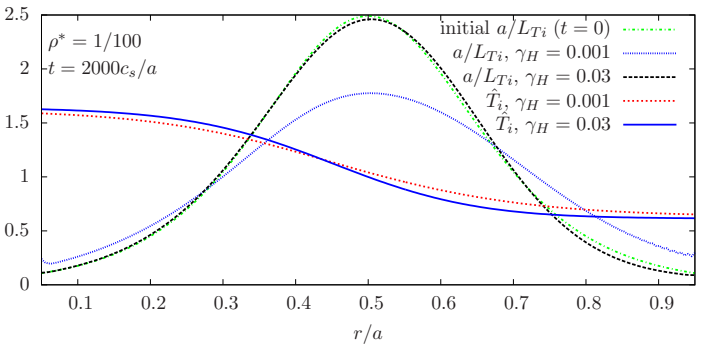

Figure 4.4.5.: Relaxation of the temperature profile for $\rho^* = 1/100$ due to neoclassical fluxes, depending on the Krook-type heating rate γ_H. The initial gradient profile is shown for comparison. It is only weakly relaxed for $\gamma_H = 0.03$. The temperature profile for $\rho^* = 1/300$ (not shown) is very close to the initial profile at all simulation times.

4.4.5. Neoclassical heat balance equation

Any other possible ρ^* effects are masked in Fig. 4.4.4 by the influence of the heat source, which therefore deserves a more detailed discussion. Let us first note that the effects of the heat source in a global simulation are twofold. (i) By construction, the Krook heat source draws the temperature moment of F_1 towards the initial profile (without affecting the density moment). (ii) In steady state, heat fluxes and heat sources/sinks must be self-consistent. Since the heat flux is radially outward, a source of energy is expected in the core, while towards the edge a sink must be provided.

Note that also the radial Dirichlet boundary conditions can play the role of an energy source/sink at the plasma edge. Consider a plasma volume that is conveniently chosen to be at thin slice around a flux surface. Obviously, a sink of energy is present when the energy flux into that volume exceeds the outgoing flux, i.e. when the radial derivative of the heat flux is largely negative. For a Krook term, this sink is *not necessarily* found at the plasma edge. In extreme situations, we even obtain a radially inward heat flux in steady state as the effect of this internal cooling. Additionally, energy input is peaking where the derivative of Q is large and positive, leading, in general, to an unphysical power deposition as well. When internal cooling and heating is large, the resulting equilibrium can, of course, be quite different from the local result, where periodic boundary conditions are applied and no additional source term is needed to maintain the strength of the drive term.

The neoclassical continuity relation

We now explicitly monitor the energy input and output of the Krook terms by taking the v^2 moment of the neoclassical equation (Eq. (2.2.1) with added source terms) and performing a flux surface average. The time evolution of the energy profile is thus given by

$$\begin{aligned}
\frac{\partial}{\partial t}\left\langle \int \mathrm{d}^3\, v \frac{m_a}{2} v^2 F_{1a} \right\rangle = &-\left\langle \frac{m_a}{2} \int v^2 \langle C_a^L[F] \rangle \mathrm{d}^3 v \right\rangle \\
&+ \left\langle \frac{m_a}{2} \int v^2 v_\parallel \left[\left(\hat{\mathbf{b}}_0 \cdot \nabla \right) F_{1a} - \mu \left[\left(\hat{\mathbf{b}}_0 \cdot \nabla \right) B_0 \right] \frac{1}{m_a v_\parallel} \frac{\partial F_{1a}}{\partial v_\parallel} \right] \mathrm{d}^3 v \right\rangle \\
&+ \left\langle \frac{m_a}{2} \int v^2 \mathbf{v}_d \cdot \left[\frac{\nabla n_{0a}}{n_{0a}} + \frac{\nabla T_{0a}}{T_{0a}} \left(\frac{m_a v_\parallel^2/2 + \mu B_0}{T_{0a}} - \frac{3}{2} \right) \right] F_{0a} \mathrm{d}^3 v \right\rangle \\
&+ \left\langle \frac{m_a}{2} \int v^2 \mathbf{v}_d \cdot \nabla F_{1a} \mathrm{d}^3 v \right\rangle \\
&+ \left\langle \frac{m_a}{2} \int v^2 \left(S_{KH}[F_{1a}] + S_{KP}[F_{1a}] + S_{\mathrm{buff}}[F_{1a}] \right) \mathrm{d}^3 v \right\rangle ,
\end{aligned}$$

where, obviously, the time derivative vanishes in steady state. In equilibrium, there must be a balance between sources, sinks, and transfer terms. Collisions provide energy transfer between species, but here we focus on ion-ion collisions that conserve energy. The parallel (z, v) advection terms is conservative as well. In up-down symmetric geometry that we consider here, also the third term on the right hand side, the neoclassical drive term, yields no contribution to the energy balance. Sources and sinks of energy are exclusively given by the Krook-type heat and particle sources. Additionally, GENE offers optional Krook-type buffer zones at the radial boundary that would have the same effect. The drift term $\mathbf{v}_d \cdot \nabla F_1$ transfers energy from one to another radial position. We will see shortly that this term is related to the divergence of the heat flux. We are left with the balance between the transport term and the Krook terms. The normalized version reads

$$-\Big\langle \int \hat{v}^2 \hat{v}_d^x \partial_{\hat{x}} \hat{F}_{1a} \Big\rangle = \Big\langle \int \hat{v}^2 \left(\hat{S}_{KH}[\hat{F}_{1a}] + \hat{S}_{KP}[\hat{F}_{1a}] + \hat{S}_{\mathrm{buff}}[F_{1a}] \right) \mathrm{d}^3\hat{v} \Big\rangle , \quad (4.4.3)$$

where $\hat{v}_d^x = \left(\hat{T}_{0a}(x_0)/\hat{q}_a \right) \hat{K}_x(x,z) \left(\hat{\mu}\hat{B}_0(x,z) + 2\hat{v}_\parallel^2 \right) / \hat{B}_0(x,z)$ denotes the normalized radial drift velocity. Following the normalization rules of Sec. 3.2, we have divided both sides of Eq. (4.4.3) by the constant

$$\frac{c_{\mathrm{ref}}}{L_{\mathrm{ref}}} \frac{\rho_{\mathrm{ref}}}{L_{\mathrm{ref}}} n_{\mathrm{ref}} T_{\mathrm{ref}} \hat{T}_{0a}(x_0) \hat{n}_0(x_0) = \frac{Q_{GB}}{\rho_{\mathrm{ref}}} \hat{p}_{0a}(x_0) ,$$

in which the gyro-Bohm energy flux is identified. We find $\hat{\mathbf{v}}_d \cdot \nabla \hat{F}_{1a} = \hat{v}_d^x \partial_{\hat{x}} \hat{F}_{1a}$, because the neoclassical equilibrium does not depend on y and, furthermore, the drift velocity has no parallel component. The right-hand side of Eq. (4.4.3) can be summarized as $\langle \hat{S}_H \rangle$, denoting the total heat input due to Krook terms. Furthermore, the left-hand side can be interpreted as the divergence of a heat flux, which leads to a continuity equation

$$\frac{\rho_{\mathrm{ref}}}{L_{\mathrm{ref}}} \frac{1}{\hat{\mathcal{A}}(x)} \frac{\partial}{\partial(x/L_{\mathrm{ref}})} \Big\langle \hat{\mathcal{A}}(x) \frac{\hat{\tilde{Q}}_a^{\mathrm{neo}}(x)}{\hat{p}_0(x_0)} \Big\rangle = \Big\langle \hat{S}_{Ha} \Big\rangle , \quad (4.4.4)$$

where the derivative is renormalized to the macroscopic scale L_{ref} and $\mathcal{A}(x) = V'(x) = 2\pi \iint J(x', z')\delta(x - x')\mathrm{d}x'\mathrm{d}z'$ is the flux surface area, which equals the first derivative of the enclosed volume V. A simple interpretation is obtained by integrating the above relation about a small volume of the width Δx around a flux surface. The total heat sources/sinks inside this volume must equal the difference between outward and inward energy transport rates

$$P_a^{\mathrm{out}} - P_a^{\mathrm{in}} = \Big\langle \mathcal{A}(x + \Delta x/2) \tilde{Q}_a^{\mathrm{neo}}(x + \Delta x/2) \Big\rangle - \Big\langle \mathcal{A}(x - \Delta x/2) \tilde{Q}_a^{\mathrm{neo}}(x - \Delta x/2) \Big\rangle$$

that consider the difference between the inner and outer flux surface areas. A more complete transport equation is given in Ref. [56], taking into account also

collisional heating as well as classical and anomalous transport. Here, we focus on neoclassical transport, such that these additional terms vanish. However, we derive the continuity relation Eq. (4.4.4) by employing the following (modified) flux definition

$$\hat{\tilde{Q}}_a^{\mathrm{neo}}(x) = \frac{\tilde{Q}_a^{\mathrm{neo}}(x)}{Q_{GB}} \equiv -\hat{p}_0(x_0)\frac{1}{\hat{\mathcal{A}}(x)}\int^x \left[\hat{\mathcal{A}}(x')\Big\langle \int \hat{v}^2 \hat{v}_d^x \partial_{\hat{x}'} \hat{F}_{1a}\,\mathrm{d}^3\hat{v}\Big\rangle\right]\mathrm{d}\hat{x}'\,, \tag{4.4.5}$$

which, in general, does not coincide with the standard definition

$$\hat{Q}_a^{\mathrm{neo}}(x) = \frac{Q_a^{\mathrm{neo}}(x)}{Q_{GB}} = \hat{p}_0(x_0)\Big\langle \int \hat{v}^2 \hat{v}_d^x \hat{F}_{1a}\,\mathrm{d}^3\hat{v}\Big\rangle\,,$$

because the drift velocity $\hat{v}_d^x$ and v^2 are actually functions of x, due to the variation of the magnetic geometry. We have

$$\begin{aligned}&\frac{1}{\hat{\mathcal{A}}(x)}\partial_{\hat{x}}\Big\langle \hat{\mathcal{A}}(x)\hat{\tilde{Q}}_a^{\mathrm{neo}}(x)\Big\rangle \\ &\quad = \frac{1}{\hat{\mathcal{A}}(x)}\partial_{\hat{x}}\Big\langle \hat{\mathcal{A}}(x)\hat{Q}_a^{\mathrm{neo}}(x)\Big\rangle - \hat{p}_{0a}(x_0)\Big\langle \int \left[\partial_{\hat{x}}\hat{v}^2\hat{v}_d^x\hat{J}_v\right]\hat{F}_{1a}\,\mathrm{d}\hat{v}_\parallel\mathrm{d}\mu\mathrm{d}\phi\Big\rangle\,.\end{aligned} \tag{4.4.6}$$

Note that the additional term is one order smaller in ρ^*. Consequently it vanishes in the local limit, in which $\hat{v}_d^x$, v^2 and J_v do not depend on x, and both fluxes become equivalent.

Back-transformation to particle space and the gyroaverage

Continuity relations are to be evaluated in particle space (as opposed to evaluating them in gyrocenter space). Consequently, the pull-back operation has to be employed for the above velocity space moments, equivalent to the flux definitions presented in Sec. 2.3.2. In our case, no electromagnetic fields are considered. We thus interpret the velocity space integration as $\int \mathrm{d}^3v(\cdots) = \int \delta(\mathbf{X}-\mathbf{x}+\boldsymbol{\rho})(\cdots)J_v\mathrm{d}v_\parallel\mathrm{d}\mu\mathrm{d}\phi$, which includes the gyroaverage operation and accounts for the transformation to particle coordinates.

Numerical results

To observe the energy balance we define yet another test case (case II in Tab. 4.4.1) by reducing the width of the temperature gradient profile from 0.2 to 0.05. Possible effects of the radial boundary condition are minimized in this way. We further set $a/L_n = 0$ and choose $\gamma_H = 0.01$ for the Krook heat source coefficient. The particle source is small and does not yield a significant contribution to the energy balance equation. Buffer zones are not employed. In circular geometry, the enclosed volume of a flux surface is $V = 2\pi R \times \pi r^2$, thus the flux surface area is $\mathcal{A} = V' = 4\pi^2 Rr$.

Circular geometry also has $x = r$ and $g^{xx} = 1$, which turns the continuity equation into

$$\frac{\rho_{\text{ref}}}{L_{\text{ref}}} \frac{1}{\hat{x}} \frac{\partial}{\partial(x/L_{\text{ref}})} \left\langle \hat{x} \tilde{Q}_i^{\text{neo}} \right\rangle = \hat{p}_{0a} \left\langle \hat{S}_{H,a} \right\rangle . \tag{4.4.7}$$

We integrate both sides to obtain an expression for the flux surface averaged neoclassical flux

$$\left\langle \hat{\tilde{Q}}_i^{\text{neo}} \right\rangle (x) = \frac{L_{\text{ref}}}{\rho_{\text{ref}}} \hat{p}_{0a}(x_0) \frac{1}{\hat{\mathcal{A}}(x)} \int^{\hat{x}} \hat{\mathcal{A}}(\hat{x}') \left\langle \hat{S}_H(\hat{x}') \right\rangle \mathrm{d}\hat{x}', \tag{4.4.8}$$

in relation to the integrated heat source profile.

The temperature and density profiles resulting from the described setup are depicted in Fig. 4.4.6, where we also show the final profiles in steady state (temporal convergence is found at $t = 10000\, a/c_s$). Note that the density gradient is quite perturbed and the temperature gradient is somewhat relaxed. In Fig. 4.4.7 the final heat flux profiles are compared to the integrated heat source from Eq. (4.4.8) and local results (based on relaxed temperature and density). Furthermore, Fig. 4.4.7 visualizes the continuity relation Eq. (4.4.7). It is found that the refined ($\tilde{Q}_i^{\text{neo}}$) energy flux perfectly balances the source/sink terms, while the standard (Q_i^{neo}) definition shows qualitative agreement. Local results are in good agreement with the standard definition, up to the outer half of the tokamak, where the heat balance forces the flux to become negative. In conclusion, ρ^* effects are seen in the refinement of the flux definition, while global simulation are also influenced by heat sources profiles. Both effects have their origin in the nonlocal $\mathbf{v}_d \cdot \nabla F_1$ term that also causes the background gradients to relax. In the narrow steep gradient zone of the the relaxed profiles, the local simulation yields a slightly ($\sim 10\%$) larger flux than the refined global value.

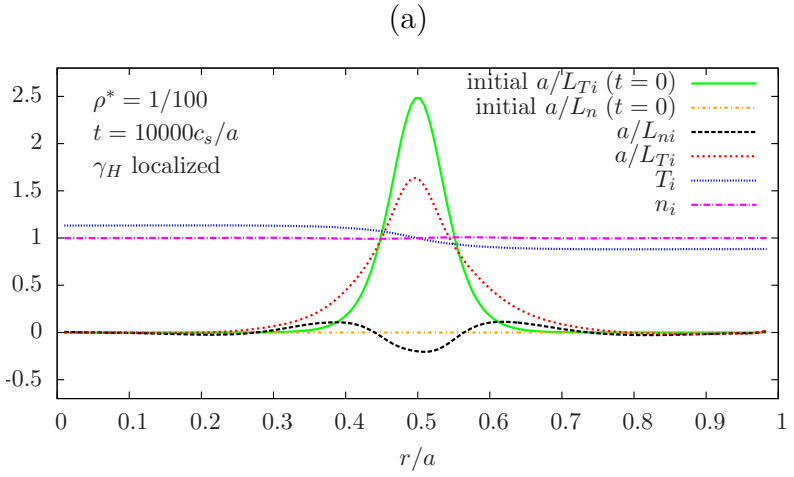

Figure 4.4.6.: Temperature and density profiles for case II parameters are shown. Saturated profiles for $\rho^* = 0.01$ and $\gamma_H(x) = 0.01$ are taken at $t = 10000\, a/c_s(x_0)$, where they are stationary.

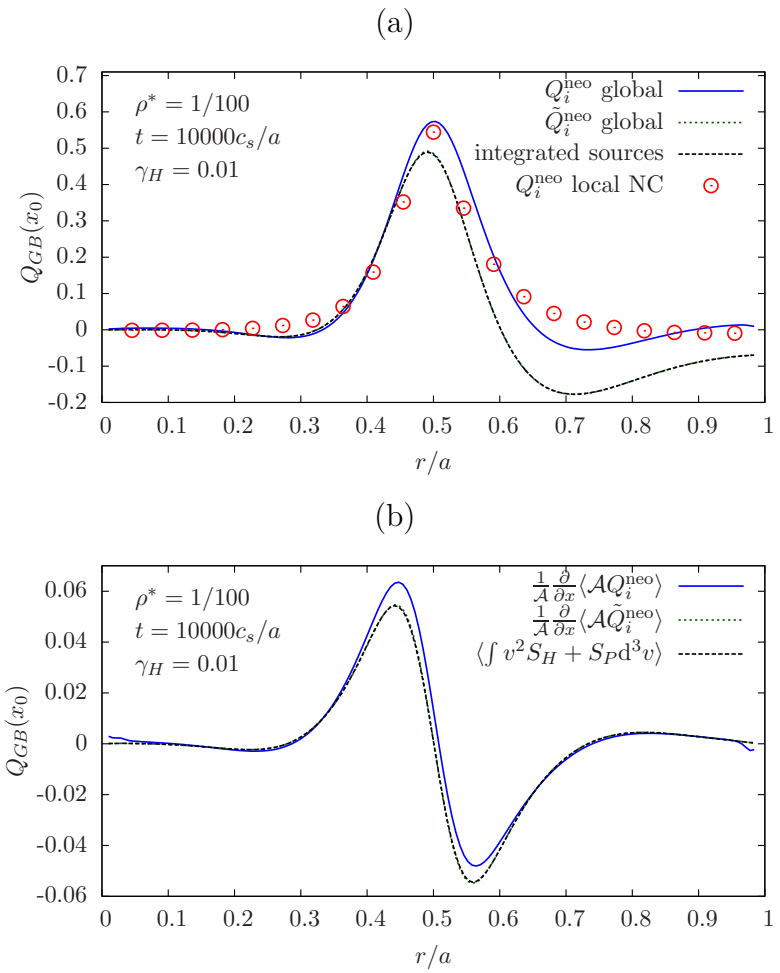

Figure 4.4.7.: The neoclassical energy balance is visualized using the refined and standard definitions of the neoclassical flux. Case II parameters are taken whith $\gamma_H = 0.01$ at $t = 10000\, a/c_s(x_0)$. (a) comparison of the heat flux to the integrated heat source profile and local simulations. (b) the heat source profile and the divergence of the neoclassical flux are shown.

4.5. Numerical tests of neoclassical transport simulations at low/high collisionality

We have seen in Sec. 4.3 that, obviously, neoclassical transport strongly depends on collisionality. Before, we have used a rather large value of $\nu_i^* = 0.5$. At low collisionality, we use $\nu_i^* = 0.05$ here, one obtains smaller fluxes and larger time-scales. We therefore perform a sensitivity study with respect to numerical settings of neoclassical transport computations at high/low collisionality. In particular, we systematically vary the Krook heat source coefficients (also at low collisionality) and furthermore enable hyperdiffusion terms. The basic setup is case III of Tab. 4.4.1,

using $\rho^* = 1/180$. The simulations presented in this Section are meant to show the limitations of numerical terms, we therefore use fixed, but very large simulation times, where the neoclassical fluxes only exhibit an extremely slow time evolution (compare Figs.4.4.1(a) and 4.4.4). We, however consider the fluxes well converged for radii larger than $0.2\,a$. In this way, we can identify two effects of the variation of a numerical coefficient: The first and most important effect is the modification of the neoclassical equilibrium itself, the other is the modification of the time evolution towards this equilibrium.

4.5.1. Influence of the heat source at low/high collisionality

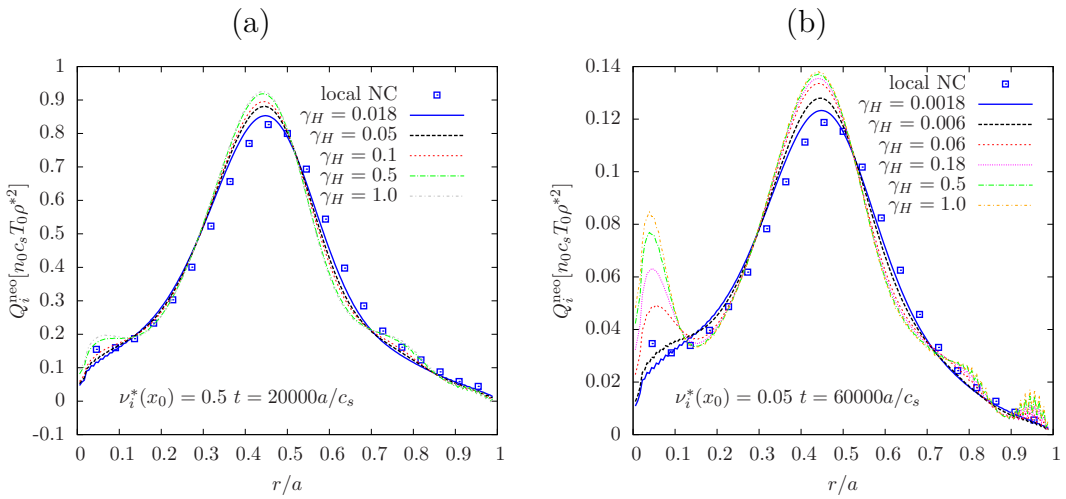

Figure 4.5.1.: Influence of the Krook-type heat source on the neoclassical heat flux (a) for $\nu_i^* = 0.5$ (b) for $\nu_i^* = 0.05$. The simulation times are chosen as $t = 20000\,a/c_s$ (a) and $t = 60000\,a/c_s$(b). For comparison, we show the local result for saturated gradient profiles.

We begin with a variation of the Krook-type heat source coefficient γ_H that is required to achieve steady state in a global gradient driven simulation. Since the particle flux is small in these simulations, we include a small ($\gamma_P = 0.001$) particle source, but do not consider its effect here. Figure 4.5.1 shows that large values of γ_H lead to more peaked flux profiles. Also, at the inner boundary up to $r/a = 0.2$ the heat flux is increased, which is considered artificial, since at these small radii the time-scale for saturation is very large and we do not see convergence in the given simulation time. One could expect that an increased heating coefficient decreases the saturation time-scale, but the data of Fig. 4.5.1 shows that this is not the case. Instead, a larger coefficient γ_H simply increases the flux perturbation at small radii and leads to stronger peaking.

Determining the correct magnitude of γ_H

We derive a rough rule to determine the magnitude of γ_H that keeps profiles reasonably constant and, at the same time, does not modify the heat flux profile too strongly. We presume that that neoclassical heat flux on a given flux surface is mostly local (it depends on the plasma parameters on that flux surface only) and thus follows the gyro-Bohm scaling $Q^{\text{neo}} \sim \int v^2 v_D F_1 \sim Q_{GB} = n_0 c_s T_0 \rho^{*2}$. In equilibrium, the heat source term should balance the neoclassical flux according to Eq. (4.4.8). With the scaling argument $Q^{\text{neo}} \sim S_H \sim \gamma_H F_1 \sim \rho^{*2}$ (and $F_1 \sim \rho^*$) , it is clear that γ_H should, at least approximately, scale linearly with ρ^*. Comparing to local computations in Fig. 4.5.1 we can measure the artificial peaking of Q_i^{neo} due to the Krook term. The present simulations have been performed for $\rho^* = 1/180$, where a coefficient $\gamma_H = 0.018$ gives a satisfying result for a collisionality $\nu_i^* = 0.5$. When smaller (larger) fluxes are expected, for example at smaller (larger) gradients or collisionality, then also a smaller (larger) value for γ_H is appropriate. This trend is confirmed by the $\nu_i^* = 0.05$ simulations of Fig. 4.5.1. Taking a simple linear relation between γ_H and Q^{neo}, the (rough) estimate

$$\gamma_H \approx \frac{Q^{\text{neo}}}{Q_{GB}} \times \rho^* \tag{4.5.1}$$

gives a first impression what value of γ_H should be used. The gyro-Bohm normalized heat flux may be approximated by local simulations that are substantially cheaper.

4.5.2. Influence of hyper-diffusion at low/high collisionality

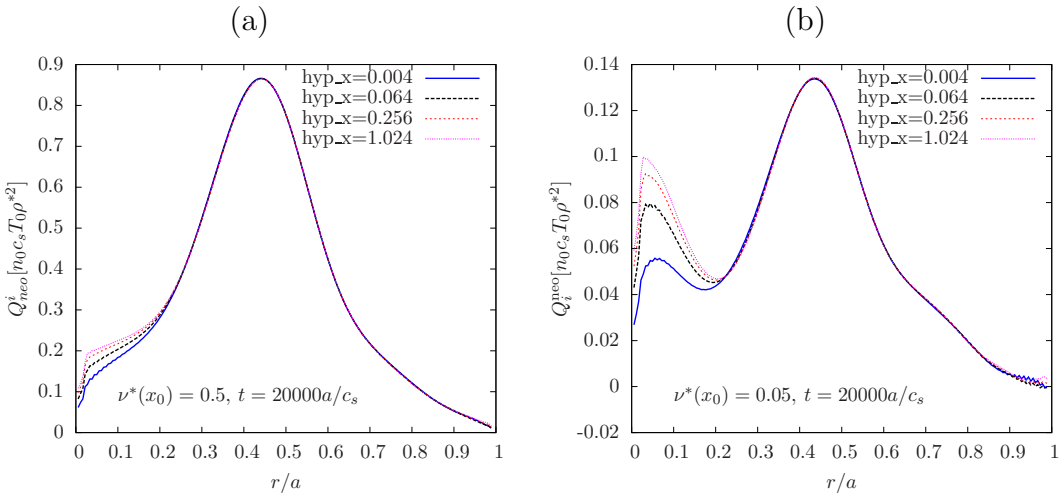

Figure 4.5.2.: Influence of radial hyperdiffusion on the neoclassical heat flux (a) for $\nu_i^* = 0.5$ and (b) for $\nu_i^* = 0.05$ each taken at $t = 20000\, a/c_s$. The heat source parameter is $\gamma_H = 0.05$.

Hyperdiffusion coefficients are usually introduced to remove sub-grid fluctuations that otherwise perturb the physical result. They can be avoided by using large numerical grid resolution, but this is not always affordable. GENE allows for the use of hyperdiffusion in the parallel direction z, parallel velocity $v_\parallel$, and in the radial coordinate x, which are the coordinates that involve finite-difference discretized derivatives. Here, $v_\parallel$ hyperdiffusion is not considered, because its influence on neoclassical transport is found to be weak. The reason is that collisions already provide some (physically motivated) diffusion in velocity space. We want to clarify in this Section, to what degree the remaining hyper-diffusion terms perturb the neoclassical results. We will generally find that these terms do not play a major role when the neoclassical solution is smooth even without hyperdiffusion. When this hyperdiffusion-free solution has some small scale structure, however, hyperdiffusion increases the neoclassical heat flux. For smaller heat flux (we take smaller collisionality as a control parameter), the results are more sensitive to hyperdiffusion. As a first test, Fig. 4.5.2 shows the influence of the radial hyperdiffusion, the numerical coefficient is hyp_x. It is seen that well within the simulation domain, x-hyperdiffusion has no influence. Only at the inner boundary $r < 0.2\,a$, where our results did not yet reach temporal convergence due to the extremely large saturation time scale, Q_i^{neo} is increasingly enhanced with hyp_x.

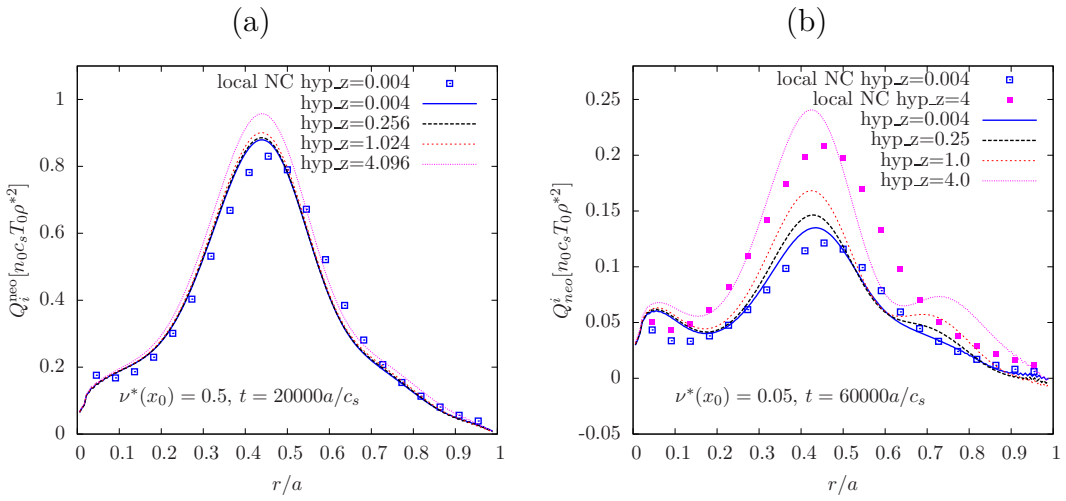

Figure 4.5.3.: Influence of parallel hyperdiffusion on the neoclassical heat flux (a) for $\nu_i^* = 0.5$ and (b) for $\nu_i^* = 0.05$. The coefficient $\gamma_H = 0.05$ is used for the Krook-type heat source. For comparison, local results (based on the final temperature profile for the smallest value of γ_H) are shown.

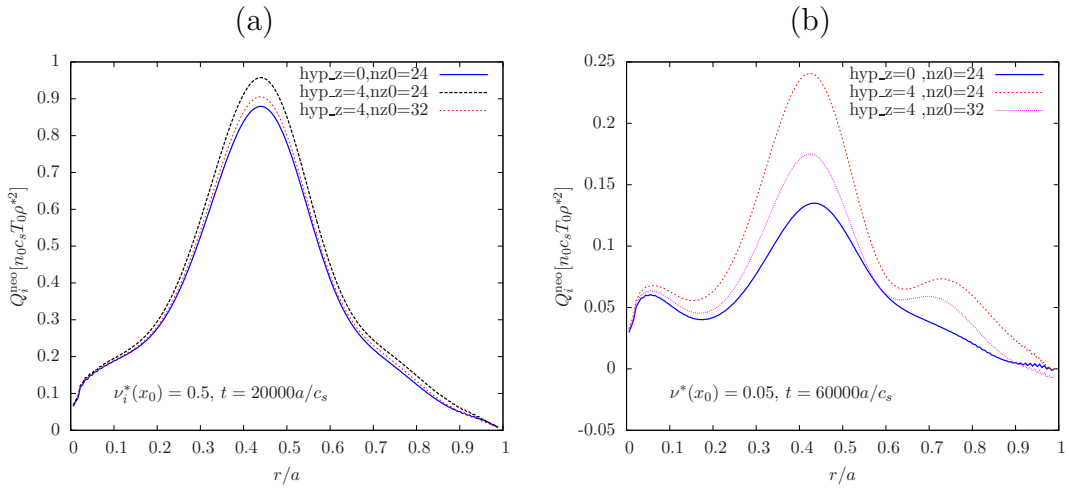

Figure 4.5.4.: Influence of parallel hyperdiffusion on the neoclassical heat flux at increased z resolution (a) for $\nu_i^* = 0.5$ (at $t = 20000\, a/c_s$), and (b) for $\nu_i^* = 0.05$ (at $t = 60000\, a/c_s$). Reasonable temporal convergence is governed for $r/a > 0.2$.

Parallel (z) hyperdiffusion is tested by varying the coefficient hyp_z. Figure 4.5.3 shows an artificially enlarged heat flux all over the radial domain that is obtained for increased parallel hyperdiffusion. At higher collisionality $\nu_i^* = 0.5$, the heat flux increase of ~9% is moderate, even for a relatively large hyperdiffusion coefficient hyp_z=4. The smaller collisionality case ($\nu_i^* = 0.05$) is affected more strongly by such a large hyperdiffusion, in the studied case a heat flux increase of 80% is found. Although the saturated temperature profile does essentially not depend on hyp_z, the local results depicted in Fig. 4.5.3 confirm the flux-increasing effect of z-hyperdiffusion. A further test using 32 (instead of 24) grid points in z reduces the deviation substantially: Fig. 4.5.4 shows that for $\nu_i^* = 0.5$ (0.05) the heat flux is only 3% (30%) larger. An explanation is found in the following: Increased resolution reduces numerical errors in the finite differencing scheme, that generate some unphysical small-scale structure in the distribution F_a. On the other hand, the 4th derivative of F_a that is implemented in the z-hyperdiffusion term, becomes large, when F_a involves such small scales. In consequence, a less pronounced influence of z-hyperdiffusion (at constant hyp_z) is expected for increased resolution.

4.6. Global benchmark between GENE and ORB5

4.6.1. Definition of the benchmark case

Finally, the prediction of neoclassical transport of the global version of the GENE code is benchmarked against the PIC code ORB5 described in Ref. [24] (and references therein). The simulation setup defined tor this purpose is case III of Tab. (4.4.1) described Sec. 4.4.2, using $\nu_i^* = 0.5$ and $\rho^* = 1/180$ in global CBC geometry. For simplicity, we do not consider the electron species and run without any electric field in both codes. Additionally, all sources and sinks are switched off, which lets the temperature profile relax in time. It is therefore important to match the simulation time, for which several collision times τ_{ii} are chosen. Both codes perform initial value computations with $f_1 = 0$ as the initial condition.

Hyperdiffusion terms are disabled, because Sec. 4.5 shows that they can easily perturb the neoclassical equilibrium. Our choice of the field-particle collision operator for GENE is the self-adjoint form, with the test-particle operator acting on f. In the local version of GENE, these collision operator settings have lead to good agreement with the NEO code in the collisionality regime considered here. The self-adjoint like-particle collision operator used in ORB5 is equivalent, it includes pitch-angle scattering as well as energy diffusion terms. The numerical implementation is, however, very different in PIC and Vlasov codes.

4.6.2. Comparison of GENE and ORB5 results

We now turn to the code comparison by monitoring the ion neoclassical energy flux Q_i^{neo} and ion contribution to the bootstrap current $j_{Bi} = \langle u_{\|i} B_0 \rangle$, given by Eqs. (2.3.11) and (2.3.16). The particle flux Γ_i^{neo} is not considered in this benchmark, because it is at least a factor of 10 smaller than the heat flux and decays further for larger simulation times.[8] After some initial oscillations, the time trace of Fig. 4.6.1 begins to change very slowly (at least for Q_i^{neo}). Although the amplitude of the initial oscillations in Q_i^{neo} is slightly larger in GENE, their time-scale is the same, because it is determined by τ_{ii}, the ion-ion collision time. We show in Fig. 4.6.2 that the radial profiles for Q_i^{neo} and j_{Bi} at $t = 2\tau_{ii}$ are slightly smaller in GENE, but nevertheless, a satisfactory agreement is found at all radial positions. These results show that global neoclassical computations with GENE compare well to another, numerically very different code.

[8] Adiabatic electrons actually require a vanishing particle flux.

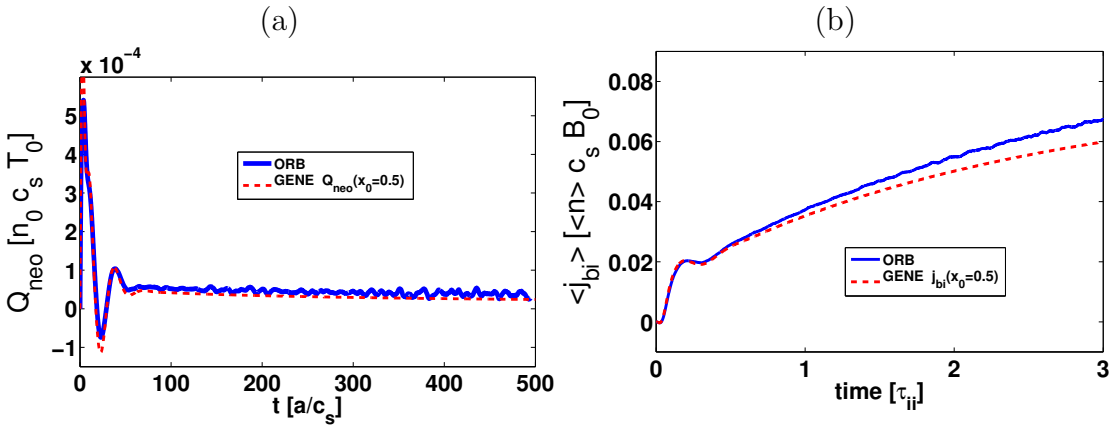

Figure 4.6.1.: Time traces of (a) the ion neoclassical energy flux Q_i^{neo} and (b) the ion contribution to the bootstrap current $j_{Bi} = \langle u_{\parallel i} B_0 \rangle$, both evaluated at the box center $r/a = 0.5$. Results for GENE and ORB5 are shown. After initial oscillations, saturation begins on the scale of several collision times τ_{ii}. The heat-flux is slowly decaying, because no heat sources are present and the gradient is therefore decreasing gradually.

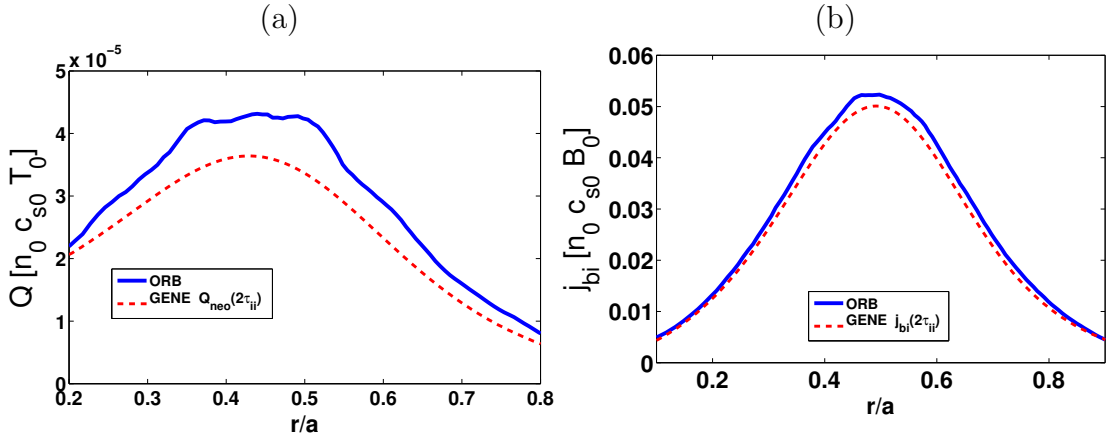

Figure 4.6.2.: Profiles of (a) the neoclassical heat flux Q_i^{neo} and (b) the ion contribution to the bootstrap current $j_{Bi} = \langle u_{\parallel i} B \rangle$. GENE results are evaluated at the simulation time $t = 2\tau_{ii}$ and ORB5 results are averaged over a small time window around $t = 2\tau_{ii}$.

4.7. Chapter summary

In conclusion, we have shown in this chapter that the GENE code (and in particular the implemented collision operator) is suited for the numerical prediction of neoclassical heat and particle transport. We have considered kinetic electrons and

a single species of ions to successfully benchmark with the NEO code in the local limit. The energy and momentum conserving terms of the collision operator are an important ingredient for these computations and the self-adjoint form of C^F is shown to improve the agreement, in particular for the electron contributions Q_e^{neo} and j_{Be} to heat flux and bootstrap current. The latter can correctly be computed up to relatively large collisionality regimes around $\nu_c \sim 0.01$. We note in this context that turbulence simulations show inherent statistical fluctuations and within these the particular choice of the model for the field particle operator virtually makes no difference.

Global neoclassical computations have been performed in the limit of adiabatic electrons. The nonlocal term $\mathbf{v}_d \cdot \nabla F_{1a}$ allows relaxation of the background gradients. It has been confirmed that the local limit is valid for the system size parameter $\rho^* = 1/300$, when the initial temperature gradient is maintained by a Krook-type heat source. Using $\rho^* = 1/100$, agreement between the local and the global GENE versions is found when a weak Krook coefficient is employed that lets the temperature gradient relax by about 25%. In global computations a Krook-type heat source can strongly contribute to the equilibrium neoclassical solution, in particular for large values of ρ^*. This Krook term actually provides not only energy sources, but also (possibly internal) energy sinks. By noting that, in steady state, a heat continuity equation is to be fulfilled, we have pointed out a clear difference to local simulations. In extreme cases, the Krook term enforces a radially inward flux, although the neoclassical drive term $v_D \nabla f_0$ is still positive. This situation is never given in the local limit that works without sources and sinks. Differences between local and global computations that result from finite-size effects, are thus often covered by the Krook-type heat source. The heat continuity relation is exaclty fulfilled in numerical simulations, when using a refined definition of the neoclassical heat flux, which coincides with the standard definition in the local limit and can thus be seen as an $\mathcal{O}(\rho^*)$ correction.

Further numerical tests have shown that hyper-diffusion terms tend to increase the neoclassical heat flux. We note that the neoclassical equilibrium is found to be reasonably smooth in phase space (for manageable grid resolution) such that it was not necessary to include hyperdiffusion terms. In contrast, hyperdiffusion is often used in turbulence simulations with moderate resolution to remove spurious small-scale fluctuations that would otherwise lead to incorrect results. Consequently, these tests are important not only for the computation of neoclassical transport alone, but also form the basis for simultaneous turbulence-neoclassics simulations (see e.g. Ref. [47]), a topic that is left for future work. A clear trend was seen when decreasing collisionality (and thereby Q_i^{neo}). The low collisionality case ($\nu_i^* = 0.05$) was stronger (up to 80%) modified by hyperdiffusion terms, compared to the $\nu_i^* = 0.5$ case (less than 10%). Noting that collisionality well below $\nu_i^* = 0.05$ can be reached in experiments, these issues should be kept in mind when the neoclassical equilibrium is to be computed at small collisionality and combined with turbulence runs that require hyperdiffusion. On the other hand, neoclassical transport is small in low-collisional plasmas, such that the overall transport is usually be dominated

by anomalous fluxes. In the letter case, 80% relative errors in the neoclassical value are likely to be negligible for the total heat and particle flux.

Finally, we have performed a benchmark of neoclassical transport between the global GENE code and the numerically very different particle-in-cell code ORB5. The overall satisfying agreement gives some confidence in the implementation of the global collision operator and shows the feasibility of global neoclassical computations with GENE.

5. Microtearing turbulence in standard tokamaks

5.1. Introduction and overview

In burning ITER [4] plasmas, the fusion processes will predominantly heat the electrons. It is thus important to understand and be able to predict electron thermal transport via microturbulence in magnetically confined plasmas. In this context, many key aspects are still under investigation, and the overall picture continues to evolve. Prominent examples include the contributions of sub-ion-gyroradius scale turbulence driven by electron temperature gradient (ETG) modes [57] and the role of magnetic stochasticity caused by small-scale reconnecting modes. The latter question has recently been addressed anew by means of high-resolution gyrokinetic turbulence simulations [9, 58, 59, 60, 61], building on fairly recent hardware and software advances. These modern methods allow to follow up on theoretical considerations which started already decades ago.

In 1973, Stix argued that even minute magnetic perturbations can greatly enhance the electron thermal transport if these perturbations are resonant.[62] Microinstabilities are a possible source of such perturbations, provided that they exhibit a resonant component of the vector potential, $\tilde{A}_{1\parallel}$. The magnitude of this resonant component, which is essentially an integral of $\tilde{A}_{1\parallel}$ along the field line, crucially depends on the parity of the perturbation. In an up-down symmetric tokamak, eigenmodes (with a vanishing radial wavenumber k_x) are characterized by either tearing (even) or ballooning (odd) parity with respect to $\tilde{A}_{1\parallel}$, as illustrated in Fig. 5.1.1. Importantly, the well-known ion temperature gradient (ITG) modes and trapped electron modes (TEM), at $k_x = 0$, belong to the second category.[1] The corresponding field-line integral vanishes and thus cannot directly break field lines. Magnetic stochasticity can be expected, however, when tearing-parity modes, such as the microtearing mode, are present and create small-scale magnetic islands which may overlap to create a stochastic field. In such a stochastic field, the fairly large parallel heat conductivity is coupled to the cross-field component, which may greatly enhance electron heat transport. First results in this area have already been obtained in the 1970's by several authors.[63, 64, 65, 66] Moreover, it has recently been proposed that in finite

[1] Vanishing radial wavenumber generally dominates the growth rate spectrum of an instability. Even for finite radial wavenumber, ITG and TEM modes predominantly exhibit ballooning parity.

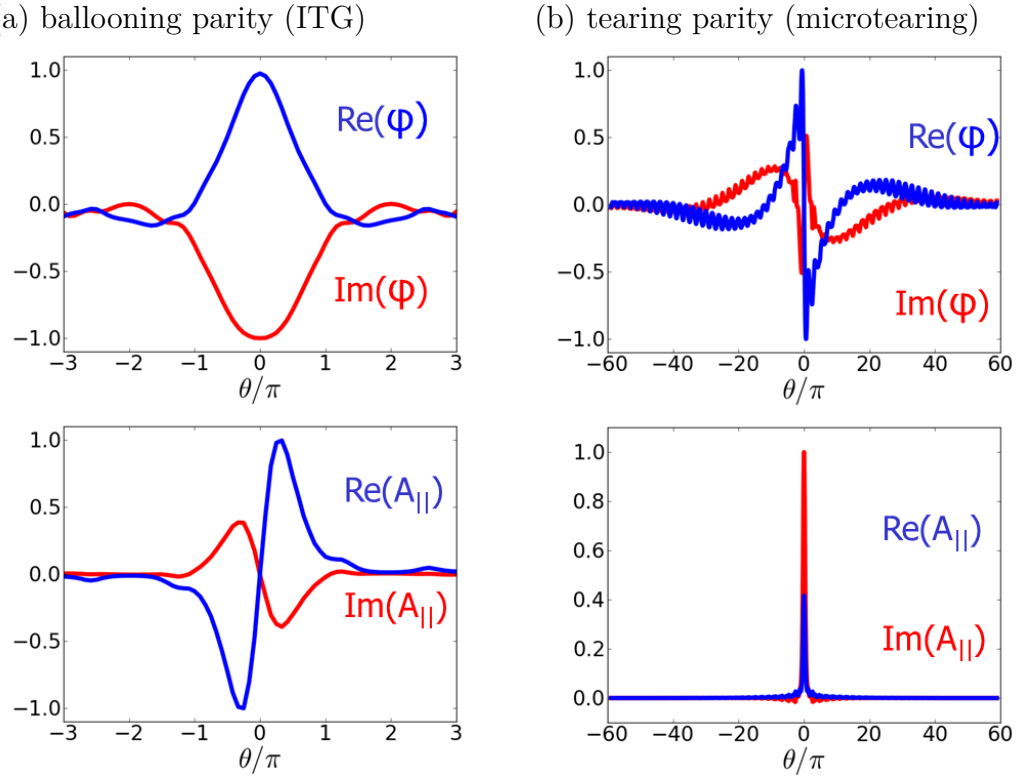

Figure 5.1.1.: Illustration of ballooning and tearing parity modes in field-line following coordinates. The ballooning angle θ is the coordinate along the field line. The wave numbers are $k_y = 0.11$ in both cases and simulations have been performed for ASDEX Upgrade geometry.

β_e ITG/TEM turbulence, linearly stable microtearing modes can be excited via a nonlinear coupling to zonal modes.[59] Interestingly, this can explain both the occurrence of stochastic fields [60] and the quadratic scaling of the magnetic transport which contradicts standard quasilinear transport models.[67]

In the present work, the focus lies on linearly unstable microtearing modes. From the published analytical work it is not entirely clear whether stabilizing or destabilizing terms dominate under realistic experimental conditions.

Therefore, linear gyrokinetic studies have been undertaken in the last decade, indicating a role of microtearing modes first in spherical (small aspect ratio) [68, 69, 70, 71, 72, 73, 74, 75, 76] and later also in standard (medium aspect ratio) [77, 78, 79] tokamak plasma. Moreover, improved confinement regimes of reversed field pinch plasmas may involve microtearing modes.[80] Among other things, these gyrokinetic computations revealed another drive mechanism related to magnetic curvature (thus not accessible in early slab models) which adds to the complexity of the linear mode.[77] Exploring various physical parameter regimes, different types of microtearing modes have been identified. In spherical tokamaks, operating at high β_e, they exist at rather high perpendicular mode numbers of $k_y\rho_i \sim 1$, whereas in

standard tokamaks, one typically finds $k_y\rho_i \sim 0.1$. A quite extreme difference in the radial scales between fine-scale parallel electron current ($j_{1\parallel e}$) as well as electrostatic potential (ϕ_1) structures and large-scale $\tilde{A}_{1\parallel}$ perturbations is commonly seen, an effect which makes it computationally expensive to compute even linear modes.

To predict the resulting level of turbulent electron heat transport, however, it is required to transcend linear theory. A semi-analytic transport prediction of Drake and co-workers has been used successfully to interpret the results of a rather collisional discharge in the National Spherical Torus Experiment (NSTX).[75, 81] However, such analytical treatments of the nonlinear microtearing problem suffer from severe simplifications.

Investigations of the nonlinear dynamics of microtearing modes by means of *ab initio* gyrokinetic simulations are extremely valuable in this context and are thus the subject of this work. While we focus on standard tokamak plasmas, it is worthwhile noting that within the last two years progress in predicting microtearing turbulence has been reported also for spherical tokamaks. Turbulence level and thermal transport is greatly enhanced with increasing electron temperature gradient, as expected from linear physics. Interestingly, a series of simulations performed for a certain NSTX discharge reproduces the experimentally determined favorable scaling with collisionality.[58, 82, 83]

It should be pointed out that these simulations are extremely demanding in terms of both the required computational resources and the level of detail in the physics model. For example, in the radial direction, high resolution and a large domain size are needed, due to the aforementioned multi-scale features in $\tilde{A}_{1\parallel}$ and $\tilde{\phi}_1$. For this reason, computations are commonly performed in the local (flux-tube) limit, neglecting radial dependencies of quantities like temperature, density, their gradients, and magnetic geometry. The local approximation is expected to hold when the tokamak minor radius a becomes much larger than the gyroradius ρ_i. While finite machine size effects usually stabilize modes like the ITG instability due to profile shearing [84, 39, 85], it is *a priori* not clear how microtearing modes are affected.

After giving a brief introduction to the linear theory of microtearing modes in Sec. 5.2, we thus begin our gyrokinetic study by investigating microtearing modes in radially global geometry in Sec. 5.3. A system size scan of linear microtearing modes is performed in Sec. 5.4. Since it turns out that even for relatively small machines the local limit is adequate, the flux-tube version of GENE is used in the following. In Sec. 5.5, the AUG discharge 26459 is studied with respect to critical electron temperature gradient and β_e. The two following Sections are devoted to two important aspects of the linear instability, which are the influence of collisions (Sec. 5.5.1) and the characteristics of the current layer at the mode rational surface (Sec. 5.6). The prediction of electron heat transport requires to include nonlinear physics. In Sec. 5.7 results on gyrokinetic microtearing turbulence simulations are presented, employing a geometry model assuming concentric circular flux surfaces.[55] We investigate (i) what sets the saturation levels of the magnetic field fluctuations, (ii) in which way the magnetic fluctuation level is linked to the heat transport level, and (iii) which kind of physics sets the saturation amplitudes and

thus the transport levels in the quasisteady turbulent state. Since both the plasma parameters chosen to perform the simulations and the obtained level of thermal transport are close to what is found in experiments, microtearing modes are established as an additional candidate for explaining turbulent transport in (standard) tokamaks.

5.2. An intuitive picture of the linear microtearing mode

Microtearing modes are the small-scale gyrokinetic analogues of the well-known magneto-hydrodynamic (MHD) tearing modes [6, 86, 87], although they involve quite different physics. While the MHD tearing modes gain free energy by relaxing the magnetic field to a lower-energy state, microtearing modes draw free energy from the background electron temperature gradient. The discovery of de-stabilization of small-scale tearing modes due to an electron temperature gradient is generally attributed to a work of Hazeltine in 1975.[63] The most prominent feature of tearing modes is the break-up and reconnection of magnetic field lines by the formation of a narrow current layer about a mode rational flux surface. Besides collisionless reconnection processes (due to finite electron inertia), also a certain level of collisionality facilitates magnetic reconnection. Drake and co-workers contributed significantly to the theoretical understanding of microtearing modes by providing an intuitive picture for the instability mechanism in three regimes named collisionless ($\nu_{ei}/|\omega| \ll 1$), semi-collisional ($\nu_{ei}/|\omega| \gg 1$ and $\Delta_J/\rho_i \ll 1$), and collisional ($\nu_{ei}/|\omega| \gg 1$ and $\Delta_J/\rho_i \gg 1$).[64] Here, $\nu_{ei} = 4\pi n_e e^4 \ln\Lambda (2T_e)^{-3/2} m_e^{-1/2}$ denotes the electron-ion collision rate, ω is a typical mode frequency, Δ_J is the width of the current layer, and ρ_i is the ion gyroradius. Modern tokamaks, characterized by high temperatures, mostly operate in the semicollisional and collisionless regimes. Importantly, the semicollisional regime, which is only accessible in numerical work, typically yields the most robust tearing instabilities.

A review of the existing literature leads to the conclusion that (even) the linear physics of the microtearing mode is surprisingly complicated. We take the opportunity to give a brief summary of the derivation of a dispersion relation and discuss necessary simplifications. A useful overview can also be found in Ref. [77], for example. Two drive mechanisms are reported, one being the so-called time-dependent thermal force that is present even in slab geometry and relies on a certain degree of collisionality [63, 64, 88, 81, 89, 90, 91, 92, 93, 94]. In toroidal geometry, collisional effects at the trapped-passing boundary provide another drive mechanism for the microtearing mode in the weakly collisional (banana-) regime.[65, 95, 96]

We will focus on the thermal force drive in slab geometry in this introduction, and only briefly discuss toroidal modifications. As a starting point we note that the safety factor, defined as $q(r) = B_{0\phi}(r)/B_{0\theta}(r)$, varies with the flux surface label r. Therefore, certain mode rational surfaces exist for poloidal mode number m and

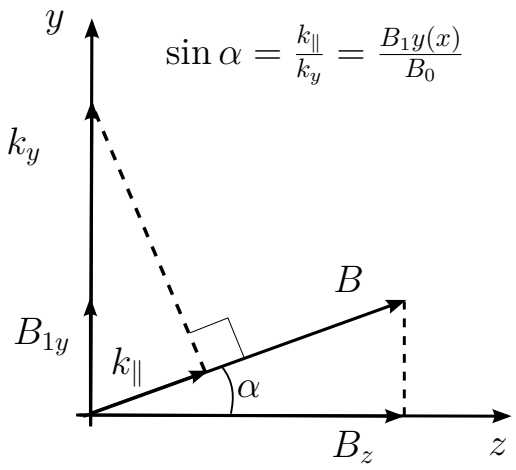

Figure 5.2.1.: Vector relations of the wave vector **k** is illustrated in sheared slab geometry that is often used in analytical work (like Ref. [64]) Close to the rational surface at $x = 0$ one has $k_\parallel = k_y x/L_s$ width the shear length $L_s = B_0/\left(\partial_x B_{1y}\right)$. The angle $\alpha(x)$ is enlarged for clarity. By comparison to Eq. (5.2.1) (and redefining the sign of $k_\parallel$) one finds the equivalent $L_s = qR/\hat{s}$ of the shear length in toroidal geometry.

toroidal mode number n, characterized by $nq(r_0) = m$. At these rational surfaces, a (n, m) solution of the linearized Vlasov-Maxwell system may close in itself after an integer number of poloidal turns,[2] where the parallel wavenumber $k_\parallel$ is allowed to vanish. Introducing $x = r - r_0$, one often approximates $k_\parallel$ [6, 96]

$$k_\parallel = \frac{m - nq}{qR} \approx \left.\frac{-n\partial_r q}{qR}\right|_{r_0} x = -\frac{\hat{s}}{qR} k_y x \tag{5.2.1}$$

with the usual definitions of the binormal wave number $k_y = nq_0/r_0$ and the magnetic shear $\hat{s} = (r_0/q_0)\partial q/\partial r$. By means of a geometric argument illustrated in Fig. (5.2.1) we find the equivalent expression $k_\parallel = -k_y x/L_s$ for sheared slab geometry, where L_s is the shear length.

We characterize microinstabilities by the associated electromagnetic potential perturbations $\tilde{A}_{1\parallel}$ and $\tilde{\phi}_1$ and assume a space-time dependence $\left[\tilde{A}_{1\parallel}, \tilde{\phi}_1\right] = \left[A_{1\parallel}(x), \phi_1(x)\right] \exp(-i\omega t + ik_y y + ik_\parallel z)$ to have

$$\begin{aligned} B_{1x} &= ik_y A_{1\parallel}(x, k_y, k_\parallel) \\ B_{1y} &= -\partial_x A_{1\parallel} \\ E_{1\parallel} &= -(1/c)\partial_t A_{1\parallel} - k_\parallel \phi_1. \end{aligned} \tag{5.2.2}$$

For low β plasmas one may neglect parallel magnetic field perturbations (they are a factor of β smaller than their perpendicular counterpart). Tearing parity modes

[2] Magnetic confinement forces possible perturbations to have small perpendicular extension, but allows for a larger parallel correlation length.

are characterized by a vector potential $A_{1\parallel}$ that is even about $x = 0$ such that $B_{1y}(0) = 0$. Such a vector potential is self-consistently generated by a parallel current along the strong background field B_0. Those modes lead to magnetic reconnection and the formation of magnetic islands. The corresponding parity of the electrostatic potential ϕ_1 is odd.[3] Microtearing modes are radially localized and thus the boundary condition $A_{1\parallel}(x) \propto \exp(k_y|x|)$ is applied.[4] Instability occurs when at the rational surfaces a growing parallel current perturbation $j_\parallel$ reinforces itself through the electron response in Ampère's law

$$\left(\frac{\partial^2}{\partial x^2} - k_y^2\right) A_{1\parallel} = -\frac{4\pi}{c} j_{1\parallel} \,. \tag{5.2.3}$$

The vector potential, generated by the current in turn induces a parallel electric field

$$E_{1\parallel} = -\frac{1}{c}\frac{\partial}{\partial t} A_{1\parallel} = i\frac{\omega}{c} A_{1\parallel} - k_\parallel \phi_1 \,, \tag{5.2.4}$$

where $\omega = i\gamma + \omega_r$ denotes the (complex) frequency. Ultimately, this electric field accelerates electrons and enhances the current perturbation. We can write down a generalized Ohm's law

$$j_{1\parallel} = \sigma_{\parallel e} E_{1\parallel} \,, \tag{5.2.5}$$

which formally allows solving for a dispersion relation by combining Eqs. (5.2.3), (5.2.4), and (5.2.5). The detail and the difficulty of the calculation lies in determining the electron conductivity $\sigma_{\parallel e}$.[5] This is done by taking the $v_\parallel$ moment of the (gyro- or drift-) kinetic equation and solving for $E_\parallel$, a very challenging task that can only be completed when strong assumptions are made to simplify the equations. It is thus not surprising that various flavors of the microtearing mode appear, depending also on choice of the collision operator.

The simplifications applied here require the parallel current $j_{1\parallel}$ to be strongly localized within $|x| < \Delta_J$ around the mode rational surface, where the inverse transit time is smaller than the mode frequency,

$$v_{te} k_\parallel(x) \lesssim \omega \,. \tag{5.2.6}$$

Here, v_{te} is the thermal electron velocity and $k_\parallel(x)$ is the x-dependent parallel wave number that vanishes right at the rational surface. In the opposite limit, when the transit time exceeds the mode frequency, the electrons will see an oscillating mode, which reduces their response in Ampère's law. Obviously, Eq. (5.2.6) does

[3] The opposite parity is a fundamental property of the equations also found in up-down symmetric toroidal geometry.[97, 98]

[4] Applying this boundary condition is equivalent to matching the solution for the MHD tearing mode to the outer (current free) MHD solutions, resulting in the tearing parameter Δ'.[93]

[5] The ion contribution can be ignored due to the comparably very large mass

not include the effect of collisional broadening and should therefore only be valid in the semicollisional to collisionless regime. Another point of view is connected to the parallel force balance. When $k_\parallel$ is significantly larger than zero, electrons are adiabatic and thus a current can only be generated in close proximity to the rational flux surface. A quantitative discussion of the current layer width is given in Sec. (5.6) by means of gyrokinetic simulations. In the following, $\Delta_J \ll \rho_i$ is implied. To analytically derive a dispersion relation for microtearing modes we will now (i) neglect the potential ϕ_1 within the current layer and (ii) take $A_{1\parallel}$ constant across the current layer. The latter is commonly called constant-$A_{1\parallel}$ or constant-Ψ approximation.[6] However, the derivative $\partial A_{1\parallel}/\partial x$ is discontinuous across the layer. We illustrate our assumptions on the the mode structure in Fig. 5.2.2, using a numerically computed gyrokinetic example. Both (i) and (ii) are motivated by the smallness of Δ_J and the tearing parity properties $\phi_1(x) = 0$ and $A_{1\parallel}(x) \neq 0$ at $x = 0$. It is now possible to insert Eqs. (5.2.4) and (5.2.5) into Eq. (5.2.3), divide by $A_{1\parallel}(0)$ and integrate the result across the current layer to obtain

$$\frac{1}{A_{1\parallel}(0)}\frac{\mathrm{d}A_{1\parallel}}{\mathrm{d}x}\bigg|_{-\Delta_J}^{\Delta_J} = \frac{4\pi i\omega}{c^2}\int_{-\Delta_J}^{\Delta_J}\sigma_{\parallel e}(x)\mathrm{d}x$$

where the left hand side is identified as the tearing stability parameter

$$\Delta' = \frac{1}{A_{1\parallel}(0)}\frac{\mathrm{d}A_{1\parallel}}{\mathrm{d}x}\bigg|_{-\Delta_J}^{\Delta_J} \sim -2k_y \tag{5.2.7}$$

evaluated here in the high modenumber limit neglecting k_y^2 against ∂_x^2 in the layer. The boundary condition $A_{1\parallel} \sim \exp(-k_y|x|)$ for $|x| \gg 1$ is applied. Note that in this case, Δ' is negative. Further assuming a slab geometry model, as well as $\omega/\nu_{ei} \ll 1$ (which is the semicollisional regime, since we take $\Delta_J \ll \rho_i$ and neglect ϕ) and $\gamma \ll \omega_r$, the dispersion relation can be solved and written in the form [93]

$$\frac{\omega_r}{(v_{te}/a)} = k_y\rho_e\left(\frac{a}{L_{ne}} + \frac{5}{4}\frac{a}{L_{Te}}\right) \tag{5.2.8}$$

$$\frac{\gamma}{(v_{te}/a)} = N_1\left(\frac{a^2}{L_{Te}^2}\right)\left(k_y^2\rho_e^2\right)\frac{1}{\nu_{ei}/(v_{te}/a)} - N_2\left(\frac{k_y^2}{k_0^2}\right)\left(\frac{a}{L_s}\right) \tag{5.2.9}$$

where dependencies not required in this discussion are hidden in the factors $N_{1,2}$ and $k_0^{-1} = c/\omega_{pe}$ is the collisionless skin depth. Note that the real frequency $\omega = \omega_{*e}^T = k_y\rho_e v_{te}(1/L_{ne}+(5/4)/L_{Te})$ is closely related to the diamagnetic frequency, which reflects the drift character of the mode. The first term in Eq. (5.2.9) represents the electron temperature gradient drive corresponding to the time-dependent thermal force. The second term represents magnetic field line bending, and this

[6] Ψ means the magnetic flux in this context.

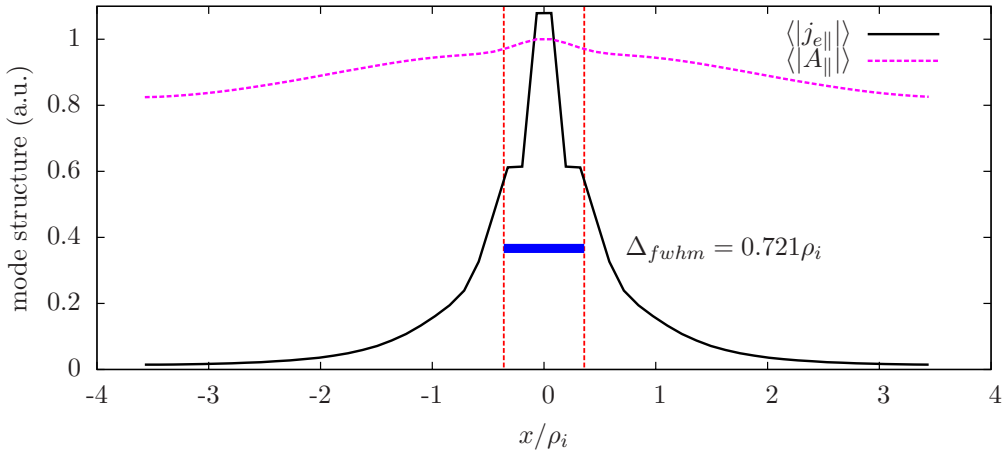

Figure 5.2.2.: Flux surface averaged mode structure of $j_{e\parallel}$ and $A_\parallel$ for $k_y\rho_i = 0.14$, as simulated with GENE in the local approximation. Defining $2\Delta_J = 0.72\rho_i$ as the full width at half maximum, as shown in the figure, we obtain $\Delta' = -0.21/\rho_i$ from Eq. (5.2.7). For more detailed analysis, we refer to Sec. 5.6, where also the parallel dependence is accounted for.

term is stabilizing because Δ' is negative. Clearly, within these approximations, microtearing growth can be understood as the successful competition of these two terms of Eq. (5.2.9). It is interesting to note that due to the gradient drive, $\gamma \sim 1/\nu_{ei}$ in the considered semicollisional regime.

Already in Ref. [93] it is stated that the assumptions underlying Eq. (5.2.9) are generally not met in experiments, which is underlined by numerical methods to solve the dispersion relation. One reason is that experiments are set up mostly between the collisionless and semi-collisional limits and this is where the growth rate is found to be largest (see also [92, 83]). This intermediate collisionality regime is, however not easily accessible analytically. Moreover, at low magnetic shear, the constant-$A_\parallel$ approximation breaks down, leading to a non-monotonic dependence of γ on magnetic shear. Furthermore, Gladd and co-workers [93] pointed out the potential role of $\tilde{\phi}$ in destabilizing the current layer in the context of a semi-analytic theory, thereby further complicating the physical picture. A stabilizing role of $\tilde{\phi}$ is expected for larger current layers,[64] because the additional electric field $\tilde{E}_{\parallel\phi} = -\nabla\tilde{\phi}_1$ short-circuits the response $E_{\parallel A} = -(1/c)\,\partial_t \tilde{A}_{1\parallel}$.

Another limitation imposed here is the choice of slab geometry within which toroidal effects are ignored. As mentioned above, in toroidal geometry another drive mechanism is reported. A sophisticated analysis by Connor *et al.* [96], however, leads to the conclusion that these modes are linearly stable for realistic tokamak parameters in the regime $\nu_{ei}/\epsilon > \omega > \nu_{ei}$. In the same work the damping effect of the collisional broadening of the passing Landau resonance is explained.

5.3. Global linear microtearing modes in ASDEX Upgrade

We begin our gyrokinetic studies by performing a linear stability analysis of the AUG shot 26459 with GENE. This well diagnosed H-Mode discharge shows Type II ELMs (Edge Localized Modes) and is characterized by strong plasma shaping and high density, with high triangularity, high elongation, and high q_{95}. Discharges where Type II ELMs are created start as standard H-Modes with Type I ELMs and are then pushed upwards to a near double-null configuration.[99, 100] When the plasma density is sufficiently high, Type I ELMs develop into the faster and weaker Type II ELMs. Additionally, the electron temperature decreases in the outer core region. Due to the high density, the collisionality is rather large, which is why one might expect tearing modes to appear. However, we find $\nu_{ei}/|\omega| < 10$, and thus the collisional regime defined in Ref. [64] is not reached.

The results presented below correspond to the Type II ELM phase. Temperature and density profiles as well as magnetic geometry are averaged over a time-slot between 4.0 and 4.6 seconds of that discharge. The measured data for temperature and density are taken from the AUG database (see Fig. 5.3.1). The resulting pressure gradient in the plasma edge, together with the signals of the magnetic pickup coils, serves as input boundary conditions for the CLISTE code that reconstructs the equilibrium. The resulting safety factor profile is depicted in Fig. 5.3.3. The field-aligned coordinate system used in GENE is then obtained with the TRACER module. In this work, $\rho_{\mathrm{tor}} = x/a$ is used as a radial coordinate, where $a = \sqrt{(\Psi_{\mathrm{tor,sep}}/(\pi B_0))}$ is the effective minor radius, such that the separatrix is located at $\rho_{\mathrm{tor}} = 1$.

Using these profiles as input, we perform global linear GENE simulations of microtearing modes in toroidal geometry. Fig. 5.3.2 shows the $\tilde{A}_{1\parallel}$ and $\tilde{\phi}_1$ contour plots for $n = 11$ perturbations. For the most unstable microtearing mode, one can identify the dominant poloidal mode number $m = 24$. The electrostatic potential perturbation and the parallel electron current shown in Fig. 5.3.3 are rather localized about the corresponding mode rational surface of $q = 24/11$, while the $\tilde{A}_{1\parallel}$ perturbation is more extended. The plasma parameters at this position ($\rho_{\mathrm{tor}} = 0.6$) are: $\beta_e = 0.00423$, $\nu_{ei} = 0.685\, c_s/a$, $q = 2.18 \approx 24/11$, $\hat{s} = 1.31$, $a/L_{Te} = 3.02$, $a/L_n = 0.376$, $a/L_{Ti} = 2.185$, $T_i/T_e = 1.192$, and $\rho^* = 1/330$.[7] For this particular run, we reduced the ion temperature gradient to $a/L_{Ti} = 1.6$, which speeds up the computation due to a shorter transient phase. However, local runs have shown that the microtearing instability is indeed the most unstable mode also for the nominal value of a/L_{Ti}. Convergence studies show that a radial grid spacing of $0.2\,\rho_i$ is required to obtain the correct growth rate.

[7] We define the electron beta as $\beta_e = 8\pi n_e T_e/B_0^2$ and the electron-ion collision rate as $\nu_{ei} = 4\pi n_e e^4 \ln\Lambda (2T_e)^{-3/2} m_e^{-1/2}$.

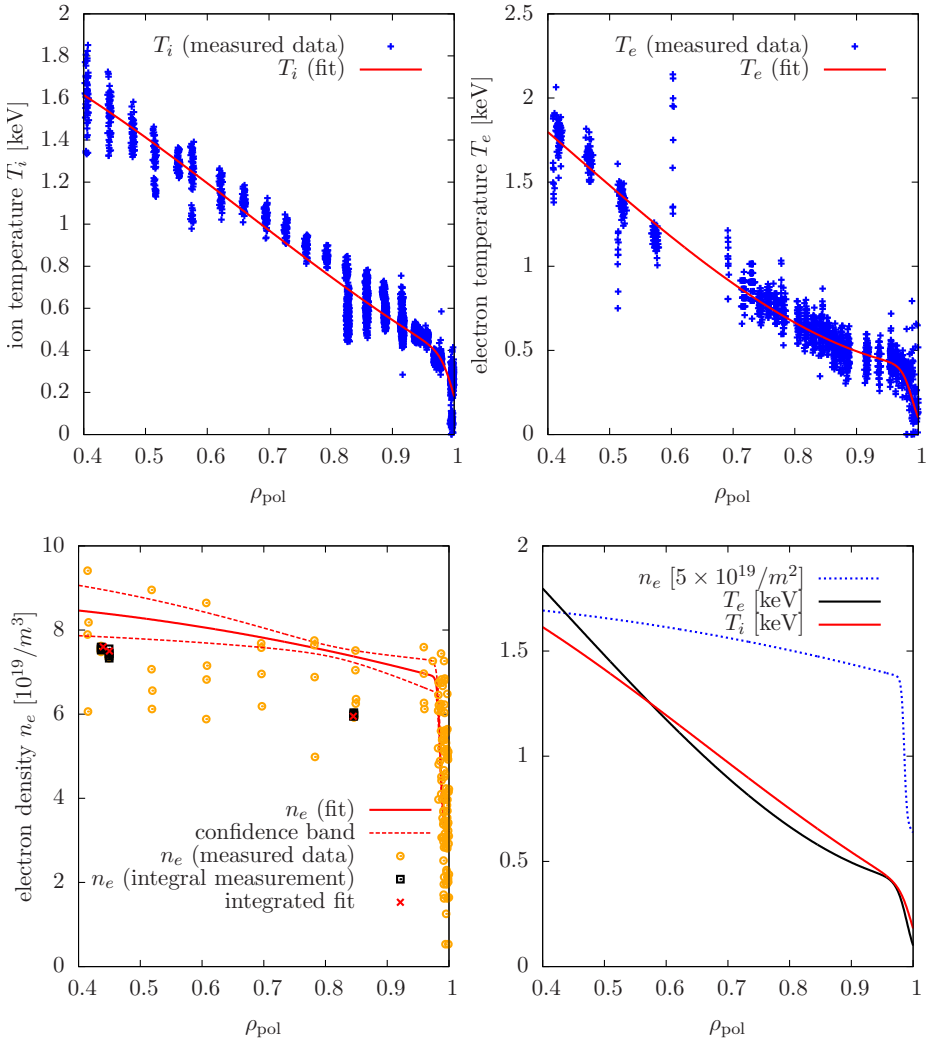

Figure 5.3.1.: Temperature and density profile fits and measured data points from the AUG data base for discharge 26459 in the time interval between 4.0 and 4.6 seconds. We restrict ourselves to $\rho_{\mathrm{pol}} > 0.4$ ($\rho_{\mathrm{tor}} > 0.29$) to obtain a more accurate fit in the outer region. For the density, the confidence band of the extended tanh fit is given. The interferometer density measurement (black squares) is well matched when one integrates the density fit along the corresponding line of sight (red crosses).

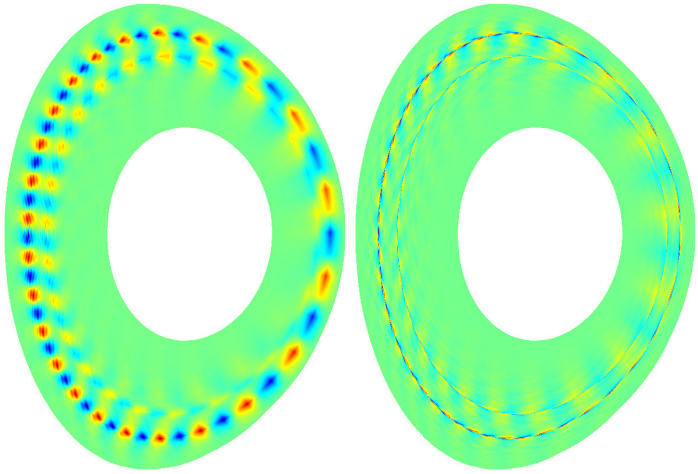

Figure 5.3.2.: Contours of $\tilde{A}_{1\parallel}$ and $\tilde{\phi}_1$ in the poloidal plane for $n = 11$ are shown. The most unstable microtearing mode is localized at the $q = 24/11$ flux surface and has $m = 24$ in this case. The mode rotates in the electron diamagnetic direction (counter-clockwise) in our convention. $\tilde{A}_{1\parallel}$ forms larger structures, while $\tilde{\phi}_1$ is closely bound to the mode rational surface.

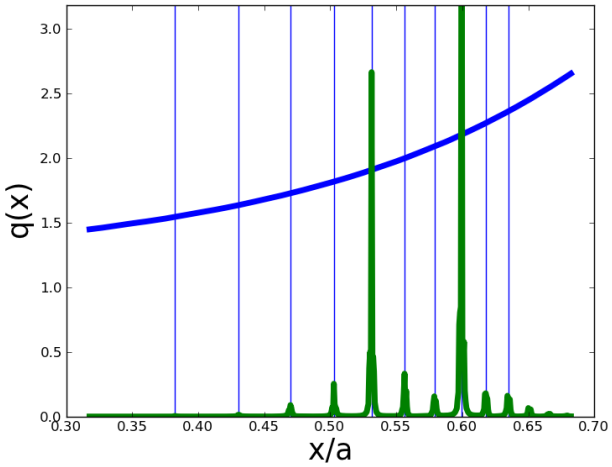

Figure 5.3.3.: The q profile of AUG discharge 26459 is shown (blue line). The electron current perturbations, $j_{1\parallel e}$ (shown in green color), peak at the rational flux surfaces for $n = 11$ that are indicated by vertical lines. For the chosen time slice, the fastest growing mode $m = 24$ is not yet completely dominating.

5.4. System size effects

Having established that global GENE simulations of actual AUG discharges exhibit microtearing instabilities, a natural follow-up question is to which degree these modes are influenced by nonlocal effects. To address this issue, it is useful to perform systematic scans in the parameter $\rho^* = \rho_i/a$ which sets the ratio of the typical turbulence scale length and the machine minor radius a. Of fundamental interest is the convergence behavior in the local limit, $\rho^* \to 0$. For these ρ^* variations, we fix both the radial box length in units of a and the grid spacing of $0.2\rho_i$. Therefore the number of radial grid cells increases as $1/\rho^*$, and the simulations become more computationally expensive for smaller ρ^*. The profile of the electron temperature gradient is peaked at the center of the radial domain ($x_0/a = 0.5$) in all the runs. This is also where we place the $q_0 = 3$ mode rational surface. We thus expect the mode with the maximum growth rate at this position. The binormal wave vector is $k_y\rho_i = 0.12$, which corresponds to the toroidal mode number $n_0 = (x_0/a)\, q_0^{-1}\, (k_y\rho_i)\, (\rho^*)^{-1}$. The dependence on ρ^* in this relation implies that larger devices involve more unstable mode numbers. For $\rho^* = 1/50$, the mode density is very low, and only a few modes fall into the typical low k_y regime of linear instability.

Now, Fig. 5.4.1 shows that the local result is even valid for relatively large values of ρ^*. This is somewhat surprising, since ITG modes are known to be strongly stabilized with increasing ρ^*.[85, 101] A possible explanation can be found in the fundamentally different mode structure. One of the stabilizing ρ^* effects is the variation of the diamagnetic drift velocity ω_* across the width of typical eddies, which is associated with some intrinsic shearing. When the shearing rate becomes comparable to the growth rate, the ITG mode is stabilized. In a similar fashion, shearing due to zonal flows saturates the ITG instability. One can understand this by noting that a sheared ITG eddy is linearly damped. In contrast to an ITG mode, in which all relevant fluctuating fields have comparable scale lengths in radial direction, microtearing modes show inherent multiscale features. The vector potential $\tilde{A}_{1\parallel}$ is fairly large-scale, but other fields like $j_{1\parallel e}$, $\tilde{\phi}_1$, and T_{1e} are peaked (within few ρ_i) about the rational flux surfaces. Those narrow structures are apparently less susceptible to radial shearing effects. However, a certain level of ρ^* stabilization is seen in cases for which ω_* is still essentially constant across the extremely narrow current layers, indicating that other fields (like $\tilde{A}_{1\parallel}$) also play a role in the instability mechanism. In Fig. 5.4.1, we further observe that the limit $\rho^* \to 0$ is correctly captured.

We note in passing that in some cases, two microtearing modes at different radial positions have very similar growth rates, including the one shown in Fig. 5.4.1. Thus, long (initial-value) simulations are required to clearly identify the fastest growing mode. We also point out that careful convergence tests have been performed for $\rho^* = 0.01$, confirming the need for significant computational resources. In particular, it was found that 40×16 points in $(v_\parallel, \mu)$ velocity space and 24 points in the field-line following direction z are required, as well as a radial grid spacing of $0.2\rho_i$. Here, we use a phase space domain characterized by $L_x/a = 0.6$, $L_{v_\parallel} = 3.28 v_{Ta}$,

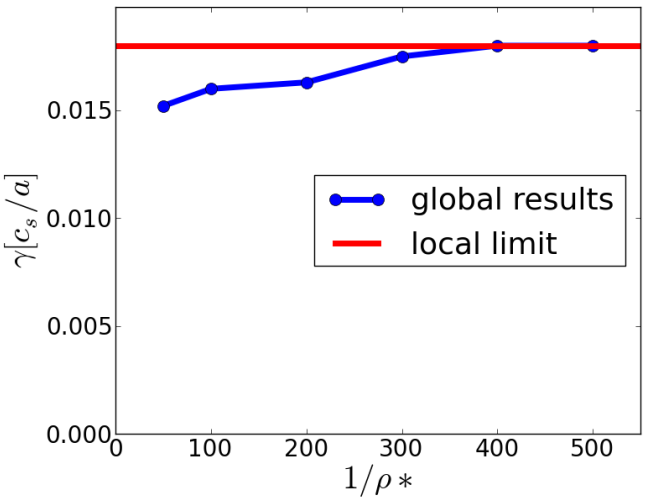

Figure 5.4.1.: ρ^* variation in radially global simulations with fixed gradient profile and binormal wave number $k_y\rho_i = 0.12$. Even at large ρ^*, profile shear stabilization is moderate, and the local limit $\rho^* \to 0$ is correctly captured.

and $L_\mu = 11T_a/B_0$ for plasma species a. In practice, up to 10,000 CPU-hours are required per linear simulation.

5.5. Local simulations for ASDEX Upgrade discharge 26459

We have verified in the previous section that the (linear) microtearing instability is well represented by the local limit even for moderate values of ρ^*. AUG has typical ρ^* values of a few times 10^{-3} and usually falls into that regime. The results presented below are obtained with the local (flux-tube) version of the GENE code. The reason for that is the increased simplicity and computational efficiency of local compared to global computations.

Using local runs, we first determine the linear growth rate as a function of the radial position ρ_{tor}. The physical parameters for these simulations are extracted from the AUG data base. We summarize them in Tab. 5.5.1 in the right column (2). Fig. 5.5.1 shows that microtearing modes of binormal wavenumber $k_y\rho_i = 0.12$ have a positive growth rate in the outer half of the torus. The growth rate decreases towards the edge, most likely because a/L_{Te} decreases in the particular temperature profile used. (In addition, the position of the maximum growth rate might have moved in k_y space.) The modes rotate in the electron diamagnetic direction (in our sign convention, this corresponds to negative frequency), and the magnitude of the real frequency is about 50 to 100 kHz. A k_y spectrum shows that ITG modes are also expected at higher k_y values. We can distinguish these modes by measuring the parity of $\tilde{A}_{1\|}$ as a function of the parallel coordinate z (corresponding to the

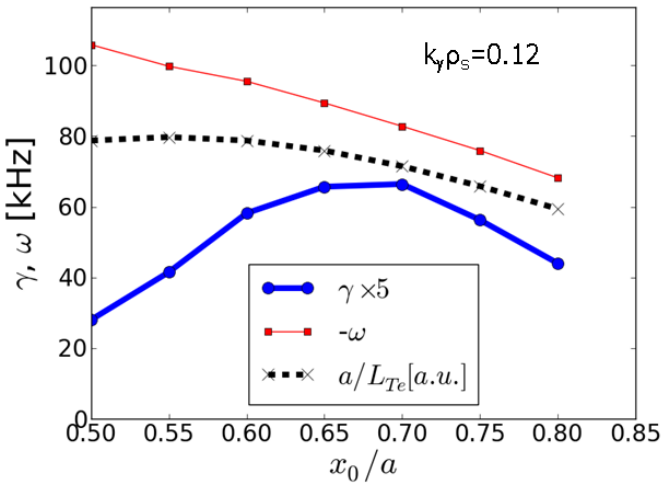

Figure 5.5.1.: A local scan over the radial position $\rho_{\text{tor}} = x/a$ shows that microtearing modes are unstable over a wide range in the outer half of the tokamak core. For the fixed binormal mode number $k_y\rho_i = 0.12$, the real frequency is around 50 to 100 kHz.

ballooning angle θ). $\tilde{A}_{1\|}(\theta)$ is even (odd) for microtearing (ITG) modes. Also, the ITG real frequency has opposite (positive) sign and yields a smaller ratio ω/k_y. For the spectrum at the radial position $\rho_{\text{tor}} = 0.8$ shown in Fig. 5.5.2, the plasma parameters have been slightly modified, see Tab. 5.5.1 in the left column (1). The used gradients match better the $\rho_{\text{tor}} = 0.5$ position that are listed in Tab. 5.7.1. In particular, β_e has been increased from 0.003 to 0.004 and a/L_{Ti} has been decreased from 2.2 to 1.6. These modifications make the microtearing modes more pronounced and weaken, to some degree, the ITG modes. However, the overall picture remains unchanged. ETG modes are not shown in the graph, although they also have positive growth rates.

Simulation results on pure microtearing turbulence suggest that the linear coexistence of microtearing instabilities and ITG modes observed in Fig. 5.5.2 carries over into the nonlinear regime, because (a) the transport peak is found at wavenumbers slightly lower than the range of ITG activity and (b) the turbulence level of microtearing modes is only weakly susceptible to (possibly ITG driven) zonal flows. The results of corresponding nonlinear simulations are detailed in Sec. 5.7. In the following, we will focus on investigations concerning the linear critical gradients instead. It is widely known that once a certain critical ion temperature gradient is exceeded, heat transport due to ITG modes increases rapidly with increasing gradient. The resulting heat flux usually does not allow the profile gradient to significantly exceed the critical value, implying profile stiffness. This critical gradient, however, experiences a nonlinear up-shift in ITG turbulence. Interestingly, in the analysis of nonlinear simulations in Sec. 5.7, we will see that a similar effect is expected for microtearing turbulence. Strong transport only sets in once a threshold

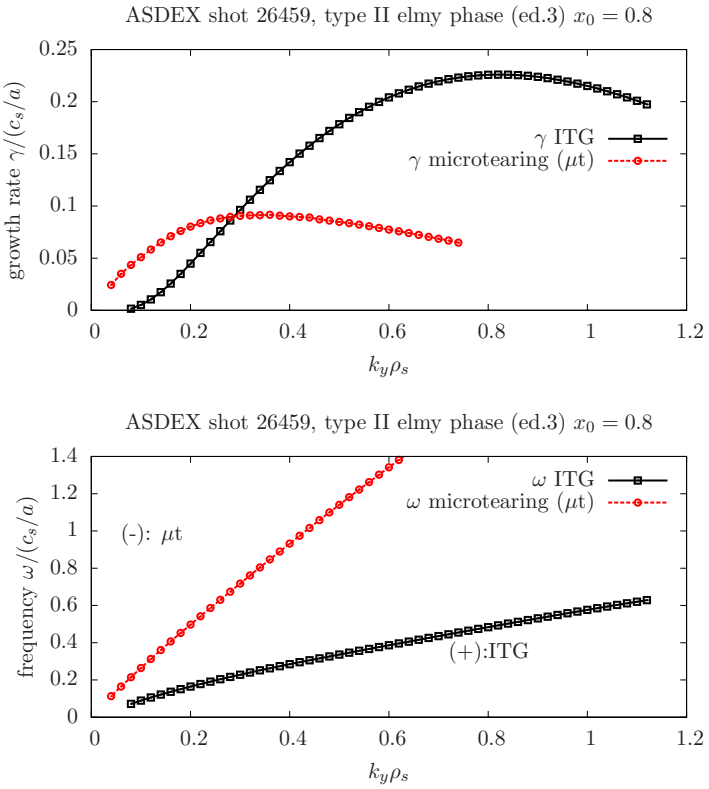

Figure 5.5.2.: Microtearing modes dominate the low-k_y region. They coexist with an ITG branch at higher wavenumbers. The ETG instability at $k_y\rho_s \sim 2$ is not shown. When comparing to the results from the AUG database, slightly modified plasma parameters are used, see Tab. 5.5.1.

Table 5.5.1.: Comparison of the parameters used for Fig. 5.5.2 (1) to the values derived from the AUG database at $\rho_{\text{tor}} = 0.8$ (2). Fig. 5.5.1 is based on the latter set (2).

parameter set	(1)	(2)
ρ_{tor}	0.8	0.8
a/R	0.37	0.37
a/L_{Te}	2.5	1.63
a/L_{Ti}	1.8	2.08
a/Ln	0.43	0.30
T_i/T_e	1.0	1.2
m_i/m_p	2	2
ρ^*	0.00304	0.00304
$\beta_e[\%]$	0.4	0.25
$\nu_{ei}/(c_s/a)$	0.97	1.54
q	3.7	3.7
$\hat{s}$	2.48	2.48

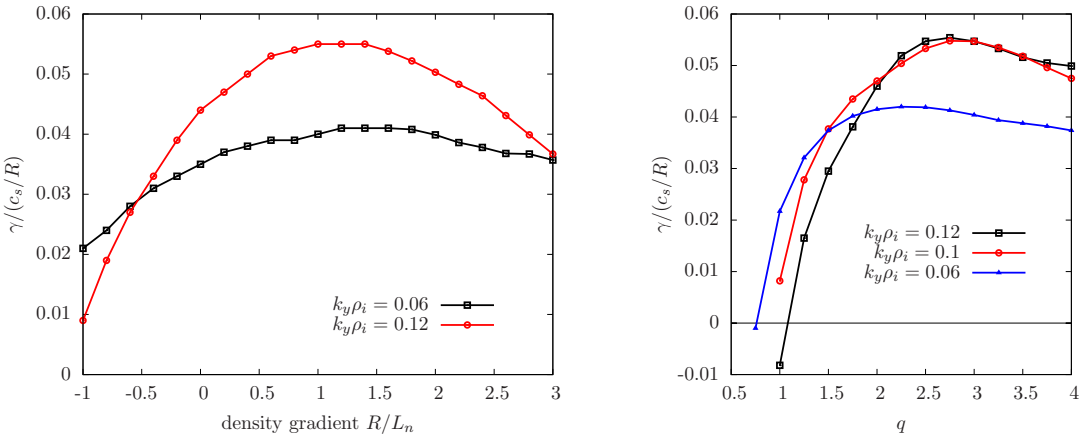

Figure 5.5.3.: Variation of microtearing growth rate with R/L_n and q is shown in circular geometry. Nominal parameters are $q = 3$, $\hat{s} = 1$, $R/L_n = 1$.

in the magnetic field fluctuation amplitude (and therefore in the drive strength) is exceeded.

In all gyrokinetic studies to date, a threshold behavior in the parameters a/L_{Te} and β_e has been observed. Sensitivities on the density gradient seem to depend on the specific parameter regime and magnetic geometry. NSTX high-k microtearing is damped by a/L_n around the experimental value: An $\eta_e = L_n/L_T$ drive is reported [102] and other discharges suggest that stability depends on the ratio ν_{ei}/ω, that is modified by a/L_n.[83] AUG results have shown a a/L_n drive including a threshold [79] in the plasma edge, and circular geometry results shown in Fig. (5.5.3) exhibit a weak dependence around realistic values for $0 \lesssim a/L_n \leq 2$. Fig. 5.5.3 also shows the influence of the safety factor q. Strong de-stabilization is found for $1 \lesssim q \lesssim 2$, but for larger values of q that are relevant in the outer-core region of a standard tokamak, the dependence is found to be moderate. This study of critical parameters for microtearing thus focuses in particular on a/L_{Te} and β_e, the results are depicted in Fig. 5.5.4. The instability threshold for a/L_{Te} is increased for decreasing β_e in the low-wavenumber limit, but the experimental reference values for both a/L_{Te} and β_e (Tab. 5.5.1) are well above this threshold. The critical parameter study performed for the reference AUG discharge 26459 reveals that microtearing modes at low k_y have a smaller critical gradient than ITG modes. Thus some relevance of such modes is expected: If the temperature gradients of both species (electrons and ions) are ramped up together, microtearing sets in first.

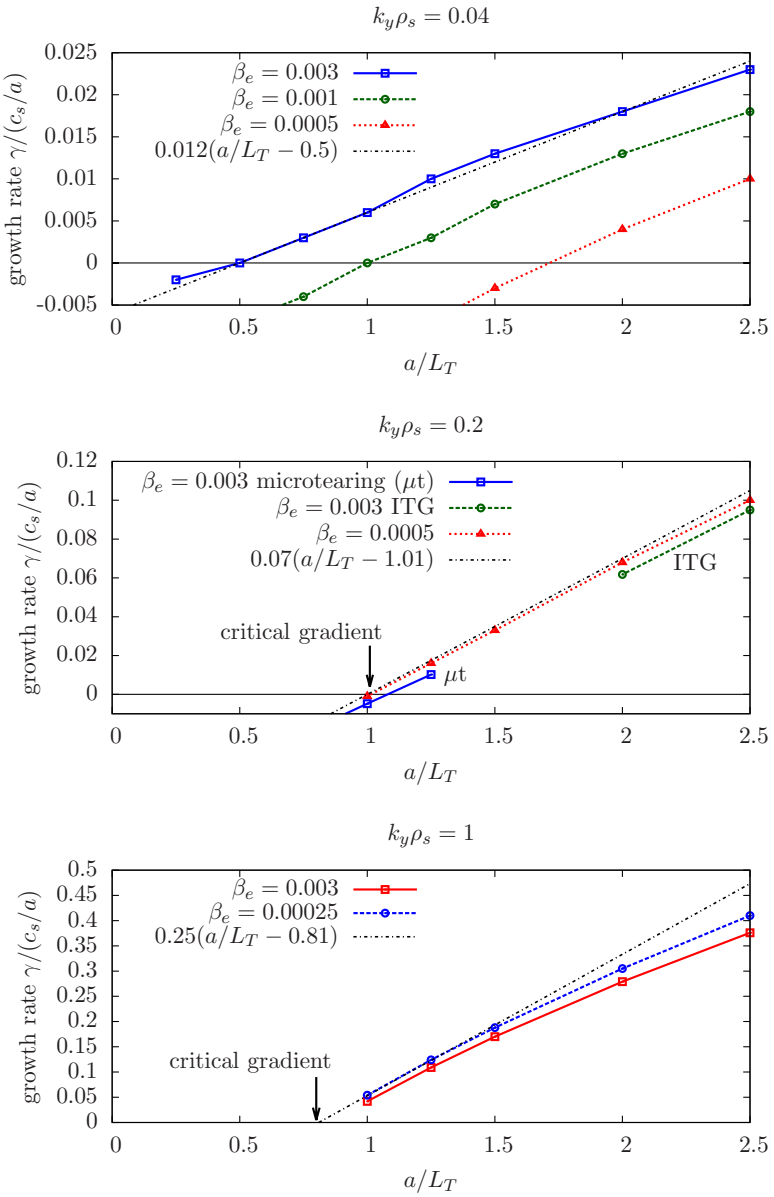

Figure 5.5.4.: Critical gradient studies for three values of $k_y\rho_i$ and three values of β_e. The gradients a/L_{Ti} and a/L_{Te} are changed simultaneously. At the lowest $k_y\rho_i = 0.04$ microtearing modes are found with $(a/L_T)_{\text{crit}} = 0.5$, at the nominal value for β_e, the threshold increases with decreasing β_e, thus a critical β_e threshold can be found for constant gradient. At intermediate $k_y\rho_i = 0.2$, $\beta_e = 0.003$ the critical gradient is around unity, and microtearing modes set in first. Higher β_e leads to a stronger presence of microtearing modes in this interesting regime. At $k_y\rho_i = 1$ ITG modes dominate with a critical gradient of 0.8.

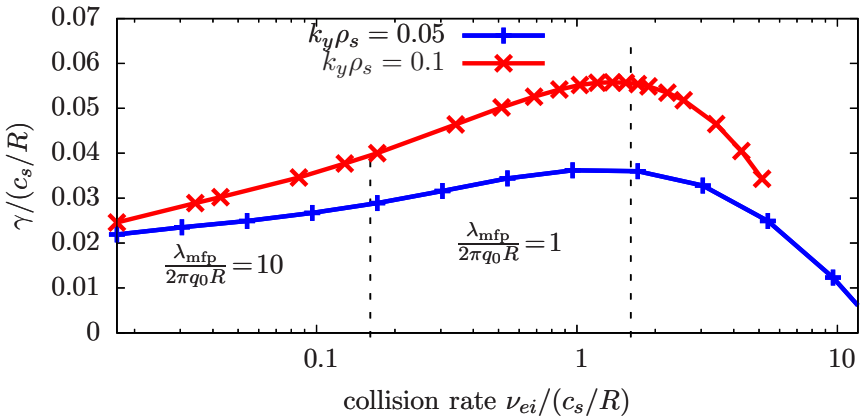

Figure 5.5.5.: The dependence of the microtearing growth rate on the collision frequency is moderate. A maximum growth rate is reached at intermediate collision frequencies , where $\nu_{ei}/|\omega| \sim 1 - 10$, consistent with early slab-geometry calculations [92, 93] and gyrokinetic simulations [77, 83]. In ITER baseline outer core plasmas, the collisionality is still large enough for a microtearing instability, even if other plasma parameters like a/L_{Te} are kept constant.

5.5.1. Role of collisions

Including collisions is essential for studying microtearing modes, since the associated resistivity facilitates magnetic reconnection.[8] Moreover, one of the tearing mode drive mechanisms, the time derivative of the thermal force, requires finite collisionality. It is responsible for the energy transfer from the background temperature profile to the mode. In the weakly collisional regime (very low values of ν_{ei}), where the thermal force essentially vanishes, alternative microtearing drive mechanisms are expected to be too weak to overcome the stabilizing terms.[105, 96, 106] On the other hand, in the opposite limit of strong collisionality, the microtearing mode is also stabilized. Here the intuitive picture is that collisional decorrelation strongly inhibits electron motion along field lines, such that a current layer cannot be established. Early theoretical work showed that experimental conditions, which are typically between the collisionless and (semi-)collisional limit, often can not be treated in a purely analytic fashion, even in slab geometry.[92, 93] We note in passing that one important ingredient in these calculations is an appropriate energy dependence of the collision frequency ν_{ei}.

Further progress was achieved when Applegate and co-workers performed linear gyrokinetic simulations of microtearing modes in a systematic fashion.[77] As they also showed a few years ago, the energy dependence of ν_{ei} actually becomes less important when going from slab to toroidal geometry, and the qualitative behavior of

[8] Collisionless reconnection is possible as well (see e.g. [103, 104]), but does not play a major role in the context of microtearing modes, since the maximum growth rate is found in the intermediate collisionality regime.

the growth rate, peaking in the intermediate collisionality regime relevant to experiments is preserved. The latter finding is confirmed via GENE simulations presented in Fig. 5.5.5. Here, one observes that the growth rate changes only moderately over several orders of magnitude in ν_{ei}. A maximum is found around collision frequencies at which the mean-free-path λ_{mfp} approximately equals the connection length $2\pi qR$, and it is more pronounced for larger mode numbers. Collisionality scales as $\nu_{ei} \sim nT^{-3/2}$ and is thus smaller in hotter plasmas. Our standard-tokamak parameter set (compare Sec. 5.7) is, however, still microtearing unstable when the collision frequency obtained for the ITER baseline scenario at $\rho_{\mathrm{tor}} \sim 0.7 - 0.8$ is inserted, even if other plasma parameters like the temperature gradients are kept constant. Thus, the present work is also relevant to future tokamak devices.

5.6. Microtearing mode current layers

We now turn to gyrokinetic investigations of a fundamental aspect of the physics behind the microtearing instability, which is the (temperature gradient driven) creation of a parallel current at a resonant flux surface, $q = m/n$. Interest arises, in particular, in the width of this current layer mainly for two reasons: (1) the comparison with analytic predictions yields insights into the underlying physics, and (2) the actual theoretical/numerical treatment can be validated. For example, the assumption of unmagnetized (adiabatic) ions only holds for $\Delta_x \ll \rho_i$, and the validity of this criterion can be tested. Resolving the current layer in gyrokinetic simulations generally requires very fine radial resolution (much more than what is needed for growth rate convergence). Thus, the simulations are performed in flux-tube geometry with a rational surface in the radial domain center. For illustration, a typical mode structure of the electron parallel current in the x-z plane is shown in Fig. 5.6.2. One obvious difference with respect to existing theories is the peculiar parallel structure of $j_{1\parallel e}$, which is linked to the strong ballooning of $\tilde{A}_{1\parallel}$ shown in Fig. 5.6.1.

In the following, we will present linear gyrokinetic simulations with GENE in order to shed light on the impact of a wide range of plasma parameters on the microtearing current layer. To compare with the intuitive picture given in Sec. 5.2, Eq. (5.2.6) is evaluated at the distance $x = \Delta_J$, expressing $k_\parallel$ by means of Eq. (5.2.1). The resulting expression

$$\frac{\Delta_J}{\rho_i} = \frac{q}{\hat{s}} \frac{\omega/(c_s/R)}{k_y \rho_i} \sqrt{\frac{m_e}{m_i}} \tag{5.6.1}$$

characterizes the analytic prediction of the current layer width. The numerical eigenmodes computed with GENE are assessed by measuring the full width at half maximum of $j_{1\parallel e}(z = -\pi, x)$ at the torus inboard side. This position is chosen because we generally observe a widening at the outboard side. This structure actually corresponds to finite $k_\parallel$ at $x = 0$ and already gives some hint that the analytic model

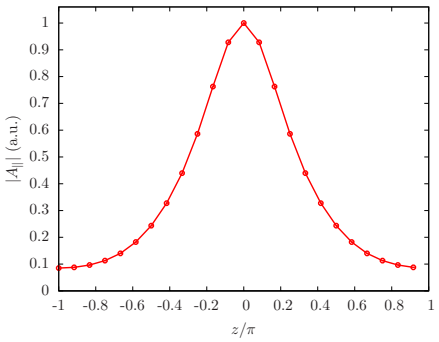

Figure 5.6.1.: Typical parallel structure of $A_\parallel$ developed by a microtearing mode. A strong $k_\parallel = 0$ (resonant) component exists, but also non-vanishing $k_\parallel$ contributions are obvious.

might be too simple. The particular structure of this widened mode generally depends on the plasma parameters, but the narrow layer at the inboard side appears to be universal. In these simulations, basically all the plasma parameters entering Eq. (5.6.1) have been varied. The frequency is actually not an input parameter, of course, but has been varied through the dependence on the electron temperature gradient $\omega \sim a/L_{Te}$, which is, in fact, approximately linear. Also an increase of ω with the density gradient a/L_n is observed, in general agreement with the analytic slab result Eq. (5.2.8), reflecting the the drift-wave character of microtearing modes.

The simulation data suggest that some basic physics is indeed captured correctly by the intuitive model: The overall trends depicted in Fig. 5.6.3 are generally reproduced. To give some examples, an increase in q, as well a decrease in ω or $\hat{s}$ widens the current layer, as expected. Quantitative agreement is only obtained in the sense that current layers tend to be as thin as $(0.1 - 0.5)\,\rho_i$, while the exact value can not be predicted by Eq. (5.6.1). We want to point out that the derivation of Eq. (5.6.1) does not consider collisional broadening of the current layer. For collisional plasmas ($\nu_{ei} \gg \omega$) the modification $\Delta_{J,\nu} = \Delta_J\sqrt{\nu_{ei}/\omega}$ has been estimated by Gladd and co-workers in Ref. [93]. Simulations varying collisionality within $0.1 \lesssim \nu_{ei}/\omega \lesssim 6$ (magenta squares in Fig. 5.6.3) show indeed broader current layers for larger collisionality. Note that ν_{ei} influences ω and thus enters Eq. (5.6.1) indirectly. The remaining runs fix the collision frequency in the intermediate collisionality regime $\nu_{ei} = 0.02 v_{te}/R$ where $\nu_{ei} \sim \omega$. Moreover, it is noteworthy that Eq. (5.6.1) predicts too small values of Δ_J for AUG geometry with rather high shear $\hat{s} = 1.7$ and deuterium ions for which a $0.02 < k_y\rho_s < 0.12$ scan is shown in Fig. 5.6.3. Note that due to $\omega \propto k_y$ for drift waves, a constant current layer width is predicted from Eq. (5.6.1) when k_y is varied. In Fig. 5.6.3(b) we use a Gladd-type estimate $\Delta_J\sqrt{\nu_{ei}/2\omega}$ (adding a factor $1/\sqrt{2}$). This improved model indeed exhibits enhanced agreement with the gyrokinetic data points obtained by the variation of ν_{ei} and k_y (both changing the ratio ν_{ei}/ω).

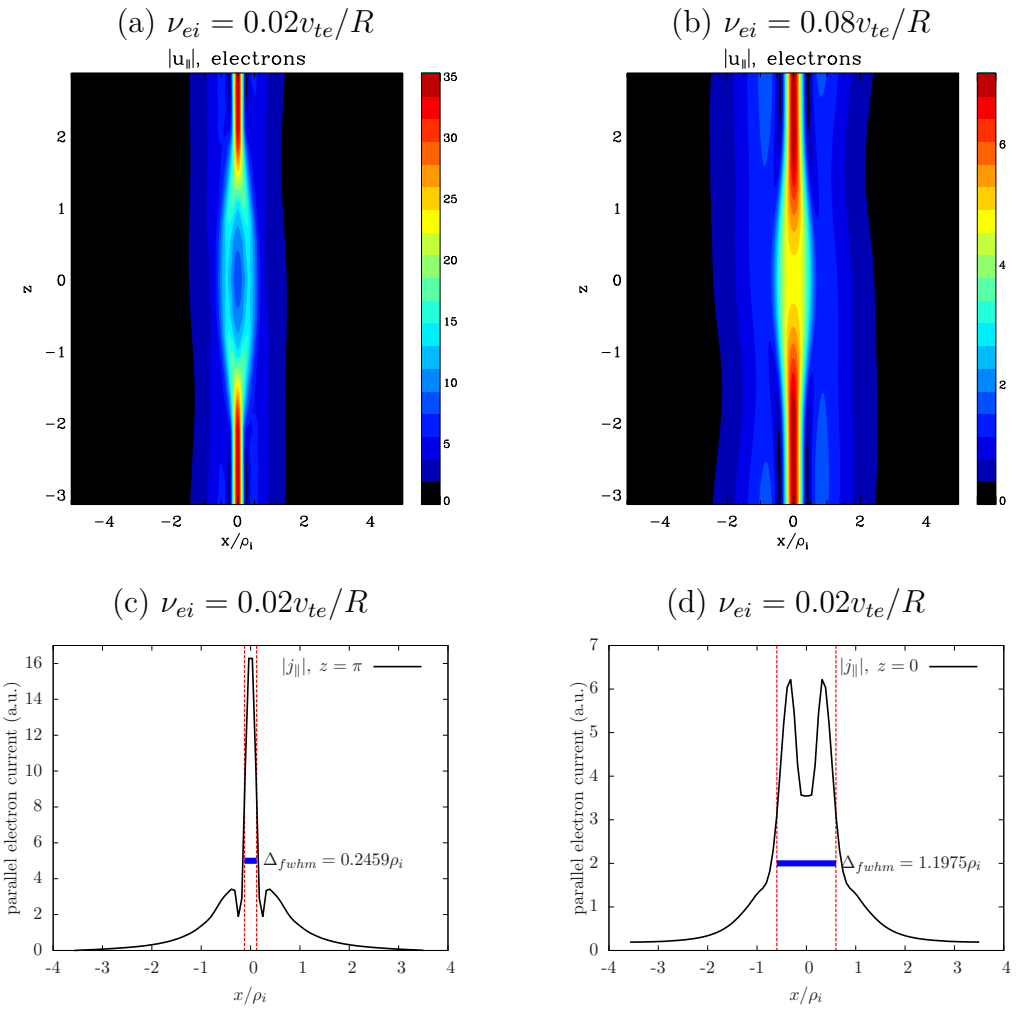

Figure 5.6.2.: Typical structure of a current layer of a microtearing mode in the $x - z$ plane and taken at the torus inboard ($z = \pi$) and outboard ($z = 0$) side. While (a),(c),(d) use $\nu_{ei} = 0.02 v_{te}/R$, the nominal value, (b) has higher collisionality $\nu_{ei} = 0.08 v_{te}/R$ and a wider current layer. Lack of radial resolution will smear out the fine structure at $z = 0$ and lead to the conclusion of a wider layer.

We have also investigated the impact of $\tilde{\phi}_1$ on the standard-tokamak microtearing mode, motivated by the diverse effects mentioned in Sec. 5.2 and gyrokinetic findings for the MAST and NSTX spherical tokamak. In MAST, zeroing out $\tilde{\phi}_1$ is found to be stabilizing [77], suggesting that $\tilde{\phi}_1$ actively takes part in the instability mechanism, in accordance to slab theory [93]. In NSTX, on the other hand, a destabilizing effect is observed when $\tilde{\phi}_1$ is weakened, which is consistent with Z_{eff} scalings reported in Refs. [82, 83]. Some standard tokamak GENE results are shown in Fig. 5.6.3: The data points marked by red diamonds are obtained zeroing out $\tilde{\phi}$ for a q scan in circular geometry. The modification of the growth rate or the current layer width is rather small. Measuring the mode growth, we find the trend that including $\tilde{\phi}_1$ is destabilizing for $q \lesssim 3$ and stabilizing for $q \gtrsim 3$. This is clear evidence for the existence of different flavors of the microtearing mode, an interesting aspect which remains to be better understood.

5.7. Turbulent transport due to microtearing modes

Table 5.7.1.: Plasma parameters for $\rho_{\text{tor}} = 0.5, 0.65, 0.8$ of ASDEX Upgrade shot 26459 compared with the circular model used for the turbulence simulations.

	Circular	AUG 0.5	AUG 0.65	AUG 0.8
x/a	0.40	0.50	0.65	0.80
a/R	0.37	0.37	0.37	0.37
a/L_{Te}	0.9-2.2	2.855	2.686	1.627
a/L_{Ti}	0.000	2.088	2.343	2.077
a/L_n	0.370	0.341	0.365	0.303
T_i/T_e	1.000	1.113	1.218	1.209
$\nu_{ei}/(c_s/a)$	2.310	0.405	0.873	1.542
$\beta[\%]$	0.600	0.586	0.363	0.251
q	3.000	1.811	2.449	3.703
$\hat{s}$	1.000	0.794	1.583	2.478
m_i/m_p	1	2	2	2

Finally we turn to the simulation results on nonlinear gyrokinetic microtearing turbulence for standard tokamak plasmas that have also been reported in Ref. [9]. The nominal parameters for the nonlinear simulations are summarized in Tab. 5.7.1 (normalized to the minor radius and labeled as "Circular"). For comparison, the values for AUG discharge 26459 are shown. The value of q and ν_{ei} fit the outer core regime, while the other parameters are close to those at the $\rho_{\text{tor}} = 0.5$ surface. It is worth mentioning that increasing q has been shown to increase the microtearing growth rate in this regime up to values of $q \sim 3$, above which increasing q (and keeping all other parameters constant) is slightly stabilizing (see Fig. 5.5.3). The

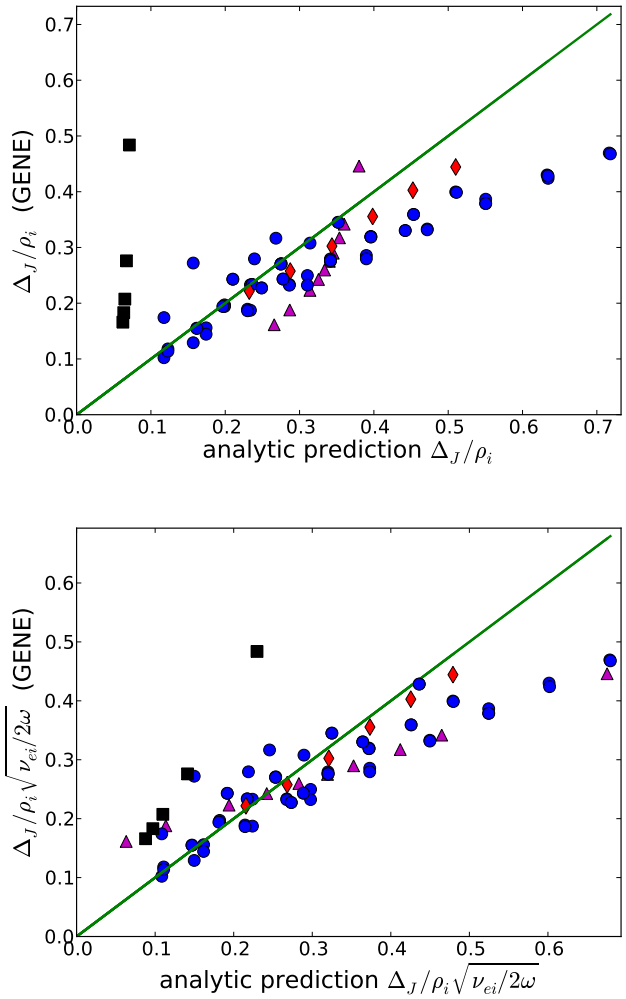

Figure 5.6.3.: Comparison of analytic predictions for the current layer width to gyrokinetic simulation results. (a) uses Eq. (5.6.1) for Δ_J, while (b) considers a collisional correction as described in the text. Blue dots vary $q, \hat{s}, \omega$ and m_e/m_i, magenta triangles vary collisionality (and thus ω), red diamonds vary q with $\tilde{\phi} = 0$, and black squares vary k_y in AUG geometry. The full width at half maximum of $j_{1\|e}$, taken at the torus inboard side, is smaller than ρ_i. In the intermediate collisionality regime considered here, zeroing out $\tilde{\phi}$ has no significant influence.

ion temperature gradient has been set to zero for the nonlinear simulations to avoid multi-mode drive and to make the already demanding computations more tractable. It has been verified that the ion temperature gradient does not modify the microtearing branch, but it can be seen in Fig. 5.7.1 that the ITG branch disappeared. As a second simplification, an analytic model for the magnetic equilibrium, assuming concentric circular flux surfaces, is taken.[55] This change also does not affect the microtearing mode substantially. We may thus expect that many qualitative and semi-quantitative features found in the nonlinear simulations will carry over to more realistic cases.

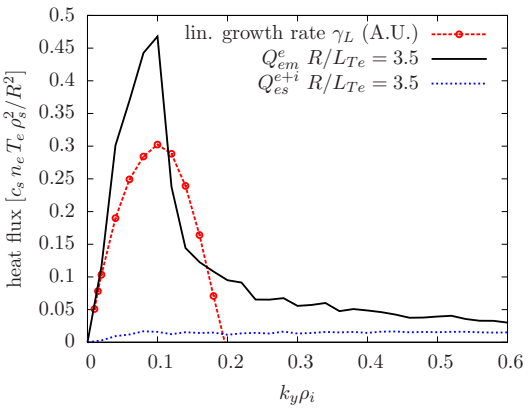

Figure 5.7.1.: Typical transport spectrum for pure microtearing turbulence in standard tokamaks. The electron heat flux is predominantly of magnetic nature and peaks at very low values of k_y. Unlike in ITG turbulence, the peaks of the heat flux and linear growth rate are found to almost coincide, with only a minimal nonlinear down-shift.

Convergence studies indicate that (for these physical parameters) a nominal resolution of $384 \times 64 \times 24 \times 32 \times 16$ grid points in $x \times y \times z \times v_\parallel \times \mu$ phase space is required. The domain width in the perpendicular plane is set by $l_x = 150\rho_i$ and $l_y = 300\rho_i$, resulting in a radial grid spacing of $\Delta_x \sim 0.5\rho_i$.[9] The velocity space domain is $l_{v\parallel} = l_{v\perp} = 3v_{Ta}$ for species a. It has been verified that the linear growth rate is reasonably converged for all involved mode numbers.

5.7.1. General features of microtearing turbulence

A typical resulting transport spectrum obtained by means of GENE is displayed in Fig. 5.7.1. While the particle flux is very low, one observes that the heat flux is dominated by the magnetic component Q_e^{em} in the electron channel, generally providing more than 80% of the total transport.

[9] This grid spacing is slightly larger than the current layers found on the high-field side ($z = \pi$), but smaller than the current layer on the low-field side. Nonlinear runs show no severe change when doubling the grid spacing.

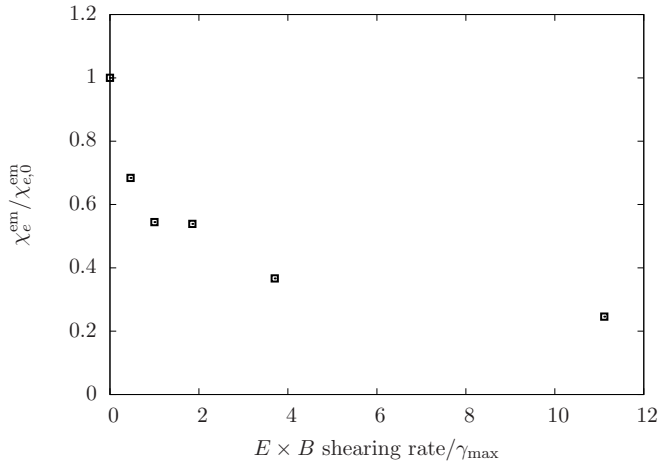

Figure 5.7.2.: Impact of an equilibrium $E \times B$ shear flow on microtearing turbulence measured in electron heat diffusivity. The saturated electron heat flux is reduced, but even with $E \times B$ shearing rates exceeding the linear growth rate by a factor of 10, about 20% of the initial transport level remains.

An interesting aspect of microtearing turbulence is the impact of an equilibrium $E \times B$ shear flow. A series of GENE simulations addressing this question is shown in Fig. 5.7.2. Here, the response of the saturated turbulent state (for the nominal parameters) to a number of different external $E \times B$ shearing rates (see Ref. [107]) is provided. Somewhat surprisingly, microtearing turbulence, in the parameter regime studied here, seems to be only mildly susceptible to $E \times B$ shearing. This finding is in line with the observed weak dependence on nonlocal effects discussed above, and indicates that microtearing modes in standard tokamaks tend to be rather robust with respect to equilibrium shear flows.

5.7.2. Magnetic fluctuation amplitude

Given this result, let us now return to simulations of microtearing turbulence without flow shear. In a first step, we will focus on the magnetic fluctuation levels: what sets them and how do they depend on various plasma parameters? According to a model developed by Drake and co-workers in Ref. [81], one should expect a relative fluctuation amplitude of the magnetic field of

$$\tilde{B}_{1x}/B_0 \sim \rho_e/L_{Te} \tag{5.7.1}$$

where ρ_e is the thermal electron gyroradius. This estimate was obtained in the collisional limit within the framework of a drift-kinetic theory, neglecting parallel dynamics. The results from about a dozen GENE simulations for different values of R/L_{T_e} and different numerical resolutions are displayed in Fig. 5.7.3. The Drake expectation is shown for comparison as a dashed line. Interestingly, it describes the gyrokinetic simulation results quite well, indicating that the general physical

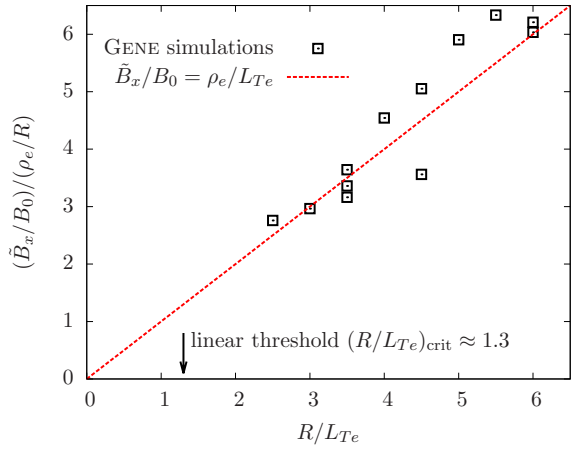

Figure 5.7.3.: Microtearing modes saturate at a fluctuation level of $\tilde{B}_{1x}/B_0 \sim \rho_e/L_{T_e}$. Using the nominal resolution and others, each of which represents a reduction by 1/3 or 1/2 in one of the phase space directions, leads to only moderate scatter.

reasoning underlying it might also apply (possibly in some refined form) to the three-dimensional gyrokinetic system. We will return to this important point later. In this context, we would like to note, however, that the magnetic fluctuation amplitude is sensitive to plasma parameters such as β_e or ν_{ei}, as well as various geometrical quantities. As an example, a β_e scan is shown in Fig. 5.7.4(a), for dependencies on ν_{ei} we refer to the linear results of Fig.(5.5.5) and also Ref. [82]. Given that the linear microtearing instability exists only if β_e exceeds a certain threshold ($\sim 10^{-3}$ in the present case), it comes as no surprise that the magnetic fluctuation level increases with increasing β_e. Thus, the Drake formula should only be viewed as a rough estimate which captures some of the main effects but ignores such additional parameter dependencies.

5.7.3. The role of magnetic stochasticity

In a second step, we would now like to investigate in which way the magnetic fluctuation level is linked to the associated transport level. As mentioned before, the thermal transport associated with microtearing turbulence is dominated by the magnetic contribution in the electron channel. The corresponding electron heat diffusivity $\chi_e^{\rm em}$ is given in terms of the electron heat flux $Q_e^{\rm em}$ via

$$Q_e^{\rm em} = -\, n_e \chi_e^{\rm em} \nabla T_e \,. \tag{5.7.2}$$

This diffusivity, as obtained from a set of about 15 GENE simulations (varying the electron temperature gradient and β_e), is found to be well described by a Rechester-Rosenbluth ansatz

$$\chi_e^{\rm em} \sim v_{te} L_C (\tilde{B}_{1x}/B_0)^2 \,, \tag{5.7.3}$$

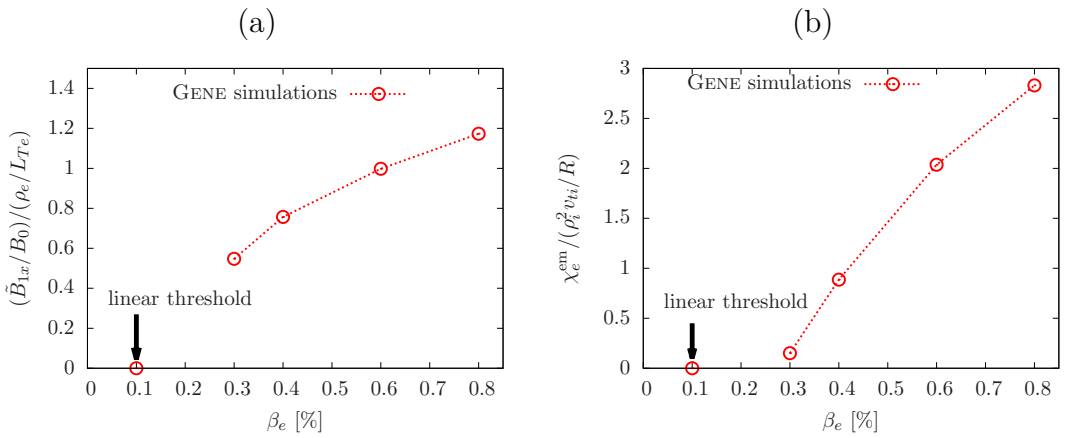

Figure 5.7.4.: Influence of the plasma parameter β_e on (a) the magnetic field fluctuation amplitude and (b) the electron magnetic heat diffusivity. The electron temperature gradient is $R/L_{T_e} = 4.5$ in all simulations.

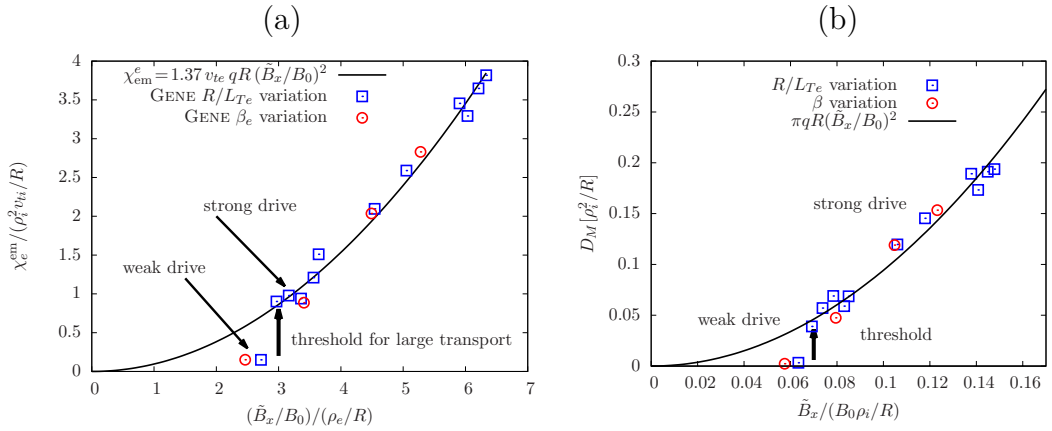

Figure 5.7.5.: (a) Electron heat diffusivity as a function of the relative fluctuation level of the magnetic field. The GENE results are described well by the Rechester-Rosenbluth model $\chi_e^{\mathrm{em}} = \eta\, v_{te}\, qR\,(\tilde{B}_{1x}/B_0)^2$ with $\eta = 1.37$. (b) Magnetic diffusivity computed from GENE data with Eq. (5.7.4). The quasilinear result $D_M = \pi qR(\tilde{B}_{1x}/B_0)^2$ is well applicable in the present regime. We find two outliers at small amplitude, where stochasticity is not established and thus also the Rechester-Rosenbluth model breaks down, as explained in the text.

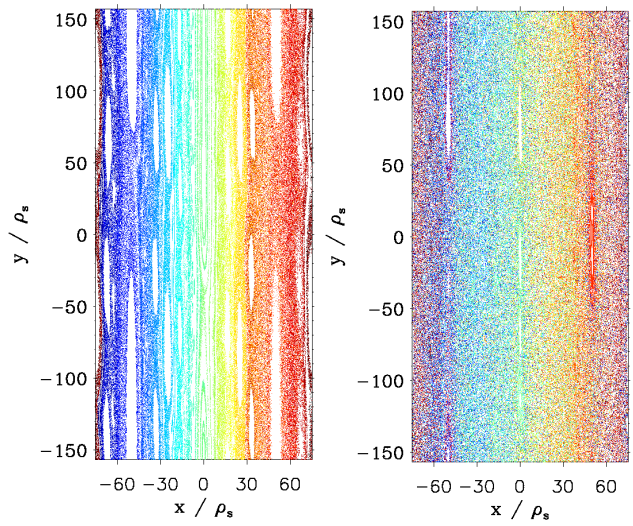

Figure 5.7.6.: Poincaré plots of magnetic field lines intersecting the perpendicular plane on the outboard side for weak drive ($a/L_{Te} = 0.925$, left-hand plot) and stronger drive ($a/L_{Te} = 1.3$, right-hand plot). The observed features are discussed in the text.

as can be seen in Fig. 5.7.5(a). Obviously, the onset of strong transport is subject to a nonlinear up-shift that also is observed in the beta scaling shown in Fig. 5.7.4(b). The reason for this behavior is that a certain threshold in the linear drive strength has to be overcome to create magnetic fluctuations large enough to fulfill the Chirikov criterion for island overlap.[108] Only then, a fully stochastic field (an assumption underlying the Rechester-Rosenbluth ansatz) can be established. In two weakly driven cases, one at $a/L_{Te} = 0.925$ and one at $\beta_e = 0.003$, the transport is significantly overestimated by Eq. (5.7.3). As can be observed in the Poincaré plots of Fig. 5.7.6 in these cases the microtearing modes only create small, non-overlapping magnetic islands, preventing a full stochastization. In this context, we would like to point out a certain analogy with the well-known Dimits-shift [109] that describes the damping of weakly driven ITG turbulence due to zonal flows. Of course, the underlying physics is completely different in these two scenarios.

The degree of stochasticity may also be quantified by using a field-line tracer to measure the field line diffusivity

$$D_M = \lim_{l\to\infty} \frac{\langle (r_i(l) - r_i(0))^2 \rangle}{l} \tag{5.7.4}$$

in the simulation data. Here, $l = 2\pi q R n_{\mathrm{pol}}$ measures the distance along the field line i. For the tracing, the magnetic field configuration is held fixed, taking snapshots of the turbulent time-trace of $\tilde{B}_1$. We get sufficient statistics when following a field line about $n_{\mathrm{pol}} = 1000$ poloidal turns and averaging over about 100 field lines. Field-line following particles, of course, experience time-dependent fluctuations. Meaningful data is thus obtained by averaging over a large number of D_M

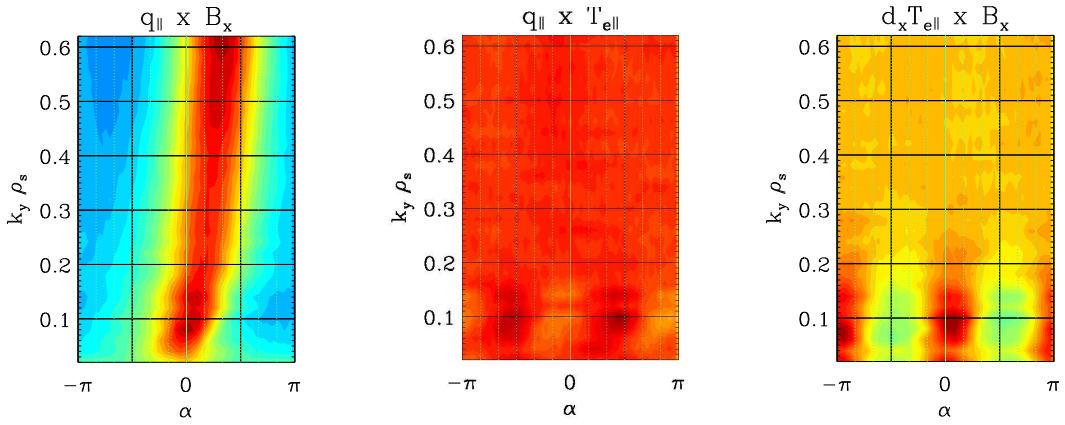

Figure 5.7.7.: Cross phase analyses in the strongly driven microtearing turbulence. In the region of transport peak at $k_y\rho_i \sim 0.2$, $\tilde{q}_{1\|}$ and $\tilde{B}_{1x}$ are in phase (left) while $\tilde{q}_{1\|}$ and $\tilde{T}_{1\|}$ have random phase (middle). In conclusion, $\mathcal{T}_3$ dominates over $\mathcal{T}_1$, and Eq. (5.7.3) is applicable. On the right panel the cross phase analysis of $\tilde{B}_x$ with $\tilde{T}_{e\|}$ is shown

snapshots. As expected, Fig. 5.7.5(b) shows that the weakly driven cases exhibit a significantly lower value of D_M compared to more strongly driven microtearing turbulence. For the latter cases, we find the magnetic diffusivity to be well characterized by the quasilinear result $D_M = L_C(\tilde{B}_{1x}/B_0)^2$, with the auto-correlation length taken as $L_C = \pi qR = \pi\Delta k_\|^{-1}$ and the parallel spectral width $\Delta k_\|$.[110] This correlation length can be modified by collisional decorrelation when the electron mean free path $\lambda_{\mathrm{mfp}} = v_{te}/\nu_{ei}$ becomes small. Following Ref. [111], we introduce an effective length $L_{\mathrm{eff}} = \pi((qR)^{-1} + \lambda_{\mathrm{mfp}}^{-1}) = 0.94L_C$, in this case. The presented results for stochastic heat transport are in good agreement with the heat flux expression $Q_e^{\mathrm{st}} = \sqrt{2/\pi}\, f_p\, v_{te} D_M\; n\partial T/\partial r$ of Ref. [60]. This is valid for small particle flux and refines slab geometry results of Ref. [111] by taking into account the passing particle fraction $f_p \approx 1 - \sqrt{r/R}$. The corresponding heat diffusivity (including the small collisional correction) is given as $\chi_e^{\mathrm{st}} = \sqrt{2/\pi}\, f_p\, v_{te}\, L_{\mathrm{eff}}/L_C\, D_M$, which yields $\eta = 1.45$, about 5% above the fit on the simulated data in Fig. 5.7.5.

One can also take another point of view, writing the radial electron heat flux as

$$Q_e^{\mathrm{em}} = \langle \tilde{q}_{e\|}\tilde{B}_{1x}\rangle/B_0 \tag{5.7.5}$$

with

$$\tilde{q}_{e\|} = -n_{e0}\chi_{e\|}\left(\frac{\mathrm{d}\tilde{T}_{1e\|}}{\mathrm{d}z} + \frac{\tilde{B}_{1x}}{B_0}\frac{\mathrm{d}\tilde{T}_{1e\|}}{\mathrm{d}x} + \frac{\tilde{B}_{1x}}{B_0}\frac{\mathrm{d}T_{0e}}{\mathrm{d}x}\right). \tag{5.7.6}$$

The three terms on the right-hand side denote the components of $\nabla_\| T$ along the perturbed magnetic field lines. We refer to them as $\mathcal{T}_1$, $\mathcal{T}_2$, and $\mathcal{T}_3$ in the following. The parallel conductivity has been computed for slab geometry as $\chi_{e\|} = 9/(5\sqrt{\pi})\,(v_{te}/k_\|)$

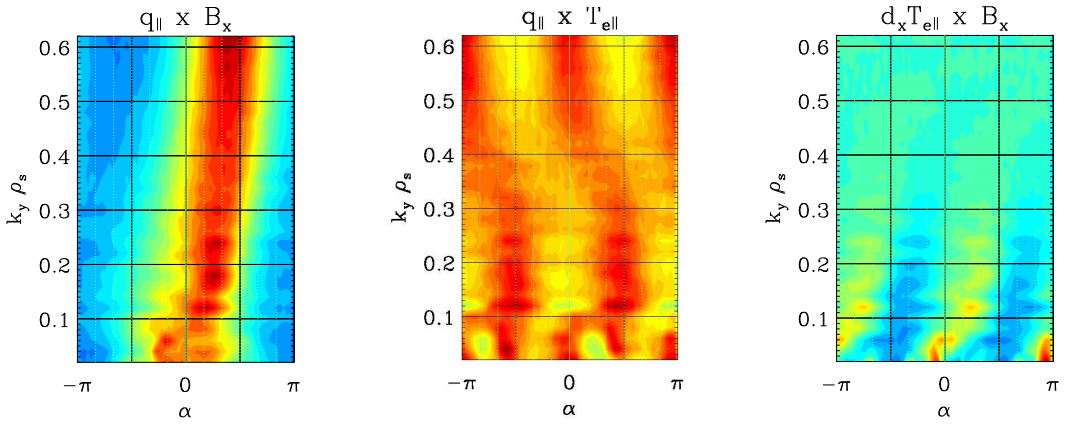

Figure 5.7.8.: In weakly driven cases, the cross phase corresponding to $\mathcal{T}_3$ (left) is less pronounced at the transport peak $k_y\rho_i \lesssim 0.1$. Also, $\tilde{q}_{e\|}$ is partially in phase with $\tilde{T}_{1e\|}$, as seen in the middle panel. One can thus expect modifications to the Rechester-Rosenbluth model, Eq. (5.7.3). On the right panel the cross phase analysis of $\tilde{B}_{1x}$ with $\tilde{T}_{1e\|}$ is shown

in the adiabatic limit.[112] In our toroidal model with quasiperiodic boundary conditions along the field line, technically there is no quantity like $k_\|$, but we may estimate $k_\| \sim 1/(qR)$. Doing this, one obtains Eq. (5.7.3), provided $\mathcal{T}_3$ dominates.

Indeed, the dominant role of $\mathcal{T}_3$ can be confirmed by observing cross phase relations between the fluctuating quantities shown in Figs. 5.7.7 and 5.7.8. In typical strong microtearing turbulence cases, one concludes $\mathcal{T}_3 \gg \mathcal{T}_1$ from the fact that $\tilde{q}_\|$ and $\tilde{T}_{1\|}$ have random phases and a tendency to anticorrelate at a phase of $\pi/2$, while $\tilde{q}_\|$ and $\tilde{B}_{1x}$ are correlated around the transport peak in k_y. In weakly turbulent cases, the correlation of $\tilde{q}_\|$ and $\tilde{B}_{1x}$ is less pronounced, in particular, at the transport peak $k_y \sim 0.06$, and at the same time, $\tilde{q}_\|$ and $\tilde{T}_{1\|}$ are partially correlated. One can conclude that in these weakly driven cases, Eq. (5.7.3) is not applicable and, as a result, the diffusivity is over-predicted. The second term, $\mathcal{T}_2$, may also contribute, in principle. We conclude from the rightmost panels of Figs. 5.7.7 and 5.7.8 that $\partial_x\tilde{T}_{1\|}$ and $\tilde{B}_x$ are in phase (between $-\pi/8$ and $\pi/4$) in both cases. As stated before, in the strongly driven case, $\tilde{q}_\|$ and $\tilde{B}_{1x}$ are in phase and thus also $\tilde{q}_\|$ and $\left(\partial_x\tilde{T}_{1\|}\right)\tilde{B}_{1x}$ are correlated. In the weakly driven case, a similar conclusion can be drawn. The cross phases $\alpha(\tilde{q}_\| \times \tilde{B}_{1x})$ are similar to $\alpha(\partial_x\tilde{T}_{1\|} \times \tilde{B}_{1x})$ in the important low-ky regime. Thus, the main difference between those two cases lies in the importance of $\mathcal{T}_3$ for the heat diffusivity.

In the present context, we would like to note that the application of diffusivity models may also be restricted by completely different physics. Del Castillo-Negrete [113] has shown that the electron heat flux along perturbed magnetic field lines can, in general, be non-diffusive. Nonlocal effects (in the parallel direction) actually prohibit the description of the radial heat flux in terms of a simple diffusivity. In the present gyrokinetic simulations, no such non-diffusive behavior has been found,

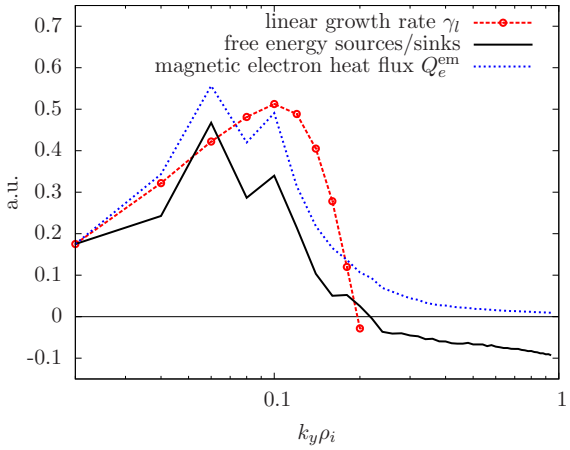

Figure 5.7.9.: Time-averaged (magnetic) electron heat flux spectrum in k_y space for $R/L_{T_e} = 3.5$. The linear growth rate spectrum is shown for comparison. Net free energy dissipation is found at $k_y\rho_i > 0.2$.

however.

5.7.4. Aspects of the nonlinear saturation mechanism

In a third and final step, we will now address the question which kind of physics actually sets the saturation amplitudes in the quasi-steady turbulent state. In other words, which are the mechanisms behind the observed relationship $\tilde{B}_{1x}/B_0 \sim \rho_e/L_{Te}$? We get some first hints by inspecting the time-averaged electron heat flux spectrum for one of the nonlinear runs. As is shown in Fig. 5.7.9, the linear growth rate spectrum drops to zero at $k_y\rho_i \sim 0.2$ while a substantial fraction of the transport is driven at much higher wave numbers. This is in noticeable contrast to ITG or trapped electron mode driven microturbulence (see, e.g., Refs. [114, 115]) and demonstrates that microtearing modes are able to transfer free energy to small perpendicular scales quite efficiently. We also show a spectrum of free-energy sources or sinks [116] to demonstrate that (only) the small scales act as a net sink.

To understand this aspect better, it is helpful to recall that individual microtearing modes have a peculiar mode structure. In particular, the electrostatic potential ϕ and the parallel electron current $j_{1\|e}$ are highly anisotropic in the perpendicular plane: Fine radial scales are present at rather long wavelengths in the y direction. In Fourier space, the same feature is expressed by the fact that at a single $k_y\rho_i \sim 0.1$, a microtearing mode involves a large number of k_x modes which are coupled via the parallel boundary condition.[117] The $\mathbf{E} \times \mathbf{B}$ nonlinearity couples a Fourier mode $\mathbf{k} = (k_x, k_y)$ with two modes $\mathbf{k}'$ and $\mathbf{k}''$, provided the relation $\mathbf{k} = \mathbf{k}' + \mathbf{k}''$ holds. Once the mode amplitude is large enough to allow for nonlinear dynamics, each mode is able to interact with other modes *and* itself, quickly spreading free energy in wave number space and exciting high-k modes which are linearly stable.

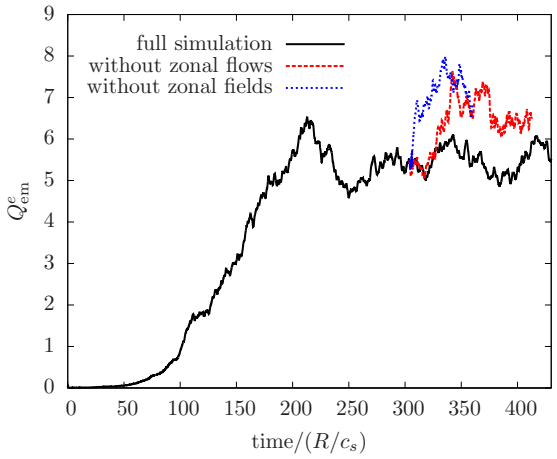

Figure 5.7.10.: Time traces of the magnetic heat flux in microtearing turbulence. A case with self-generated zonal flows is modified by (i) zeroing out zonal flows and (ii) zeroing out zonal fields. The response is fast, but the average heat flux only increases by about 20%.

Performing a secondary instability analysis of the self-coupling process, one finds that modes at twice the value of k_y grow linearly with time at a rate of several v_{ti}/R times the square of the primary mode's (normalized) amplitude Φ_p. Thus, such transfer processes are comparable to the linear growth rates of about $0.1\,v_{ti}/R$ for $\Phi_p \sim 0.1$. The observed mode amplitudes are comparable to these values, supporting the notion that the nonlinear interactions tend to establish perpendicular small-scale isotropy in the system by enhancing high-k_y fluctuations – and damping high-k_x fluctuations.

Although the mode couplings just described also create zonal flows and fields,[118] the latter are not decisive in this context as shown in Fig. 5.7.10 by zeroing them out: this test changes the transport level by at most 20%. Instead, the key is the observed strong transfer of free energy to small perpendicular scales. It is evident that free energy pumped into the system via linear drive terms at some rate must be dissipated at the same rate to obtain a saturated turbulence state. Thus, we may assume a balance between the maximum linear growth rates $\gamma_l^{\max}$ and the nonlinear damping rates γ_{nl}, in the same spirit as, e.g., Refs. [81, 119, 120]. In the present case, one may want to model the latter by $\gamma_{nl} = \chi_e^{\rm em} k_{\rm diss}^2$ in terms of Eq. (5.7.3) and a typical perpendicular dissipation scale $k_{\rm diss} \gtrsim 0.2/\rho_i$ as long as field line stochasticity prevails. Using an expression like $\gamma_l^{\max} \propto (R/L_{T_e})^2\, v_{ti}/R$, the Drake estimate, $\tilde{B}_{1x}/B_0 \sim \rho_e/L_{Te}$, could be recovered. However, linear simulations rather suggest something close to an offset-linear dependence of $\gamma_l^{\max}$ on R/L_{Te}, where both the zero crossing and the slope depend on various plasma parameters (like β_e) in a nontrivial fashion. Thus, the relation found in Fig. 5.7.3 is not universal, and one should take this fact into account when trying to predict microtearing-induced transport.

5.7.5. Experimentally relevant thermal transport

Finally, we would like to address the question if the resulting transport levels are sufficiently large to be considered experimentally relevant. To assess this issue, we use the plasma parameters corresponding to the AUG discharge 26459. These include $R = 1.65$ m, $B_0 = 2.37$ T, $T_{0e} = 1.09$ keV, $n_{0e} = 7.94 \times 10^{19}$ m^{-3}, and $\rho^* = 0.003$. For an electron temperature gradient of $a/L_{Te} = 1.85$ ($R/L_{Te} = 5$) and the otherwise nominal parameters summarized in Tab. 5.7.1, we find a magnetic perturbation level of $\tilde{B}_{1x}/B_0 \sim 3.5{\cdot}10^{-4}$ and a corresponding electron heat diffusivity of $\chi_e^{\mathrm{em}} \sim 1.4$ m^2/s. These numbers suggest that microtearing turbulence must be considered an additional candidate for explaining the observed anomalous heat losses in present-day and future (standard) tokamaks.

5.8. Summary and conclusions

In summary, the work presented in this chapter—based on comprehensive gyrokinetic simulations—provides strong evidence for the existence of microtearing turbulence in standard tokamak devices. In particular, using realistic global MHD equilibria and experimentally measured temperature and density profiles, microtearing modes are observed at various mode rational surfaces in the outer core of AUG discharge 26459. A study of system size effects was performed by variation of the parameter ρ^* in a circular geometry model. The finite temperature gradient profile width, which is known to substantially weaken ITG modes was shown to be less effective for microtearing modes. The growth rate obtained in global simulations stays close to that in the local limit even for narrow temperature gradient profiles, strongly supporting a local treatment of the microtearing problem. In addition, the microtearing mode is found to be only weakly affected by background $E \times B$ shear flows. Therefore, in the remainder of this work, nonlocal and equilibrium shear flow effects have been neglected.

In terms of linear physics, several peculiar features of microtearing modes in standard tokamaks have been observed. Interestingly, their growth rate spectrum tends to peak at rather low binormal wavenumbers of $k_y\rho_s \sim 0.1$, which allows them to co-exist with ITG/TEM modes at larger wavenumbers. The most critical plasma parameters turn out to be β_e and a/L_{Te}, with the linear threshold of the latter typically below the respective value of a/L_{Ti} for ITG modes. In addition, collisions play an important role. Although gyrokinetic simulations exhibit stabilization when decreasing collision frequency, microtearing modes are still expected to appear in low-collisionality plasmas like those in ITER. Overall, the linear physics of microtearing modes remains to be better understood, as was exemplified by a study on the radial width of the current layer. While at the torus inboard side, the observed trends roughly coincide with the predictions of common analytical models, the latter do not account for the parallel mode structure.

In nonlinear simulations, one finds that the heat transport is dominated by the

magnetic component in the electron channel, which can be well described by means of a Rechester-Rosenbluth model. Examining nonlinear effects, one concludes that the saturation levels of the magnetic field fluctuations are set by a balance between large-scale drive and small-scale dissipation. Strong transport is found to set in as soon as a certain threshold in the fluctuation amplitude is overcome and the Chirikov criterion for island overlap is fulfilled, resulting in a nonlinear up-shift of the critical electron temperature gradient. An analogy to the well-known Dimits shift for ITG modes can be seen here, although the underlying physics is completely different.

Finally, we inserted the plasma parameters of an actual AUG discharge (shot 26459) into the scaling laws suggested by the simulation data, obtaining electron heat diffusivities of up to a few m^2/s. It should be noted that transport strongly depends on the precise value of the electron temperature gradient. Evaluating these results, the present work points towards a role of microtearing turbulence in standard tokamaks, including ITER.

6. Conclusions

In future tokamak devices, strong electron heating is expected due to the NBI, ICRH and ECRH heating systems as well as fusion alpha particles. To enable precise theoretical predictions for electron thermal transport, it is thus important to further evolve the overall picture. Besides electron-scale (high-wavenumber) turbulence, magnetic perturbations that create a stochastic field structure are a possible source of enhanced electron heat transport. The main goal of this work was to clarify whether magnetic field perturbations due to microtearing modes are relevant in realistic scenarios, focusing on standard tokamaks like the future experimental reactor ITER and the currently running experiment ASDEX Upgrade. Since analytical theory is forced to undertake severe simplifications, a numerical approach is needed to study this problem. A set of gyrokinetic simulations have been performed and analyzed, using the turbulence code GENE, which allows for radially global simulations including electromagnetic fluctuations and realistic geometry. The collision operator included in GENE has been further developed and tested in the course of this work.

Below, we summarize the main results of each chapter and discuss possibilities for future work.

6.1. Summary

Aspects of gyrokinetic theory

The gyrokinetic equations implemented in the GENE code have been presented and relevant aspects of their derivation have been given. Since previous analytical work on microtearing modes indicates an important role of collisions, we discussed in detail, how collision operators are included in the gyrokinetic framework. We developed a model operator that is self-adjoint and locally conserves particle number, momentum, and energy. While the electromagnetic part of the collision-free (Vlasov) equation that is implemented in GENE is well benchmarked, benchmarks of collisional simulations have previously been restricted to linear TEM cases. We thus derived the equations for neoclassical equilibrium computations, which provide an excellent test scenario for collisions. Importantly, the neoclassical drive term $\mathbf{v}_D \cdot \nabla F_{0a}$ has been included, which is often neglected in turbulence simulations. Furthermore, the (formally second-order) drift term $\mathbf{v}_D \cdot \nabla F_{1a}$ has been taken into account for nonlocal neoclassical computations. This term vanishes in the local limit, but it is believed to be relevant in steep gradient zones and in transport bar-

riers. The radial fluxes of particles, parallel momentum, and energy have been split into neoclassical and turbulent contributions to illustrate that these two problems are connected in the global case, but decouple in the local limit.

The GENE code

The GENE code solves the gyrokinetic equations on a fixed grid in the five-dimensional phase space. To that aim, a convenient normalization has been introduced and the methods of discretization, as well as Krook-type heat sources are described. The structure of the equations has been shown to allow for initial value computations, eigenvalue computations, as well as the use of an algebraic solver for the neoclassical equilibrium. Because they form the basis of our results, all three approaches have been briefly described. In the course of this work, the aforementioned self-adjoint form of the collision operator, as well as several features regarding neoclassical computations have been implemented.

Neoclassical transport

Setting up neoclassical computations with GENE allowed us to perform thorough tests of the implementation of the collision operator. Operating in the local limit, the presented benchmarks with the NEO code show that GENE is capable to correctly compute neoclassical fluxes with kinetic electrons. Overall, better agreement was found when an improved (self-adjoint) collisional model was used in GENE.

We performed radially global neoclassical computations that allow for the relaxation of the kinetic profiles and therefore exhibit a balance between sources and sinks in steady state. To exactly fulfill this energy balance in the simulations, a refined definition of the neoclassical heat flux has been employed, which accounts for the radial variation of the drift velocity. Comparisons with local simulations confirmed the existence of nonlocal neoclassical effects at large values of the system-size parameter ρ^*.

Finally, we have performed a benchmark of neoclassical transport between the global GENE code and the PIC code ORB5. Both codes are very different from a numerical point of view, but produce very similar physical results. This confirmed the correctness of the implementation of the global collision operator and showed that the GENE code is well suited for global neoclassical computations.

Microtearing turbulence

Finally, we addressed the question whether enhanced electron heat transport can be attributed to tearing mode turbulence. The physics involved is indeed quite different from the $\mathbf{E} \times \mathbf{B}$ advection processes that usually dominate ITG or TEM turbulence. The small-scale magnetic perturbations of tearing modes form magnetic islands at rational surfaces, which may overlap to produce a stochastic magnetic field structure. Due to the large parallel mobility of electrons, heat diffusion in such fields

can become substantial. While gyrokinetic heat transport predictions for spherical tokamaks have recently been published by other authors, the present work—based on comprehensive gyrokinetic simulations—provides strong evidence for the existence of microtearing mode turbulence in standard tokamak devices.

In particular, using realistic equilibria and experimentally measured temperature and density profiles, microtearing modes are observed at various mode rational surfaces in the outer core of AUG discharge 26459. A study of system size effects strongly supports local treatment, which allows for extensive parameter variations (including collisionality), leading to the conclusion that microtearing modes also appear in ITER plasmas. Interestingly, in standard tokamaks they are allowed to co-exist with ITG/TEM modes in the linear wavenumber spectrum. Overall, the linear physics of microtearing modes remains to be better understood, as was exemplified by a study on the radial width and parallel structure of the current layer, where common analytical models cannot always capture the observed trends.

In terms of nonlinear physics, the electron heat transport is dominated by the magnetic component, which can be described by a Rechester-Rosenbluth model and thus increases quadratically with the saturated value of the magnetic field fluctuation amplitude. The latter can be understood in view of a balance between a large-scale linear drive and nonlinear dissipation at smaller scales. Moreover, it was found that the Chirikov criterion for island overlap implies a threshold for the linear drive strength, resulting in an effective nonlinear up-shift of the critical electron-temperature gradient. An analogy to the well-known Dimits-shift for ITG modes can be seen here, although the underlying physics is completely different. Inserting the plasma parameters of an actual AUG discharge (shot 26459), one obtains electron heat diffusivities of up to a few m^2/s, depending mainly on the precise value of the electron temperature gradient. Consequently, the present work points towards a role of microtearing turbulence in standard tokamaks, including ITER.

6.2. Possibilities for future work

Further code development: Collisions

Collisions play an important role in gyrokinetics, since they provide the physically motivated sink of free energy. The current implementation of the Landau-Boltzmann collision operator in GENE accounts for finite Larmor radius effects in test-particle collisions, but neglects them in the field-particle operator. While this has not been important for the present studies, future investigations must explore their impact, in particular when high wavenumbers $k_\perp \rho_i \gg 1$ are involved. Moreover, improving on the symmetry properties of the discretization scheme is desirable, since these symmetries are required to analytically prove free energy dissipation and Boltzmann's H-theorem.

Global neoclassical computations

A possible extension of the computations presented in this thesis is the global simulation of turbulence, starting from a neoclassical equilibrium. Nonlinear interactions between the neoclassical equilibrium and turbulent fluctuations are of special interest, but have not yet been studied with continuum gyrokinetic codes like GENE. With respect to heat and particle sources that are necessary to obtain a steady state in the simulation, Krook terms have been employed thus far. A more realistic power deposition profile would be reached in flux-driven simulations, which typically require very long simulation times and are thus not attempted here. Furthermore, it could be interesting to apply the global neoclassical solver to tokamak discharges that exhibit internal transport barriers, where strong deviations from local results are expected.

Microtearing turbulence

We have shown that microtearing modes are a possible candidate to explain anomalous electron heat transport. Our nonlinear simulation scenario, however, has not considered the ITG instability despite its typical co-existence with microtearing modes in the linear wavenumber spectrum. The most natural extension to our work is thus to study the interaction between ITG and microtearing modes in fully developed turbulence. Such simulations are very demanding and we leave them for future work.

A. The gyroaveraged Fokker-Planck operator

A.1. Explicit transformation to guiding center coordinates

The gyrokinetic equation evolves the gyrocenter distribution function F_{1a} in time, which is evaluated at the gyrocenter position $\mathbf{X}$. It is of significant computational advantage to evaluate the collision operator with this distribution as well. Thus far, the collision operator has been written in terms of the particle distribution, that is evaluated at particle position $\mathbf{x}$. While it is well justified to evaluate the macroscopic background $F_0(\mathbf{X})$ at gyrocenter instead of particle position, this is not a-priori clear for the microscopic perturbation f_1. However, according tho Eq. (2.1.29) that has been derived in the limit of long collisional mean free path λ_{mfp} it is actually correct to evaluate the gyroaveraged operator $\langle C[\langle F(\mathbf{X}^{(gc)})\rangle]\rangle$ with the guiding center distribution at guiding center position $\mathbf{X}^{(gc)}$ instead of $f(\mathbf{x})$, retaining only zeroth order terms in $\epsilon_\nu = \rho_a/\lambda_{\mathrm{mfp}}$. A sophisticated transformation of of the Fokker-Planck operator Eq. (2.1.13) to guiding center coordinates is given by Brizard [28] for isotropic background species making use of a non-canonical Poisson bracket structure. The results are equivalent to the transformation presented in this section and remove fast-angle dependencies due to a background magnetic field that is non-uniform, but constant in time. The difference between gyro center and guiding center coordinates will not be considered for collisions. In the drift-kinetic limit $k_\perp \rho \to 0$ this treatment is consistent also with the conservation properties Eq. (2.1.23).

A.1.1. Test particle operator

A transformation of Eq. (2.1.13) to guiding center phase space coordinates Z_i involves the Jacobian of this transformation in the phase space divergence $J^{-1}\frac{\partial}{\partial \mathbf{Z}} \cdot J()$. One explicit choice are pitch-angle coordinates $Z_i = \{\mathbf{X}, v, \xi, \theta\}$ with the Jacobian $J_{\mathrm{pitch}} = v^2$ and $\xi = v_\parallel/v$. Such coordinates are used, for example in Ref. [16] to denote Eq. (2.1.13). The GENE code uses $Z_i = \{\mathbf{X}, v_\parallel, \mu, \theta\}$ with parallel velocity $v_\parallel$, magnetic moment $\mu = \sqrt{v_\perp^2/2mB_0}$ and gyroangle θ as velocity space coordinates, where $v_\perp^2 = v_x^2 + v_y^2$. The guiding center coordinates are

$$\mathbf{X} = \mathbf{x} - \boldsymbol{\rho}(\theta) \tag{A.1.1}$$

with $\mathbf{x} = \{x, y, z\}$. We take the gyration vector and velocity as

$$\boldsymbol{\rho} = \frac{v_\perp}{\Omega}\left[\hat{\mathbf{e}}_1 \cos\theta - \hat{\mathbf{e}}_2 \sin\theta\right]$$
$$\mathbf{v} = v_\parallel \mathbf{b}_0 + v_\perp\left[-\hat{\mathbf{e}}_1 \sin\theta - \hat{\mathbf{e}}_2 \cos\theta\right],$$

to find that the velocity space Jacobian $J_v = B_0/m_a$ is constant in velocity space.[1] With the Jakobi matrix

$$\mathbf{G} = \begin{pmatrix} \frac{\partial X}{\partial v_x} & \frac{\partial Y}{\partial v_x} & \frac{\partial Z}{\partial v_x} & \frac{\partial v_\parallel}{\partial v_x} & \frac{\partial \mu}{\partial v_x} & \frac{\partial \theta}{\partial v_x} \\ \frac{\partial X}{\partial v_y} & \frac{\partial Y}{\partial v_y} & \frac{\partial Z}{\partial v_y} & \frac{\partial v_\parallel}{\partial v_y} & \frac{\partial \mu}{\partial v_y} & \frac{\partial \theta}{\partial v_y} \\ \frac{\partial X}{\partial v_z} & \frac{\partial Y}{\partial v_z} & \frac{\partial Z}{\partial v_z} & \frac{\partial v_\parallel}{\partial v_z} & \frac{\partial \mu}{\partial v_z} & \frac{\partial \theta}{\partial v_z} \end{pmatrix} = \frac{1}{v_\perp}\begin{pmatrix} 0 & \rho_a & 0 & 0 & -2\mu\sin\theta & -\cos\theta \\ -\rho_a & 0 & 0 & 0 & -2\mu\cos\theta & \sin\theta \\ 0 & 0 & v_\perp & v_\perp & 0 & 0 \end{pmatrix}.$$

the diffusion tensor and advection vector of Eq. (2.1.9) are transformed according to the chain rule of derivatives as

$$\frac{\partial}{\partial \mathbf{v}} \cdot \overleftrightarrow{\mathcal{D}}_{ab} \cdot \frac{\partial}{\partial \mathbf{v}} = \frac{1}{J_v}\frac{\partial}{\partial \mathbf{Z}} \cdot J_v \overleftrightarrow{\mathcal{D}}^Z_{ab} \cdot \frac{\partial}{\partial \mathbf{Z}} \tag{A.1.2}$$
$$\overleftrightarrow{\mathcal{D}}^Z_{ab} = \mathbf{G}^T \overleftrightarrow{\mathcal{D}}_{ab} \mathbf{G}$$

$$\frac{\partial}{\partial \mathbf{v}} \cdot \mathbf{R}_{ab} = \frac{1}{J_v}\frac{\partial}{\partial \mathbf{Z}} \cdot J_v \mathbf{R}^Z_{ab} \tag{A.1.3}$$
$$\mathbf{R}^Z_{ab} = \mathbf{G}^T \mathbf{R}_{ab}(z)$$

Note that position and velocity coordinates are mixed by Eq. (A.1.1) and, consequently, $\overleftrightarrow{D}^Z_{ab}$ and $\mathbf{R}^Z_{ab}$ have nonvanishing (X, Y) spatial components. The desired form of the collision operator

$$\langle C^T_{ab}[\langle F\rangle]\rangle = \frac{1}{J_v}\frac{\partial}{\partial \mathbf{Z}} \cdot \left(J_v \langle \overleftrightarrow{\mathcal{D}}^Z_{ab}\rangle \frac{\partial \langle F\rangle}{\partial \mathbf{Z}} + J_v \langle \mathbf{R}^Z_{ab}\rangle \langle F\rangle \right)$$

is constructed by gyroaverage $\langle\rangle = \frac{1}{2\pi}\int_0^{2\pi} \mathrm{d}\theta$ to consistently remove the fast gyration time-scale from the equations. Thereby, the spatial components of $\langle \mathbf{R}^Z_{ab}\rangle$ vanish, while the spatial part of $\langle \overleftrightarrow{D}^Z_{ab}\rangle$ decouples from the velocity components. The gyroangle component is decoupled itself and thus we can identify $F = \langle F\rangle$ from now on. Detailed calculations are found in Ref. [15]. Here, the results are summarized with the difference of using the f_a/f_M form. Because the Landau-Boltzmann collisions are local in particle space, a spatial guiding center diffusion operator

$$\langle C^{T,\perp}_{ab}[F_a]\rangle = \frac{1}{J_v}\frac{\gamma_{ab} n_{0b} T_{0b}}{m_a^2 m_b \Omega_a^2}\frac{1}{v^5}\left(v^2 \Phi_1(x_b) + \frac{3B_0\mu}{m_a}\Phi_2(x_b)\right)\nabla_\perp \cdot J_v F_{Ma} \nabla_\perp \frac{F_a}{F_{Ma}} \tag{A.1.4}$$

[1] Canonical transformation (e.g. Ref. [27]) yields $J_v = B^*_{0\parallel}/m_a = B_0/m + \mathcal{O}(\beta)$. This (small) difference is neglected here.

is found that describes the repositioning of the guiding center after a collision. This term is referred to as a FLR correction to the test particle collision operator. The remaining diffusion/advection operator in guiding center velocity space $\mathbf{V} = (v_\parallel, \mu)$ reads

$$\langle C_{ab}^{T,V}[F_a]\rangle = \frac{1}{J_v}\frac{\gamma_{ab} n_{0b}}{m_a m_b}\frac{\partial}{\partial \mathbf{V}} \cdot J_v F_{Ma}\left(\frac{T_{0b}}{m_a v^5}\begin{bmatrix} \frac{2\mu B_0}{m_a}\Phi_1 + v_\parallel^2\Phi_2 & 6\mu v_\parallel \Phi_2 \\ 6\mu v_\parallel \Phi_2 & \frac{2m_a}{B_0}v_\parallel^2\mu\Phi_1 + 4\mu^2\Phi_3 \end{bmatrix}\cdot\frac{\partial}{\partial \mathbf{V}}\right. \tag{A.1.5}$$
$$\left. + \left(1 - \frac{T_{0b}}{T_{0a}}\right)\frac{\Phi_3}{v^3}\begin{bmatrix} v_\parallel \\ 2\mu \end{bmatrix}\right)\frac{F_a}{F_{Ma}},$$

which equals Eq.(2.1.40).

A.1.2. Field particle operator and discussion of FLR effects

Test particle collisions involve velocity space derivatives at constant particle position $\mathbf{x}$, not at constant gyrocenter position $\mathbf{X}$, which is why the gyrodiffusion terms in the test-particle operator appear. A gyroaveraged field-particle operator thus has the form

$$\begin{aligned}\left\langle C_{ab}^F[f_b]\right\rangle_a = & \frac{\left\langle \delta\dot{\mathcal{P}}_{\parallel ba}\right\rangle_a C_{ab}^T[v_\parallel f_{Ma}]}{\int \mathrm{d}^3v\, v_\parallel C_{ab}[v_\parallel f_{Ma}, f_{Mb}]} \\ & + \frac{\left\langle \delta\dot{\boldsymbol{\mathcal{P}}}_{\perp ba} C_{ab}^T[\mathbf{v}_\perp f_{Ma}]\right\rangle_a}{\frac{1}{2}\int \mathrm{d}^3v\, \mathbf{v}_\perp \cdot C_{ab}(\mathbf{v}_\perp f_{Ma}, f_{Mb}]} \\ & + \frac{\left\langle \delta\dot{\mathcal{E}}_{ba}\right\rangle_a C_{ab}^T[v^2 f_{Ma}]}{\int \mathrm{d}^3v\, m_a v^2 C_{ab}[v^2 f_{Ma}, f_{Mb}]},\end{aligned} \tag{A.1.6}$$

where the notation $\langle\rangle_a$ denotes gyroaverage considering gyration orbits of species a. Note that the perpendicular momentum transfer coefficient is gyroangle-dependent. The transfer terms

$$\begin{aligned}\delta\dot{\mathcal{P}}_{\parallel ba} &= -\int m_b v_\parallel \left\langle C_{ba}^T[f_b]\right\rangle_b J_v \mathrm{d}v_\parallel \mathrm{d}\mu \\ \delta\dot{\boldsymbol{\mathcal{P}}}_{\perp ba} &= -\int m_b \left\langle \mathbf{v}_\perp C_{ba}^T[f_b]\right\rangle_b J_v \mathrm{d}v_\parallel \mathrm{d}\mu \\ \delta\dot{\mathcal{E}}_{ba} &= -\int m_b v^2 \left\langle C_{ba}^T[f_b]\right\rangle_b J_v \mathrm{d}v_\parallel \mathrm{d}\mu\end{aligned} \tag{A.1.7}$$

involve gyroaverages at species b (we explicitly write them in $(v_\parallel, \mu, \theta)$ coordinates here). Neglecting the FLR effects has the following consequences. (i) gyroaverages

for different particle species are equal. (ii) guiding center and gyrocenter distributions are equal.[2] (iii) the perpendicular term $\left\langle \mathbf{v}_\perp C_{ba}^T[f_b] \right\rangle_b$ vanishes. In this limit one identifies $\left\langle \left\langle C_{ba}^T[f_b(x)] \right\rangle_b \right\rangle_a = \left\langle C_{ba}^{T,V}[F_b(X)] \right\rangle$ from Eq. (A.1.5) (note the change of coordinates) and thus computes the transfer rates Eq. (A.1.7) directly from the test-particle operator. This property nicely translates into numerical implementation. Several authors [16, 20, 21, 28, 121] have discussed operators including FLR corrections. In this thesis FLR corrections in the collision term are believed to play a minor role and are thus neglected. A corresponding extension of the GENE code is planned, though.

[2]This becomes clear by examining the pull-back operator Eq. (2.1.51).

B. The scanscript and parallelization efficiency

In the course of this thesis some effort was made to improve the GENE code's capability of running large parameter sets. GENE features to invoke several instances of GENE subroutines, processing a set of input files in parallel. A perl script has been extended to provide the necessary input file structure for GENE. This so-called scanscript parses the input parameters file for parameter scans. Its detailed functionality and syntax is provided in the GENE users manual Ref. [122]. Automatic parallel efficiency tests are by default performed previous to every parameter scan. Parallelization efficiency is measured by the total wall clock time used for a Runge-Kutta timestep, which is computed as the wall-clock time per time step multiplied with the number of CPUs used. A typical result is shown in Fig. B.0.1. An important feature is the maximum of parallel efficiency at a processor number of 32 in this case. For larger number of processors, MPI communication becomes inefficient, while for smaller number of processors, cash memory is not optimally used. The optimum between these two effects is generally machine dependent and hard to predict. Consequently, the automated procedure provided here helps to reduce computation time. Using optimal parallelization efficiency yields significant speedup, in particular for large parameter scans.

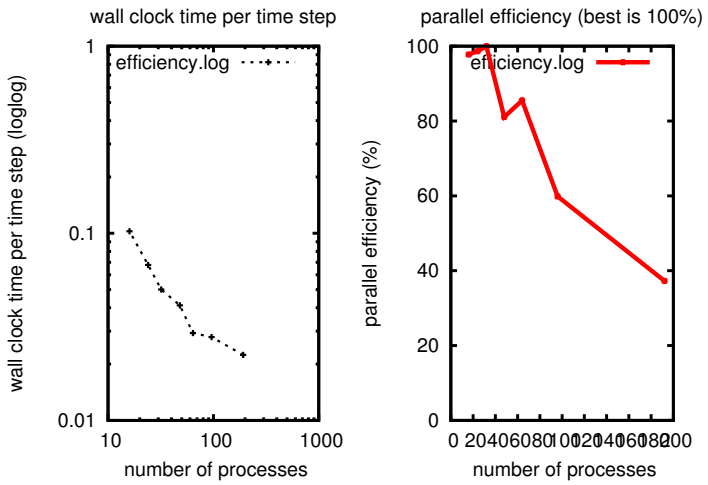

Figure B.0.1.: Efficiency scan. The wall clock time per step decreases up ot 192 processes, but efficiency decreases to 40% of the optimum that is reached with 32 processes in this case.

Bibliography

[1] The Alpha Collaboration, G. B. Andresen, M. D. Ashkezari, M. Baquero-Ruiz, W. Bertsche, P. D. Bowe, E. Butler, C. L. Cesar, M. Charlton, A. Deller, S. Eriksson, J. Fajans, T. Friesen, M. C. Fujiwara, D. R. Gill, A. Gutierrez, J. S. Hangst, W. N. Hardy, R. S. Hayano, M. E. Hayden, A. J. Humphries, R. Hydomako, S. Jonsell, S. L. Kemp, L. Kurchaninov, N. Madsen, S. Menary, P. Nolan, K. Olchanski, A. Olin, P. Pusa, C. Ø. Rasmussen, F. Robicheaux, E. Sarid, D. M. Silveira, C. So, J. W. Storey, R. I. Thompson, D. P. van der Werf, J. S. Wurtele, and Y. Yamazaki, Nat. Phys. **7**, 558 (2011).

[2] J. M. Stone, J. F. Hawley, C. F. Gammie, and S. A. Balbus, Astrophys. Journal **463**, 656 (1996).

[3] S. A. Balbus and J. F. Hawley, Rev. Mod. Phys. **70**, 1 (1998).

[4] "http://www.iter.org," (2012).

[5] W. Horton, Rev. Mod. Phys. **71**, 735 (1999).

[6] J. Wesson, *Tokamaks*, 3rd ed. (Clarendon Press - Oxford, 2004).

[7] P. Helander and D. Sigmar, *Collisional Transport in Magnetized Plasmas*, 1st ed. (Cambridge University Press - Cambridge, UK, 2002).

[8] F. L. Hinton and R. D. Hazeltine, Rev. Mod. Phys. **48**, 239 (1976).

[9] H. Doerk, F. Jenko, M. J. Pueschel, and D. R. Hatch, Phys. Rev. Lett. **106**, 155003 (2011).

[10] H. Doerk, F. Jenko, T. Görler, D. Told, M. J. Pueschel, and D. R. Hatch, Phys. Plasmas **19**, 055907 (2012).

[11] S. I. Braginskii, Reviews of Plasma Physics **1**, 205 (1965).

[12] D. L. Book, "NRL (Naval Research Laboratory) plasma formulary, revised," (2011).

[13] L. D. Landau, Physikalische Zeitschrift der Sowjetunion **10**, 154 (1936).

[14] R. Hazeltine and F. Waelbroeck, *Framework of Plasma Physics*, Frontiers in Physics (Perseus Books - Reading, Massachusetts, 1998).

[15] F. Merz, *Gyrokinetic Simulation of Multimode Plasma Turbulence*, Ph.D. thesis, Universität Münster (2009).

[16] H. Sugama, T.-H. Watanabe, and M. Nunami, Phys. Plasmas **16**, 112503 (2009).

[17] J. Candy and E. A. Belli, Phys. Rev. Lett. **106**, 235003 (2011).

[18] E. A. Belli and J. Candy, Plasma Phys. Controlled Fusion **54**, 015015 (2012).

[19] E. Belli and J. Candy, APS Meeting Abstracts , CP9.00075 (2011).

[20] M. Barnes, I. G. Abel, W. Dorland, D. R. Ernst, G. W. Hammett, P. Ricci, B. N. Rogers, A. A. Schekochihin, and T. Tatsuno, Phys. Plasmas **16**, 072107 (2009).

[21] I. G. Abel, M. Barnes, S. C. Cowley, W. Dorland, and A. A. Schekochihin, Phys. Plasmas **15**, 122509 (2008).

[22] S. Brunner, unpublished, private communication (2010).

[23] Z. Lin, W. M. Tang, and W. W. Lee, Phys. Plasmas **2**, 2975 (1995).

[24] T. Vernay, S. Brunner, L. Villard, B. F. McMillan, S. Jolliet, T. M. Tran, A. Bottino, and J. P. Graves, Phys. Plasmas **17**, 122301 (2010).

[25] X. Q. Xu and M. N. Rosenbluth, Phys. Fluids B **3**, 627 (1991).

[26] R. G. Littlejohn, J. Math. Phys. **23**, 742 (1982).

[27] A. J. Brizard and T. S. Hahm, Rev. Mod. Phys. **79**, 421 (2007).

[28] A. J. Brizard, Phys. Plasmas **11**, 4429 (2004).

[29] D. Told, *Gyrokinetic Microturbulence in Transport Barriers*, Ph.D. thesis, Universität Ulm (2012).

[30] T. Görler, *Mulitscale Effects in Plasma Microturbulence*, Ph.D. thesis, Universität Ulm (2009).

[31] J. Candy, R. E. Waltz, S. E. Parker, and Y. Chen, Phys. Plasmas **13**, 074501 (2006).

[32] Y. Idomura, M. Ida, S. Tokuda, and L. Villard, J. Comput. Phys. **226**, 244 (2007).

[33] S. Jolliet, *Gyrokinetic particle-in-cell global simulations of ion-temperature-gradient and collisionless trapped-electron mode turbulence tokamaks*, Ph.D. thesis, École Polytechnique Fédérale de Lausanne (2009).

[34] W. D'Haeseleer, *Flux Coordinates and Magnetic Field Structure: A Guide to a Fundamental Tool for Plasma Theory* (Springer Verlag, 1991).

[35] E. A. Belli and J. Candy, Plasma Phys. Controlled Fusion **50**, 095010 (2008).

[36] P. Helander, Phys. Plasmas **7**, 2878 (2000).

[37] P. Helander, Plasma Phys. Controlled Fusion **37**, 57 (1995).

[38] T. Görler, "Local GENE Observables," GENE documentation–http://www.gene.rzg.mpg.de.

[39] T. Görler, X. Lapillonne, S. Brunner, T. Dannert, F. Jenko, F. Merz, and D. Told, J. Comput. Phys. **230**, 7053 (2011).

[40] T. Dannert, *Gyrokinetische Simulation von Plasmaturbulenz mit gefangenen Teilchen und elektromagnetischen Effekten*, Ph.D. thesis, Techniche Universität München (2004).

[41] F. Merz, C. Kowitz, E. Romero, J. Roman, and F. Jenko, Comput. Phys. Commun. **183**, 922 (2012).

[42] C. Kowitz, *Preconditioning for Fast Linear Computations with the Plasma Turbulence Code GENE*, Ph.D. thesis, Technische Universität München (2011).

[43] M. J. Pueschel, T. Dannert, and F. Jenko, Comput. Phys. Commun. **181**, 1428 (2010).

[44] B. F. McMillan, S. Jolliet, T. M. Tran, L. Villard, A. Bottino, and P. Angelino, Phys. Plasmas **15**, 052308 (2008).

[45] S. Hirshman and D. Sigmar, Nucl. Fusion **21**, 1079 (1981).

[46] R. Balescu, *Transport Processes in Plasmas*, 1st ed. (North-Holland, Amsterdam, 1988).

[47] T. Vernay, S. Brunner, L. Villard, B. F. McMillan, S. Jolliet, T. M. Tran, and A. Bottino, Phys. Plasmas **19**, 042301 (2012).

[48] H. Sugama and W. Horton, Phys. Plasmas **3**, 304 (1996).

[49] L. Onsager, Phys. Rev. **37**, 405 (1931).

[50] L. Onsager, Phys. Rev. **38**, 2265 (1931).

[51] R. Balescu, Phys. Fluids B **3**, 564 (1991).

[52] "http://www.mcs.anl.gov/petsc/," (2012).

[53] M. Taguchi, Plasma Phys. Controlled Fusion **30**, 1897 (1988).

[54] M. Oberparleiter, *Neoklassischer Transport*, Master's thesis, Universität Bayreuth (2011).

[55] X. Lapillonne, S. Brunner, T. Dannert, S. Jolliet, A. Marinoni, L. Villard, T. Görler, F. Jenko, and F. Merz, Phys. Plasmas **16**, 032308 (2009).

[56] M. Barnes, I. G. Abel, W. Dorland, T. Görler, G. W. Hammett, and F. Jenko, Phys. Plasmas **17**, 056109 (2010).

[57] F. Jenko, W. Dorland, M. Kotschenreuther, and B. N. Rogers, Phys. Plasmas **7**, 1904 (2000).

[58] W. Guttenfelder, J. Candy, S. M. Kaye, W. M. Nevins, E. Wang, R. E. Bell, G. W. Hammett, B. P. Leblanc, D. R. Mikkelsen, and H. Yuh, Phys. Rev. Lett. **106**, 155004 (2011).

[59] D. R. Hatch, M. J. Pueschel, F. Jenko, W. M. Nevins, P. W. Terry, and H. Doerk, Phys. Rev. Lett. **108**, 235002 (2012).

[60] W. M. Nevins, E. Wang, and J. Candy, Phys. Rev. Lett. **106**, 065003 (2011).

[61] E. Wang, W. M. Nevins, J. Candy, D. Hatch, P. Terry, and W. Guttenfelder, Phys. Plasmas **18**, 056111 (2011).

[62] T. H. Stix, Phys. Rev. Lett. **30**, 833 (1973).

[63] R. D. Hazeltine, D. Dobrott, and T. S. Wang, Phys. Fluids **18**, 1778 (1975).

[64] J. F. Drake and Y. C. Lee, Phys. Fluids **20**, 1341 (1977).

[65] L. Chen, P. H. Rutherford, and W. M. Tang, Phys. Rev. Lett. **39**, 460 (1977).

[66] J. D. Callen, Phys. Rev. Lett. **39**, 1540 (1977).

[67] M. J. Pueschel, M. Kammerer, and F. Jenko, Phys. Plasmas **15**, 102310 (2008).

[68] M. Kotschenreuther, W. Dorland, Q. P. Liu, M. C. Zarnstorff, R. L. Miller, and Y. R. Lin-Liu, Nucl. Fusion **40**, 677 (2000).

[69] M. H. Redi, S. M. Kaye, W. Dorland, R. Bell, C. Bourdelle, S. Ethier, D. Gates, G. Hammet, K. Hill, B. LeBlanc, D. McCune, J. Menard, D. Mikkelsen, G. Rewoldt, and E. Synakowski, 31st EPS Conf. on Controlled Fusion and Plasma Physics (Tarragona) , P (2004).

[70] M. H. Redi, W. Dorland, C. L. Fiore, D. Stutman, J. A. Baumgaertel, B. Davis, S. M. Kaye, D. C. McCune, J. Menard, and G. Rewoldt, 32nd EPS Conf. on Controlled Fusion and Plasma Physics (Tarragona) , P (2005).

[71] H. R. Wilson, J.-W. Ahn, R. J. Akers, D. Applegate, R. A. Cairns, J. P. Christiansen, J. W. Connor, G. Counsell, A. Dnestrovskij, W. D. Dorland, M. J. Hole, N. Joiner, A. Kirk, P. J. Knight, C. N. Lashmore-Davies, K. G. McClements, D. E. McGregor, M. R. O'Brien, C. M. Roach, S. Tsaun, and G. M. Voss, Nucl. Fusion **44**, 917 (2004).

[72] D. J. Applegate, C. M. Roach, S. C. Cowley, W. D. Dorland, N. Joiner, R. J. Akers, N. J. Conway, A. R. Field, A. Patel, M. Valovic, and M. J. Walsh, Phys. Plasmas **11**, 5085 (2004).

[73] C. M. Roach, D. J. Applegate, J. W. Connor, S. C. Cowley, W. D. Dorland, R. J. Hastie, N. Joiner, S. Saarelma, A. A. Schekochihin, R. J. Akers, C. Brickley, A. R. Field, M. Valovic, and the MAST Team, Plasma Phsy. Controlled Fusion **47**, B323 (2005).

[74] D. J. Applegate, *Gyrokinetic Studies of a Spherical Tokamak H-mode Plasma*, Ph.D. thesis, University of London (2006).

[75] K. L. Wong, S. Kaye, D. R. Mikkelsen, J. A. Krommes, K. Hill, R. Bell, and B. Leblanc, Phys. Rev. Lett. **99**, 135003 (2007).

[76] K. L. Wong, S. Kaye, D. R. Mikkelsen, J. A. Krommes, K. Hill, R. Bell, and B. Leblanc, Phys. Plasmas **15**, 056108 (2008).

[77] D. J. Applegate, C. M. Roach, J. W. Connor, S. C. Cowley, W. Dorland, R. J. Hastie, and N. Joiner, Plasma Phsy. Controlled Fusion **49**, 1113 (2007).

[78] L. Vermare, C. Angioni, A. Bottino, A. G. Peeters, and ASDEX Upgrade Team, J. Phys. Conference Series **123**, 012040 (2008).

[79] D. Told, F. Jenko, P. Xanthopoulos, L. D. Horton, E. Wolfrum, and ASDEX Upgrade Team, Phys. Plasmas **15**, 102306 (2008).

[80] I. Predebon, F. Sattin, M. Veranda, D. Bonfiglio, and S. Cappello, Phys. Rev. Lett. **105**, 195001 (2010).

[81] J. F. Drake, N. T. Gladd, C. S. Liu, and C. L. Chang, Phys. Rev. Lett. **44**, 994 (1980).

[82] W. Guttenfelder, J. Candy, S. M. Kaye, W. M. Nevins, E. Wang, J. Zhang, R. E. Bell, N. A. Crocker, G. W. Hammett, B. P. LeBlanc, D. R. Mikkelsen, Y. Ren, and H. Yuh, Phys. Plasmas **19**, 056119 (2012).

[83] W. Guttenfelder, J. Candy, S. M. Kaye, W. M. Nevins, R. E. Bell, G. W. Hammett, B. P. Leblanc, and H. Yuh, Phys. Plasmas **19**, 022506 (2012).

[84] T. Görler, X. Lapillonne, S. Brunner, J. Chowdhury, T. Dannert, F. Jenko, B. F. McMillan, F. Merz, D. Told, and L. Villard, J. Phys. Conference Series **260**, 012011 (2010).

[85] B. F. McMillan, X. Lapillonne, S. Brunner, L. Villard, S. Jolliet, A. Bottino, T. Görler, and F. Jenko, Phys. Rev. Lett. **105**, 155001 (2010).

[86] H. P. Furth, J. Killeen, and M. N. Rosenbluth, Phys. Fluids **6**, 459 (1963).

[87] H. P. Furth, P. H. Rutherford, and H. Selberg, Phys. Fluids **16**, 1054 (1973).

[88] J. F. Drake and Y. C. Lee, Phys. Rev. Lett. **39**, 453 (1977).

[89] A. B. Hassam, Phys. Fluids **23**, 2493 (1980).

[90] A. B. Hassam, Phys. Fluids **23**, 38 (1980).

[91] M. Rosenberg, R. R. Dominguez, W. Pfeiffer, and R. E. Waltz, Phys. Fluids **23**, 2022 (1980).

[92] D. A. Dippolito, Y. C. Lee, and J. F. Drake, Phys. Fluids **23**, 771 (1980).

[93] N. T. Gladd, J. F. Drake, C. L. Chang, and C. S. Liu, Phys. Fluids **23**, 1182 (1980).

[94] R. R. Dominguez, M. Rosenberg, and C. S. Chang, Phys. Fluids **24**, 472 (1981).

[95] P. J. Catto and M. N. Rosenbluth, Phys. Fluids **24**, 243 (1981).

[96] J. W. Connor, S. C. Cowley, and R. J. Hastie, Plasma Phsy. Controlled Fusion **32**, 799 (1990).

[97] D. R. Hatch, *Mode Analyses of Gyrokinetic Simulations of Plasma Microturbulence*, Ph.D. thesis, University of Wisconsin - Madison (2010).

[98] D. R. Hatch, P. W. Terry, F. Jenko, F. Merz, M. J. Pueschel, W. M. Nevins, and E. Wang, Phys. Plasmas **18**, 055706 (2011).

[99] J. Boom, E. Wolfrum, I. Classen, P. de Vries, M. Maraschek, W. Suttrop, C. P. von Thun, A. Donné, B. Tobias, C. Domier, N. Luhmann Jr, H. Park, and the ASDEX Upgrade Team, Nucl. Fusion **52**, 114004 (2012).

[100] E. Wolfrum, M. Bernert, J. E. Boom, A. Burckhart, I. G. J. Classen, G. D. Conway, T. Eich, R. Fischer, A. Gude, A. Herrmann, N. C. Luhmann, Jr., M. Maraschek, R. McDermott, H. K. Park, T. Pütterich, J. Vicente, B. Wieland, M. Willensdorfer, and the ASDEX Upgrade Team, Plasma Phsy. Controlled Fusion **53**, 085026 (2011).

[101] T. Görler, X. Lapillonne, S. Brunner, T. Dannert, F. Jenko, S. K. Aghdam, P. Marcus, B. F. McMillan, F. Merz, O. Sauter, D. Told, and L. Villard, Phys. Plasmas **18**, 056103 (2011).

[102] D. R. Smith, W. Guttenfelder, B. P. LeBlanc, and D. R. Mikkelsen, Plasma Phsy. Controlled Fusion **53**, 035013 (2011).

[103] M. J. Pueschel, F. Jenko, D. Told, and J. Büchner, Phys. Plasmas **18**, 112102 (2011).

[104] R. Numata, W. Dorland, G. G. Howes, N. F. Loureiro, B. N. Rogers, and T. Tatsuno, Phys. Plasmas **18**, 112106 (2011).

[105] S. C. Cowley, R. M. Kulsrud, and T. S. Hahm, Phys. Fluids **29**, 3230 (1986).

[106] J. F. Drake, T. M. Antonsen, Jr., A. B. Hassam, and N. T. Gladd, Phys. Fluids **26**, 2509 (1983).

[107] G. W. Hammett, W. Dorland, N. F. Loureiro, and T. Tatsuno, in *APS Meeting Abstracts* (2006) p. 1136P.

[108] B. V. Chirikov, Phys. Rep. **52**, 263 (1979).

[109] A. M. Dimits, G. Bateman, M. A. Beer, B. I. Cohen, W. Dorland, G. W. Hammett, C. Kim, J. E. Kinsey, M. Kotschenreuther, A. H. Kritz, L. L. Lao, J. Mandrekas, W. M. Nevins, S. E. Parker, A. J. Redd, D. E. Shumaker, R. Sydora, and J. Weiland, Phys. Plasmas **7**, 969 (2000).

[110] J. A. Krommes, C. Oberman, and R. G. Kleva, J. Plasma Phys. **30**, 11 (1983).

[111] R. W. Harvey, M. G. McCoy, J. Y. Hsu, and A. A. Mirin, Phys. Rev. Lett. **47**, 102 (1981).

[112] Z. Chang and J. D. Callen, Phys. Fluids B **4**, 1167 (1992).

[113] D. Del-Castillo-Negrete and L. Chacón, Phys. Rev. Lett. **106**, 195004 (2011).

[114] F. Jenko, T. Dannert, and C. Angioni, Plasma Phys. Controlled Fusion **47**, B195 (2005).

[115] T. Dannert and F. Jenko, Phys. Plasmas **12**, 072309 (2005).

[116] H. Sugama, M. Okamoto, W. Horton, and M. Wakatani, Phys. Plasmas **3**, 2379 (1996).

[117] M. A. Beer, S. C. Cowley, and G. W. Hammett, Phys. Plasmas **2**, 2687 (1995).

[118] F. Jenko and A. Kendl, Phys. Plasmas **9**, 4103 (2002).

[119] W. Dorland, F. Jenko, M. Kotschenreuther, and B. N. Rogers, Phys. Rev. Lett. **85**, 5579 (2000).

[120] F. Merz and F. Jenko, Phys. Rev. Lett. **100**, 035005 (2008).

[121] A. A. Schekochihin, S. C. Cowley, W. Dorland, G. W. Hammett, G. G. Howes, E. Quataert, and T. Tatsuno, Astrophys. J., Suppl. **182**, 310 (2009).

[122] The GENE Development Team, "GENE User Manual," GENE documentation–http://www.gene.rzg.mpg.de.

List of publications

Publications in peer-reviewed journals

1. D. R. Hatch, M. J. Pueschel, W. M. Nevins, F. Jenko, P. W. Terry and H. Doerk
Origin of Magnetic Stochasticity and Transport in Plasma Microturbulence
Phys. Rev. Lett. **108**, 235002 (2012)

2. H. Doerk, F. Jenko, T. Görler, D. Told, M. J. Pueschel and D. R. Hatch
Gyrokinetic prediction of microtearing turbulence in standard tokamaks
Phys. Plasmas **19**, 055907 (2012)

3. H. Doerk, F. Jenko, M. J. Pueschel, and D. R. Hatch.
Gyrokinetic Microtearing Turbulence
Phys. Rev. Lett. **106**, 155003 (2011)

4. J. Goold, H. Doerk, Z. Idziaszek, T. Calarco and Th. Busch
Ion-induced density bubble in a strongly correlated one-dimensional gas
Phys. Rev. A **81**, 041601(R) (2010)

5. H. Doerk, Z. Idziaszek and T. Calarco
Atom-ion quantum gate
Phys. Rev. A **81**, 012708 (2010)

Oral and poster presentations

1. H. Doerk, F. Jenko, T. Görler, D. Told, M. J. Pueschel and D. R. Hatch
Tearing Mode Turbulence in ASDEX Upgrade: Gyrokinetic Simulations
(oral presentation)
IPP Theory Meeting, Schloss Liebenberg, December 2011.

2. H. Doerk, F. Jenko, T. Görler, D. Told, M. J. Pueschel and D. R. Hatch
Tearing-mode turbulence in standard tokamaks: Gyrokinetic prediction
(invited talk)
APS DPP annual meeting, Salt Lake City, November 2011.

3. H. Doerk and F. Jenko
Field line breaking in tokamaks (oral contribution)
Winter School Turbulence, Les Houches, February 2011

4. H. Doerk and F. Jenko
   Gyrokinetic studies of microtearing turbulence (oral presentation)
   IPP Theory Meeting, Schloss Ringberg, December 2011.

5. H. Doerk and F. Jenko
   Progress in gyrokinetic simulation of microtearing turbulence
   (oral presentation)
   Gyrokinetics for ITER workshop, Wolfgang-Pauli-Institut,Vienna, March 2010.

6. H. Doerk and F. Jenko
   Progress in gyrokinetic simulation of microtearing turbulence
   (oral presentation)
   IPP theory meeting, Sellin, December 2009.

7. H. Doerk and F. Jenko
   Progress in gyrokinetic simulation of microtearing turbulence (oral presentation)
   Math and ITER workshop, CIRM, Marseille, October 2009.

8. H. Doerk, Z. Idziaszek and T. Calarco
   Controlled atom-ion entanglement (poster presentation)
   SFB TR 23 workshop, Schloss Reisensburg, December 2008

9. H. Doerk, Z. Idziaszek and T. Calarco
   An atom-ion quantum gate (oral presentation)
   Presentation of a diploma thesis, Universität Ulm, December 2008

10. H. Doerk, Z. Idziaszek and T. Calarco
    Atom Ion Gate (oral presentation)
    Oberseminar Complex Quantum Dynamics , Universität Freiburg, May 2008

11. H. Doerk, Z. Idziaszek and T. Calarco
    Atom-ion quantum gate (poster presentation)
    DPG Frühjahrstagung, Darmstadt, March 2008